In vitro analysis of viral fusion and receptor binding with a focus on selected arthropod-borne viruses of the families *Bunyaviridae* and *Togaviridae*

David Bitto

A thesis submitted for the degree of

Doctor of Philosophy

Green Templeton College
Nuffield Department of Clinical Medicine
Division of Structural Biology
Oxford Particle Imaging Centre

Trinity term 2014

Table of contents

Abstract 8

Acknowledgements 9

1. Introduction 10

1.1. The importance of bunyaviruses and alphaviruses 10

1.2. Endocytosis, intracellular membrane traffic and phospholipids 12

1.2.1. Endocytosis: Overview 12

1.2.2. The endo – lysosomal pathway and low pH 13

1.2.3. Intracellular lipid distribution 14

1.2.4. Early and late endosomes, multivesicular bodies and lysosomes 16

1.3. The cell entry of enveloped viruses 19

1.3.1. Viral receptor binding at the cell surface 19

1.3.2. N-linked glycosylation 21

1.3.3. Viral endocytosis 26

1.3.4. Viral fusion 28

1.4. Bunyaviruses and alphaviruses: Molecular and structural biology. 34

1.4.1. Bunyaviruses 34

1.4.2. Alphaviruses 36

1.5. The cell entry of bunyaviruses and alphaviruses 37

1.5.1. Bunyavirus entry 37

1.5.2. Alphavirus entry 39

1.6. Electron cryo-microscopy and icosahedral reconstruction of enveloped icosahedral viruses 40

1.7. Aims 49

2. Materials and Methods 52

2.1. Cells and viruses 52

2.2. SDS-PAGE, western and dot blots 55

2.3. Pyrene labelling of viruses 57

2.4. Liposomes 58

2.5. Lipid mixing and content release assays 60

2.5.1. Lipid mixing of UUKV-pyr and SFV-pyr at pH 5 60

2.5.2. Lipid mixing of UUKV-pyr, BUNV-pyr and SFV-pyr at pH 4.5 . 61

2.5.3. Low pH and temperature dependence of UUKV-pyr 62

2.5.4. Content mixing assays 63

2.6. Low pH inactivation of UUKV 63

2.7. DC-SIGN expression and purification 64

2.7.1. Primers and plasmids 64

2.7.2. Sub-cloning the DC-SIGN fragments: Polymerase chain reaction, restriction digestion and ligation 66

2.7.3. Bacterial transformation and plasmid preparation 67

2.7.4. Protein expression in HEK cells 70

2.7.5. Protein purification: Diafiltration, nickel-NTA affinity chromatography and gel filtration 71

2.8. Enzyme-linked immune sorbent assay (ELISA) 72

2.9. Electron cryo-microscopy and tomography: sample preparation ... 74

2.9.1. Plunge-freezing of SSIP-1 and UUKV particles 74

2.9.2. Plunge-freezing of liposomes and virus-liposome complexes . 75

2.9.3. Plunge-freezing of SFV-DC-SIGN complexes 76

2.10. Electron cryo-microscopy in single particle mode 77

2.11. Icosahedral reconstruction of SSIP-1, UUKV and SFV-DC-SIGN particles 78

2.12. Two-dimensional image processing of UUKV spikes 82

2.13. Electron cryo-microscopy and tomography of UUKV liposome complexes 84

2.14. Fluorescence activated cell sorting (FACS) of UUKV infected cells 85

2.15. Virus glycan digestion and glycan analysis 86

2.16. Dynamic light scattering 87

2.17. UUKV-liposome flotation assays 88

3. Structural analysis of the Uukuniemi phlebovirus at low pH 89

3.1. Rationale 89

3.2. Icosahedral reconstruction of UUKV at neutral pH 91

3.3. Icosahedral reconstruction of the bacteriophage SSIP-1 99

3.4. Two-dimensional analysis of a phlebovirus at low pH 103

4. Structural and functional analysis of phlebovirus fusion 108

4.1. An in vitro fusion assay for Uukuniemi phlebovirus fusion 108

4.1.1. Rationale 108

4.1.2. Uukuniemi virus fluorescence labelling 111

4.2. UUKV lipid mixing 113

4.2.1. Efficient UUKV lipid mixing requires both negatively charged and cone-shaped phospholipids 113

4.2.2. UUKV lipid mixing: Low pH and temperature dependence ... 121

4.3. Liposome content release in presence of UUKV 124

4.4. Electron cryotomography of phlebovirus–liposome complexes ... 130

4.5. Physiological relevance of BMP in UUKV infection 137

5. Arbovirus – DC-SIGN interactions 140

5.1. Rationale 140

5.2. The N-linked glycosylation of UUKV and SFV 143

5.3. Production and purification of soluble DC-SIGN ectodomains for electron cryo-microscopy 147

5.4. Cryo-EM of SFV–DC-SIGN complexes and icosahedral reconstruction 152

6. Discussion 159

6.1. Summary 159

6.2. Icosahedral reconstruction of phleboviruses in native conditions 161

6.3. Low pH and phlebovirus fusion 163

6.3.1. Structural analysis of phlebovirus fusion at low pH 163

6.3.2. *Phlebovirus* fusion 168

6.3.3. Physiological analysis of phlebovirus fusion 179

6.4. Arbovirus-receptor interactions at the cell surface 182

6.4.1. DC-SIGN interactions with Semliki Forest virus 182

6.4.2. Future search for other phlebovirus receptors 187

6.5. Concluding remarks 189

7. References 191

8. Abbreviations 211

9. Appendix 213

9.1. Codon optimized DC-SIGN cDNA sequence (Geneart, 5' to 3') .. 213

9.2. Protein sequence encoded by the Geneart DC-SIGN nucleotide sequence 214

9.3. Publications and manuscripts in preparation based on work performed in this thesis 214

9.4. Supplementary figures 214

In vitro analysis of viral fusion and receptor binding with a focus on selected arthropod-borne viruses of the families *Bunyaviridae* and *Togaviridae*

David Bitto
A thesis submitted for the degree of *Doctor of Philosophy*
Green Templeton College, Nuffield Department of Clinical Medicine,
Division of Structural Biology, Oxford Particle Imaging Centre
University of Oxford, Trinity term 2014

Abstract

Emerging arthropod-borne viruses, such as alphaviruses and bunyaviruses, represent a serious threat to human and animal health worldwide, and for most of them, vaccines and specific treatments are unavailable. Viral host cell entry can be divided into several entry checkpoints, and the most important checkpoints for low pH-dependent enveloped viruses, such as bunyaviruses and alphaviruses, include receptor binding at the cell surface and, followed by endocytosis, low pH dependent membrane fusion from within intracellular compartments. A more thorough understanding of the detailed mechanisms allowing the viruses to pass these checkpoints is a pre-requisite for the design of viral entry inhibitors.

This thesis reports the *in vitro* analysis of native alphavirus-receptor interactions, with the help of electron cryo-microscopy and icosahedral reconstruction of virus-receptor complexes, using the prototypic alphavirus Semliki Forest virus (SFV) and the C-type lectin DC-SIGN. Together with results from collaborative work on SFV glycosylation, this study provides progress in defining the binding sites of DC-SIGN at the surface of SFV.

Second, an *in vitro* system for phlebovirus fusion was developed using standard fluorometry, and has been characterized with the help of electron cryo-microscopy. It was discovered that negatively charged phospholipids with a conical shape, including the late endosomal phospholipid BMP, allow efficient phlebovirus fusion *in vitro*, thereby providing a possible rationale for phlebovirus fusion in late endosomes. Furthermore, electron cryo-microscopy of phlebovirus-liposome complexes allowed the capture of early stage fusion intermediates and laid the basis for possible future higher resolution studies of these fusion intermediates.

Acknowledgements

First and foremost, I would like to thank my supervisors Juha Huiskonen and Kay Grünewald for their support, helpful discussions, and for giving me the opportunity to study at the Oxford Particle Imaging Centre (OPIC). My special thanks go to both Juha Huiskonen and Thomas Bowden for being great mentors and teachers, for the countless times they helped me, and for involving me in collaborative work.

I would also like to thank all the people from OPIC, but especially Alistair Siebert for his efforts to keep the electron microscopes in good shape and Robin Parsons for taking care of the containment laboratories. I also thank the people from the Division of Structural Biology (Strubi), and especially Margaret Jones for her great help in the laboratory, Weixian Lu for help with transfections, but also the students and post-docs for helping and useful discussions. I further thank Consuelo Anzilotti from the group of Peter Donnelly for helping with fluorescence activated cell sorting. Finally, I thank Pierre-Yves Lozach for first having introduced me to the exciting world of bunyaviruses during my previous studies in Zurich, and without whom I would not have considered doing doctoral studies on bunyaviruses.

Last but not least, I would like to thank the University of Oxford for having awarded me the Mary Goodger scholarship, the Academy of Finland for having funded the bulk of my studies, and Green Templeton College, for having provided financial help that allowed me to take part in international conferences to present my work.

I dedicate this thesis to my parents, Eugen and Simone.

1. Introduction

1.1. The importance of bunyaviruses and alphaviruses

The *Bunyaviridae* family is one of the largest virus families known to date, and is subdivided into the five genera: *Orthobunyavirus, Phlebovirus, Nairovirus, Tospovirus* and *Hantavirus* [1]. Most bunyaviruses are arthropod-borne viruses (arboviruses), and vectors include for example ticks, mosquitoes and thrips [2], while members from the *Hantavirus* genus are spread by rodents [3]. Many bunyaviruses infect humans and vertebrate animals, while members from the *Tospovirus* genus infect plants [4]. Bunyavirus infections in vertebrates may be asymptomatic, or show symptoms ranging from mild febrile illness to severe disease, including hemorrhagic fever, encephalitis, hepatitis and organ failure, often with high fatality rates, which is why some bunyaviruses are listed as potential bioterrorism agents [5]. Very recent bunyavirus outbreaks include for example the Schmallenberg virus (genus *Orthobunyavirus*) outbreak in Europe, affecting livestock [6] and the severe fever with thrombocytopenia syndrome (SFTSV, genus *Phlebovirus*) outbreak in China, with a 30% fatality rate in humans [7]. This underlines that bunyaviruses are a current problem, that they can emerge worldwide, and that they can spread to new areas, which is partly due to redistribution of arthropod vectors, possibly due to climate change [8]. Bunyaviruses therefore represent a continuous and serious threat to human and animal health. Other notable examples of disease causing bunyaviruses include for example Rift Valley

fever virus (genus *Phlebovirus*), affecting mostly livestock, but also humans, with more recent outbreaks also in Egypt and the Arabian peninsula [9], as well as the highly pathogenic Crimean-Congo hemorrhagic fever virus (*Nairovirus* genus*)*, which has been causing infections over much of the Old World [10].

There are approved animal vaccines for a limited amount of bunyaviruses [11], but approved vaccines for humans and specific antiviral drugs are still unavailable, which leaves large populations of humans and animals at risk towards this emerging threat. Hence, there is an urge to better understand the infection of bunyaviruses. There are many points of view from which a viral infection needs to be understood, but one of the most important is to understand virus-host cell interactions during the virus replication cycle. Viruses, as obligate intracellular parasites absolutely depend on their host cells in order to spread, and one focus in the field of virus-host cell interactions is to find potential viral or cellular targets that could be used for interference with the viral life cycle. Although the study of bunyavirus entry has recently become a more active field of study (especially for phleboviruses), many steps are not yet characterized in great enough detail. More research in bunyavirus infection is therefore needed, with new results hopefully forming a more solid basis for the development of better treatments.

Alphaviruses (of the family *Togavirus*) are also medically important arboviruses, transmitted by certain mosquitoes, such as *Aedes aegypti*

and *Aedes albopictus,* but also of the species *Anopheles* and *Culex*, depending on the particular alphavirus species [12]. Pathogenic alphaviruses usually cause symptoms such as arthralgia, fever and encephalitis, which may be fatal in severe cases, depending on the virus [12]. Important members include for example Chikungunya virus, Sindbis virus and Semliki Forest virus, but also eastern, western and Venezuelan equine encephalitis virus. Alphaviruses are distributed worldwide, and some (eastern, western and Venezuelan equine encephalitis viruses) have also been listed as potential bioterrorism agents, with potentially serious fatality rates [5]. Except for the equine encephalitis viruses, alphavirus infections usually have a low fatality rate. To my knowledge, no approved vaccines or specific treatments against alphaviruses are currently available.

1.2. Endocytosis, intracellular membrane traffic and phospholipids

1.2.1. Endocytosis: Overview

Endocytosis is an essential cellular mechanism that allows the internalization of material from the extracellular environment, which may include fluids, solutes, particles (*e.g.* growth factors, lipoproteins, cell debris), or even other cells (*e.g.* bacteria). The highly diverse nature of endocytosed material is one reason why there is a whole spectrum of different endocytic pathways. Endocytosis is usually achieved by the action of certain cellular proteins, some of which include the receptors that bind the ligands at the cell surface, whereas other cellular proteins help in

shaping the plasma membrane around the ligand-bound receptors, in order to engulf and internalize the bound ligands within membrane vesicles. Endocytosis is usually highly regulated and triggered by the ligands binding at the cell surface, causing intracellular signaling events that initiate endocytosis. The most important endocytic pathways include clathrin-mediated endocytosis and caveolae-mediated endocytosis, both of which are dynamin-dependent, as well as macropinocytosis and phagocytosis, both of which heavily depend on the actin cytoskeleton. There are also other, less common entry pathways, such as lipid-raft dependent endocytosis. The different types of endocytosis are reviewed in [13] and will not be further discussed here, as they are not within the scope of this thesis. Importantly, however, most of these different endocytotic pathways are hijacked by pathogens, including viruses, in order to infect their target cells [14].

1.2.2. The endo – lysosomal pathway and low pH

Receptor ligation at the cell surface may trigger the internalization of receptor–cargo complexes, and most internalized ligands are first targeted to the main intracellular sorting stations called early endosomes. From there, the internalized ligands are transported to other destinations, such as back to the plasma membrane, the recycling endosome, the Golgi apparatus, or they are routed towards the cellular degradation pathway, which, *via* the late endosomes, leads to lysosomes, where degradation of proteins, lipids, and glycans by host cell hydrolases takes place [15, 16].

Perhaps the most striking feature of the degradation pathway is that the pH decreases gradually, from the early endosomes (pH ~ 6) to late endosomes (pH 5 – 6), and finally lysosomes (pH 4.5 – 5) [15], which ensures that the low pH dependent lysosomal hydrolases are most active in lysosomes. Intraluminal pH drop is catalysed by large transmembrane complexes called V-ATPases ([17], pumping H^+ against the transmembrane gradient, by ATP hydrolysis), as well as ATP-independent Na^+/H^+ exchangers in, for example, recycling endosomes [18]. Chloride channels are also important in endosomal acidification, as a provider of counter-ions for H^+ [19].

1.2.3. Intracellular lipid distribution

Most cellular membranes, including early and late endosomes, lysosomes, recycling endosomes, the Golgi apparatus, as well as the plasma membrane, can be identified by a distinct set of protein and lipid species they harbour. The most important lipid markers include the phosphoinositides, which are phospholipids carrying an inositol moiety that is linked to the phosphate group within the headgroup of the phospholipid. The hydroxyl groups of the inositol moiety can be phosphorylated by substrate – specific phosphoinositide kinases and de-phosphorylated by substrate – specific phosphoinositide phosphatases [20]. Many of these kinases and phosphatases are recruited by so-called Rab GTPases, which are specific for certain intracellular compartments [21], as are the phosphorylation states of inositol [20]. For example, early endosomes

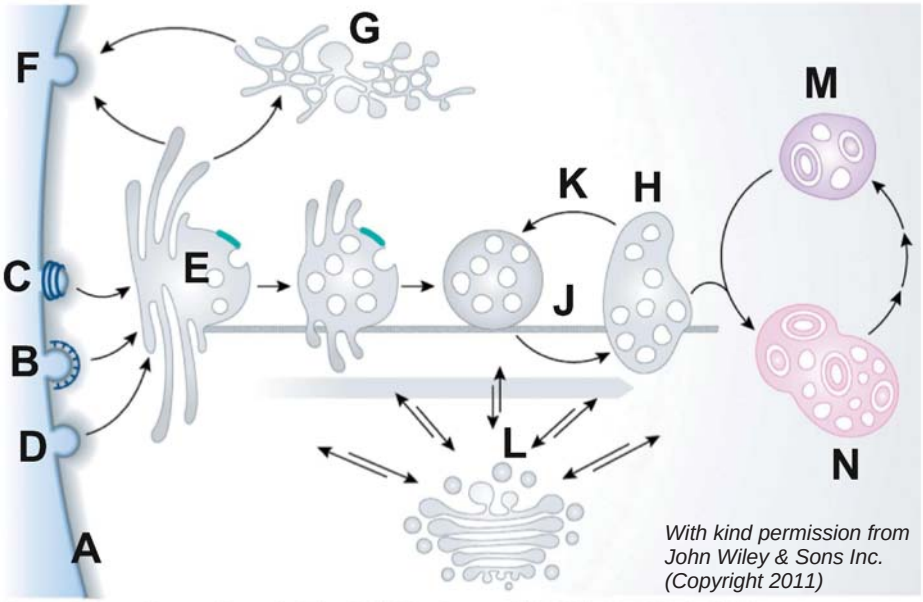
usually have phosphatidylinositol-3-phosphate, whereas late endosomes have phosphatidylinositol-3,5-bisphosphate [20]. Apart from serving as markers for different organelles, phosphoinositides have important biological roles, the most important of which is that they are ligands for a vast number of different proteins. These proteins include important factors involved in, for example, intracellular membrane traffic (*e.g.* ESCRT proteins, important for intraluminal vesicle formation in endosomes), or intracellular signalling (*e.g.* protein kinases and phosphatases involved in signalling, such as Akt/PKB or PTEN) [20].

Another cellular phospholipid species that is unequally distributed in cellular membranes, is the late endosomal phospholipid bis(monoacylglycero)phosphate (BMP), otherwise also called LBPA (lyso-bisphosphatidic acid), although only the former accurately describes the chemical structure. BMP is found on the internal membranes of late endosomes and lysosomes [22, 23], where it functions as an important regulator of lipid degradation (*e.g.* sphingolipid degradation, [24]), lipid (*e.g.* cholesterol) transport [25], as well as protein transport (*e.g.* mannose-6-phosphate receptor recycling, [26]) towards other cellular compartments. It is believed that lysosomes are the site of BMP synthesis [27]. Phosphatidylglycerol (found in the endoplasmatic reticulum and in mitochondria), as well as the mitochondrial phospholipid cardiolipin, although not accumulating in late endosomes and lysosomes, have both been proposed to be precursors for BMP [28]. However, a more recent

report proposed that only phosphatidylglycerol, but not cardiolipin, is used for the *de novo* biosynthesis of BMP [29]. Other phospholipids, such as phosphatidylcholine and phosphatidylethanolamine, can usually be found in all compartments, although in different proportions [30]. Cholesterol and sphingomyelin are most concentrated in the Golgi apparatus, the plasma membrane and early endosomes [22, 30]. In addition to compartment-specific lipid distribution, the leaflet distribution of lipids within lipid bilayers can be asymmetric as well. For example, phosphatidylserine is mostly situated on the cytosolic leaflet of cellular membranes, predominantly within the plasma membrane, but also in endosomes [31].

1.2.4. Early and late endosomes, multivesicular bodies and lysosomes

Early endosomes can be identified by their shape, as well as the protein and lipid composition facing the cytosol (*e.g.* phosphatidylinositol-3-phosphate and the small GTPase Rab5 [20, 21]), and they are mostly situated relatively close to the plasma membrane. Early endosomes typically are vacuolar, with tubular extensions [16], the latter of which are involved in membrane traffic for recycling or transport to the Golgi apparatus, whereas the vacuolar part matures towards late endosomes (Figure 1.1). There are two principal models that describe the maturation from early to late endosomes. One is described in figure 1.1, and is based on a gradual maturation of early endosomes to become late endosomes.



Adapted from Huotari *et al.*, The EMBO Journal (2011) 30, 3481–3500.

Figure 1.1. Endocytosis and intracellular traffic.

Extracellular cargo is endocytosed by one of the endocytic pathways at the plasma membrane (A), such as clathrin-mediated endocytosis (B), caveolae-mediated endocytosis (C), or other non-clathrin, non-caveolin mediated endocytosis pathways (D), and mostly transported towards early endosomes (E). Cargo either gets sorted into the tubular domains, or into the vacuolar domains of the early endosomes. Cargo in the tubular domains is for example recycled back to the plasma membrane (F), or towards recycling endosomes (G), from which recycling to the plasma membrane may follow (F). The early endosome gradually matures into a late endosome (H), while obtaining an increased amount of intraluminal vesicles (ILV's), and while being centripetally (towards the cell nucleus) transported in a microtubule - dependent (J) fashion. Maturing early endosomes may then undergo fusion with late endosomes (K). The late endosome also has substantial vesicular traffic with the trans-Golgi network (TGN, L), and fuses with the lysosome (M) to form the endolysosome (N), in which extensive hydrolysis of contents takes place due to low pH dependent lysosomal hydrolases. The endolysosome then matures into a lysosome, which may fuse with a new late endosome.

In the other model, separate entities, so-called multivesicular bodies (MVB's), otherwise called endosomal carrier vesicles (ECV's), are formed through membrane fission from early endosomes. In the latter model, MVB's represent intermediate compartments between early and late endosomes that are transported *via* microtubules towards late endosomes, with which they fuse [32]. Fission events from early endosomes targeted towards late endosomes have indeed been observed [33]. There is evidence for both the MVB and gradual maturation models, and it has been proposed that the two models may describe endosomal maturation of two distinct sub-populations of early endosomes, one of which is situated closer to the plasma membrane (and following the MVB model) and the other situated closer to the perinuclear space [16, 32] (following the gradual maturation model). However, whatever the proposed model, the maturation from early to late endosomes entails the formation of intraluminal vesicles (ILV's) within the endosomes, de-connection from the plasma membrane recycling pathway, adoption of a more spherical shape (loss of tubular domains), as well as microtubule dependent transport towards the perinuclear space [16, 32]. One function of ILV formation is the breakdown of ubiquitinated signalling complexes, and hence their removal from the cytoplasm. Ubiquitinated signalling receptors themselves help in the recruitment of the ESCRT (Endosomal sorting complex required for transport) complexes, which in turn mediate the sorting and invagination of these ubiquitinated complexes, as well as

vesicle scission into the endosomal lumen to form endosomal ILV's [34, 35]. Late endosomes are enriched in the phospholipid BMP [22], and have roles in protein and lipid transport (see 1.2.3.), which also includes the transport of hydrolases to lysosomes. The interior of late endosomes is more acidic and more enriched in intraluminal vesicles than for early endosomes [15, 22]. Characteristic protein markers for late endosomes are both the small GTPase Rab7 [21] and the late endosomal/lysosomal membrane protein Lamp1 [15, 21]. Late endosomes eventually fuse with lysosomes, the latter of which are characterized by their very electron dense lumen [16]. The main role of lysosomes is to hydrolytically degrade their contents, which is why they contain high amounts of low pH dependent hydrolases [15], which are highly efficient at the very acidic local pH ~4.5.

1.3. The cell entry of enveloped viruses

1.3.1. Viral receptor binding at the cell surface

Enveloped viruses infect their host cells by membrane fusion, which is catalyzed by the viral fusion proteins. Fusion does not occur spontaneously but requires the activation of the fusion proteins by a cellular cue, such as low pH in endosomes, receptor binding, glycoprotein cleavage, or a certain combination of the latter mechanisms, depending on the virus. Whilst some viruses, such as retroviruses and herpesviruses, are able to enter host cells by fusion from the plasma membrane, caused by receptor ligation at the cell surface triggering conformational changes in

the viral fusion proteins [36, 37], most enveloped viruses are endocytosed and fuse from within intracellular compartments. Viral endocytosis usually requires binding to a specific entry receptor at the cell surface that mediates endocytosis. Importantly, one has to differentiate between real entry receptors, which are necessary for viral infection and usually internalize the virions, and attachment factors, which increase the concentration of virions at the cell surface, as to increase to likelihood to engage the entry receptor [38]. Such attachment factors often dramatically increase infection efficiency, and interestingly, many viruses use the same attachment factors (Figure 1.2). One example is the C-type lectin called dendritic cell specific ICAM-3 grabbing non-integrin (DC-SIGN). DC-SIGN is highly expressed on immature dendritic cells as well as alveolar macrophages [39], and the viruses that bind DC-SIGN include important arboviruses, such as flaviviruses (*e.g.* dengue virus, hepatitis C virus [40, 41]), alphaviruses (*e.g.* Sindbis virus, Semliki Forest virus [42, 43]) and phleboviruses (Rift Valley fever virus, Severe fever with thrombocytopenia syndrome virus [44, 45]). DC-SIGN may increase infection *in cis* (*e.g.* in the case of dengue virus) or *in trans* (*e.g.* in the case of HIV) [46]. In the former case, DC-SIGN increases infection of the cells it is expressed on, whereas in the latter case, DC-SIGN increases the infection of cells with which the DC-SIGN expressing cell interacts. Interestingly, DC-SIGN internalization of phleboviruses causes host cell infection and thus

phleboviruses were the first shown to use DC-SIGN as a real entry receptor [44].

1.3.2. N-linked glycosylation

N (asparagine) – linked glycans often are abundant on viral surface glycoproteins, and viral glycoproteins have in fact been important in defining general principles in N-linked glycosylation, such as the link of glycan structure to protein quality control in the endoplasmatic reticulum (ER), with central factors being the ER lectins calnexin and calreticulin [47]. N-glycans are synthesized both from the cytosolic and luminal side of the endoplasmatic reticulum (ER), and are attached to a lipid anchor called dolichol. The complete N-glycan (GlcNAc2Man9Glc3; GlcNAc = N-acetylglucosamine, Man = Mannose, Glc = Glucose) is then transferred, co-translationally, and covalently, onto target protein asparagines in the ER by a protein complex called oligosaccharyltransferase (OST). The potential asparagine ligands on the target protein are those that follow the amino acid sequence motif (sequon) N-X-S/T, where X can be any amino acid except proline [48]. However, not all such sequons are efficiently glycosylated. Other factors, such as sequon proximity to the C-terminus (the further away from the C-terminus, the more efficiently the site is glycosylated), as well as the amino acid preceding the sequon, may have an impact on glycosylation efficiency [49]. N-glycans on properly folded glycoproteins are further processed as they are transported from the ER towards the Golgi apparatus and the specific steps are shown in Figure

1.3. Mammalian N-glycans usually have low mannose content and incorporate so-called “complex” monosaccharides, such as N-acetylglucosamine, galactose and sialic acid.

The glycan composition of N-glycans on glycoproteins largely depends on proper accessibility of the N-glycans towards ER and Golgi glycosidases and glycosyltransferases, and consequently, the absence of such accessibility may lead to incomplete glycan processing. Reduced accessibility may for example be due to steric hindrance caused by N-glycans being located in protein cavities, inaccessible for the processing enzymes [50]. N-glycans of glycoproteins synthesized in insects cells tend to be either highly mannosylated or paucimannose-like, whereas galactose, N-acetylglucosamine and sialic acid are mostly absent, which may be due to lack of expression or decreased activity of the corresponding glycan processing enzymes [51]. This explains the presence of high mannose glycans at the surface of arboviruses derived from insect cells, and is the main reason why they are ligands for the high mannose specific C-type lectin DC-SIGN.

A

Table 1. Examples of attachment receptors for animal viruses

Family	Virus	Receptor	Reference
Adenoviridae	Adenovirus	CAR	53
		HSPGs	32
		sialic acid	128
Bunyaviridae	Hantavirus	β_3 integrins	129
Caliciviridae	Norovirus	HSPGs	130
Circoviridae	Circovirus	CSPGs	131
		HSPGs	
Filoviridae	Ebola virus	DC-SIGN	93
Flaviviridae	Dengue virus	DC-SIGN	88
		HSPGs	132
	HCV	DC-SIGN	90
		HSPGs	1
		SR-B1	97
Herpesviridae	CMV	HSPGs	133
		DC-SIGN	92
	HSV1 and 2	HSPGs	8
		CSPGs	18
	KSV (HHV8)	DC-SIGN	77
		HSPGs	76
		$\alpha_3\beta_1$, $\alpha_2\beta_1$	75
	HHV7	CD4	134
Orthomyxoviridae	Influenza A virus	α2,3 sialic acid (avian)	104
		α2,6 sialic acid (human)	96
		mannose receptor	
Paramyxoviridae	RSV	HSPGs	135
	Sendai virus	α2,3 sialic acid	136, 137
Picornaviridae	Coxsackie	CAR	53
		$\alpha_v\beta_3$	138
	Rhinovirus	ICAM-1 (CD54)	50
	Rhinovirus 87	sialic acid	139
	Rhinovirus 89	HSPGs	3
	FMDV	HSPGs	140
		$\alpha_v\beta_3$	141
	Echovirus	$\alpha_2\beta_1$, $\alpha_v\beta_3$	57 142
Poxviridae	Vaccinia virus	HSPG	143
		CSPG	144
Retroviridae	HIV	CD4	145
		HSPGs	6
		DC-SIGN	94
		Langerin	82
		mannose receptor	
	HTLV	DC-SIGN	146
		HSPGs	25
Reoviridae	Rotavirus	α2,6 or α2,3 sialic acid*	110
		$\alpha_2\beta_1$, α_4	61, 65
Rhabdoviridae	Rabies virus	NCAM	147

*Animal strains of rotavirus use terminal sialic acid for attachment to target cells but evidence to date suggests that human strains do not.

Adapted from Jolly CL, Sattentau QJ., Adv Exp Med Biol. 2013; 790: 1-23.

With kind permission from Springer Science + Business Media (Copyright 2006).

B

Table 1
DC-SIGN and L-SIGN Are Receptors for a Broad Range of Viruses

	Virus family	Virus	Mechanisms	Viral envelope protein(s)*
DNA	*Herpesviridae*	CMV	*cis*, *trans*, *trans*-enh.	gB
RNA	*Coronaviridae*	SARS	*cis* ?, *trans*	Spike
	Filoviridae	Ebola	*cis* ?, *trans*	GP
		Marburg	*cis* ?	GP
	Flaviviridae	Dengue	*cis*	E
		HCV	*trans*	E1/E2
	Retroviridae	HIV-1/-2	*cis*, *trans*, *trans*-enh.	gp120
		SIV	*cis*, *trans*, *trans*-enh.	gp120
	Togaviridae	Sindbis	*cis* ?	E1 or E2 (?)

* Viral envelope protein(s) bound by DC-SIGN or L-SIGN. *cis*, *cis*-infection; CMV, cytomegalovirus. HCV, hepatitis C virus; HIV, human immunodeficiency virus; SARS, severe acute respiratory syndrome virus; SIV, simian immunodeficiency virus; *trans*, *trans*-infection; *trans*-enh, *trans*-enhancement.

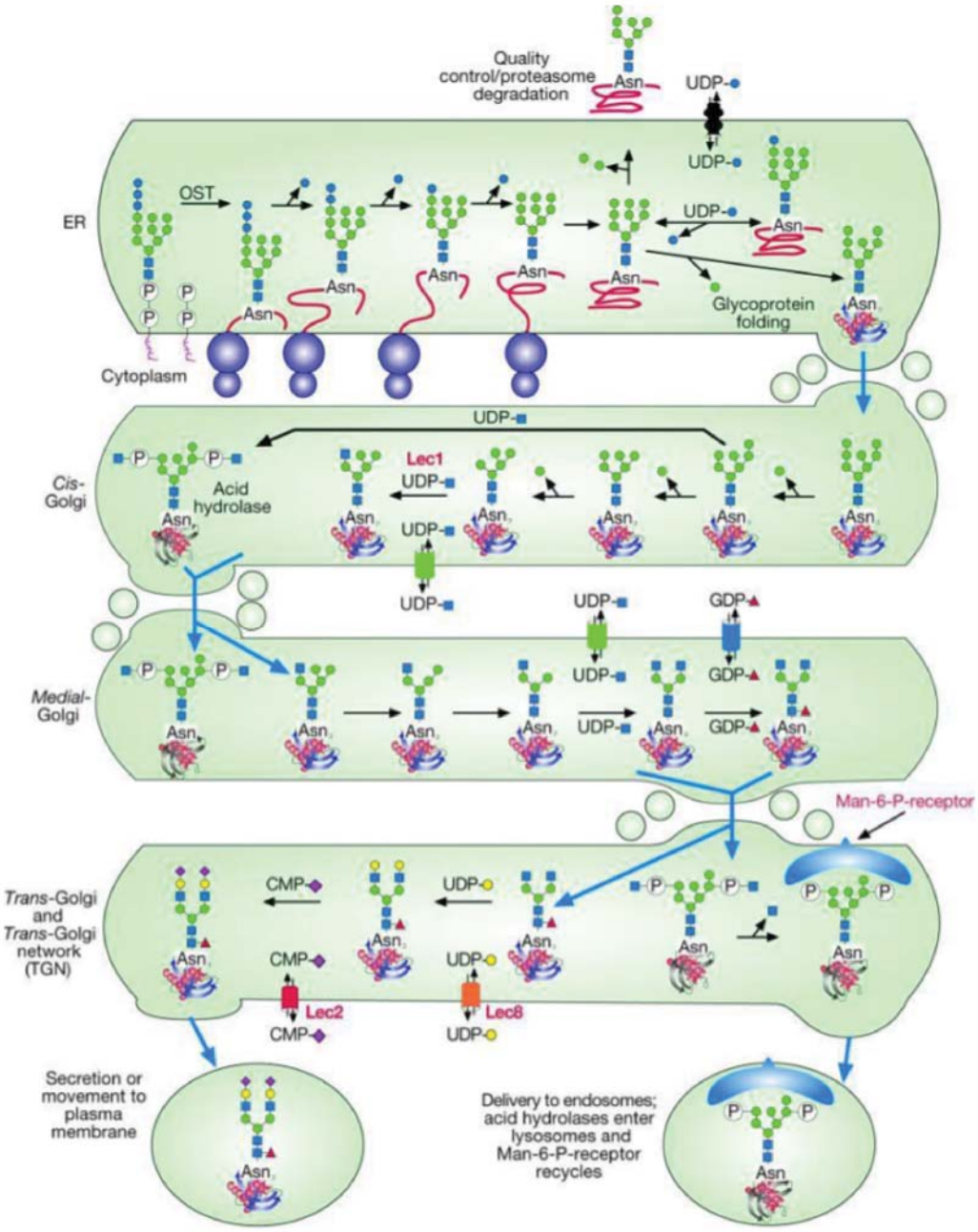
Adapted from Lozach *et al.*, Methods Mol Biol. 2007; 379: 51-68

With kind permission from Springer Science + Business Media (Copyright 2007).

Figure 1.2. Viral attachment factors and the importance of the C-type lectin DC-SIGN.

A.) Virus families are indicated in the first column, virus genera or species in the second column, and the cellular attachment factor in the third column. The fourth column indicates the references in the book chapter the table was taken from, not the references in this thesis. Note that many viruses bind DC-SIGN. The list is not exhaustive.

B.) Table depicting viral DC-SIGN ligands. The viral genome type is indicated in the first column, the virus families in the second column, the virus species in the third column, the possible enhancing effect of DC-SIGN in the third column, and the related viral glycoprotein ligand in the last column. The list is not exhaustive.



Adapted from Stanley P, *Schachter* H, *Taniguchi* N. *N-Glycans*. *In: Varki* A, Cummings RD, Esko JD, et al., editors. Essentials of Glycobiology. 2nd edition. Cold Spring Harbor (NY): Cold Spring Harbor Laboratory Press; 2009. Chapter 8

Figure 1.3. N-glycan processing in the endoplasmatic reticulum (ER) and the Golgi apparatus of mammalian cells.

Blue circles indicate glucose, green circles mannose, blue squares N-acetylglucosamine, yellow circles galactose, red triangles fucose and purple squares sialic acid. The letter "P" in a circle indicates a phosphate group, Asn = Asparagine. OST = oligosaccharyltransferase.

With kind permission from The Consortium of Glycobiology Editors, La Jolla, California (Copyright 2009).

Originally published in:
R Kornfeld, S Kornfeld, Assembly of Asparagine-Linked Oligosaccharides, (1985), Annual Review of Biochemistry Vol. 54: 631-664.

1.3.3. Viral endocytosis

Many enveloped viruses, such as vesicular stomatitis virus (VSV, genus *Vesiculovirus*, family *Rhabdoviridae* [52, 53]), or Semliki Forest virus (genus *Alphavirus*, family *Togaviridae*, [54]), use clathrin-mediated endocytosis. Other viruses may use more than one pathway, for example the phlebovirus Uukuniemi virus [55], as well as influenza virus [56] use both clathrin and non-clathrin mediated pathways. Other viruses use macropinocytosis, caveloae-dependent endocytosis [14], or even other, less characterized pathways, as shown in Figure 1.4. Although endocytic mechanisms are highly diverse, depending on the virus and receptors used, the intracellular trafficking of viruses, in terms of the nature of the target compartments, is somewhat less diverse, as outlined in the next paragraph. It is believed that one reason for viruses being endocytosed is that they can use intracellular transport in order to be released as close as possible to their replication sites, which may be close to the endoplasmatic reticulum (ER), where protein translation takes place.

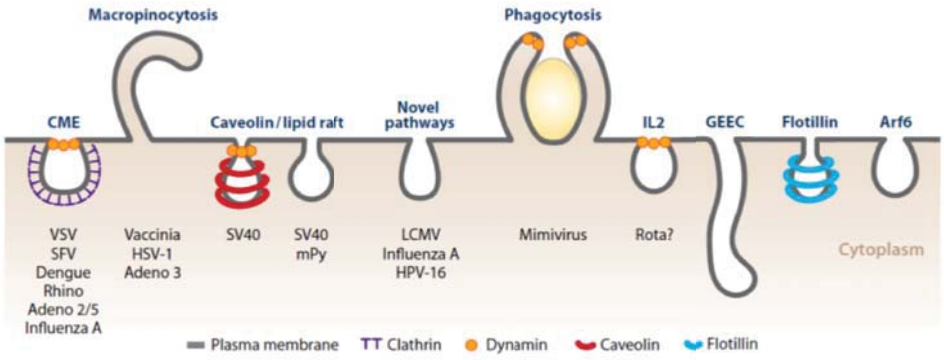
After endocytosis, viruses are mainly routed towards early endosomes, the main sorting station within the cell. These include viruses coming from, for example, clathrin-mediated endocytosis, as well as caveolae-mediated endocytosis. Macropinocytosis first leads to the formation of the so-called macropinosome, which later merges with the lysosomal pathway [57]. For most of the endocytosed viruses, the most important change that takes place in endosomes, as compared to the cell surface, is the significant pH

drop [15, 16]. Most viruses that get endocytosed use the low pH as a trigger for activation of the viral fusion proteins. Some viruses penetrate cells from early endosomes, whereas others are transported to late endosomes before penetration. Viruses entering cells from late endosomes are referred to as late-penetrating viruses, and they include viruses such as influenza virus (*Orthomyxoviridae*), Rift Valley fever virus (*Bunyaviridae*), dengue virus (*Flaviridae*), and lymphocytic choriomeningitis virus (LCMV, *Arenaviridae*) [55, 58–61]. Accordingly, the fusion proteins of these viruses may have a lower pH activation threshold than the early penetrating viruses. A good illustration of how pH thresholds can define the entry point of low pH dependent viruses can be seen with the usually early penetrating alphavirus Semliki Forest virus (SFV): The SFV-*fus1* mutant has a lower pH activation threshold (pH < 5.5, [62]), causing the mutant virus to fuse from within late endosomes [62, 63]. There may be other reasons, in addition to low pH, for penetration from within late endosomes. For example, dengue virus uses negatively charged phospholipids in late endosomes to allow a stalled fusion intermediate to progress towards complete fusion [59]. Filoviruses are trafficked to late endosomes/lysosomes, because their surface glycoproteins need to be proteolytically cleaved by local host cell proteases called cathepsins [64], and because the virions need the late endosome/lyososome specific receptor NPC1 to infect host cells [65].

1.3.4. Viral fusion

The process of viral membrane fusion is believed to occur through several intermediates, but the first firm contact between viruses and target membranes is achieved by a triggered (*e.g.* by low pH in endosomes) conformational change of viral fusion proteins, causing the exposure of hydrophobic fusion loops at the viral surface, followed by insertion of these newly exposed fusion loops into target membranes, which results in the viral glycoproteins bridging the viral and target membranes [66, 67]. Subsequent conformational changes in these fusion proteins pull both the viral and target membranes into closer proximity. The energy to catalyze this pulling mechanism is stored within the metastable conformation of the viral fusion proteins and is also needed to compensate for the repulsive forces building up between the viral and target membranes as they approach each other in the fusion process. As a result, the initial contact area between viral and target membranes can be expected to be very small. Direct evidence for such a small initial contact area in viral fusion could for example be seen in influenza fusion with liposomes [66], where the viral spikes caused so-called target membrane “dimples”. If both viral and target membrane lipid bilayers come together close enough, the outer leaflets of the two membranes may enter a so-called hemifusion intermediate, which may or may not result in lipid mixing between the two outer membrane leaflets. If direct contact, but no lipid mixing takes place, then both compartments are in a so-called restricted fusion intermediate

[68], in which the outer lipid bilayer leaflets are in contact, but do not mix lipids, presumably due to protein-mediated restriction of lipid diffusion. If lipid mixing ("unrestricted" hemifusion) occurs, the fusion proteins may cause the progression of the "unrestricted" hemifusion intermediate towards a so-called hemifusion diaphragm [69, 70], which is a dilated version of the hemifusion intermediate, and eventually leads to fusion pore formation, expansion and genome release. Only once the fusion pore is stabilized, the fusion event can be considered as complete. A sketch of fusion through hemifusion is shown in figure 1.5. Fusion between lipid bilayers in absence of fusion proteins has been monitored in *vitro* at low pH [23], which, however, may have been due to the presence of certain intrinsically fusogenic phospholipids, and may not reflect physiological fusion, which is usually highly regulated. It is also not clear whether these protein-free fusion events are complete fusion events that progress any further than hemifusion.

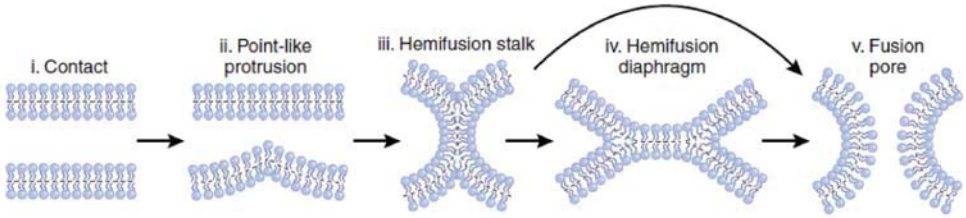


Adapted from Mercer J, Schelhaas M, Helenius A. Annu Rev Biochem. 2010;79:803-33

Copyright (2010) by Annual Reviews.

Figure 1.4. Viral entry pathways at the cell surface.

The different cell entry pathways hijacked by viruses are indicated. Virus species using the indicated entry pathways are indicated below the schematic.



Adapted from Chernomordik LV, Kozlov MM. Nat Struct Mol Biol. 2008 Jul;15(7):675-83

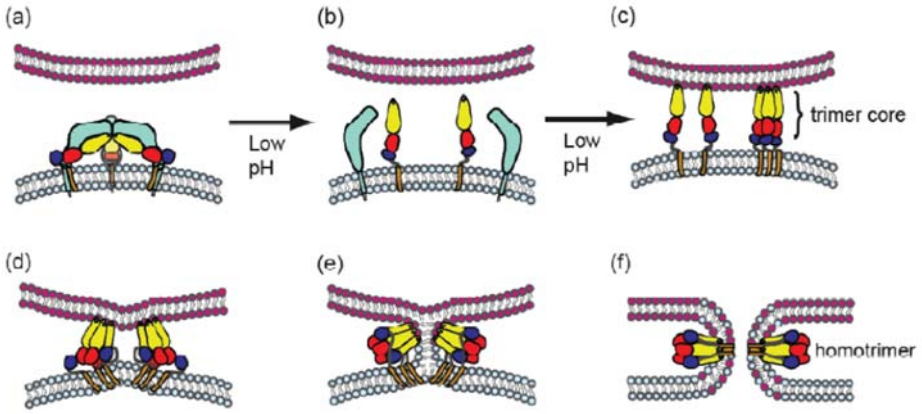
Figure 1.5. A schematic representation of bilayer architecture during fusion through hemifusion.

Reprinted by permission from Macmillan Publishers Ltd. (Copyright 2008)

The final conformation of the viral fusion proteins is usually a post-fusion trimer. However, not all viral fusion proteins are the same. Viral fusion proteins are usually subdivided into three classes, named 1, 2 and 3, and are extensively reviewed in [71–73]. This classification is mainly based on the three-dimensional structure, sub-domain organization, as well as localization of the viral hydrophobic fusion loop within the fusion proteins. Briefly, class 1 fusion proteins are usually trimeric in pre- and post-fusion states, rich in alpha-helices and the fusion loop is located at the N-terminus [71]. Important class 1 fusion viruses include ortho- and paramyxoviruses, as well as arenaviruses. In class 2 fusion proteins, the hydrophobic fusion loop is internal rather than N-terminal, the overall structure is beta-strand rich and the initial configuration is homo- or heterodimeric, progressing towards homotrimers during the course of membrane fusion [73]. Important viruses with class 2 fusion proteins include flaviviruses, alphaviruses and bunyaviruses. Class 3 fusion proteins possess both alpha-helices and beta-strands, in addition to internal, bipartite fusion peptides [72]. Class 3 fusion proteins are usually trimers in their pre- and post-fusion states, and important representatives are vesicular stomatitis virus, baculovirus and herpesviruses.

Alphaviruses, flaviviruses and bunyaviruses are low pH dependent, and the reason why low pH changes the conformation of certain viral fusion proteins, is that these fusion proteins have a pH sensor that is composed of histidines getting protonated at low pH (see for example [74]). Class 2

fusion mechanisms have been studied extensively, especially for alphaviruses. Alphavirus fusion requires both cholesterol and sphingomyelin in target membranes for efficient fusion. Cholesterol is needed for binding, whereas sphingomyelin is required for fusion [75]. The fusion threshold has been determined to be at around pH 6 [75, 76], and entry kinetics are compatible with entry from early rather than late endosomes [33]. Low pH exposure leads to glycoprotein E1/E2 dissociation, fusion loop exposure of E1 and binding of E1 to the target membrane via extended E1 intermediates [67]. This is followed by E1 trimerization and backfolding of virus proximal domain III towards the distal domains I and II, which leads to membrane fusion (see Figure 1.6). The flavivirus fusion mechanism via the E protein is believed to be similar, but without a strict requirement for both cholesterol and sphingomyelin [59, 77]. The detailed fusion mechanism of phleboviruses, or any other bunyavirus, has not been studied.



Adapted from: Kielian M, Chanel-Vos C, Liao M. Viruses. 2010 Mar 26;2(4):796-825

Figure 1.6. A schematic representation of alphavirus fusion.

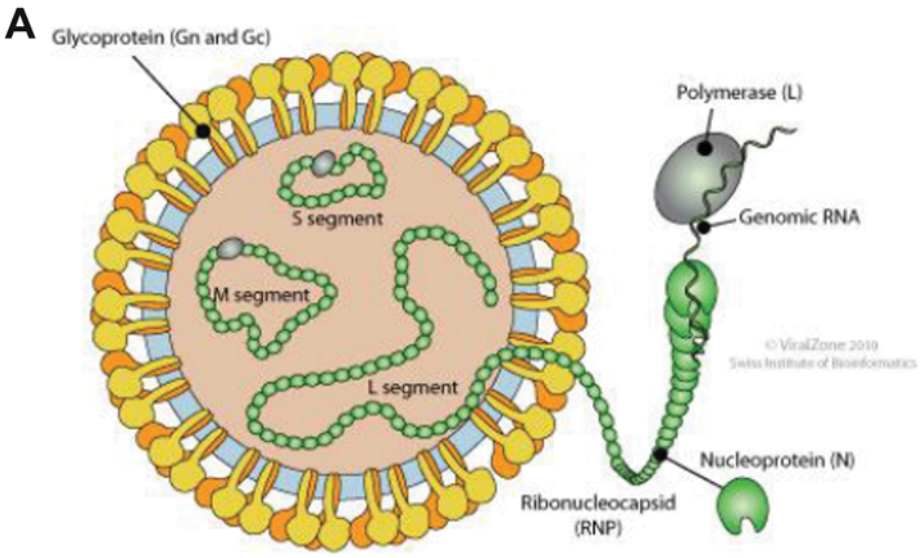
(a) At neutral pH, glycoprotein E2 (light blue) and E1 (coloured in yellow, red and dark blue) from trimers of heterodimers. (b) Low pH causes glycoprotein dissociation and (c) E1 extension and insertion of the hydrophobic fusion loops into the target membranes, followed by homotrimerization. (d) The E1 domain III (dark blue) folds back onto domains I and II (red and yellow, respectively), causing hemifusion (e). Further conformational changes bring the fusion loop and the transmembrane domains of E1 into close proximity, causing fusion pore formation (f).

Figure originally published in: Claudia Sánchez San Martín, Catherine Y. Liu, Margaret Kielian, 2009, volume 17, issue number 11 (pages 514-521); Dealing with low pH: entry and exit of alphaviruses and flaviviruses, reprinted here with kind permission from Elsevier (Copyright 2009).

1.4. Bunyaviruses and alphaviruses: Molecular and structural biology

1.4.1. Bunyaviruses

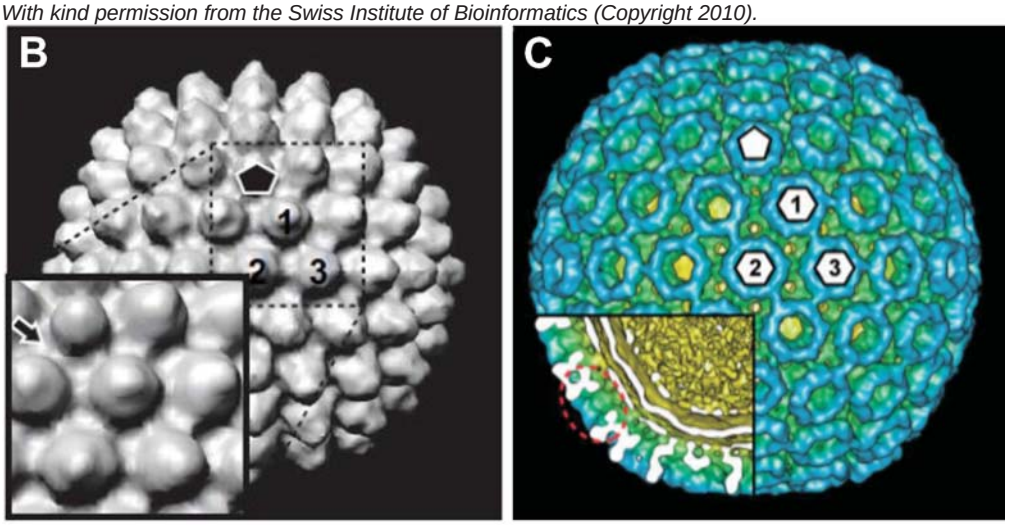
Bunyaviruses are enveloped viruses with a spherical to oval shape (*e.g.* phleboviruses are spherical with a diameter of 100-125 nm [78, 79], whereas hantaviruses are rather oval with a diameter of 120-160 nm [80]), and a single negative stranded, tripartite RNA genome. The three RNA segments are called L, M and S (for large, medium and small, in the order of decreasing length) segments and they encode four structural proteins. S codes for the nucleocapsid protein (N), which packages the viral genome to form so-called ribonucleoprotein particles (RNP's) [1]. The viral RNP's interact with the glycoprotein tails of the viral surface glycoprotein G_N [81]. The M segment codes for the polypeptide precursor p110, which is post-translationally cleaved by host cell proteases to form the membrane glycoproteins G_N and G_C. The L segment encodes the RNA dependent RNA polymerase (RdRp), which catalyzes viral transcription and replication [1]. A sketch of a typical bunyavirus is depicted in figure 1.7. G_N and G_C were proposed to form heterodimers in mature phlebovirus virions [78], although, a previous study, using different methodology, proposed homodimers [82]. The phlebovirus G_C is a class II fusion protein [83], whereas, to date, the role of G_N remains confined to virion assembly [81].



Adapted from the ViralZone web resource (www.expasy.org/viralzone/):

Hulo C, de Castro E, Masson P, Bougueleret L, Bairoch A, Xenarios I, LeMercier P. Nucleic Acids Res. 2011, Jan;39(Database issue):D576-82

With kind permission from the Swiss Institute of Bioinformatics (Copyright 2010).



Adapted from Overby AK *et al.*, PNAS 2008, 105 (7): 2375-9.

Adapted from Huiskonen *et al.*, J Virol. 2009, 83 (8): 3762-9.

Figure 1.7. Bunyavirus architecture and phlebovirus structure.

A.) Typical architecture of a bunyavirus particle. The blue circle indicates the lipid bilayer.

B.) Cryo-EM structure of Uukuniemi phlebovirus at neutral pH. Note the pointed structure of the spikes. The icosahedral fivefold axis is indicated as a pentagon. Numbers indicate distinct pseudohexameric spikes.

Figure copyright (2008) by the National Academy of Sciences, U.S.A.

C.) Cryo-EM structure of Rift Valley fever phlebovirus at neutral pH. Note the hollow structure of the spikes. The icosahedral fivefold axis is indicated with a pentagon and the distinct pseudohexameric spikes with hexagons and numbers, respectively.

Figure copyright (2009) by the American Society for Microbiology.

Depending on the virus, two non-structural proteins called NSs and/or NSm, which have a role in viral replication and assembly, are also expressed. For example, NSs is an important inhibitor of the host innate antiviral immune response [84]. The role of NSm is less well understood, however, localization studies indicate that it plays a role in virion assembly [85]. Most bunyaviruses are not highly structured, with the exception of the icosahedral phleboviruses, such as Uukuniemi virus (UUKV) and Rift valley fever virus (RVFV) ([78, 79], Fig. 1.7), which have an icosahedral glycoprotein shell with a T = 12 triangulation number. Interestingly, RVFV spikes form hollow cylinders [78], whereas UUKV spikes have a “pointy” appearance at neutral pH [79]. At slightly acidic pH 6, UUKV formed hollow cylinders as well [79]. Some *Bunyavirus* genera have locally restricted symmetry elements, such as tetrameric glycoprotein assemblies for hantaviruses, or tripodal assemblies for orthobunyaviruses [80, 86].

1.4.2. Alphaviruses

Alphaviruses are composed of the glycoproteins E1 and E2, where E1 is the fusion protein and E2 the receptor binding protein [87]. Alphaviruses have a single positive stranded RNA genome that encodes a polyprotein each for structural and non-structural proteins. The structural proteins include, apart from the glycoproteins E1 and E2, the capsid protein C, as well as the glycoproteins E3, and 6K [87]. The polyprotein is cleaved by viral (*e.g.* the capsid protein C cleaves itself, or nsP2, which cleaves the non-structural polyprotein to form nsP1-4) and host cell proteases (*e.g.*

furin, signal peptidase). For example, the precursor p62 is cleaved by furin in the Golgi apparatus and yields the glycoproteins E3 and E2. The capsid protein forms an icosahedral lattice at a triangulation of T=4, and encapsulates the RNA genome. The capsid in turn is encapsulated by a lipid bilayer that contains both glycoproteins E1 and E2 [87]. The glycoprotein E3 is usually lost during virus maturation, and it has been proposed that its role is to protect premature low pH inactivation of E1 in the Golgi apparatus, during virus maturation [88]. The 6K protein is believed to be involved in virus budding [89], and is virtually absent in mature virions. The glycoproteins E1 and E2 form an icosahedral lattice at the virion surface (T=4) and the glycoprotein E2 interacts with the viral capsid proteins. The viral spikes are composed of trimers of E1/E2 dimers, and alphaviruses are usually 65-70nm in diameter [87].

1.5. The cell entry of bunyaviruses and alphaviruses

1.5.1. Bunyavirus entry

Bunyavirus entry receptors remain largely unknown, except for phleboviruses, for which the C-type lectin DC-SIGN [44] has been observed to mediate binding and endocytosis, and for hantaviruses, which use integrins [90]. Most bunyaviruses use clathrin-mediated endocytosis (*Nairovirus*, *Orthobunyavirus, Hantavirus* and *Phlebovirus*) [55, 91–93] although phleboviruses may use a clathrin-independent pathway in addition [55]. The phlebovirus Rift Valley fever virus can also use caveolin-dependent entry [94]. It is believed that the endocytosed virions are

transported to early endosomes, and consistently, recent reports showed dependence on the early endosomal Rab5, but independence of Rab7 [55, 91, 92]. From this, it was concluded that orthobunyaviruses and nairoviruses penetrate host cells from early endosomes [91, 92]. On the other hand, phleboviruses co-localized with the late endosomal markers Rab7 and Lamp1, had entry kinetics and low pH activation thresholds consistent with entry from late endosomes, and were dependent on close-to-physiological temperatures [55]. Physiological temperatures [95], as well as intact microtubules [14, 16], are important for early endosome maturation. Interestingly, nairovirus entry was microtubule-dependent [86], which challenged nairovirus entry from early endosomes. Consistently, recent studies proposed nairovirus entry from multivesicular bodies [97]. Furthermore, phlebovirus entry depended on the cellular v-SNARE VAMP3 [98], which is located on autophagosomes and is used in fusion of the latter to late endosomes [99]. Inhibition of VAMP3 led to failure of phlebovirus transport to late endosomes and blocked infection [98], thus suggesting a potential role of autophagosomes in intracellular phlebovirus transport to late endosomes after viral endocytosis. Phleboviruses are thus classified as late-penetrating viruses, which is in contrast to early penetrating viruses, such as Semliki forest virus (SFV), or vesicular stomatitis virus (VSV). Although VSV entry kinetics and pH activation threshold (pH>6) clearly suggest entry from early endosomes [52, 100], the site of VSV penetration still remains controversial, as others suggested

fusion with late endosomal intraluminal vesicles, followed by backfusion to the endosomal limiting membrane [101]. Whether phleboviruses use such a backfusion mechanism is unclear.

1.5.2. Alphavirus entry

The prototypic alphavirus Semliki Forest virus (SFV) is believed to enter cells by clathrin-mediated endocytosis and from early endosomes [63], and the post-fusion remains of SFV connected to the host cell membrane are believed to be transported to late endosomes and lysosomes for degradation [33]. The use of early endosomal (sphingomyelin and cholesterol [102]), rather than late endosomal phospholipids, the low pH activation threshold (pH ~ 6.2, [76]), as well as cell entry kinetics of SFV (half maximal penetration after 6 minutes [33]) suggest entry from early endosomes. Although it is generally accepted that clathrin, cholesterol and low pH are important for alphavirus entry [87], the intracellular compartment from which alphaviruses penetrate cells, is not conserved. For example, the cell entry of Venezuelan equine encephalitis virus (VEEV) depended on Rab7, and thus it was concluded that VEEV enters cells from late endosomes [103]. Alphaviruses can use a range of cell surface receptors, and they include for example DC-SIGN and L-SIGN [42, 43], laminin receptor [104], and heparan sulphate [105]. Sindbis virus has recently been proposed to use the natural resistance-associated macrophage protein (NRAMP) as entry receptor [106]. As can be seen, alphaviruses are promiscuous in receptor usage, and there is still room for

more candidates, because many of the proposed receptors are cell surface attachment factors (*e.g.* DC-SIGN, L-SIGN, heparan sulphate) and not real entry receptors. DC-SIGN is a very important attachment factor because it is hijacked by so many other viruses, and because it is used directly after transmission via a mosquito bite (see above), thus making it an important target in early alphavirus infection.

1.6. Electron cryo-microscopy and icosahedral reconstruction of enveloped icosahedral viruses

Technological advancements in electron cryo-microscopy have revolutionized the field of the structural biology of viruses in recent years, such that structures of icosahedral enveloped virions are now possible at near atomic resolution [107, 108]. The main advantage of electron cryo – microscopy (cryo-EM) over X-ray crystallography, as well as negative-stain electron microscopy is that viral particles can be viewed in their native aqueous environment and without use of contrast-enhancing chemicals, for example negative stains, such as uranyl-acetate, which may compromise the structure of biological samples (*e.g.* particle distortion, or even partial collapse), especially if the particles are unfixed. The sample preparation protocol for cryo-EM employs flash-freezing, or vitrification, of aqueous solutions, which can easily be obtained by plunge-freezing samples at liquid nitrogen temperature (80K), using liquid ethane [109]. The contrast obtained from images obtained of plunge-frozen specimens comes from the atoms of the virus particles themselves, which are mainly

the carbon, nitrogen, oxygen and phosphorus atoms from the proteins, lipids and nucleic acids. Because these atoms have atomic numbers close to those of the solvent atoms (low atomic number cations and anions from *e.g.* sodium chloride, as well as oxygen from water), electron cryo-microscopy images have low contrast [110].

Electrons can be described as a wave (de Broglie), and therefore have a certain energy (or wavelength), amplitude and phase. The electrons are coming from an electron source (*e.g.* a field emission gun (FEG) or a tungsten filament), and are accelerated to a discrete energy level that can range up to a few hundred kilo-electronvolts (keV), depending on the microscope used. The electron beam is focused by condenser lenses, after which the condensed beam hits the sample. The different atoms present in the sample cause scattering of the electrons, thus allowing the generation of electron diffraction patterns in the objective back-focal plane. The objective lens focuses these scattered electrons back into an image of the sample [110, 111]. The magnification of the sample is achieved by the projector lenses which project the image onto a fluorescent screen or a detector.

There are two predominant scattering events in electron scattering: elastic and inelastic scattering. Inelastic scattering occurs when electrons collide with the atoms of the sample, once, or multiple times, resulting in loss of energy for the colliding electron. These electrons damage the sample (radiation damage [110–112]), create loss of information from the image,

and are therefore not wanted. To minimize the radiation damage, cryo-EM images are usually obtained with low electron dose, typically using 20 electrons/Å^2 or less. A common strategy used to minimize the detection of inelastically scattered electrons is to use an energy filter that is permissive towards electrons with an energy range close to what is expected for elastically scattered electrons. Elastic scattering occurs if electrons are scattered without collision and without loss of energy [110–112]. These are the electrons we are interested in, as they form useful contrast in the image.

Heavy atomic nuclei (*e.g.* uranium nuclei) cause high electron scattering angles and contribute to amplitude contrast because these electrons do not pass through the objective aperture, and are therefore removed from the image [113], which causes the acquisition of a “black” signal for the heavy atoms. Lighter atoms cause weaker, yet significant scattering and contribute to phase contrast. How is phase contrast created in an electron microscope? The source of phase contrast are the scattered electrons, which, due to spherical lens aberration, are refracted differently by the objective lens, according to their scattering angle caused by the atoms in the sample (*e.g.* electrons with lower diffraction angle are less efficiently refracted by the objective lens). This causes a resolution-dependent phase shift of the diffracted electron waves, relative to the transmitted, unscattered electron waves, thus causing either constructive or destructive interference between the scattered and the unscattered electron beam in

the objective back focal plane. These interference events in turn cause phase contrast. Because the electron waves do not interfere with each other in the image plane, there is virtually no contrast when the specimen is in focus. Therefore, in electron cryo-microscopy, images are taken away from focus, which magnifies the effect of wave interference. However, the problem with this technique is that the image obtained is not a direct representation of the object. Electron micrographs obtained away from focus are modulated by the so-called contrast transfer function (CTF [112]) that makes information stored in the image different from the object in the specimen.

The CTF is a function that describes the contrast in the image as a function of spatial resolution. The components that characterize the CTF include the following: i.) Phase reversals at distinct spatial resolutions. The positions of the phase reversals depend on the defocus. ii.) Resolution dependent envelope function that dampens the signal-to-noise ratio in the image, in other words, the higher the spatial frequency, the lower the signal-to-noise ratio. Factors contributing to the envelope function include lens aberrations such as spherical aberration, lack of perfect beam coherence (how parallel the beam is, which depends on the electron source), as well as sample thickness (causing inelastic scattering). The consequence of the phase reversals in the CTF is that there is a defocus-dependent contrast enhancement of features in the object at certain resolution ranges and complete loss (at the points at which the amplitude

of the CTF is zero) or reversal of contrast at other resolutions. However, this can be accounted for by recording micrographs at different defoci and by CTF correction. CTF correction means division of the image by the CTF, as to restore its original information as much as possible.

Electron microscope images are two-dimensional projections of a three dimensional object with a distinct orientation relative to the direction of view. How can the three-dimensional information be reconstructed from these projections? First, the particles are selected and boxed out of the micrographs, using a box slightly larger than the particle itself. The following tasks are then to assign the particle centre (phase origin) and its correct orientation. It is important to have as many different orientations as possible, as to represent the three-dimensional object as closely as possible to the real structure. In general, one assumes that particle orientations are randomly distributed in the sample. The orientations of the particles relative to each other are sufficient to build a three-dimensional model.

Two very important concepts that allow the determination of particle orientation from a two-dimensional projection of a three-dimensional volume, are called the “central section theorem” and “common lines” [112, 114, 115]. Also, the spatial information in an image can be represented mathematically as complex exponentials (containing sine and cosine wave terms), and the mathematical operation used to obtain this representation is called a Fourier transform [111]. Fourier transformed images can be

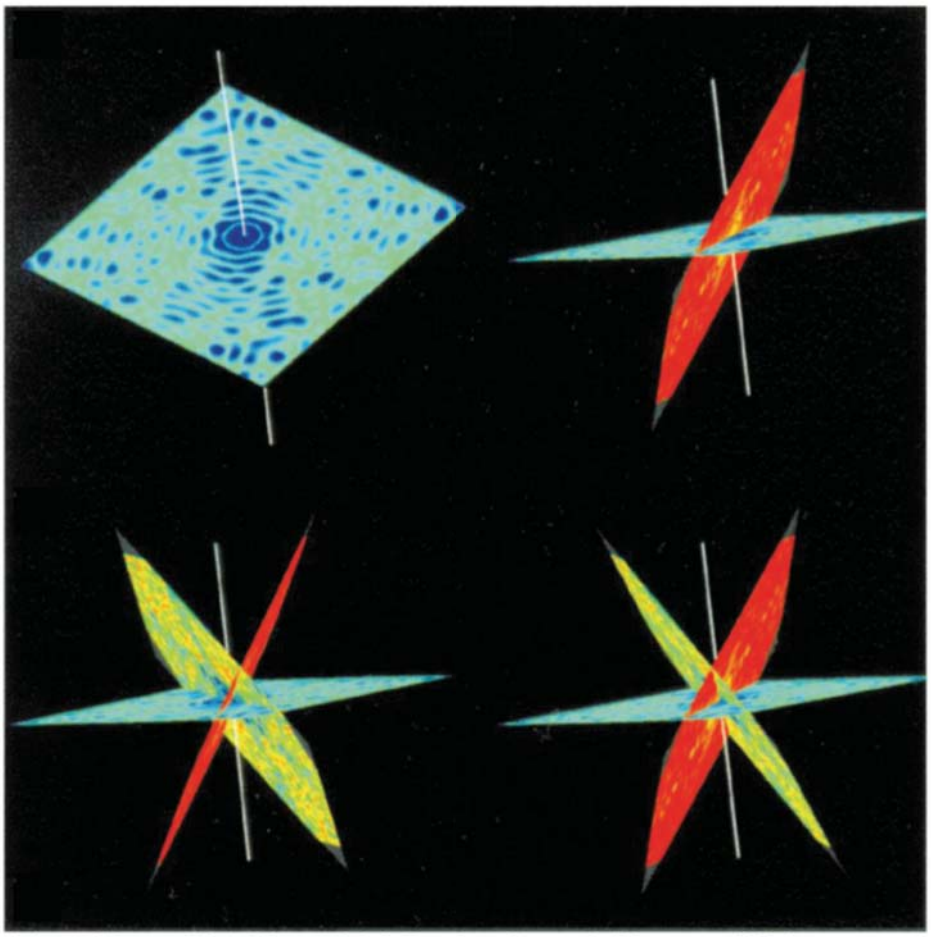
represented in reciprocal space (Fourier space), which in this case corresponds to a spatial frequency domain. The central section theorem states that in Fourier space, a two-dimensional projection is a central slice of a three-dimensional volume. This means that one could view a three-dimensional Fourier spectrum as an infinite sum of two-dimensional Fourier spectra in different orientations, but with a common origin. Each pair of projections intersects each other in Fourier space along one line where their values are nearly identical. This line is called a common line (or a pair of common lines as one line comes from the first projection and another line from the second projection). Pairs of common lines are also created by symmetry operations on individual views of a symmetric object in Fourier space that do not go along the symmetry axes of the object. These pairs of common lines, one line of which is derived from a symmetry operation and one from its inverse, can therefore be regarded as intersections between symmetry-related views of the same projection, and are thus called self-common lines (Figure 1.8 A). For example, an icosahedrally symmetric object has 37 pairs of self-common lines [112, 115], with every orientation having a subset of self-common lines with distinct angular spacing relative to each other, which in turn define the particle orientation. The 37 pairs of common lines in icosahedral particles are obtained as follows: 2 pairs of common lines for each of the 6 fivefold axes of symmetry (12 pairs), 1 pair of common lines for each of the 10 threefold axes of symmetry (10 pairs), and 1 pair of common lines for each

of the 15 twofold axes (15 pairs). This gives a total of 15+12+10 = 37 pairs of common lines for each Fourier transform of each icosahedral particle projection image. The quality of the angular assignment based on self-common lines is assessed by the common lines phase residuals [112, 115], which give a measure of how well the phases agree with each other along the common lines related by symmetry.

Common lines in Fourier space have a similar concept in real space. These real space common lines (or sinogram common lines, see figure 1.8 B) can be found as follows. The two-dimensional projection image is rotated around the particle centre at certain angular intervals, and projected into a one-dimensional line. All of these line projections together form a new image called a sinogram [114]. This is followed by finding shared real space common lines (or shared tilt axes) between different orientations (or sinograms) via a so-called sinogram correlation function, which in turn defines the relative particle orientations [114].

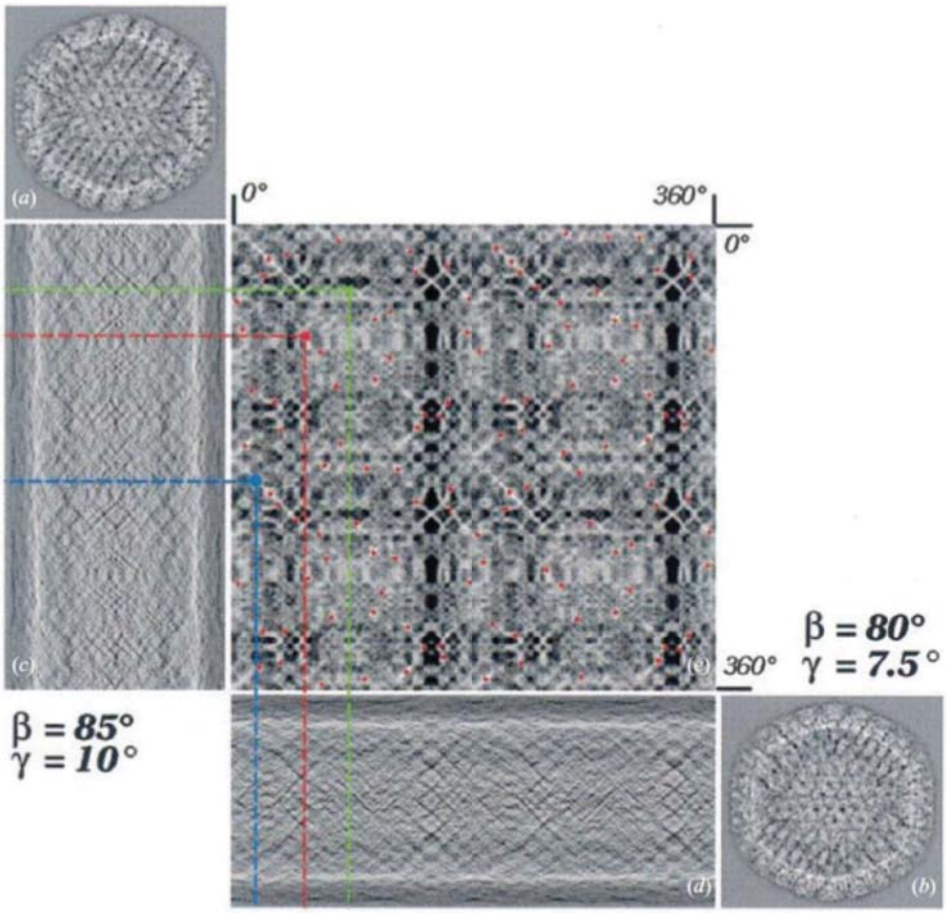
Once the initial particle orientations are found and assigned, the particles are reconstructed by back-projection of two-dimensional particle views into three-dimensional space, and an initial three-dimensional model is obtained [112, 114]. Such a three-dimensional model is usually of low quality, because of errors in the orientation assignment. However, the model is improved by iterative refinement of the particle orientations and centering.

A



Adapted from: S.D. Fuller and S.J. Butcher, Journal of Structural Biology 1996, 116:48–55 *With kind permission from from Elsevier (Copyright 1996).*

B



Adapted from: van Heel et al., Quarterly Reviews of Biophysics 2000, 33 (4):307-369
Copyright (2000) by Cambridge University Press.

Figure 1.8. Fourier space and real space common lines.

A.) Description of Fourier space pairs of self-common lines. A Fourier transform of a two-dimensional projection derived from a three-dimensional object in a particular orientation (in this case of the bacteriophage PRD1, see S.D. Fuller and S.J. Butcher Journal of Structural Biology 1996, 116:48–55) is depicted as a blue plane. Rotation of the blue plane around a threefold symmetry axis (pointing towards the reader) yields a new plane (red) that intersects the initial plane along a line. This line is a "pair of common lines", because one line belongs to the blue plane and one to the symmetry-related red plane. Between the two common lines within such a pair, the values of the phases in the respective Fourier transforms along the lines are identical. The inverse symmetry operation around a threefold axis of symmetry yields a third plane (yellow) which intersects both the blue and the red plane along pairs of common lines. Note that in this case and for each plane, two pairs of common lines are obtained.

B.) Description of real space common lines and sinogram correlation functions, using two class averages of icosahedral HSV-1 capsids (see van Heel et al., Quarterly Reviews of Biophysics 2000, 33 (4):307-369). Two different class averages are shown in (a) and (b). The class averages are rotated in discrete angular steps along an axis projecting towards the reader and going through the center of the projections. After each rotation step (1° steps), the class-average is projected onto a one-dimensional line, each of which is stacked on top of an analogous line obtained from the previous rotation step, to produce a series of stacked lines derived from rotations between 0° and 360°, called a sinogram, as depicted in (c) and (d). Each line from the sinogram of the first class average is compared to each line of the sinogram of the second class average by cross-correlation, and the values of the cross-correlation function are indicated in (e). These values are high if the cross-correlation between the lines is high, and the relative disposition of these highly correlating lines between the sinograms defines the relative orientation of the class averages from which the sinograms are derived. Highly symmetric objects, such as icosahedral viruses have multiple real space common lines with high cross-correlation between class averages, as highlighted by the blue, green and red lines. The indicated values for β and γ indicate Euler angles (defined in van Heel et al., Quarterly Reviews of Biophysics 2000, 33 (4):307-369), as determined by sinogram cross-correlation.

There are different ways of particle refinement, including for example polar Fourier transform [116], or maximum likelihood based [117, 118] refinement. What these approaches have in common, is that they use an averaged three-dimensional initial particle model (and therefore relatively low noise) as a template for optimizing the particle orientations of the dataset, which is done iteratively, until the resolution does not improve anymore. The resolution is usually determined by Fourier shell correlation [112], which uses a correlation function between two halfsets of the data and correlates the structure factors in Fourier space as a function of their spatial frequency. Because higher frequencies (corresponding to the fine details in the images) are increasingly closer to the noise level (due to the CTF envelope function, errors in the image alignment and imperfections of the detector), the correlation decreases with higher resolution. The spatial frequency at which the correlation falls below a certain threshold, defines the resolution of the three-dimensional model.

1.7. Aims

The aims of this thesis were to study cell entry checkpoints of selected arboviruses from the *Bunyavirus* (Uukuniemi phlebovirus) family and the *Togavirus* (alphavirus Semliki Forest virus) family *in vitro*. These checkpoints included receptor binding and membrane fusion. To my knowledge, there are no structural studies of virion-receptor interaction for either virus family, and while fusion has been extensively studied for alphaviruses, detailed studies on bunyavirus fusion are scarce. Receptor

binding and fusion are essential elements in the entry of these medically important virus families, and in order to be able to develop components that could block these viruses from entering their host cells, it is crucial to understand how exactly these virus–host cell interactions work. Virus–receptor interactions at high resolution have the potential to define the viral epitopes used in this interaction. While crystallography is clearly the best method to define such interactions at the single receptor-ligand interaction level, it currently does not allow a visualization of the interaction in the context of complete enveloped virus particles.Virus–receptor [119], as well as virus–antibody binding sites can extend over several protomers, and not just a single protein [120], and may contain non-protein components, such as glycans, or lipids [119, 121, 122]. Studying virus-receptor interactions in the context of complete virus particles is therefore essential, if one wants to understand physiological virus–receptor interactions, and if one wants to find antibodies that may compete with these binding sites. The only method capable of visualizing such interactions at high resolution and in native conditions, using enveloped viruses, is electron cryo-microscopy. In this thesis, the focus in virus–receptor interaction will be on the interaction of alphaviruses with the C-type lectin DC-SIGN. As mentioned above, dengue virus–DC-SIGN interactions have been studied earlier [119], and showed that the carbohydrate recognition domain (CRD) of DC-SIGN preferentially binds dengue virus around the icosahedral two-fold axes [119], and this knowledge may be important for the design of

neutralizing antibodies that compete with DC-SIGN binding. In this thesis, a similar study will be conducted on the DC-SIGN interaction with alphaviruses, using electron cryo-microscopy and icosahedral reconstruction.

The second, and principal aim of this thesis was to functionally and structurally characterize the cell entry of phleboviruses, with a focus on viral fusion. The aim was to establish an *in vitro* virus–liposome system for phlebovirus fusion, in order to elucidate the basic requirements for low pH dependent fusion in late endosomes. The next step was to structurally characterize fusion intermediates at low pH, using electron cryo-microscopy, in order to get an understanding of the phlebovirus fusion mechanism. Earlier studies showed that Uukuniemi phlebovirus shows conformational changes at pH 6 [79], whereas more recent studies showed that the Uukuniemi phlebovirus has a productive fusion threshold of pH 5.4 [55]. In order to study UUKV fusion at a fusion-competent pH, the idea was to first study the structure of isolated, unfixed UUKV particles at pH 5, and then to extend this to a virus–liposome system, in order to find possible fusion intermediates that allow more insight into the phlebovirus fusion mechanism.

2. Materials and Methods

2.1. Cells and viruses

BHK-21 cells and Uukuniemi virus (UUKV) strain S23 were kindly provided by Anna Överby (Umeå, Sweden). BHK-21 cells used only for Bunyamwera virus (BUNV) production, as well as BUNV, were kindly provided by Richard Elliott (Glasgow, UK). All BHK-21 cells were grown in Glasgow Modified Eagle Medium (GMEM, Life Technologies, UK) supplemented with 5-10% v/v foetal bovine serum (FBS, PAA labs, USA, or Sigma Aldrich, UK), 10% v/v tryptose phosphate broth (Sigma Aldrich, UK), 20mM HEPES (Life Technologies, UK), and at 37 °C in 5% v/v CO_2 atmosphere. C6/36 cells were from Yuguang Zhao (Oxford, UK) and were grown in Schneider's Drosophila medium (Life technologies, UK), supplemented with 10% v/v FBS, 2% w/v L-glutamine (PAA labs, USA), and grown at 28 °C in 5% v/v CO_2. UUKV was propagated by infection of BHK-21 cells at a multiplicity of infection (m.o.i.) of 0.1. BHK-21 cells were inoculated for 1 hour at 37 °C with virus in serum-free growth media, and the inoculum replaced by virus-free and serum-free growth media. The cells were left to incubate for 40-48 hours at 37 °C, after which the supernatant was collected and cleared of cell debris by low speed centrifugation (3,000×g, 30 minutes at 4°C). Virus was pelleted from the cleared supernatant by ultracentrifugation (25,000 rpm and 2h at 4°C in a Beckman SW32 rotor) over a 20% w/v sucrose (Sigma Aldrich, UK) cushion and the pellet (= concentrated virus) was left to dissolve overnight

at 4°C in neutral pH buffer (10 mM TRIS or 20 mM HEPES buffers, Melford, UK) containing 100 mM NaCl (Melford, UK) and used either for electron cryo-microscopy or further purified over a linear 10–50% w/v sucrose gradient in resuspension buffer. Linear sucrose gradients were prepared with a Gradient Master (BioComp Instruments, Inc., Canada), according to the manufacturer's instructions. Alternatively, for testing specific infectivity of UUKV in absence of ultracentrifugation, cleared UUKV supernatant was concentrated over a 30 kDa cut-off membrane (Vivaspin 15R, Sartorius Stedim, UK) and further purified over a linear Nycodenz (Progen, Germany) gradient. UUKV titers were determined by immunohistochemistry (focus-forming unit assay), similarly as described [55]. Briefly, cells were infected with serial dilutions of UUKV in serum-free growth media, supplemented with 0.2% w/v cell culture grade BSA (Sigma Aldrich, UK) for 1h, followed by removal of the virus inoculum and incubation in GMEM 0.8% w/v carboxymethylcellulose (CMC, Sigma Aldrich, UK), 0.5% v/v FBS (to keep the cells alive) for 3 – 4 days. The CMC was discarded and cells were washed twice with phosphate buffered saline (PBS, Sigma Aldrich, UK) to remove residual CMC and fixed for 20 minutes at room temperature in formaldehyde (Sigma Aldrich, UK), diluted to 4% w/v in PBS. The cells were then permeabilized with permeabilization buffer (1× PBS, 1% saponin w/v, 5 mM EDTA and 2% v/v FBS, all from Sigma Aldrich, UK), for 30 minutes at room temperature. This was followed by detection of UUKV proteins using a polyclonal anti-UUKV

serum antibody (diluted 1/2000 in permeabilization buffer) produced in rabbit (kindly provided by Anna Överby, Umeå, Sweden), followed by incubation with a horse-radish peroxidase coupled goat anti-rabbit antibody (Vector labs PI-1000, UK), diluted 1/2000 in permeabilization buffer. Cells were washed with PBS, and the foci were detected with the help of a 3,3'-diaminobenzidine (DAB) peroxidase detection kit (Vector labs, UK) according to the manufacturer's instructions. The total viral glycoprotein concentration was estimated from SDS-PAGE of virus preparations in presence of a BSA standard (Fisher Scientific, UK). Specific infectivity (ffu/mol or ffu/µg viral glycoprotein) was estimated by division of viral titers by the estimated total viral glycoprotein concentration. Semliki Forest virus (SFV, strain pSP6-SFV4, kindly provided by Margaret Kielian, Albert Einstein College of Medicine, NY, USA) and Bunyamwera virus were produced similarly as described for UUKV here, with the following modifications: SFV virus production time in BHK-21 cells was limited to 20–24 hours post-infection. SFV production in C6/36 cells was allowed for ~136 hours and cells were infected at a multiplicity of infection of 1. For BUNV infection, cells were infected at a multiplicity of infection of ~0.01. Both BUNV and SFV titers were determined by plaque assay. Plaque assays were done in presence of CMC, as described for the UUKV ffu assay above, with the modification that after fixation, viral plaques were detected by a staining with an

aqueous 1% w/v Crystal Violet (Sigma Aldrich, UK) solution. In addition, incubation times in CMC were ~2.5 days for SFV.

2.2. SDS-PAGE, western and dot blots

SDS-PAGE was either done in 5%/12% stacking gel/separating gel combinations, or in 4-15% pre-cast gradient gels (purchased from Biorad, UK). For manual gel casting, using glass plates, plastic coombs and casting stations from Biorad, UK, end concentrations of 12% w/v acrylamide/bis-acrylamide (Severn Biotech, UK), 375 mM TRIS pH 8.8, 0.1% w/v SDS (Melford, UK) were pre-mixed in de-ionized water and the acrylamide/bis-acrylamide polymerized with the help of 0.1% w/v ammonium-persulfate (APS, Sigma Aldrich, UK) and ~6 µL of N,N,N′,N′-tetramethylethylenediamine (TEMED, Sigma Aldrich, UK) per 10 mL of SDS gel solution. For stacking gels, 5% w/v acrylamide/bis-acrylamide, and 125 mM TRIS pH 6.8 was used instead. Two volumes of virus preparation were denatured in one volume of non-reducing sample buffer (33.3% v/v glycerol (Sigma Aldrich, UK), 187.5 mM TRIS pH 6.8, 3% w/v SDS), supplemented with 2 mM EDTA (to limit viral protein aggregation), and not boiled, whereas purified proteins were loaded in reducing (=non-reducing sample buffer supplemented with 15% v/v β-mercaptoethanol, Sigma Aldrich, UK) sample buffer and boiled for 5-10 minutes at 95 °C. The gels were run in presence of low range molecular weight markers (Biorad, UK), in SDS running buffer (25mM TRIS, 192mM Glycine, 0.1% w/v SDS, pH 8.3–8.5) for about 45–60 minutes between 150V and 250V.

Protein gels were stained with SimplyBlue SafeStain (Invitrogen, UK), according to the manufacturer's instructions and de-stained in de-ionized water. SDS-gels used for western blots included a BenchMark (hexahistidine-tagged) Protein Ladder (Life technologies, UK) when a hexahistidine tagged protein was loaded, as well as a dual color pre-stained protein marker (Biorad, UK), to assess successful protein transfer onto the nitrocellulose membrane (GE Healthcare, UK). For western blots, nitrocellulose membranes and SDS gels were sandwiched using an Invitrogen XCell II Blot Module and NuPAGE transfer buffer (Life technologies, UK) in 20% v/v Ethanol (Sigma Aldrich, UK). Transfer was done at 30V for 1 h 10 min. Nitrocellulose membranes were blocked in 5% low-fat milk (Marvel Original, UK) for 2 h at room temperature or at 4 °C overnight. Hexahistidine-tagged proteins were detected by using a mouse monoclonal anti-pentahistidine antibody (Qiagen 34660, UK, used 1/1000) and a goat anti-mouse antibody coupled to horse radish peroxidase (HRP, Sigma Aldrich A0168, UK, used 1/5000 – 1/10000). Incubation times were 1 h for each antibody at room temperature and wash steps were performed with phosphate-buffered saline (PBS, Sigma Aldrich, UK), or after incubation with the second antibody, with PBS including 0.05% v/v Tween-20 (Melford, UK). The HRP reaction was performed by using a standard ECL detection kit (GE healthcare, UK) and the blots developed either on film (GE healthcare, UK), using a Xograph Imaging Systems (Compact X4) developer, or digitally, by using a Biorad digital imager.

Lipid dot blot membranes were first blocked for 1 h 20 min in 1% w/v low fat milk in PBS at room temperature (RT), which was followed by a 1h incubation using UUKV at ~5.5 µg/mL viral glycoprotein (~0.04 µM viral glycoprotein). Excess virus was removed and the membrane incubated with a rabbit anti-UUKV serum antibody (1/2000, as mentioned in 2.1.), followed by incubation with an affinity-purified goat anti-rabbit HRP (Vector labs PI-1000, UK, 1/2000 in 1% w/v milk/PBS). Each step was followed by washing in blocking buffer. After incubation with the second antibody, the membrane was thoroughly washed with PBS and developed with an ECL detection kit, as described above.

2.3. Pyrene labelling of viruses

For metabolic virus membrane labelling with pyrene, BHK-21 cells were grown in presence of 15 µg/mL 1-pyrenehexadecanoic acid (Life technologies, UK) for 48 hours prior to infection, similarly as described [123]. Viral infection and further concentration and purification steps were done as described above (2.1.), with the exception that viruses were resuspended in 6 mM succinate, 22 mM phosphate, 22 mM glycine (all purchased from Sigma Aldrich, UK) pH 7.5 including 100 mM NaCl (together called SPG buffer: SPG50N100) and purified over linear 10–50% w/v sucrose gradients in the same buffer for every preparation. The SPG buffer was used here because it has a close to linear titration profile, and pH changes in most pH ranges can thus be achieved in a more controlled fashion. The molar ratios used here for of succinate, phosphate and

glycine were adapted from a Qiagen protocol (http://www.qiagen.com/data/Products/Protein/Crystallization/ProductionReports/Protocols/PACT%20Buffer%20Protocols.pdf). Virus labelling and pyrene quenching levels were confirmed using standard fluorometry with a Varian spectrophotometer (Agilent, UK) at 345 nm excitation wavelength using 5–10 nm slit widths and 250–395 nm excitation and 430–1100 nm emission filters. Pyrene emission was measured at 475 nm for pyrene excited dimers (excimers) and at 379/390 nm for pyrene monomers. The concentrated virus stocks were stored in ~40% sucrose (the sucrose density at which the viruses sedimented within the sucrose gradient), unless indicated otherwise, in which case the sucrose was removed by desalting over a PD-10 column (Sephadex G-25, GE healthcare). In the latter case, virus fractions were collected and the present UUKV virions confirmed by SDS-PAGE and fluorometry of the pyrene label.

2.4. Liposomes

For the preparation of lipid bilayers, a mixture of different lipids (all purchased from Instruchemie BV, Netherlands) in chloroform were mixed in certain molar ratios (See Table 1), and included 1,2-dioleoyl-*sn*-glycero-3-phosphocholine (DOPC), 1,2-dioleoyl-*sn*-glycero-3 phosphoethanolamine (DOPE), 1,2-dioleoyl-*sn*-glycero-3-phospho-L-serine (DOPS), 1,2-dioleoyl-*sn*-glycero-3-phospho-(1'-*rac*-glycerol) (DOPG), bis(monooleoylglycero)phosphate (S,R Isomer) (BMP), Sphingomyelin (porcine brain) (SPM), Cholesterol (Ovine wool), L-α-

phosphatidic acid (Egg, Chicken) (PA). 1-hexadecanoyl-2-(1-pyrenedecanoyl)-sn-glycero-3-phosphocholine was purchased from Life Technologies, UK. Organic lipid solvents were evaporated in an Argon stream and the dried lipids were hydrated in SPG50N100 buffer by vortexing and pipetting up and down. For liposomes labelled with 50 mM (concentration as in [124]) Sulforhodamine B (SRB, Life technologies, UK, see also 2.5.4. for the use of SRB in fusion assays), NaCl concentration was reduced to 75 mM to balance osmotic strength. For liposomes containing 30 mM and 40 mM SRB, NaCl concentrations were adjusted to 95 mM and 85 mM, respectively. Additionally to vortexing and pipetting up and down, SRB labelled samples were subsequently hydrated for 45' to 1h at RT by gentle shaking on an orbital shaker (to maximize lipid hydration), followed by 10 freeze-thaw cycles, alternating between 37 °C and dry ice temperature, in order to obtain unilamellar membranes. Liposomes were produced by extruding hydrated lipid bilayers 21 times through 100 nm pore diameter polycarbonate filter membranes (Whatman, UK), using a mini-extruder (Avanti Polar lipids, USA). Excess SRB was removed by desalting through a PD-10 column (Sephadex G-25, GE healthcare, UK). For electron cryo-microscopy, unless indicated otherwise, liposomes were hydrated in the same way than SRB-labelled liposomes, just without SRB and in presence of 100 mM NaCl, instead of 75 mM.

Table 1: Lipid compositions of liposomes produced

Lipids	DOPC: DOPE	DOPC: DOPE: BMP	DOPC: DOPE: SPM: Chol	DOPC: DOPE: SPM	DOPC: DOPE: Chol	DOPC: DOPE: DOPS	DOPC: DOPE: DOPG	DOPC: DOPE: αPA	DOPC: DOPE: BMP: Chol	DOPC: DOPE: BMP: SPM: DOPS: PCpyr: Chol
Molar ratio	7:3	5:2:3	2.2:2.2: 2.2:3.3	5.6:2.2: 2.2	4.8:1.9: 3.3	5:2:3	5:2:3	5:2:3	3.6:1.4: 3:2	2.8:1.7: 0.4:1.1: 1.1:0.4: 2.5

Abbreviations: DOPC=1,2-dioleoyl-sn-glycero-3-phosphocholine, DOPE=1,2-dioleoyl sn-glycero-3-phosphoethanolamine, BMP=bis(monooleoylglycero)phosphate, SPM=sphingomyelin, Chol=cholesterol, DOPS=1,2-dioleoyl-sn-glycero-3-phospho-L-serine, DOPG=1,2-dioleoyl-sn-glycero-3-phospho-(1'-rac-glycerol), αPA=L-α-phosphatidic acid, PCpyr=1-hexadecanoyl-2-(1-pyrenedecanoyl)-*sn*-glycero-3-phosphocholine

2.5. Lipid mixing and content release assays

2.5.1. Lipid mixing of UUKV-pyr and SFV-pyr at pH 5

UUKV-pyr (2.4–6.9×10^7 ffu) and SFV-pyr (12–23×10^7 pfu), at similar levels of pyrene excimer fluorescence intensity, were mixed with an excess of unlabelled liposomes (200 μM total input lipid concentration) in SPG50N100 buffer at pH 7.5, in a final volume of 1 mL. The concentrated virus stocks were held in ~40% sucrose, which were diluted to very small amounts once the virus was mixed with the liposomes. In these circumstances, the amount of sucrose for SFV-pyr was negligible (<0.1% w/v), whereas it was ~1.2% w/v for UUKV-pyr. The virus-liposome mixtures were transferred to a quartz cuvette (Hellma, UK) and pre-incubated at 37 °C for 10 minutes prior to acidification, in order to reach

the desired temperature. A pre-titrated amount of 1 M HCl (usually around 25 µL) was added to reach pH 5 and the fluorescence intensity was followed for a maximum of 10 minutes post-acidification, after which the pH was measured with a microelectrode (Mettler Toledo, UK). After the pH measurement, to completely dissolve lipid bilayers, Triton X-100 (Sigma Aldrich, UK), diluted to a final concentration of 0.2% v/v in SPG50N100 pH 7.5 was added. Fluorescence measurements were done at 345 nm excitation and 475 nm emission wavelengths using 10-nm slit widths. Filters used were 250–395 nm for excitation and 430–1100 nm for emission. To quantify the extent of lipid mixing, the time-dependent lipid mixing index was calculated for each measurement, as follows. Pyrene excimer emission decrease (as function of time post-acidification) was scaled between an average pyrene excimer intensity at neutral pH (defined as 0% lipid mixing, typically the average fluorescence intensity of the last ten seconds before acidification), and an equivalent intensity average after the addition of Triton X-100 (defined as 100% lipid mixing, typically the last 10 seconds of the whole measurement, in presence of Triton X-100).

2.5.2. Lipid mixing of UUKV-pyr, BUNV-pyr and SFV-pyr at pH 4.5

Preliminary lipid mixing experiments at pH 4.5 were done as in 2.5.1., with the following modifications. 100 µM phospholipid in liposomes was used instead of 200 µM, and BUNV-pyr (~7.5×10^7 pfu) was used at the same amount of sucrose present (~1.2 % w/v) as with UUKV-pyr, although the

total pyrene excimer fluorescence used was about half of the excimer fluorescence used for both UUKV and SFV. In this particular experiment only, the sucrose in the UUKV-pyr and SFV-pyr preparations was removed by buffer exchange to sucrose-free SPG50N100, over a PD-10 desalting column. Virus fractions were tested for virus content by SDS-PAGE and pyrene fluorescence and peak fractions were used for fusion assays. Because only short term storage of concentrated virus preparations was possible in sucrose-free conditions, sucrose removal from concentrated virus stocks was only attempted in this particular instance and not used any further.

2.5.3. Low pH and temperature dependence of UUKV-pyr

To test the low pH threshold of UUKV-pyr lipid mixing with DOPC:DOPE:BMP liposomes, different amounts of 1 M HCl were added to UUKV-pyr liposome mixtures (equivalent to the mixtures in 2.5.1.) and the lipid mixing was followed over time, as described in 2.5.1. After each acidification step, the pH was confirmed by measuring with a pH microelectrode. Lipid mixing at different temperatures was performed by first setting the temperature in the dedicated cuvette slot of the fluorometer. This was followed by addition of the cuvette into the same fluorometer slot and allowing for temperature stabilization for 10 minutes (whilst measuring the fluorescence). The remainder of the experiment was conducted as described in 2.5.1.

2.5.4. Content mixing assays

UUKV-pyr (same amounts than used in 2.5.1.) was mixed with SRB-labelled liposomes and the experiment was conducted as in 2.5.1., with the following modifications. The number of liposomes used amounted to a total de-quenched SRB fluorescence of ~600 to 800 arbitrary units in presence of 0.2% Triton X-100 (using 700 V PMT voltage). The liposomes were not in excess anymore, but rather present in similar amounts than the virions (see chapter 4.3.). The experimental setup was chosen to allow simultaneous detection of both UUKV-pyr (excitation at 345 nm, emission at 475 nm) and SRB-labelled liposomes (excitation at 565, emission at 586 nm). Excitation filters of 335–620 nm and emission filters of 430–1100 nm were used, both with a slit width of 5 nm. The content mixing index was determined analogously to the lipid mixing index, and the time-dependent SRB emission intensity was scaled between emission at neutral pH (defined as 0% content release) and emission in presence of 0.2% Triton X-100 (defined as 100% content release).

2.6. Low pH inactivation of UUKV

UUKV-pyr was diluted in an end volume of 900 µL SPG50N100 pH 7.5, using the same amounts of virus as in 2.5.1, after which the pH was lowered to pH 5 by addition of a pre-titrated amount of 1 M HCl. This was followed by incubation at 37 °C for 1h and re-neutralization by using pre-titrated amounts of 1 M NaOH. In negative controls without low pH pre-treatment, sterile water was added instead of HCl and NaOH. 100 µL of

liposomes were then added to this mixture, as to reach a final concentration of liposomes at 200 μM total input phospholipid. The remainder of the experiment was then conducted as a standard lipid mixing experiment, as described in 2.5.1, and the pH confirmed after acidification by measuring with a pH microelectrode. To test whether acid pre-treatment had an effect on the infectivity of UUKV, focus-forming unit assays of acid-treated virus were performed. 25 μL of concentrated UUKV were diluted in a total volume of 1mL SPG50N100 pH 7.5. Pre-titrated amounts of 1 M HCl were added to UUKV to achieve a drop to pH 5, followed by 1h incubation at 37 °C. Addition of sterile water was used as a negative control. The pH was confirmed by pH paper with a precision of 0.2–0.3 pH units (VWR or Fisher Scientific, UK) in parallel. The virus solution was reneutralized by addition of an excess (up to 19 mL) of serum-free BHK-21 cell growth media after 1 h. The pH indicator in the serum-free growth medium (phenol red) indicated neutral pH, and was confirmed by pH paper. The resulting neutral solutions containing UUKV were subjected to serial dilutions and further to standard focus forming unit assays, as described in 2.1.

2.7. DC-SIGN expression and purification

2.7.1. Primers and plasmids

A codon-optimized full human DC-SIGN cDNA sequence was synthesized by GeneArt, Regensburg, Germany, and the full cDNA sequence as well as the translated protein sequence can be found in the appendix (See 9.1.

and 9.2.). Primers were purchased from Eurofins, UK, and designed as to extract sequences coding for selected DC-SIGN ectodomains, from the full-length DC-SIGN sequence within the GeneArt DC-SIGN sequence. The forward primers had an Age1 restriction site, whereas the reverse primer had a Kpn1 restriction site. Both primers in addition had 2–3 flanking nucleotides at the 5' end (See Table 2) to improve subsequent endonuclease cleavage efficiency. The DC-SIGN extracellular domain ECD (DC-SIGN$_{ECD}$, amino acids number 66–404 from NCBI accession number NP_066978.1), the carbohydrate recognition domain CRD (DC-SIGN$_{CRD,}$ amino acids number 250-404), and DC-SIGN including five neck repeats (amino acids number 135-404) were extracted from the GeneArt plasmid by polymerase chain reaction (PCR) and the designed primers are indicated in table 2. The pHLsec vector was a gift from Thomas Bowden and is described in [125]. pHLsec encodes a hexahistidine tag at the C-terminus, which was used for purification in nickel-NTA affinity chromatography.

Table 2: PCR primers for sub-cloning of DC-SIGN fragments into the pHLsec vector

Construct	Restriction Enzymes	Forward primer (5' → 3')*	Reverse primer (3' → 5')*
DC-SIGN + CRD	5': AgeI 3': KpnI	5` CGC**ACCGGT**AGCAAC AGCCAGCGGAACTGG 3`	5' GC**GGTACC**AGCTGG TGGAGGATTGGGGGTG 3'
DC-SIGN + 5 repeats	5': AgeI 3': KpnI	5` CGC**ACCGGT**GGGGAA CTGCCTGAAAAGTCAAAA ATGC 3`	5' GC**GGTACC**AGCTGG TGGAGGATTGGGGTG 3'
DC-SIGN ECD	5': AgeI 3': KpnI	5' CGC**ACCGGT**AGCATC AGCCAGGAACAGAGC 3'	5' GC**GGTACC**AGCTGG TGGAGGATTGGGG 3'

*Restriction sites are indicated in bold

2.7.2. Sub-cloning the DC-SIGN fragments: Polymerase chain reaction, restriction digestion and ligation

The Pyrobest polymerase kit (Takara, USA) was used for polymerase chain reactions (PCR), according to the manufacturer's instructions. The kit contained all reagents necessary for PCR, and all components were mixed in sterile water, up to an end volume of 50 µL per reaction. This included the following reagents with their respective end concentrations: deoxyribonucleotides (400 µM each), Pyrobest Buffer 2 (1×, including 1 mM Mg^{2+}), and Pyrobest polymerase (1.25 units). Included were ~10 ng per primer and ~70 ng template plasmid DNA. The samples were then transferred to a thermocycler (Biorad, UK) and PCR was performed using the following parameters. First, the samples were heated for 2 min at 96

°C, then they were cycled thirty times through the following temperatures: 30 s at 96 °C, 30 s at 55–58 °C, 45 s at 72 °C. After the last cycle, the samples were kept at 72 °C for 10 minutes to finish all ongoing replications and then cooled to 4 °C. The identity of the PCR fragments was qualitatively assessed by TAE (Tris-Acetate-EDTA buffer) - agarose gel electrophoresis. DNA samples were mixed with 5× DNA loading buffer (Life Technologies, UK) and run at 100V for 40 min on a 1% agarose gel stained with SYBR Safe stain (Life technologies, UK). The PCR fragments were cleared from impurities by using a QIAprep gel purification kit, then digested with the restriction enzymes Kpn1 and Age1 (both from NEB biosciences, UK), according to NEB recommendations. The empty pHLsec vector (1–2.5 µg) was digested in parallel with twice the amounts of each restriction enzyme, as compared to digestion of PCR fragments. All digested fragments were then loaded on a 1% TAE-agarose gel, DNA bands were visualised with the help of a UV lamp and cut out with a sterile scalpel, and the DNA eluted using a QIAprep gel purification kit. Ligations were performed by using an NEB Quick Ligation Kit, according to the manufacturer's suggestions (Quick ligation protocol), except that the ligation was performed for 15–30 min.

2.7.3. Bacterial transformation and plasmid preparation

The whole ligation mixture was added to at least 50 µL of Library Efficiency DH5α competent cells (Life technologies, UK) and kept on ice for 20 min. Heat shock was done at 42 °C for 60–90 s, followed by 2 min

incubation on ice. A maximum of 950 µL SOC media (Super Optimal broth with Catabolite repression media, Life technologies, UK) were added per tube and the cells were shaked for one hour at 37 °C. The cells were pelleted and resuspended in 200 µL SOC media, plated onto Luria-Bertani (LB, Merck, UK) agar plates containing 100 µg/mL ampicillin (ICN Biomedicals, USA) and colonies were allowed to grow overnight at 37 °C. Colonies were picked and grown overnight at 37 °C in a rotary shaker (~200 rpm) in 2 mL liquid LB supplemented with 100 µg/mL ampicillin. The cells were pelleted and subjected to plasmid preparation using a QIAprep Spin Miniprep kit. The obtained DNA was quantified with the help of a nanodrop machine and the plasmids were sequenced by Source Bioscience, UK, using pHLsec (vector-based [125]) specific sequencing primers (Table 3). Amino acid sequence alignments of the three soluble DC-SIGN constructs encoded on the pHLsec plasmids, against the full-length human DC-SIGN protein sequence encoded on the Geneart plasmid, all as translated into protein sequence (http://web.expasy.org/translate/) from the respective plasmid DNA sequences, is depicted in Figure 2.1.

Table 3: pHLsec sequencing primers

Primer	Primer sequence (5' → 3')
Forward sequencing primer	GCTGGTTGTTGTGCTGTCTCATC
Reverse sequencing primer	CACCAGCCACCACCTTCTGATAG

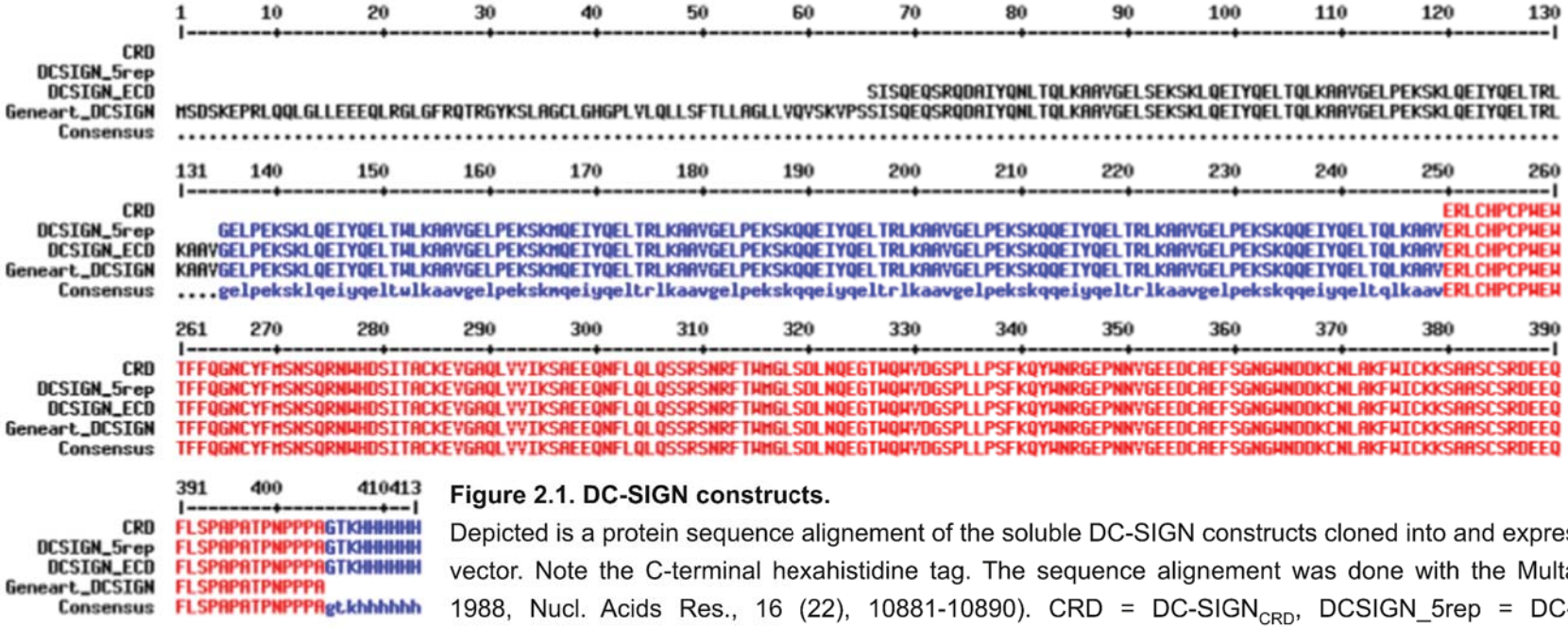


Figure 2.1. DC-SIGN constructs.

Depicted is a protein sequence alignement of the soluble DC-SIGN constructs cloned into and expressed from the pHLsec vector. Note the C-terminal hexahistidine tag. The sequence alignement was done with the Multalin software (F. Corpet, 1988, Nucl. Acids Res., 16 (22), 10881-10890). CRD = DC-SIGN$_{CRD}$, DCSIGN_5rep = DC-SIGN$_{CRD}$ + 5 repeats, DCSIGN_ECD = DC-SIGN$_{ECD}$, Geneart = Full-length human DC-SIGN, as encoded from the Geneart vector. Expected molecular weights of the DC-SIGN constructs encoded on pHLsec were calculated with the ProtParam software (Gasteiger E., Hoogland C., Gattiker A., Duvaud S., Wilkins M.R., Appel R.D., Bairoch A.; Protein Identification and Analysis Tools on the ExPASy Server; (In) John M. Walker (ed): The Proteomics Protocols Handbook, Humana Press (2005). pp. 571-607) and were as follows: DC-SIGN$_{CRD}$: 18840.8 Da, DC-SIGN$_{CRD}$ + 5 repeats: 32035.9 Da, DC-SIGN$_{ECD}$: 39823.8 Da without N-glycan. Idendical sequences shared between all constructs are in red and identical sequences shared between three constructs are shown in blue.

For large scale plasmid production, Subcloning Efficiency DH5α Competent E. Coli cells (Life technologies, UK) were transformed by heat shock as described above, with the modification that 25 µL of competent E. Coli cells were transformed with a large amount of plasmid DNA (~1 µg) and that the transformed cells were resuspended in an end volume of 100 µL SOC media, and directly plated onto LB agar plates (including 100 µg/mL ampicillin) and incubated at 37 °C overnight. Two liters of LB media supplemented with 100 µg/mL ampicillin were inoculated with a streak of bacterial colonies from the LB agar plates, and the bacteria were grown overnight in a rotary shaker (~200 rpm) at 37 °C. The grown bacteria were centrifuged at 3000×g for 30 minutes and the pellet processed to retrieve the plasmids by using a Plasmid Giga Kit (Qiagen, UK).

2.7.4. Protein expression in HEK cells

All (except one performed by myself) large scale transfections of HEK 293T cells in roller bottles, and where applicable, of HEK 293S cells [126], were kindly performed by Professor Yvonne Jones' lab technician Weixian Lu, as described [125]. The steps from harvesting the protein onwards were all done by myself. The expected molecular weights of the expressed DC-SIGN constructs are indicated in figure 2.1. Briefly, HEK cells were grown in DMEM (Sigma Aldrich, UK) supplemented with 10 % Fetal Calf Serum (FCS, Life technologies, UK), non-essential amino acids and L-Glutamine (both from Life technologies, UK) to ~90% confluence in roller bottles (Greiner Bio One, UK).

For one roller bottle, 0.5 mg of plasmid DNA were incubated for 10 minutes in presence of 1mL of 1mg/mL polyethylene-imine (PEI) in a final volume of 50 mL serum-free growth media. The mixture was then added on top of cells that contained 200 mL of fresh growth media. The roller bottles were incubated for 4–6 days at 37 °C, and the supernatant was harvested when the cells started detaching. The soluble protein containing supernatant was cleared from cell debris for 20 minutes at 3000×g, then sterile filtered over 0.22 µm Stericup Filter units (Millipore, UK) and stored at 4 °C.

2.7.5. Protein purification: Diafiltration, nickel-NTA affinity chromatography and gel filtration

To remove the chelating agents (*e.g.* EDTA) that are present in the filtered cell supernatant and that could interfere with nickel affinity chromatography, the supernatant was diafiltrated against a total of about two volumes of equilibration buffer (10 mM TRIS, 100-150 mM NaCl pH 7.4–8 in presence or absence of 5mM $CaCl_2$), using a Quixstand (GE Healthcare, UK) device with a 10 kDa cut-off. The diafiltrate was then loaded onto a pre-equilibrated 5 mL HisTrap HP column (GE healthcare, UK) and eluted by using a stepwise elution protocol that included 20 mM, 40 mM, 50 mM and 250 mM Imidazole in equilibration buffer. The main DC-SIGN peak eluted in fractions containing 250 mM imidazole, which were combined and concentrated over Amicon Ultra centrifugal filters with a 10 kDa molecular weight cut-off (Millipore, UK). The concentrated

protein was then purified over a Superdex 200 10/30 GL (GE healthcare, UK) gel filtration column. For DC-SIGN$_{ECD}$ and DC-SIGN$_{CRD}$ + 5 repeats, two main peaks eluted after the void volume: One major peak, eluting first, and one minor peak, eluting subsequently, as expected (see also [127, 128]. The first (higher) peak presumably contained DC-SIGN tetramers and was reloaded onto the gel filtration column to assess peak stability. Approximate yields were up to 0.2–1.3 mg/L cell culture supernatant. No yield was determined for the DC-SIGN$_{CRD}$ + 5 repeats construct. The yields indicated for the proteins with a neck domain refer to the tetramer peak only. The purity and identity of the eluted DC-SIGN proteins was confirmed by SDS-PAGE and Western blot, as described in 2.2.

2.8. Enzyme-linked immune sorbent assay (ELISA)

Hexahistidine-tagged constructs were subjected to a sandwich ELISA, in which UUKV formed the bottom of the sandwich, the hexahistidine-tagged protein probe the middle, and a rabbit anti-hexahistidine antibody (Abcam ab9108, UK, used 1/1000) as well as a goat anti-rabbit antibody coupled to HRP (Vector labs PI-1000, UK, used 1/1000 to 1/2000), the top of the sandwich. Briefly, UUKV particles corresponding to 4–5 pmol of total UUKV glycoprotein were plated in 96-well Nunc-Immuno PolySorp plates (Sigma Aldrich, UK) and incubated overnight at 4 °C. Alternatively, the same amount of Bovine Serum Albumine (BSA, Fisher Scientific, UK) was used as a negative control for UUKV. This was followed by removal of unbound protein and followed by a 2-hour room temperature (or overnight

at 4 °C) blocking step, using 5% w/v BSA Cohn's fraction five (Sigma Aldrich, UK) in 20 mM HEPES, 100 mM NaCl (H20N100) pH 7.2. Apart from the aforementioned DC-SIGN constructs, the following proteins were included in the UUKV binding analysis. Firstly, a C-terminally hexahistidine-tagged TIM-4 ectodomain consisting of the IgV domain and part of the mucin domain (amino acid residues 24-153 of GenBank accession No. AAH08988.1, purified as described [125]), was kindly provided by Iona Easthope and Max Crispin, Oxford, UK, and, secondly, a negative control for binding to UUKV, consisting of a paramyxovirus glycoprotein G_h ectodomain (C-terminally hexahistidine-tagged G_h residues 199-631 of GenBank accession No. AFH96011.1, was kindly provided by Thomas Bowden, Oxford, UK). The latter constructs were serially diluted in H20N100 supplemented with 5% w/v BSA fraction five and 2–5 mM $CaCl_2$ (Sigma Aldrich, UK). No $CaCl_2$ was used in presence of TIM-4. The protein dilutions were then bound to UUKV for 1 h, which was followed by incubation with the first and second antibodies for 1 h (room temperature) each in presence of 5% w/v BSA. Sample wells were washed with H20N100 containing 2–5 mM $CaCl_2$ (in presence or absence of 5% w/v BSA) after each step. After incubation with the second antibody, the wells were extensively washed (at least three times) with H20N100 supplemented with 2–5 mM $CaCl_2$ and 0.05% v/v Tween-20 (Melford, UK). This was followed by one or two wash steps in absence of Tween-20. The ELISA was developed with the help of an ABTS (2,2'-azino-bis(3-

ethylbenzthiazoline-6-sulfonic acid)) Peroxidase (HRP) Substrate Kit (Vector labs, UK), according to the manufacturer's instructions. The peroxidase reaction was stopped after ~30 minutes by adding one volume of 5% sodium dodecyl sulphate (SDS). Light absorption at 405 nm was measured using a plate reader (Tecan).

2.9. Electron cryo-microscopy and tomography: sample preparation

2.9.1. Plunge-freezing of SSIP-1 and UUKV particles

Holey carbon-coated molybdenum grids (Quantifoil, Microtools, Germany), or holey carbon-coated copper grids (C-flat, Protochips, USA) were glow-discharged for 20 seconds at highest intensity in a Harrick plasma (USA) glow discharger. Plunge-freezing devices, either built in the workshop of the Max Planck Institute of Biochemistry, Martinsried, Germany or a semi-automatic CP3 plunger (Gatan, USA), were cooled with liquid nitrogen for 20 minutes prior to addition of liquid ethane/propane (7:3 v/v) to its dedicated cup in the plunge-freezer. 3–5 µL of concentrated UUKV or 3 µL of Salisaeta icosahedral phage 1 (SSIP-1, kindly provided by Hanna Oksanen, Helsinki, Finland) were added to glow-discharged grids. SSIP-1 in 9% w/v saltwater (SW, [129]) was directly pipetted onto the grid without on-the-grid washing, and the liquid blotted for four seconds from both sides with Whatman filter paper, prior to flash-freezing in liquid ethane/propane. UUKV was washed for 10–30 s on the grid against a few hundred µL of either neutral pH buffer (20mM TRIS, 100 mM NaCl pH 7.4) or low pH buffer (20 mM MES, 100 mM NaCl pH 5), and the grid was then

carefully removed sideways, as too keep the liquid on the grid, similarly as previously established [130]. MES (2-(N-morpholino)ethanesulfonic acid) was purchased from Melford, UK. Prior to flash-freezing in liquid ethane/propane, excess liquid was blotted away with filter paper from the uncoated side of the grid, until the liquid stopped spreading on the paper (usually 2–4 seconds). Manual blotting of liquid from one side of the grid, as opposed to semi-automatic blotting from both sides was necessary after grid washing steps because of liquid volume variations on the grids, occuring after the washing steps.

2.9.2. Plunge-freezing of liposomes and virus-liposome complexes

Isolated liposomes at 1 mM total lipid concentration were plunge-frozen analogously to isolated UUKV particles (see previous section), but without any on-the-grid washing steps. For the preparation of virus-liposome complexes, sucrose gradient-purified UUKV was first diluted in sucrose-free SPG50N100 pH 7.5 buffer to reduce sucrose concentrations to negligible amounts, which was followed by ultracentrifugation. Resuspended UUKV pellets had a glycoprotein concentration of ~0.2 µM, as estimated by SDS-PAGE in presence of a BSA standard. Half a volume of liposomes (end concentration of 1mM input lipid) and half a volume of sucrose-free UUKV (end concentration of ~0.1 µM viral glycoprotein) was pre-incubated for 10 minutes at 37 °C to allow possible virus to liposome binding. 4 µL of this mixture were supplemented with 1 µL of BSA-coated 10 nm gold beads (Aurion, Netherlands) and pipetted onto holey carbon-

coated copper grids (C-flat, Protochips, USA). The grids were washed against 2 mL (= volume corresponding to an overfilled microcentrifuge tube) of pre-warmed (37 °C) SPG50N100 at pH 5.0 or pH 7.5 for 10–20 seconds, the grids carefully removed sideways from the wash buffer, as described in 2.9.1., and the liquid was manually blotted away with filter paper from the non-carbon-coated side, until the lipid stopped spreading, which was typically less than 4–5 seconds. This was instantly followed by flash freezing of the grids.

2.9.3. Plunge-freezing of SFV-DC-SIGN complexes

Sucrose gradient-purified SFV was diluted in sucrose-free 10 mM TRIS and 100 mM NaCl pH 7.4 to reduce sucrose concentrations to negligible amounts, which was followed by concentration of the resulting SFV solution over Amicon Ultra centrifugal filters (Millipore, UK) with a 30 kDa cut-off. Concentrations of sucrose-free SFV reached concentrations of up to 12 µM viral glycoprotein, as estimated by SDS-PAGE that included a BSA standard. Equal volumes of SFV (6 µM total viral glycoprotein end concentration) and DC-SIGN$_{ECD}$ (50 µM end concentration) were incubated overnight (16–17h) at 4 °C in presence of 10 mM $CaCl_2$ (similarly as described [119]) prior to plunge-freezing. The mixture was then directly pipetted onto C-flat holey carbon grids and blotted with filter paper for three seconds from both sides, prior to flash freezing in liquid ethane/propane.

2.10. Electron cryo-microscopy in single particle mode

Isolated UUKV and SSIP-1 particles, as well as SFV-DC-SIGN complexes were acquired on a Tecnai Polara electron cryo-microscope (FEI, Netherlands) operated at 300 kV and liquid nitrogen temperature (~80 K), and a standard sample mounting procedure in cryo conditions is extensively described in [131]. Samples were recorded using the software SerialEM [132]. For *Salisaeta* icosahedral phage 1 (SSIP-1), images were acquired at a nominal magnification of 59000×, which corresponded to a calibrated pixel size of 2 Å/pixel, within a defocus range of -1 to -2.6 µm. Images were recorded with a charge coupled device (CCD) camera (4096×4096 pixels, Ultrascan 4000, Gatan, USA). UUKV particle acquisition parameters were the same, except that they were acquired at a defocus of -5 µm only. The electron dose was 20 electrons/$Å^2$ per micrograph for both SSIP-1 and UUKV. The SFV-DC-SIGN complexes were acquired at a nominal magnification of 160,000×, which, using a K2 Summit (Gatan, USA) direct electron detector, led to a pixel size of 1.35 Å/pixel (0.675 Å/pixel in super-resolution mode) within a defocus range of -1 to -2.5 µm. The electrons were energy-filtered in zero-energy-loss mode using an energy filter (Quantum, Gatan, USA) with a 20-eV slit width, in order to discard inelastically scattered electrons. To be able to track beam-induced particle movements during the acquisition, 22 frames per region of interest were acquired, with a total electron dose of 16 electrons/ $Å^2$ over the 22 frames. Electron micrographs of isolated liposomes were

acquired on a Tecnai T12 microscope (FEI, Netherlands), operated at 120 kV and in low dose mode (14–22 electrons/Å^2), using a nominal magnification of 52,000×, corresponding to a calibrated pixel size of 2.16 Å/pixel. The defocus was -2 µm. Images were recorded with a CCD camera (4096×4096 pixels, Ultrascan 4000, Gatan, USA).

2.11. Icosahedral reconstruction of SSIP-1, UUKV and SFV-DC-SIGN particles

The main procedure is explained by using the example of SSIP-1. Deviations from the SSIP-1 protocol in the case of UUKV and SFV-DC-SIGN complexes are indicated, where necessary. Electron micrographs were first pre-processed, which consisted in grey value normalization and inversion (this was done in later steps for UUKV and SFV-DC-SIGN), followed by estimation of the defocus and the contrast transfer function (CTF) for each micrograph. CTF estimation was done in CTFFIND3 [133], as part of the RELION software package [118, 134]. The calculated power spectra were visually assessed versus the power spectra of the electron micrographs, using XMIPP [135] (here only used as visualization tool). The power spectra that did not visually match the fitted CTF were discarded. In the case of SFV-DC-SIGN, the full movie frames for each micrograph were aligned and averaged before pre-processing, and 20% of the worst CTF fits of the averaged frames were already discarded before visual assessment, with a remaining CTF model/data cross-correlation value of ~0.18. Virus particles were then automatically picked by using

ETHAN [136], and the selected particles were visually assessed for accuracy of picking, and de-selected or selected if necessary, using EMAN2 [137] as visualization tool. Viral particles were then boxed out of the micrographs, using a square box size of 676 pixels for SSIP-1 (700 pixels for UUKV and 680 pixels for SFV-DC-SIGN). High resolution structures are usually obtained by using model-based refinement of particle orientations. For SSIP-1 and UUKV, low resolution models were constructed directly from the data. To this end, a software called IMAGIC [138] was used. SSIP-1 particles were first translationally (x and y) aligned in three iterative steps (allowing a maximal shift of 0.2× the whole particle image, in each direction), using rotational averages of the latest aligned averages as a template. This was then followed by multivariate statistical analysis (MSA, [114, 138]), allowing particle classification and class averaging. During particle classification, a ring-shaped mask (MSA mask between 0.45 and 0.9 radial fractional units (range = 0 – 1) relative to the particle image; for UUKV this was 0.4 to 0.9) was used to allow classification only according to the viral membrane and surface proteins. The particles were then rotationally aligned against selected class averages that showed well resolved lipid bilayers and spikes, allowing rotations between -180° and 180°. In the case of UUKV, each rotational alignment step was followed by another translational alignment step, as previously described. The resulting aligned particles were subjected to a new round of MSA and class averaging. For SSIP-1, 44 class averages

(each consisting of 14–84 particles) were subjected to angular reconstitution (Euler angle assignment), using real space common lines and sinogram correlation functions, and assuming icosahedral symmetry. The obtained Euler angles were then used to reconstruct a three-dimensional volume resulting in an average correlation error of 30.6% per orientation. The same was done with UUKV particles, using 23 class averages (2–23 particles per class, 28% correlation error).

Next, the particles were classified in RELION, which included two-dimensional and three-dimensional classification, and was done to select high quality particles from the whole dataset. This was followed by three-dimensional model refinement. Both three-dimensional classification and refinement were done using a three-dimensional reference model (see below), and were executed using the University of Oxford Advanced Research Computing (ARC) facility. 30 two-dimensional classes were allowed for 3,363 SSIP-1 particles, 10 classes for 580 UUKV particles and 20 classes for 4,153 SFV-DC-SIGN particles. Classes were selected based on how sharp they looked and on the resolution estimation given by RELION (the higher, the better). 3,101 particles were selected for SSIP-1, 545 for UUKV, and 4,149 for SFV-DC-SIGN. The newly selected particles were then subjected to three-dimensional classification, using a three dimensional reference model. For SSIP-1, this was the model generated in IMAGIC. For UUKV, both the initial model constructed in IMAGIC, or alternatively, a previously published Rift Valley Fever virus (RVFV) model

(EMDB 1550, [78]) was used. For SFV-DC-SIGN, a previously published SFV model (EMD-1015, [139]) was used as a reference. To minimize model bias, all initial models were filtered to 50–60 Å resolution and the initial angular sampling was set to 3.7°. Box sizes used were 650 pixels for SSIP-1, 700 pixels for UUKV, and 592.6 pixels (800 Å) for SFV-DC-SIGN. For SSIP-1, three out of four three-dimensional classes were selected, which led to a remaining 2,865 particles. For SFV-DC-SIGN, two out of four classes were selected, and the remaining number of particles was 2,718 particles. Both SSIP-1 and SFV-DC-SIGN particles were refined in RELION, with initial global sampling rates at 1.8° and local sampling rates at 0.9°, and the resolution calculated using the gold-standard Fourier shell correlation (FSC) [140] after each refinement iteration. The refinements stopped automatically when the resolution stopped improving, which was followed by a last iteration in which the spatial frequencies were filtered to Nyquist frequency (twice the pixel size). For SFV-DC-SIGN particles, a movie processing step, as described [141], was added after the model refinement, which corrected for single particle movements in between movie frames, using the software package RELION. Briefly, single particles were extracted from individual movie frames and their isolated movement between the frames tracked, which was followed by the calculation of single particle frame weighting curves (so-called “particle polishing”), all of which is part of RELION. These weighting curves give more weight to individual particle frames that are less affected by drift and

radiation damage. Based on the particle movements and weighting curves calculated from the movie frames, new movement-corrected particle averages were calculated, and these newly aligned and average particles were subjected to three-dimensional iterative structure refinement, as described above.

Refined three-dimensional volumes were post-processed in RELION, as described [142]. Briefly, B-factors (describing the resolution dependent signal decay that comes from the CTF) were estimated [140], which was followed by B-factor sharpening of cryo-EM density maps, and density-threshold based masking of the three-dimensional model. Calculated inverse (negative) B-factors used for B-factor sharpening were -1140.4 and -353.8 for SSIP-1 and SFV–DC-SIGN complexes, respectively. The high inverse B-factor for SSIP-1 can be explained by the presence of high salt buffer, causing an increased loss of contrast. Gold standard FSC's of the masked volumes were corrected by randomized phase FSC's, as described [142], to minimize artefactual masking effects and overfitting (=cumulative fitting of noise).

2.12. Two-dimensional image processing of UUKV spikes

UUKV lipid bilayers were marked by using the Bsoft [143] filament tool and spikes were extracted in 80x80 pixel and 90% overlapping square-shaped boxes, the center of which is directly located along the line that marked the viral lipid bilayer. 22,202 spike images (from 410 particles) were obtained for UUKV at pH 5 and 21,421 spike images (from 394 particles) were

obtained for UUKV at pH 7.4. The extracted spikes were “back–rotated”, such that the spikes were pointing upwards with the help of the jrotate.py script (Dr. Juha Huiskonen, Oxford, UK). The particles were vertically aligned three times consecutively in IMAGIC, allowing a maximal shift of 14.4 nm (fractional image shift of 0.3) during each alignment, using the average of the latest aligned spikes as a reference. The aligned spikes were then subjected to MSA, using a circular mask of 18 pixels radius (10.8 nm) that included the spikes in the image centre and the lipid bilayer. This was followed by spike classification and class averaging into 30 different classes. For the preparation of radial averages, spikes of both pH 5 and pH 7.4 were combined into one single average that was vertically aligned three times, as mentioned above for the separate datasets. The separate datasets at pH 5 and pH 7.4 were then separately (vertically) aligned against the common average using the same maximal allowed shift as above. The resulting aligned spikes of each separate dataset were then radially averaged relative to a circular origin located ~43 nm centripetally to the viral membrane, using Bsoft. The latter origin was estimated by manually fitting a circle along the viral membrane and finding the circle with a certain radius that visually fitted the best, and that was compatible with previously published membrane radii (43 and 45 nm) for UUKV at different pH [79].

2.13. Electron cryo-microscopy and tomography of UUKV liposome complexes

Single-axis tomographic tilt series were collected in steps of 3° from –60° to 60° on a Tecnai Polara electron cryomicroscope operated at 300 kV, using the SerialEM software [132] in low dose mode. The total electron dose per tilt series was 100 electrons/Å^2 and the electrons were energy-filtered in zero-energy-loss mode using an energy filter (Quantum, Gatan, USA) with a 20-eV slit width. The nominal magnification used was 61,000×, which corresponded to a calibrated pixel size of 0.31 nm and the defocus was at –6 µm. The tomograms were reconstructed using the IMOD package [144], in which images were also downsampled to 0.62 nm/pixel and low-pass filtered to remove spatial frequencies higher than the first zero in the contrast transfer function (~3.5 nm spatial resolution). Smaller volumes corresponding to virus–liposome complexes were extracted from the tomograms with the help of Bsoft. 10 nm thick tomogram slices were saved as projections, using the slicer function from IMOD [144] and further filtered to 6 nm spatial resolution in Bsoft, in order to emphasize the density of lipid bilayers. Simple projection images of DOPC:DOPE liposomes in presence of UUKV at pH 5 were taken on a Tecnai F30 electron microscope (FEI, Netherlands) operated at 300 kV, using a –60 to 60° side entry cryo holder (Gatan, USA). The nominal magnification was 18,000×, leading to a calibrated pixel size of 0.73

nm/pixel. The defocus was –6 µm and the electron dose was 12 electrons/Å^2. Images were filtered to 6 nm spatial resolution.

2.14. Fluorescence activated cell sorting (FACS) of UUKV infected cells

BHK-21 cells were plated onto flat-bottom 96-well plates (SLS, UK) in presence of 50 µg/mL of the mouse anti-BMP (Tebu Biosciences Z-PLBPA, UK) antibody and grown overnight at 37 °C. Alternatively, cells were treated with 50 µg/mL of the MOPC-21 isotype control antibody (Tebu Biosciences A7-632-C, UK) or left without antibody. Where initially added, samples were held in presence of antibodies throughout the experiment. 80,000 cells were infected with UUKV at multiplicity of infection of 0.7 or 3.6, either in presence or absence if the indicated antibodies in serum-free BHK-21 growth media, including 0.2% BSA (culture grade, Sigma-Aldrich) and incubated for 1h at 37 °C. The virus inoculum was then removed and replaced with full BHK-21 growth media in presence or absence of antibodies, followed by 6 hours incubation at 37 °C. The cells were then washed with PBS, trypsinized and transferred to a round-bottom 96-well plate (SLS, UK), in which they were fixed with 4% formaldehyde for 20 minutes at room temperature. The cells were then washed in permeabilization buffer, which is PBS, 2% v/v FBS, 5mM EDTA and 1% w/v saponin (all from Sigma Aldrich, UK) and left in the same buffer overnight at 4 °C to allow thorough permeabilization. Washing steps as well as media exchange steps in round-bottom plates were performed

by centrifuging the plates at 300×g in a plate rotor at 4 °C. After permeabilization, the cells were incubated with a polyclonal rabbit anti-UUKV serum antibody (Dr. Anna Överby, Umeå, Sweden) diluted 1/1000 in permeabilization buffer. This was followed by a wash step and incubation with a goat anti-rabbit antibody coupled to AlexaFluor 488 (Life technologies) diluted 1/1000 in permeabilization buffer. Alternatively, to detect the anti-LBPA antibody, cells were incubated with a goat anti-mouse antibody coupled to AlexaFluor 647 (Life technologies). All antibody incubations were done for 1h at room temperature. Cells were washed twice with permeabilization buffer and twice with PBS to remove the detergent, after which they were held on ice until FACS acquisition. Cells were transferred to plastic tubes (SLS, UK) compatible with the cell sorter, and 5000 cells per sample were counted, using a FACS Canto I (BD Biosciences) from the laboratory of Professor Richard Cornall (Oxford, UK). Processing of the fluorescence data was done with the help of the FlowJo software, licensed by the group of Prof. Richard Cornall.

2.15. Virus glycan digestion and glycan analysis

For digestion of virions with EndoF1-GST (Elena Seiradake, Oxford, UK), 10 µL of sucrose gradient-purified SFV produced in BHK cells (0.8 µM viral glycoprotein) and 10 µL of sucrose gradient-purified SFV produced in C6/36 cells (1.7 µM viral glycoprotein) were incubated in an end volume of 34 µL at 37 °C for 16 h in presence of ~10 µg/mL (or 0.2 µM) EndoF1-GST (end concentration) in 50 mM Citrate pH 5.5. Digested SFV was

denatured with non-reducing sample buffer (see 2.2.) and subjected to SDS-PAGE analysis. For glycan analysis, at least 4 µg of total viral glycoprotein were loaded onto pre-cast 4–15% Biorad gradient gels and subjected to SDS-PAGE analysis. For SFV, adding high volumes (*e.g.* 34 µL) into each well was sufficient, whereas for UUKV, a second pelleting step was required. To this end, appropriate amounts of resuspended UUKV pellet (a few 100 µL) were diluted in serum-free BHK-21 growth media and re-pelleted over a 15% sucrose cushion in a single ultracentrifuge tube. The resulting pellet was resuspended in a remainder of supernatant and loaded onto an SDS-gel. Both SFV and UUKV were loaded in non-reducing sample buffer. The glycan bands were cut out with a sterile scalpel on a clean surface and sent to Max Crispin (Oxford, UK) for glycan analysis using ion mobility mass spectrometry.

2.16. Dynamic light scattering

Dynamic light scattering (DLS) of liposomes to determine the liposome radii was done with a DynaPro Protein Solutions Temperature Controlled Microsampler (DynaPro 99-90). Liposome preparations were diluted 1/20 in aqueous neutral buffer to an end volume of 12 µL, and at least 100 measurements in 1.5 s intervals were taken at 10% of the detector sensitivity, assuming a refractive index of 1.358 (aqueous buffer). Radii were determined via the liposomes' autocorrelation function using the accessory DLS software called Dynamics.

2.17. UUKV-liposome flotation assays

One volume of sucrose gradient purified UUKV supernatant (100 µL, with preparations usually being in the range of 10^8-10^9 ffu/mL in ~40% sucrose) was mixed with about two volumes of liposome preparation (200 µL, initial preparations were at ~2 mM total input lipid concentration) and incubated for 1h at 37 °C. The liposomes were supplemented with 1% mol of the amphiphilic dye DiD (Life technologies, UK), added to the lipids before rehydration (see 2.4. for lipid hydration protocol), to facilitate visualization of possible liposome bands within the linear sucrose gradient, after centrifugation. The virus-liposome complexes were supplemented with sucrose to a final concentration of 40% w/v sucrose in SPG50N100 pH 7.5, and added to the bottom of a linear 15–40% sucrose gradient. This was followed by overnight ultracentrifugation (~16 h) at 40000 rpm in an SW-55 rotor (4 °C). Fractions were collected from the top and subjected to SDS-PAGE and western blot analysis, as described for UUKV in 2.2. The presence of fluorescent liposomes was confirmed by fluorometry, using the Varian spectrophotometer, and exciting at 644 nm, with emission measured at 666 nm (using both 550–1100 nm excitation and emission filters, as well as 10 nm slitwidths). Alternatively, to account for a possible liposome destabilization caused by high sucrose concentrations in flotation assays, concentrated viral supernatant was mixed with liposomes, supplemented to an end concentration of 5% w/v sucrose, and loaded from the top of a linear sucrose gradient (15–45% sucrose).

3. Structural analysis of the Uukuniemi phlebovirus at low pH

3.1. Rationale

Low pH conformations of phleboviruses have never been visualized in native conditions, and the only unfixed phlebovirus electron cryomicroscopy (cryo-EM) structures available so far are the low resolution neutral pH structures of the phlebovirus called Rift valley fever virus (RVFV, at 6.1 nm resolution [145], and at 2.7 nm resolution [146]). Recent studies on chemically fixed Uukuniemi phlebovirus (UUKV) at different pH suggested that UUKV changes from a pointed spike structure at neutral pH to a hollow spike conformation at pH 6 [79]. Interestingly, the UUKV structure at pH 6 looked similar to the fixed Rift Valley fever virus structure at neutral pH [78]. Because UUKV had a fusion threshold of pH 5.4 [55], it could not be excluded that there would be another UUKV spike conformation beyond the fusion threshold, possibly more closely related to the real post-fusion conformation.

Electron cryo-microscopy (cryo-EM) and icosahedral reconstruction allows the capture of viral glycoprotein structures at the virion surface in an aqueous, native environment at near-atomic resolution [107, 108, 147], if the particles are homogenous enough to be averaged. Icosahedral symmetry greatly facilitates the achievement of high resolution, because each view in the icosahedral asymmetric unit is repeated 59 times in the

whole icosahedron, and hence less orientations than expected for a non-symmetric counterpart are required to restore the full three-dimensional information. This drastically reduces the number of particles required for a high resolution cryo-EM structure, as compared to non-symmetric structures. Although phleboviruses are icosahedral, no sub-nanometer resolution cryo-EM structure is available so far. Whether this is due to sub-optimal sample preparation causing a certain degree of conformational variation in viral particles and thus particle heterogeneity (which drastically limits the attainable resolution), or whether phleboviruses would just have an intrinsic degree of heterogeneity, or both, is not entirely clear.

Because recent studies using electron cryo-tomography of fixed virions showed that the prototypic, and most importantly, non-pathogenic (and thus easier to handle) UUKV was icosahedral [79], the idea was to record isolated UUKV particles in native conditions, using cryo-EM in single particle acquisition mode, followed by icosahedral reconstruction (which routinely delivers higher resolution than tomography, if the particles allow icosahedral reconstruction). The aim of this chapter was to perhaps obtain the first high resolution structure of a phlebovirus and possibly more information on low pH dependent glycoprotein conformations in the context of whole virions and in native conditions. Therefore, the focus was held on the cryo-EM analysis of isolated native UUKV at both neutral and low pH.

3.2. Icosahedral reconstruction of UUKV at neutral pH

The first step was to determine whether a standard method of UUKV preparation would yield a virus preparation of sufficient quality for the anticipated cryo-EM and icosahedral reconstruction studies in native conditions. Concentrated UUKV, produced in baby hamster kidney cells (BHK-21), was exposed to either neutral or low pH before plunge-freezing and electron microscopic analysis. Consistently with previous data [79], most virions looked spherical, but on the other hand, the pointed appearance of viral spikes could not be observed (Figure 3.1). As expected, there was a significant amount of particle aggregation at low pH, presumably due to the exposure of hydrophobic fusion loops, causing hydrophobic virus-virus interactions and possibly fusion (Figure 3.1. C and D).

To determine if the UUKV particles at neutral pH would be suitable for icosahedral reconstruction, 580 particles from 396 micrographs were carefully selected, as to avoid the inclusion of distorted particles as much as possible. The viral particles were processed as described in Figure 3.2. Briefly, the CTF (contrast transfer function) was estimated from the power spectra of the electron micrographs, and viral particles picked and boxed from the selected electron micrographs. The particles were aligned by two-dimensional multi-reference alignment (translational and rotational) and then classified by multivariate statistical analysis (MSA [138, 148]). What does MSA do exactly? For example, a dataset of 2,000 images with each

700x700 = $4.9x10^5$ pixels can be represented in a hyperspace with $4.9x10^5$ dimensions (one for each pixel) in which each image is a point with a certain distance from the origin. In such a hyperspace, the image dataset thus forms a cloud of points. Some points may be closer to each other than to others, and these more dense "sub-clouds" represent similar-looking images. Distinct sub-clouds therefore represent distinct groups of similar-looking images. First, MSA places a one-dimensional vector along the highest direction of variance, thus defining the axis of highest variability. Next, a second vector is placed orthogonally towards the first, pointing towards the second highest direction of variance. These vectors establish a multidimensional coordinate system with lower amounts of dimensions, as compared to the initial hyperspace. This allows a significant reduction of variability, and at the same time performs a classification of the particle images according to the newly established coordinate system, which are then averaged to form class averages. All the particles are then iteratively aligned against representative class averages to improve particle distribution in the image cloud as much as possible, until class averages are deemed suitable for angular reconstitution (*e.g.* well-resolved particle features, but distinct from class to class). In angular reconstitution of icosahedral particles, the class average is given an icosahedral view orientation which is described by the Euler angles θ, φ and ω (see also Figure 3.2). Typically, a large number of classes is chosen to allow a large number of different orientations, and the

exact number of classes is usually a trade-off between maximal number of particles per class (to maximize signal-to-noise ratio in class averages) and maximal number of classes (to maximize the number of different orientations).

UUKV class averages showed locally blurred membrane and spike densities (Figures 3.3 A to 3.3 D), which was presumably due to size heterogeneity. Two-dimensional and unsupervised particle classification with a software called RELION [118], confirmed the presence of size heterogeneity (Figure 3.3 E and 3.3 F). Possible sources of size heterogeneity could be a genuine difference in particle size or just different viewing angles towards distorted, oval shaped particles. To check whether it was possible to reconstruct a three-dimensional model from these data, the two-dimensional class averages containing locally blurred membranes and spikes were excluded as much as possible, and the remaining ones were subjected to angular reconstitution, assuming icosahedral symmetry. Three-dimensional reconstruction using the selected class averages did not yield a model with any surface features characteristic for UUKV (no distinct spike densities were visible), although the membrane and surface glycoprotein layers could be distinguished (Figure S1 A, B and C).

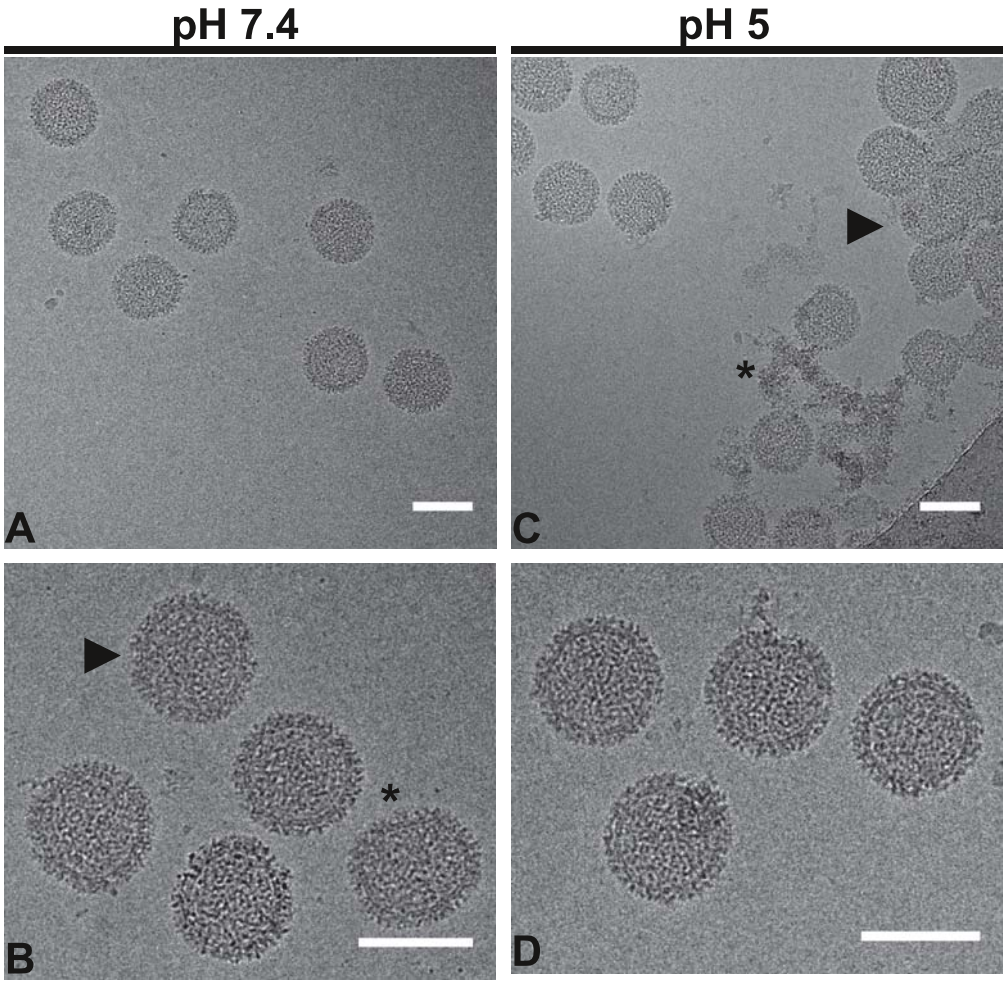


Figure 3.1. Characterization of Uukuniemi virus by electron cryo-microscopy.

Uukuniemi virus supernatant was cleared, centrifuged at high speed and the pellet resuspended in neutral pH buffer. The virus was then loaded on holey carbon copper grids and the grids were washed against either neutral pH 7.4 (A and B) or low pH 5 (C and D) buffer and plunge frozen at liquid nitrogen temperature. The virus particles were recorded with an electron cryo-microscope.

A.) Electron micrograph of UUKV at pH 7.4.

B.) Close-up of an electron micrograph of UUKV at pH 7.4. Note the spherical and spiky appearance at the virions surface, but absence of membrane distal pointy spikes (arrowhead), as well as the absence of aggregates. The asterisk indicates a distorted particle.

C.) Electron micrograph of UUKV at pH 5. Note the presence of aggregates (arrowhead), presumably due to low pH-triggered hydrophobic fusion loop exposure. The asterisk indicates debris, which could correspond to viral ribonucleoparticles.

D.) Close-up of an electron micrograph of UUKV at pH 5. Note that there is no striking morphological difference between the non-aggregating particles at pH 5, in comparison to UUKV particles at pH 7.4 in B.).

Scale bar = 100 nm

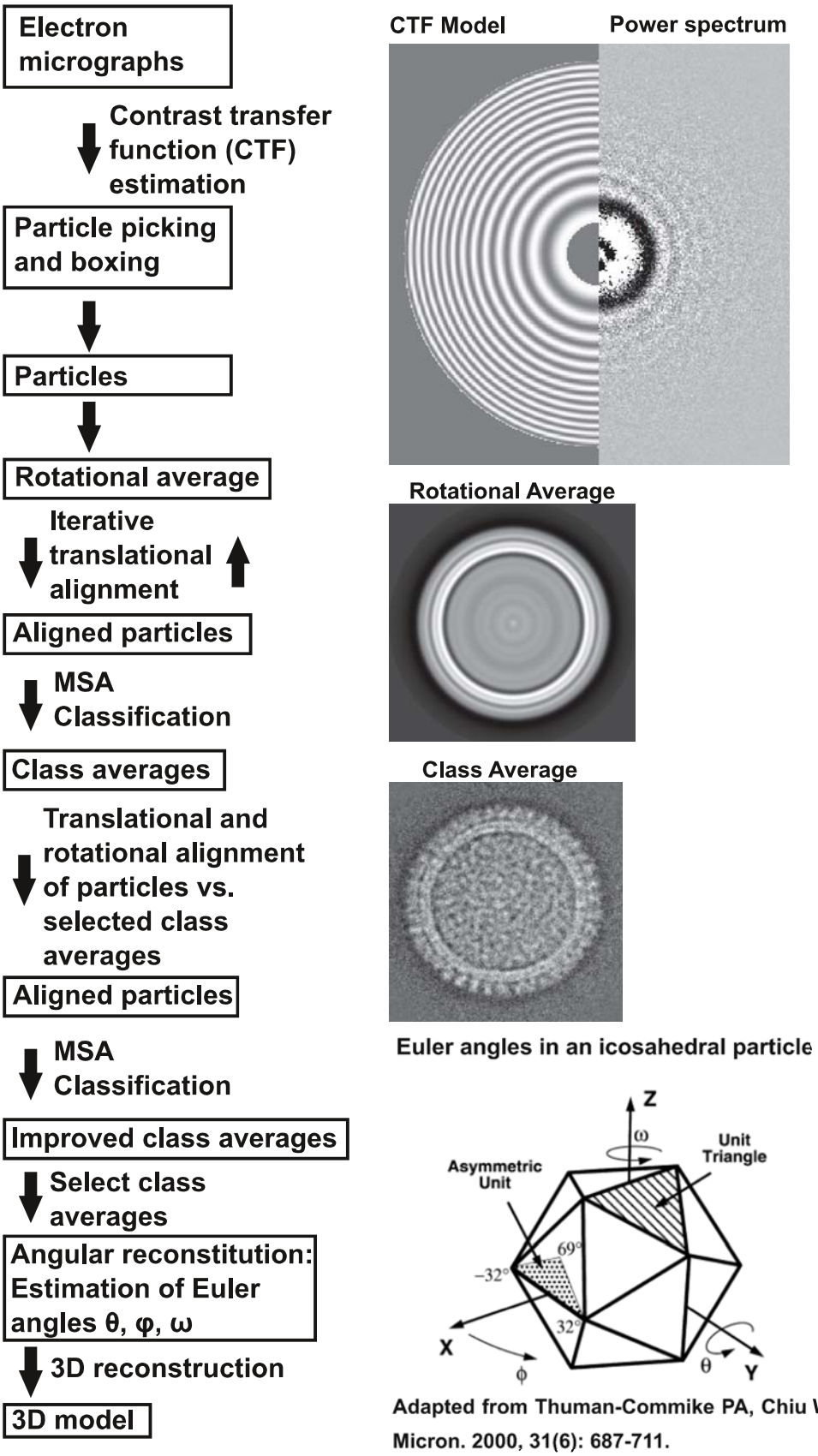


Figure 3.2.

With kind permission from Elsevier (Copyright 2000).

Schematic of the icosahedral reconstruction scheme used for construction of an initial model of UUKV. The pictures shown on the right side of the panel are shown to visually assist the designation of intermediate steps in the reconstruction workflow. The Euler angles are determined as follows: First, φ is determined by rotation along the Z axis. Second, θ is determined by rotation along the new Y axis. Finally, ω is determined by rotation around the new Z axis. The Euler angles describe the orientation of the icosahedral particle within the asymmetric unit. MSA = multivariate statistical analysis.

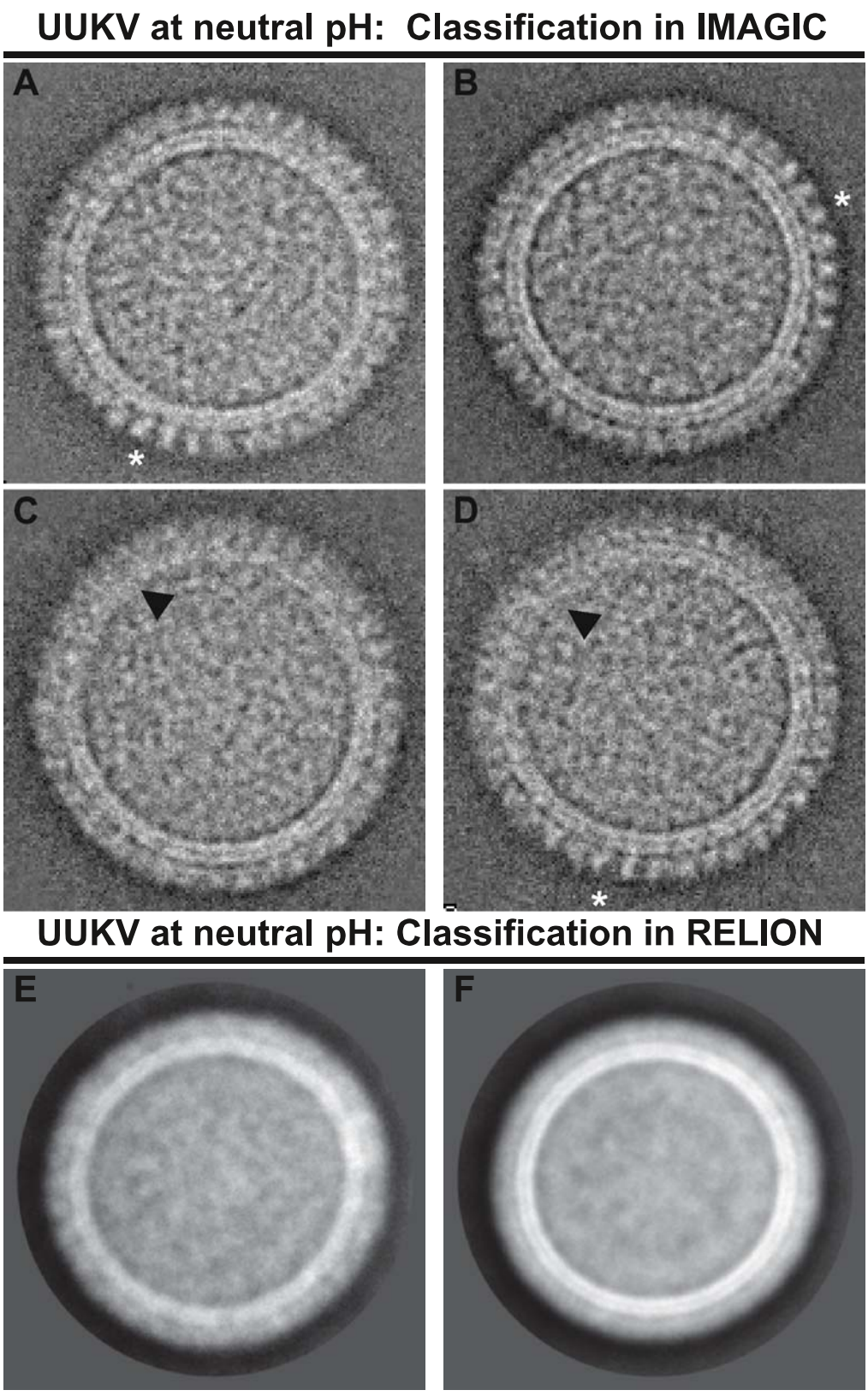


Figure 3.3. Two-dimensional classification of UUKV particles.

A.) to D.): Representative class averages of UUKV at neutral pH, classified in IMAGIC. Classes comprised round particles with a well resolved membrane and locally well resolved spikes (asterisks). Other class averages show a locally unresolved membrane as well as unresolved spikes (arrowheads). E.) and F.): Selected class averages of the same dataset, but classified in the maximum-likelihood based software RELION. Note that the class in E.) is slightly larger than the one in F.). Images are not on the same scale than in A.) to D).

As expected, three dimensional classification of viral particle images in Relion, using the UUKV initial model as a reference did not lead to the appearance of distinctly visible virus spikes (Figure S1 D). Although building an initial model directly from the acquired data is usually the best strategy if one wants to avoid bias towards a model previously reconstructed from different data, such as a structure of a closely related virus, the refinement of the current UUKV three-dimensional classes was not attempted because no improvement could expected from this point.

Because neither the initial UUKV model nor the three dimensional class averages contained any spikes, it was then proposed that perhaps if the initial model contained spikes, then it might be possible to at least obtain a low resolution model of UUKV showing the native spike conformation at neutral pH. To this end, UUKV particles at neutral pH were three-dimensionally classified in RELION, using a previously published Rift Valley fever virus (RVFV) structure as a reference [78]. One class average (class 1 of 2) showed a hint of spikes, whereas the other one did not. In both cases, the classes looked blurry (Figure S2 A, B). Model refinement of the particles in class 1, using RVFV as initial model, did not develop beyond the resolution of the initial reference map, filtered to 60 Å, and finally no spikes were visible (not shown). This confirms, however, that the three-dimensional refinement in RELION is not prone to model bias.

The observed sample heterogeneity, as well as the failure to reconstruct a three dimensional model with visible spikes seriously questions the use of

the currently used UUKV preparations for sub-nanometer resolution reconstruction. Fixed UUKV particles were prone to distortion resulting in a partial loss of icosahedral symmetry [79]. Nevertheless, in the latter study, careful selection of undistorted UUKV particles allowed the reconstruction by electron cryo-tomography. This suggests that the fixation step, performed prior to ultracentrifugation, may have helped to preserve UUKV particle structure to the extent that stable icosahedral UUKV particles could be captured, if carefully selected. It was concluded that the pelleting step in virus purification procedure may cause unfixed UUKV particles to almost completely lose icosahedral symmetry due to particle distortion. Because no three dimensional model could be obtained at neutral pH, no similar attempt was made for the UUKV particles recorded at pH 5.

Because one important aspect of this thesis was to work in native, unfixed conditions, I sought to improve the sample quality by omitting any pelleting steps of UUKV. To achieve this, infectious supernatants were concentrated over a filter membrane, using low speed centrifugation, followed by purification of the concentrated supernatant over a linear Nycodenz (a derivative of Optiprep) gradient. Nycodenz allows the formation of high density solutions in gradient purifications at relatively low concentrations, which is why it was used here instead of sucrose, with the idea to reduce osmotic pressure acting on the virions. This approach appeared to produce UUKV at a particle infectivity that is similar to those particles acquired from a protocol that involves pelleting over a sucrose

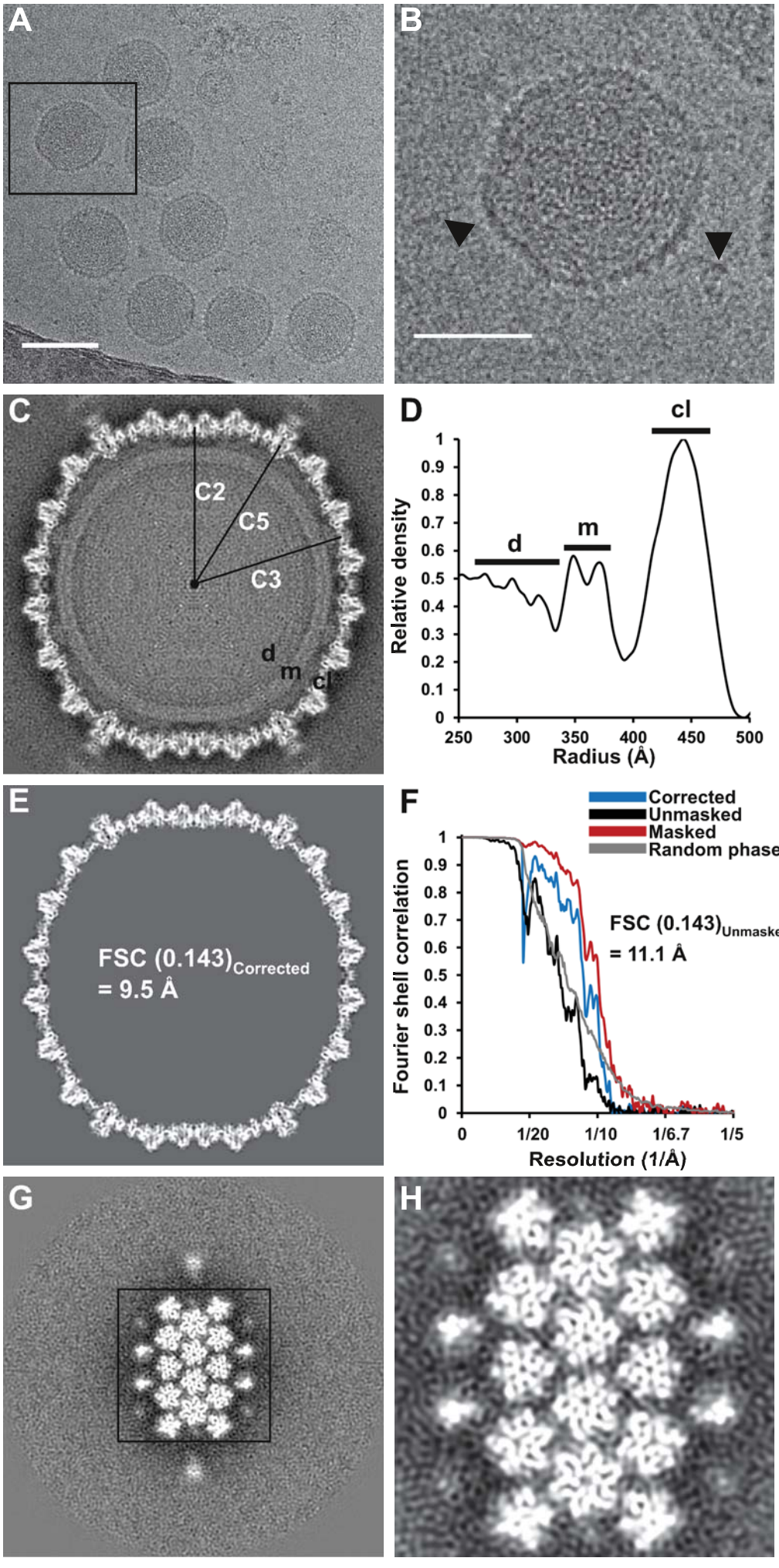
cushion, followed by a sucrose gradient (~5x10^6 ffu/µg glycoprotein for Nycodenz purified virus and 3.0×10^6 ± 0.9×10^6 ffu/µg (N=2) for sucrose gradient purified virus). Due to a lack of time, I was not able to test the Nycodenz purified particles for icosahedral reconstruction in electron cryo-microscopy. However, the new purification approach was used successfully by other members of our research group to produce a low resolution structure of UUKV spikes at neutral pH, using electron cryo-tomography and sub-tomogram averaging (see [80] for a recent application of sub-tomogram averaging). This structure confirmed that UUKV at neutral pH indeed has hollow spikes, much like Rift Valley fever virus (Figure S3), and not pointed spikes, as previously shown for fixed UUKV particles [79]. A purification protocol avoiding pelleting steps, combined with data collection using a mid-range performance electron cryo-microscope was previously used for RVFV and led to a 2.7 nm structure achieved by icosahedral reconstruction [146]. It is therefore expected that a high end electron cryo-microscope setup (*e.g.* 300 keV combined with a direct electron detector), combined with a purification protocol excluding pelleting steps, would lead to a high resolution phlebovirus (either UUKV or RVFV) structure.

3.3. Icosahedral reconstruction of the bacteriophage SSIP-1

To further engage with icosahedral reconstruction of viruses, I received a potentially icosahedral virus from a collaborator (Hanna Oksanen, Helsinki, Finland), tentatively called SSIP-1 (Salisaeta icosahedral phage

1), which infects the halophilic (salt-loving) bacterium SP9-1, and is related to another halophilic bacterium called Salisaeta longa [129, 149]. SP9-1 (and thus SSIP-1) was isolated from an experimental mesocosm (which is an artificially created environment that allows *e.g.* growth of halophilic bacteria) in Sedom, Israel. The structure of SSIP-1 was solved by electron cryo-microscopy and icosahedral reconstruction, in a joint effort between my supervisor Dr. Juha Huiskonen and myself, and resulted in a structure at 12.5 Å resolution [150]. My contributions to the publication included sample preparation for electron cryo-micoscopy, as well as data acquisition on the electron cryo-microscope.

For this thesis, I re-used the full dataset of SSIP-1 to validate the angular reconstitution protocol of UUKV particles using class averages in IMAGIC. To this end, the SSIP-1 particles were processed in a similar way than the UUKV particles, which included particle alignments, class averaging, angular reconstitution and three-dimensional reconstruction, as described in chapter 3.1. SSIP-1 already appeared to be icosahedral as seen from the electron micrographs (Figure 3.4 A and B). 3,362 particles were subjected to alignments and class averaging in IMAGIC and 44 class averages were selected (14–84 particles per class average) and reconstructed to an initial model with distinct icosahedral features and visible capsomers (Figure S4 A, B and C).


A
B
C
C2
C5
C3
d
m
cl
D
cl
d
m
Relative density
Radius (Å)
E
FSC (0.143)Corrected
= 9.5 Å
F
Corrected
Unmasked
Masked
Random phases
FSC (0.143)Unmasked
= 11.1 Å
Fourier shell correlation
Resolution (1/Å)
G
H

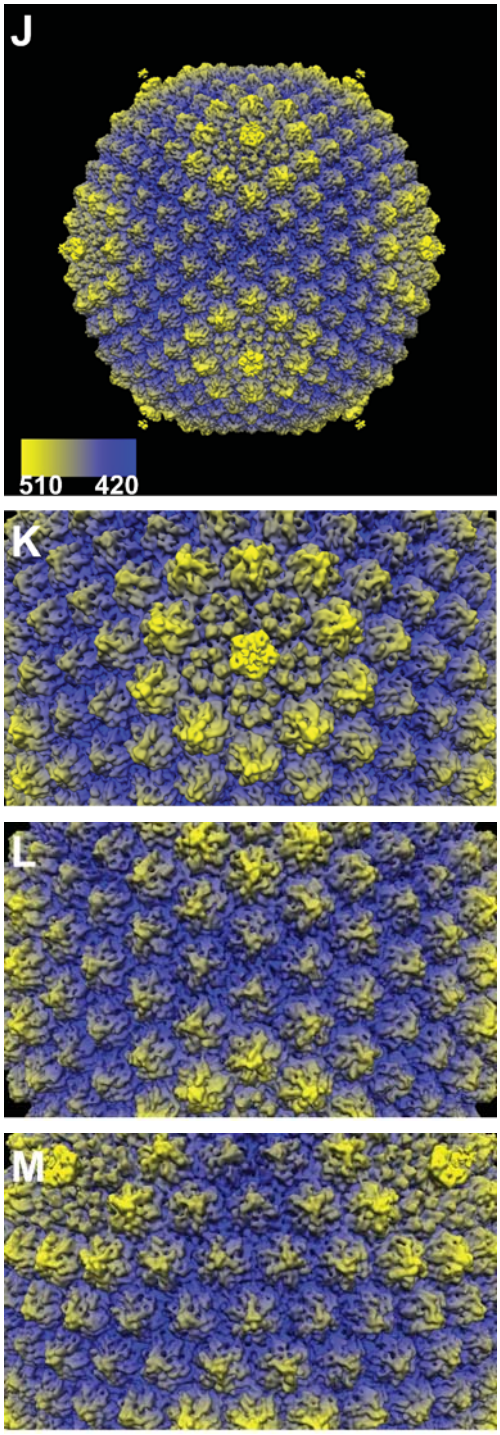


Figure 3.4. Icosahedral reconstruction of the bacteriophage SSIP-1.

A.) Electron micrograph of SSIP-1 particles (Scale bar = 100 nm).

B.) Close-up of the the particle boxed in A.). Arrowheads indicate spikes (Scalebar = 50 nm).

C.) Central slice (2 Å thick) of the B-factor sharpened SSIP-1 reconstruction (2,865 particles). Icosahedral symmetry axes are indicated as C2 (twofold), C5 (fivefold) and C3 (threefold). d = concentric rings in the particle probably corresponding to DNA, cl = capsid layer, m=membrane.

D.) Radial profile the B-factor sharpened, radially averaged SSIP-1 volume. d = DNA, m = membrane, cl = capsid layer.

E.) Same as C, but masked to higher density threshold. The resolution of the masked region is indicated.

F.) Fourier shell correlation (FSC) curves of the unmasked SSIP-1 map, partly depicted in C.) ("unmasked"), the masked SSIP-1 map in E.) ("masked"), and the FSC of the masked SSIP-1 map corrected for overfitting ("corrected"). The corrected FSC was determined by subtraction of an FSC determined by phase randomization of spatial frequencies higher than 22.16 Å ("Random phases") from the masked FSC.

G.) 2 Å thick slice of the B-factor sharpened SSIP-1 reconstruction at the surface of SSIP-1, showing the hexameric capsomers. A close-up of the boxed area in G.) is shown in H.).

J.) Three-dimensional volume of SSIP-1, rendered at 3.5σ above the mean, viewed along the icosahedral twofold axis. The colour key indicates the particle radius in Ångstroms.

K.) Close-up view of SSIP-1 along the fivefold axis.

L.) As K.), but along the twofold axis.

M.) As K.) and L.), but along the threefold axis.

To select the best particles from the dataset for the particle refinement, the particles were first classified in two dimensions in RELION, then the best classes were selected (17/30 classes, corresponding to 3101/3362 particles, see Figure S4 D and E for representative good class averages), and then re-classified in three dimensions using the initial SSIP-1 model created in IMAGIC as a reference. The particles that produced the best three-dimensional classes (three out of four) were selected (see Figure S4 F and G) and refined in RELION to 11.1 Å resolution (FSC = 0.143, Figure 3.4 F) for the whole virus map, and 9.5 Å for the masked map that included the capsid only (Figure 3.4 E and F). Because an initial model could be formed from the SSIP-1 data by angular reconstitution of class averages, and because this structure could be refined to a resolution range that is even better than what has been published (12.5 Å [150]), it is rather safe to say that the procedure used here for initial model construction is valid.

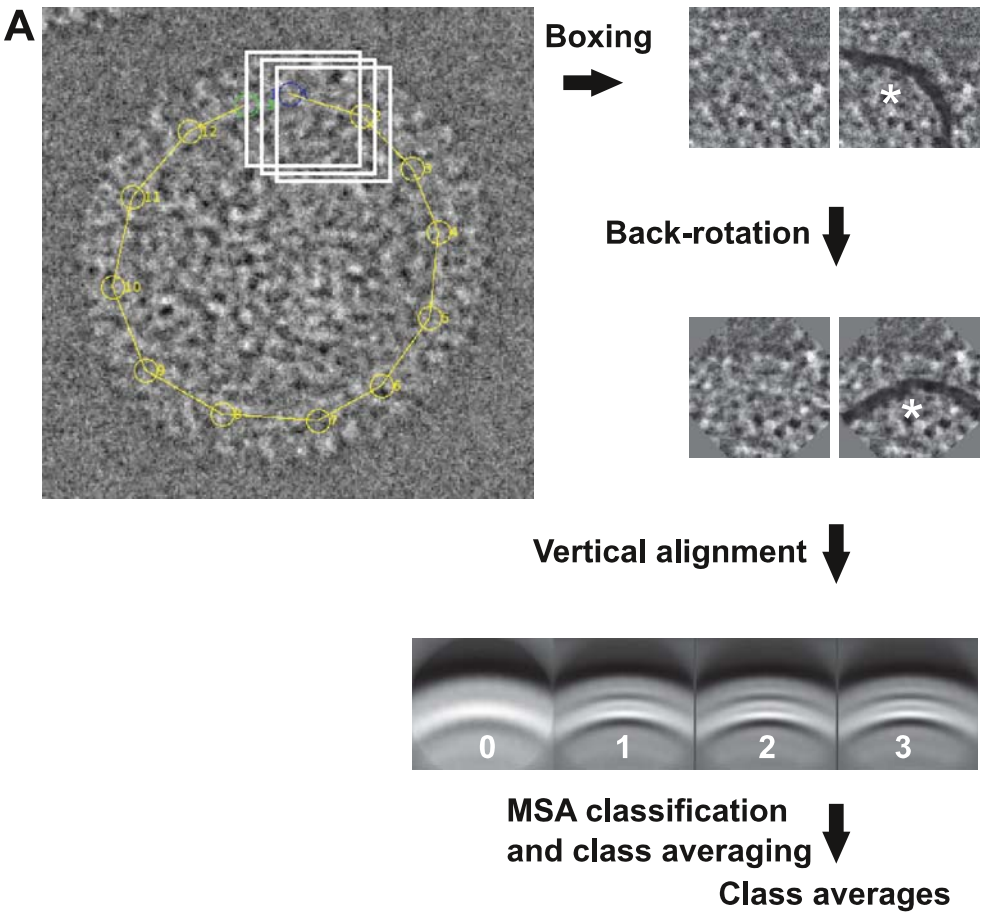
3.4. Two-dimensional analysis of a phlebovirus at low pH

Because more subtle differences between low and neutral pH forms of isolated UUKV particles were not visible from projection images, and because icosahedral reconstruction was not possible, it was decided to perform a more thorough two-dimensional analysis on the obtained UUKV datasets. To this end, viral spikes were boxed from entire virions, using 90% overlapping boxes (the shift of 10% corresponds to 8 pixels, which is equivalent to 48 Å) that included both the lipid bilayer and spikes. The

boxes were then back-rotated to make all the spikes point upwards. The spikes were then vertically aligned, classified by MSA and classes averaged (IMAGIC) to obtain different views. The workflow and class averages are visualized in Figures 3.5 A and B, respectively. As expected, no “pointy” spikes could be observed at any pH. Class averages found at neutral pH could also be found in similar-looking versions at low pH, highlighting that it was not possible to make a qualitative conclusion about whether there is a conformational change at low pH, only by comparing class averages.

To compare the spikes at neutral pH with those at pH 5 more quantitatively, all spikes, regardless of pH, were summed and vertically aligned. This average was then used as a template for separate vertical alignments of spikes at different pH. The resulting averages, separately for each pH, were radially averaged and represented in a radial density profile. A detailed picture of the processing steps is shown in Figure 3.6 A. The normalized radial profiles at pH 5 and pH 7.4 looked almost identical, with exception of the region of the viral spikes, in which the sample at pH 5 showed a shift towards higher radius (the difference is resolved by one pixel, which corresponds to 6 Å), combined with a decrease in density between the outer membrane leaflet peak and the main glycoprotein peak (Figures 3.6 B, C and D). This is consistent with a low pH triggered conformational change at pH 5, causing a centrifugal shift of a component of the glycoprotein shell towards a potential target membrane. However it

cannot be established which glycoproteins are involved and what the exact mechanism behind the observation could be. Importantly, the observed shift is too small to fully account for conformational changes that would lead to a real fusion event. This underlines the fact that a target membrane would be a necessary additive for a more accurate structural study on UUKV particle glycoprotein conformations at low pH.



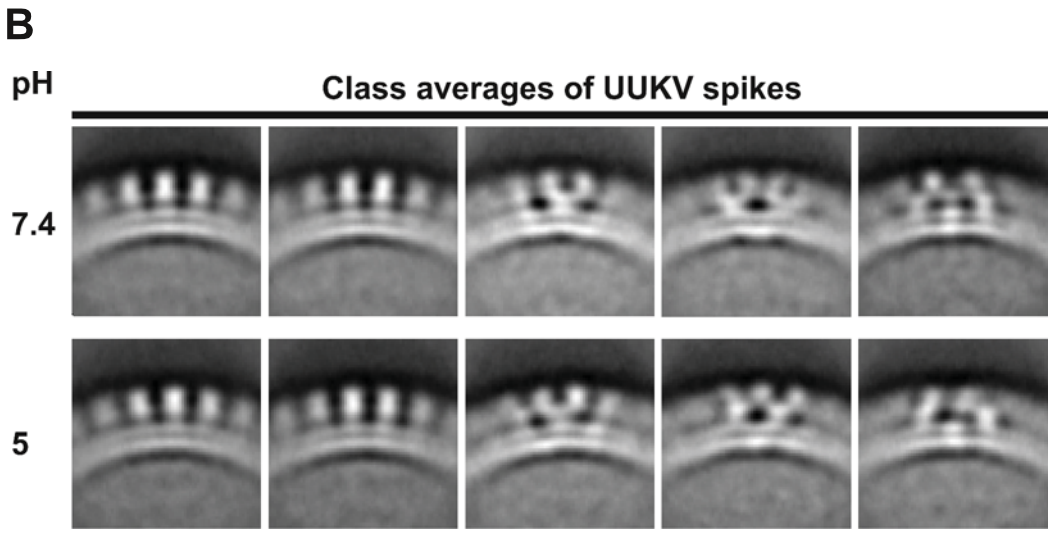


Figure 3.5. Two-dimensional analysis of Uukuniemi virus spikes at neutral and low pH.

A.) Sketch describing the boxing of spikes, back-rotation and iterative vertical alignment. The lipid bilayer in spike images is highlighted in black (asterisk).

B.) Selected class averages of spikes at pH 5 and pH 7.4. Note that selected classes at pH 7.4 can be found in similar-looking configurations at pH 5.

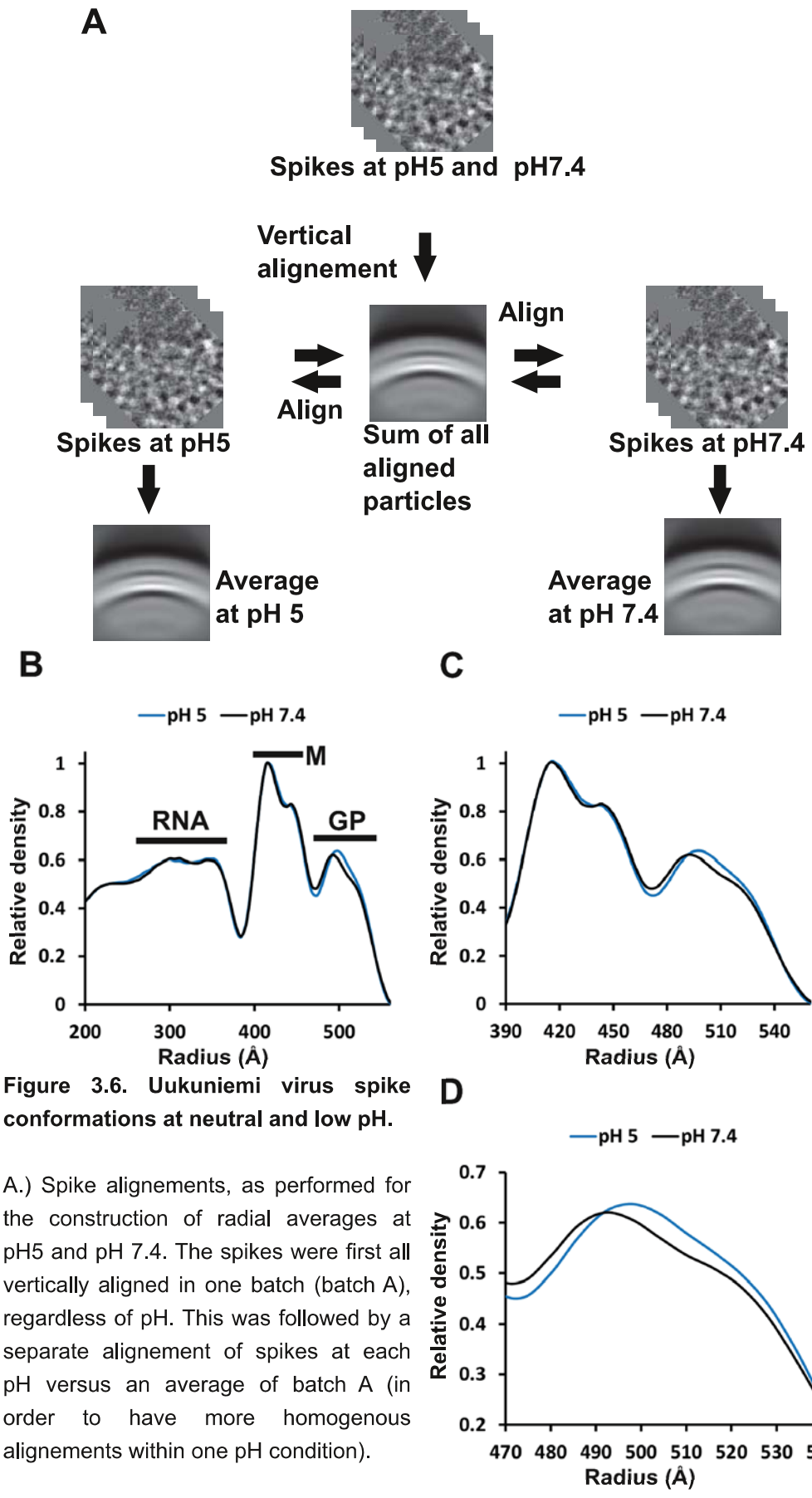


Figure 3.6. Uukuniemi virus spike conformations at neutral and low pH.

A.) Spike alignements, as performed for the construction of radial averages at pH5 and pH 7.4. The spikes were first all vertically aligned in one batch (batch A), regardless of pH. This was followed by a separate alignement of spikes at each pH versus an average of batch A (in order to have more homogenous alignements within one pH condition).

B.) Radial profiles of spikes at pH 5 and pH 7.4, taken from the approximate whole particle centre. RNA = possible RNA density, M = membrane, GP = viral glycoproteins.

C.) Same as in B.), but only showing membrane and spike densities.

D.) Same as in C.), but only showing the spike densities.

4. Structural and functional analysis of phlebovirus fusion

4.1. An in vitro fusion assay for Uukuniemi phlebovirus fusion

4.1.1. Rationale

The mechanism of viral membrane fusion is not spontaneous and requires conformational changes of viral membrane proteins, triggered by a cellular cue, such as low pH [54, 151, 152], which activates the viral membrane proteins to catalyze membrane fusion. The viral membrane fusion process as such can readily be monitored by using the phenomenon of fluorescence self-quenching (decrease in fluorescence intensity due to high concentration) and de-quenching (increase in fluorescence intensity due to dilution). Such fluorescence probes are widely available, both for labeling membranes (amphiphilic membrane dyes with one or two hydrophobic tails, such as DiD or octadecyl-rhodamine 18, both used in viral fusion studies [59, 153]) and labelling soluble contents (hydrophilic, membrane impermeable dyes, such as calcein or sulforhodamine B [66, 154]). If one assumes that the outcome of a membrane fusion event is nothing less than an increase of membrane areas and compartment volumes of both donor and target compartments to produce a common final membrane-enclosed compartment, then this is equivalent to dilution of both membrane and content dyes. Because the rate of fluorophore dilution in fusion can be assumed to be equivalent to the rate of lipid

mixing and content mixing, measuring fluorescence dequenching is an ideal approach to monitor fusion processes in real time.

Previous *in vitro* studies on receptor-free virus fusion employing fluorescence dequenching included for example studies on alphaviruses (*e.g.* Sindbis virus and Semliki Forest virus [75, 155], flaviviruses (*e.g.* tick borne encephalitis virus [77]) and orthomyxoviruses (*e.g.* influenza virus [66]). For alpha- and flaviviruses, a fluorophore covalently attached to the phospholipid tails, called pyrene, was used. The pyrene fluorophore is introduced into the virions by pre-incubating host cells with a pyrene-linked fatty acid, which is used as a precursor for cellular phospholipid biosynthesis. Because enveloped viruses incorporate host cell phospholipids into their envelope during their replication cycle, infection of metabolically labelled cells usually produces virions with pyrene-labeled phospholipids. Such a system has several advantages over virus membrane labelling after virus production, including: i.) The fluorescent label is covalently attached to the hydrophobic lipid tails of the virus phospholipids and hence transfer of the dye into target membranes, in absence of fusion, is minimized, ii.) Unspecific labelling of glycoproteins instead of the membrane, which may occur if the membrane label is introduced after virus production, leading to loss of infectivity, is minimized.

Pyrene is excited at 345 nm and has emission peaks at both 379 and 390 nm. At high concentrations, pyrene forms so-called “excited dimers”

(excimers), emitting as a broad peak around 475 nm [123]. Fusion between a pyrene-labelled donor membrane containing excimers and an unlabelled target membrane is reflected by a decrease in excimer fluorescence with a concomitant increase in monomer fluorescence (emission peaks at 379 and 390 nm). Because the pyrene based assay monitors lipid mixing, but not content mixing, it does not allow a distinction between hemifusion and fusion, only the latter of which includes fusion pore opening. To monitor fusion pore opening (content mixing), previous studies have made use of labelling viral [156] or liposome interiors [66, 154] with a soluble, membrane impermeable fluorophore that self-quenches at high concentrations and dequenches upon fusion pore opening as a result of dilution.

No *in vitro* system for studying the fusion of any bunyavirus has been developed before, and hence, the specific requirements for bunyavirus fusion, except for low pH, have remained unknown. I focused here on phlebovirus fusion, and the fluorescence-based in vitro system employed here consisted of pyrene-labeled Uukuniemi virus (UUKV-pyr) and sulforhodamine B (SRB) labelled liposomes. Because there is no spectral overlap between pyrene and SRB, it was anticipated to use both fluorophores in a simultaneous lipid and content mixing assay (Figure 4.1 A).

4.1.2. Uukuniemi virus fluorescence labelling

To simplify the experimental setup in a first step, the initial search for target membrane requirements in UUKV fusion included only pyrene-labeled virus and unlabelled liposomes. Pyrene-labeled Uukuniemi virus (UUKV-pyr) was produced by infection of BHK-21 cells pre-incubated with 1-pyrenehexadecanoic acid and purification of concentrated infectious supernatant over linear sucrose gradients. The obtained UUKV-pyr particles had pyrene excimer fluorescence that could be reduced to background levels with a concomitant increase in pyrene monomer emission by addition of detergent (Figure 4.1 B). The labelled particles retained their infectivity ($3.0\times10^6 \pm 0.9\times10^6$ ffu/µg (N=2) glycoprotein for UUKV and $7.4\times10^6 \pm 2.4\times10^6$ ffu/µg (N=3) glycoprotein for UUKV-pyr). Semliki Forest virus (SFV) was used as a control virus with known *in vitro* fusion requirements. Therefore, analogously to UUKV, and as published previously, SFV was labelled with pyrene (Figure 4.1 C). The lipid mixing assay was to be performed in a close-to-linear buffer system (containing succinate, phosphate and glycine, see materials and methods) to allow a pH drop to precise and reproducible pH values without having to add weak acids and thus additional buffer components (which may have an impact on the experiment) during the acidification step.

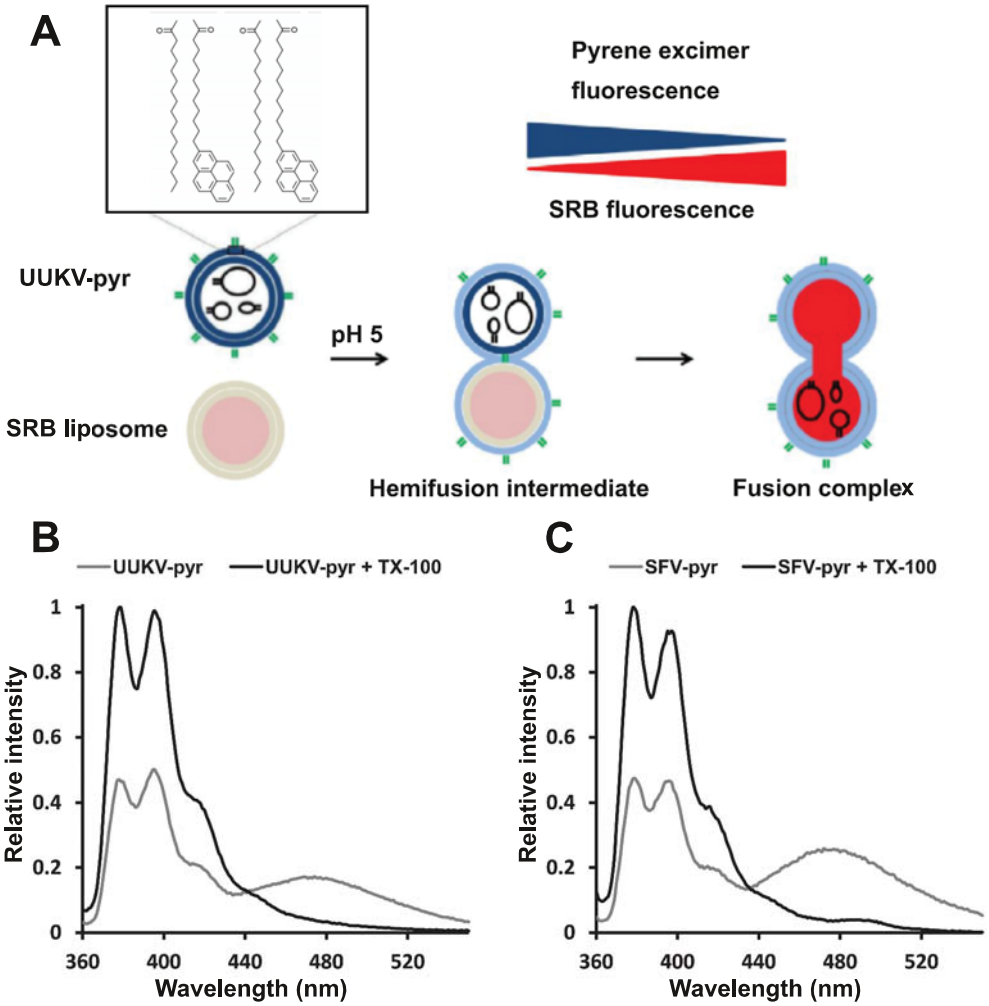


Figure 4.1. A fluorescence-based fusion assay for Uukuniemi phlebovirus.

A.) Sketch depicting the theoretical basis of the UUKV in vitro fusion assay in bulk. The UUKV membrane is metabolically labeled with pyrene (UUKV-pyr) and the liposome interior with a high concentration of sulforhodamine B (SRB). At high concentrations, the planar pyrene rings form so-called excited dimers (excimers), which have a red-shifted fluorescence emission, relative to pyrene monomers. SRB is encapsulated in liposomes at high concentrations (50 mM), which causes fluorescence self-quenching. If both components (virus and liposomes) are mixed and the pH lowered, the conformational changes of the viral glycoproteins first cause hemifusion between UUKV-pyr and the SRB-labeled liposomes. At this point, the pyrene dilutes into the liposome membrane, thus causing loss of pyrene excimers, with concomitant pyrene monomer formation, causing the red-shifted fluorescence (475 nm) to decrease and the monomer peaks (379 and 390 nm) to increase. Further conformational changes cause the progression of the hemifusion intermediate towards a fusion pore. As soon as the fusion pore opens, the SRB dilutes into the lumen of the virus, causing SRB dequenching and an increase in fluorescence. At this point, a full fusion event has happened.

B.) UUKV-pyr emission spectra in presence or absence of Triton X-100 (excitation at 345 nm).The Triton X-100 dependent loss of the broad excimer peak at 475 nm with a concomitant increase of the monomer peaks at 376 and 390 nm demonstrates that pyrene excimers are formed in the UUKV membrane.

C.) Same as in B.), but with SFV-pyr.

4.2. UUKV lipid mixing

4.2.1. Efficient UUKV lipid mixing requires both negatively charged and cone-shaped phospholipids

A multitude of studies showed that certain viruses entering from endocytic compartments have a requirement for specific lipids in the target membranes to allow fusion. For example, alphaviruses, penetrating host cells from early endosomes, require both sphingomyelin and cholesterol for fusion in early endosomes [75, 155], whereas dengue virus uses the late endosomal phospholipid bis(monoacylglycero)phosphate (BMP) to ensure that fusion occurs from late endosomes [59]. Here, the aim was to screen for target membrane lipid compositions that are permissive for UUKV lipid mixing at low pH. The molar lipid compositions used in target liposomes are indicated in Table 1 (Chapter 2). It was hypothesized that UUKV may use the late endosomal phospholipid BMP, because it penetrates target cells from late endosomes [55, 98]. BMP is highly concentrated in late endosomes and is found on internal membranes, in which it constitutes up to 60% of total phospholipids [22, 23]. The total concentration of BMP in late endosomal fractions, including the endosomal limiting membrane, is about 15% [23]. To maintain liposome stability and to be able to compare results with previous literature on fusion to BMP containing liposomes [59], I used an intermediate concentration of 30% mol BMP in target membranes, including the ubiquitous phospholipids phosphatidylcholine and

phosphatidylethanolamine, in a ratio close to the one found in late endosomes [23]. Consistently with the previous hypothesis, at late endosomal pH 5, BMP significantly increased UUKV lipid mixing, most of which took place in the first few seconds after acidification (Figure 4.2 A and B). No lipid mixing could be observed in absence of BMP, not even when cholesterol and/or sphingomyelin were present (Figure 4.2 C). As expected, Semliki Forest virus (SFV) required both sphingomyelin and cholesterol for lipid mixing, but showed only marginal lipid mixing in presence of BMP liposomes (Figure 4.2 C).

To test whether it was the negative charge of the BMP headgroup that allowed UUKV lipid mixing, other negatively charged phospholipids were tested in target membranes. These included phosphatidylserine (PS), phosphatidylglycerol (PG) and phosphatidic acid (PA), none of which are usually found on the inner leaflet of late endosomal lipid bilayers. Interestingly, UUKV lipid mixing was only observed in presence of both PA and PG, but not PS (Figure 4.2 D). Cholesterol in presence of BMP did not significantly change UUKV lipid mixing levels (Figure S5 A). Also, PA allowed significant lipid mixing of SFV that is statistically indistinguishable from UUKV lipid mixing with PA. At pH 5, it is expected that the majority of the headgroups of PG and PA are negatively charged [157, 158]. However, the carboxyl group in the PS headgroup gets increasingly protonated and therefore the headgroup gradually loses its overall negative charge [159, 160].

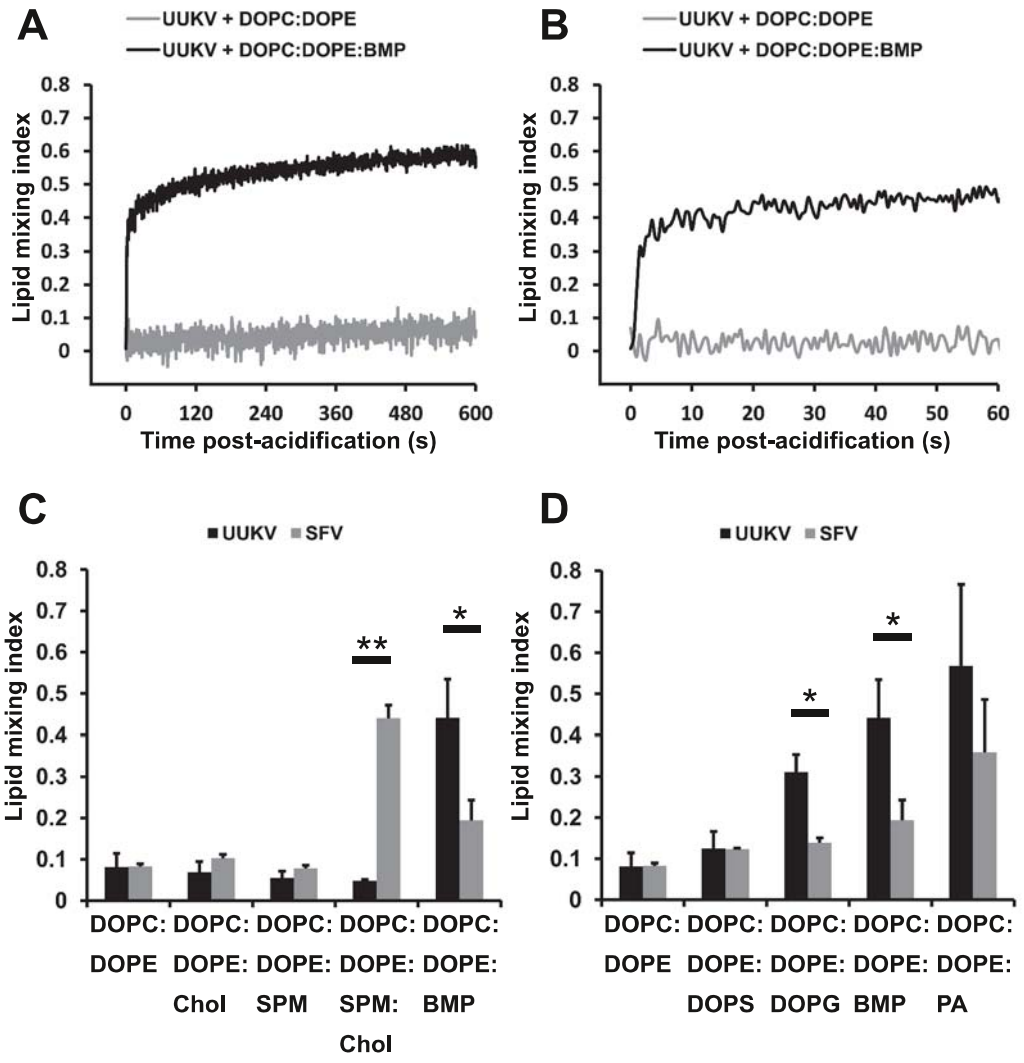


Figure 4.2. Lipid dependence of Uukuniemi virus lipid mixing.

Depiction of lipid mixing after pH drop as a function of time, liposome composition, and input virus. The fluorescence intensities are given as fractional loss of pyrene excimer fluorescence, normalized between the initial (highest) fluorescence (before the pH drop) and the final (lowest) fluorescence (after addition of Triton X-100). The loss of excimer fluorescence is indicated as "lipid mixing index". Excitation: 345 nm, emission: 475 nm. Error bars indicate one standard deviation (N=3). Significance levels: * $p \leq 0.05$, ** $p \leq 0.01$. See Table 1, chapter 2, for lipid ratios, and the following abbreviations: DOPC, DOPE, SPM, Chol, BMP, PA, DOPS, DOPG.

A.) UUKV-pyr and either DOPC:DOPE or DOPC:DOPE:BMP liposomes were incubated for 10 minutes at 37°C, then acidified to pH 5 (time point zero).

B.) Same as in A.), but depicting the first 60 seconds after acidification. Note that most of the lipid mixing occurs in the first few seconds after acidification.

C) UUKV-pyr and SFV-pyr lipid mixing in presence of liposomes at different lipid compositions, 5 minutes after acidification to pH 5.

D) Similar to C), but with different liposomal lipid compositions tested. For ease of comparison, lipid mixing in presence of DOPC:DOPE and DOPC:DOPE:BMP from C.) are included.

This is consistent with the hypothesis that the negative charge alone (in terms of the electrostatic change) on the phospholipid headgroup is the property that benefits phlebovirus fusion, because no lipid mixing was observed in presence of PS, in contrast to PA and PG. If that was indeed the case, then lipid mixing towards liposomes containing phosphatidylserine, at a pH lower than pH 5, should not be increased, because the phospholipid headgroups should be more protonated and hence more positively charged. To test this, UUKV lipid mixing to negatively charged membranes was performed at pH 4.5. Lipid mixing was increased in presence of all negatively charged lipids, but not in their absence. There was still no UUKV lipid mixing in presence of cholesterol and sphingomyelin, but interestingly there was now also lipid mixing in presence of PS (Figure S5 C). This excludes the fact that it is only the negative charge of the phospholipid headgroup in itself that is beneficial for UUKV lipid mixing. Interestingly, pyrene-labeled Bunyamwera virus (BUNV-pyr; family *Bunyaviridae*, genus *Orthobunyavirus*) showed a similar lipid mixing profile than UUKV at pH 4.5 (Figure S5 B and D), suggesting that the fusion mechanism could be a conserved feature between different genera of the *Bunyaviridae*. However, BUNV-pyr preparations were not yet optimized for the current experimental setup due to lower titers than for UUKV, and hence increased amounts of sucrose present in the lipid mixing assays (if BUNV-pyr were used at the same fluorescence intensity than UUKV-pyr), possibly interfering with the lipid mixing. It was therefore

decided to prioritize on phlebovirus fusion in a first step, in order to establish a well-characterized pipeline for UUKV fusion, which can potentially be adapted to other bunyaviruses at a later stage, following sample optimization.

Which physical parameters apart from charge alone would then increase the lipid mixing? It has been established that low pH (and in particular the protonation of the PS carboxyl group) causes a phospholipid phase transition from lamellar to inverted hexagonal in phosphatidylserine [161], which means that the spontaneous curvature of phosphatidylserine gets more negative, or in other words, phosphatidylserine becomes more conical and thus the inverted hexagonal phase becomes energetically more favorable. In the context of a lipid bilayer, this means that at low pH, PS would have a propensity to exhibit negative curvature locally. In fact, negative membrane curvature is thought to be important for hemifusion stalk formation and lipid mixing beyond a restricted hemifusion (RH = hemifusion without lipid mixing) intermediate [59, 68–70].

Because phosphatidylglycerol [162], BMP [23], and phosphatidic acid [163] are conical at neutral pH, (as opposed to phosphatidylserine which is not conical at neutral pH [161]) it could be expected that these phospholipids are intrinsically fusogenic. At low pH, and because of the negative charge of the hydrophilic headgroups, more protons would be attracted to these headgroups than at neutral pH, causing an increase in charge neutralization and hence a decrease in electrostatic headgroup to

headgroup repulsion, possibly resulting in locally increased negative bilayer curvature. The conical shape of these negatively charged phospholipids would thus be amplified at low pH, further increasing the propensity for membrane fusion or fission. This idea is corroborated by low pH dependent spontaneous vesicle fission observed in BMP containing membranes [164]. Furthermore, recently published data showed that liposomes containing high amounts of BMP spontaneously fuse to equivalent acceptor liposomes containing BMP at low pH [23]. Interestingly, SFV also fused with all the negatively charged membranes at pH 4.5, including PS-containing membranes, although at lower levels than the tested bunyaviruses. SFV lipid mixing at pH 4.5 with membranes containing sphingomyelin and cholesterol appeared less efficient than at pH 5 (Figures S5 E and 4.2), which corroborates that SFV exposure to pH 4.5 is a rather unphysiological situation, especially because SFV fuses in early endosomes (see chapter 1.5.2), where the pH is ~6 [15].

However, taken together, the data obtained so far could suggest that the observed lipid mixing in presence of negatively charged liposomes may have been a passive event caused by the fusogenic liposomes, rather than the virions. To test the possibility of spontaneous lipid bilayer fusion, donor liposomes with a phospholipid composition similar to that of UUKV ([165], see also Table 1), including 25% mol cholesterol (corresponding to the approximate cholesterol concentration found within the Golgi apparatus [166], the assembly site of UUKV), were supplemented with a

pyrene labeled phospholipid analog called 1-hexadecanoyl-2-(1-pyrenedecanoyl)-sn-glycero-3-phosphocholine at similar monomer-to-excimer ratios than found in UUKV-pyr. This corresponded to 4% mol pyrene (Figure 4.3 A).

At pH 5, these pyrene-labeled donor liposomes (mimicking UUKV-pyrene membranes in absence of viral glycoproteins) and unlabeled acceptor liposomes containing BMP only caused background level lipid mixing (Figure 4.3 B). It can therefore be concluded that the observed UUKV lipid mixing with liposomes at pH 5 requires the viral glycoproteins and that lipid mixing is most likely facilitated by the increased target membrane fusogenicity caused by negatively charged conical phospholipids, such as the late endosomal phospholipid BMP, which among the tested negatively charged lipids, is the only physiologically relevant candidate for UUKV fusion in late endosomes (because BMP is highly enriched in late endosomes, unlike the other lipids tested). Although, according to the lipid mixing data at pH 4.5, a similar concept may hold true for SFV lipid mixing towards liposomes containing BMP, it is physiologically less relevant, because SFV efficiently fuses to membranes containing sphingomyelin and cholesterol, the latter of which is mainly found in early and less so in late endosomes [22].

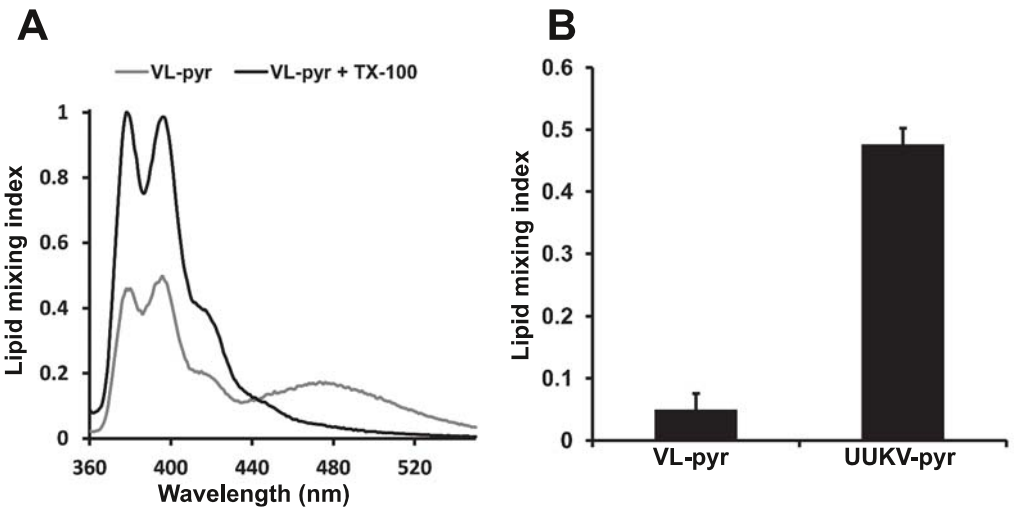


Figure 4.3. Lipid mixing of pyrene-labeled liposomes versus unlabeled DOPC:DOPE:BMP liposomes.

A.) Emission spectra of liposomes labeled with 4% mol 1-hexadecanoyl-2-(1-pyrenedecanoyl)-sn-glycero-3-phosphocholine (VL-pyr). The overall lipid composition of the liposomes was close to what could be expected for the UUKV phospholipid composition (see Table 1, chapter 2, for lipid ratios).

B.) Quantification of VL-pyr lipid mixing to DOPC:DOPE:BMP liposomes, 5 minutes after drop to pH 5. Lipid mixing of UUKV-pyr to DOPC:DOPE:BMP liposomes is indicated as a control.

Error bars represent one standard deviation (N=3).

4.2.2. UUKV lipid mixing: Low pH and temperature dependence

To further corroborate the hypothesis that UUKV may use BMP to allow entry from late endosomes, it was tested whether in presence of BMP, the pH threshold for fusion would still be consistent with late endosomal pH. Here, in presence of DOPC:DOPE:BMP liposomes, 50% UUKV lipid mixing efficiency was determined at pH 5.6 (Figure 4.4 A), which is consistent with entry from late endosomes. In a second step, it was tested whether UUKV would be inactivated after low pH treatment in absence of target membranes. Certain viruses, such as hepatitis C virus, and Semliki Forest virus (only in certain conditions), proved to be resistant towards low pH treatment in absence of target membranes [167, 168]. To test UUKV susceptibility to low pH, virions were exposed to pH 5 for 1 hour, followed by re-neutralization, addition of DOPC:DOPE:BMP liposomes, and re-acidification, as described before in the lipid dependence assays. The low pH pre-treatment had no effect on the lipid mixing of UUKV with DOPC:DOPE:BMP liposomes, whereas the lipid mixing for SFV in presence of DOPC:DOPE:SPM:Chol was strongly reduced. SFV lipid mixing with BMP containing liposomes was at levels similar to viral inactivation (~20%), regardless of neutral or low pH pre-treatment (Figure 4.4 B and C). Consistently with the fact that there is no major conformational change visible for UUKV at low pH in absence of target membranes (chapter 3), this suggested that the low pH in absence of target membranes does not inactivate the capability of UUKV for lipid

mixing. However, the titer of low pH treated UUKV decreased substantially ($2.9x10^6$ versus $8.8x10^7$ ffu/mL, n=2, for acidified and non-acidified UUKV, respectively). This corresponds to a 30-fold, but on the other hand, incomplete loss of infectivity, and in light of the preserved capacity of acid pretreated UUKV to fuse/hemifuse to liposomes, could suggest that low pH pretreatment impedes UUKV entry steps prior to lipid mixing with membranes containing BMP, but not lipid mixing itself.

All lipid mixing experiments were executed at 37 ºC in order to achieve a protein activity and membrane fluidity similarly to what is found during the infection of a mammalian cell. This approach proved to be of significant importance, because the lipid mixing efficiency was highly temperature dependent. Lipid mixing efficiency dropped to almost half at 25 ºC, as compared to lipid mixing at 37 ºC (Figure 4.4 D).

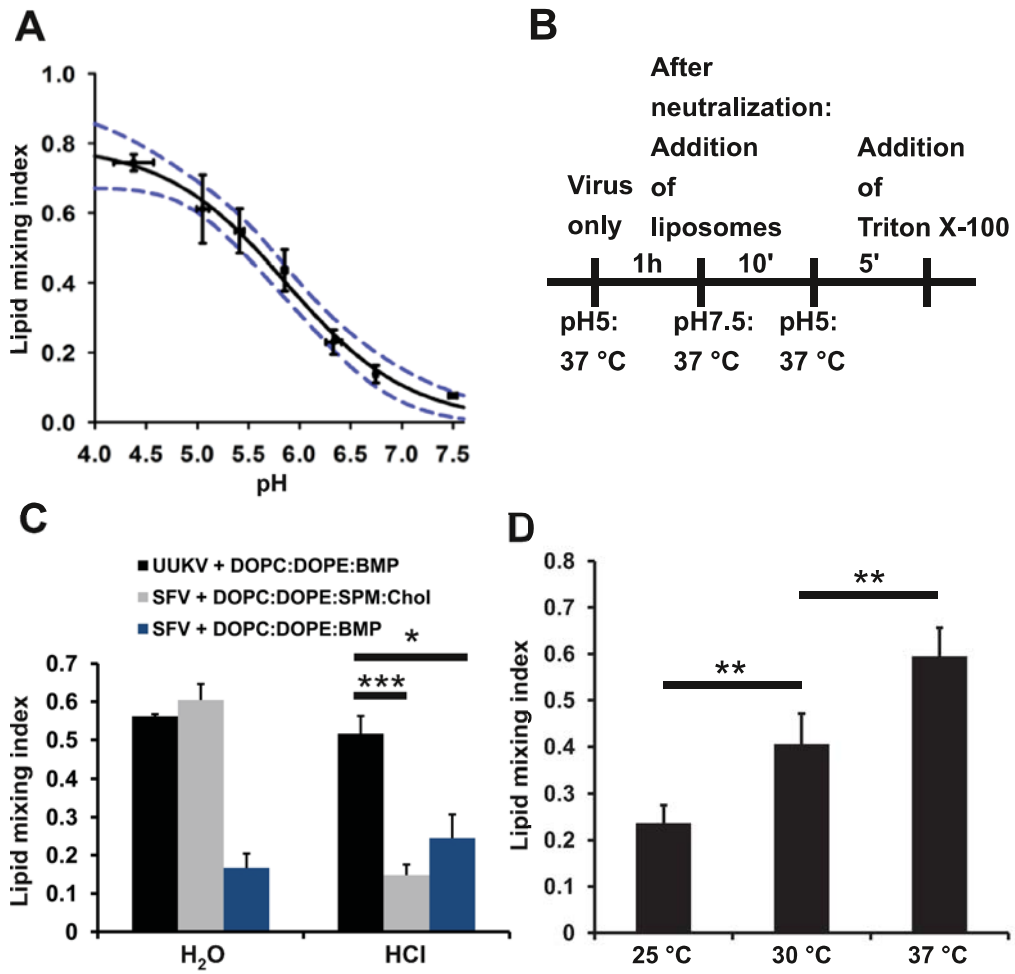


Figure 4.4. Low pH and temperature dependence of Uukuniemi virus lipid mixing.

Shown are low pH dependence and temperature dependence of UUKV-pyr lipid mixing, as well as the effect of liposome-free low pH pretreatment of either SFV-pyr or UUKV-pyr on their lipid mixing. All quantifications are at five minutes post-acidification. Error bars represent one standard deviation (N=3) unless indicated otherwise (*p ≤ 0.05, **p ≤ 0.01, ***p ≤ 0.001). Lipid ratios are given in table 1, chapter 2.

A.) Lipid mixing of UUKV-pyr with DOPC:DOPE:BMP liposomes at different pH, 5 minutes post-acidification. The blue dashed lines are confidence lines for a sigmoidal curve fit. 50% lipid mixing is achieved at pH 5.6, which is consistent with late endosomal pH.

B.) Schematic of the low pH inactivation experiment. UUKV-pyr or SFV-pyr were pre-treated at pH 5 for 1h at 37 °C in absence of liposomes, reneutralized, supplemented with an excess of liposomes, incubated for 10 minutes at 37 °C, and then re-acidified to pH 5.

C.) Quantification of lipid mixing of the acid-pretreated (HCl) or H_2O-pretreated ("mock" control) UUKV-pyr or SFV-pyr lipid mixing at 5 minutes post-acidification. Note that SFV-pyr lipid mixing to DOPC:DOPE:SPM:Chol liposomes is inhibited by low pH pre-treatment, whereas UUKV-pyr lipid mixing to DOPC:DOPE:BMP liposomes is not. Error bars for SFV-pyr + DOPC:DOPE:BMP indicate one standard deviation (N=2).

D.) Lipid mixing of UUKV-pyr with DOPC:DOPE:BMP liposomes at different temperatures at pH 5.

4.3. Liposome content release in presence of UUKV

After the conditions for efficient UUKV lipid mixing had been established, the next step was to measure both lipid and content mixing simultaneously, using sulforhodamine B (SRB) labelled liposomes. To ensure that the liposomes were unilamellar, which is of utmost importance for quantifying content release, freeze-thaw steps were included in the liposome preparation protocol. Indeed, this significantly improved liposome unilamellarity, as opposed to omission of these freeze-thaw steps, as shown in figure S6 A-D. Liposomes encapsulating 50 mM SRB were well quenched (Figure S6 E), but the amounts of SRB labeled liposomes had to be drastically decreased, as compared to the amounts of liposomes used in the previous lipid mixing assays that measured pyrene fluorescence only, because the SRB fluorescence intensity was very high in comparison to the virus-related pyrene emission, which in turn was relatively close to the detection limit of the instrument and could not be increased. However, this was convenient, because lower amounts of liposomes allow a better determination of whether content mixing is leaky (leakage = fluid release from the liposomes into the surrounding environment during fusion) or not [154].

Because there was a possibility that the liposomes were not in excess over the virions anymore in the content mixing assay setup, it was necessary to have a rough idea about the virus to liposome ratio. Using a free SRB standard curve depicting SRB concentration versus fluorescence

intensity (Analogous to Figure S6 F), it was estimated, based on the measured liposome size (determined by dynamic light scattering) and the amount of detergent-triggered SRB released from liposomes, that there are ~3x10^9 liposomes per μL in a typical liposome preparation. It was assumed that this was similar for all liposome species tested in the content mixing assay, because they all had similar hydrodynamic radii (~60–70nm).

The particle-to-pfu ratio of UUKV has not been previously determined. However, the theoretical number of glycoproteins per UUKV particle (assuming UUKV is icosahedral and follows quasi-equivalence [79]) and a rough estimate of the glycoprotein concentration per volume of viral preparation are known, which allows a rough estimate of viral particles per preparation. Over six UUKV preparations, this approach gave a mean particle-to-ffu ratio of 1/500. UUKV binding to host cells using fluorescence microscopy earlier showed “over 100 viral particles per cell for a multiplicity of infection of 0.2” [55], which confirms that the range of the UUKV particle to ffu ration estimated is reasonable. Based on these assumptions, calculations indicate that there are ~1.5x10^10 liposomes and ~2.3x10^10 virions in a typical content mixing assay. This confirmed that the liposomes were not in excess anymore over the virus particles, but rather in similar amounts.

In such conditions, at low pH, SRB dequenching in presence of BMP was significantly higher than in its absence (Figure 4.5). Cholesterol in

DOPC:DOPE:BMP liposomes did not change SRB dequenching, but significantly increased lipid mixing (Figure S6 G and H), suggesting that cholesterol might help in UUKV binding to liposomes at lower liposome concentrations. Liposomes containing BMP seemed slightly more unstable than those without BMP, indicated by the tendency of increased SRB leakage from DOPC:DOPE:BMP liposomes in absence of virus, as compared to DOPC:DOPE liposomes (Figure 4.5 A and B). However, the observed tendency remained statistically insignificant (Figure 4.5 D). Content release appeared concomitant to lipid mixing over the time range observed (Figure 4.5 C). If there was a delay in fusion pore opening with respect to lipid mixing, one would expect that lipid mixing increases more quickly than content release in the first few seconds, which was not the case here. Recent studies showed that in addition to content mixing between donor and target compartments, there may be not just content mixing between donor and acceptor compartments, but also leakage from the compartments into the surrounding medium [66]. In such cases, the monitored fluorescence dequenching may overestimate the real amount of content mixing, because a part of the dequenching is due to leakage and not content mixing. The observed UUKV SRB dequenching was unusually high (Figure 4.5), as compared to previous studies that measured content mixing [154], and therefore it was decided to test if UUKV fusion is leaky.

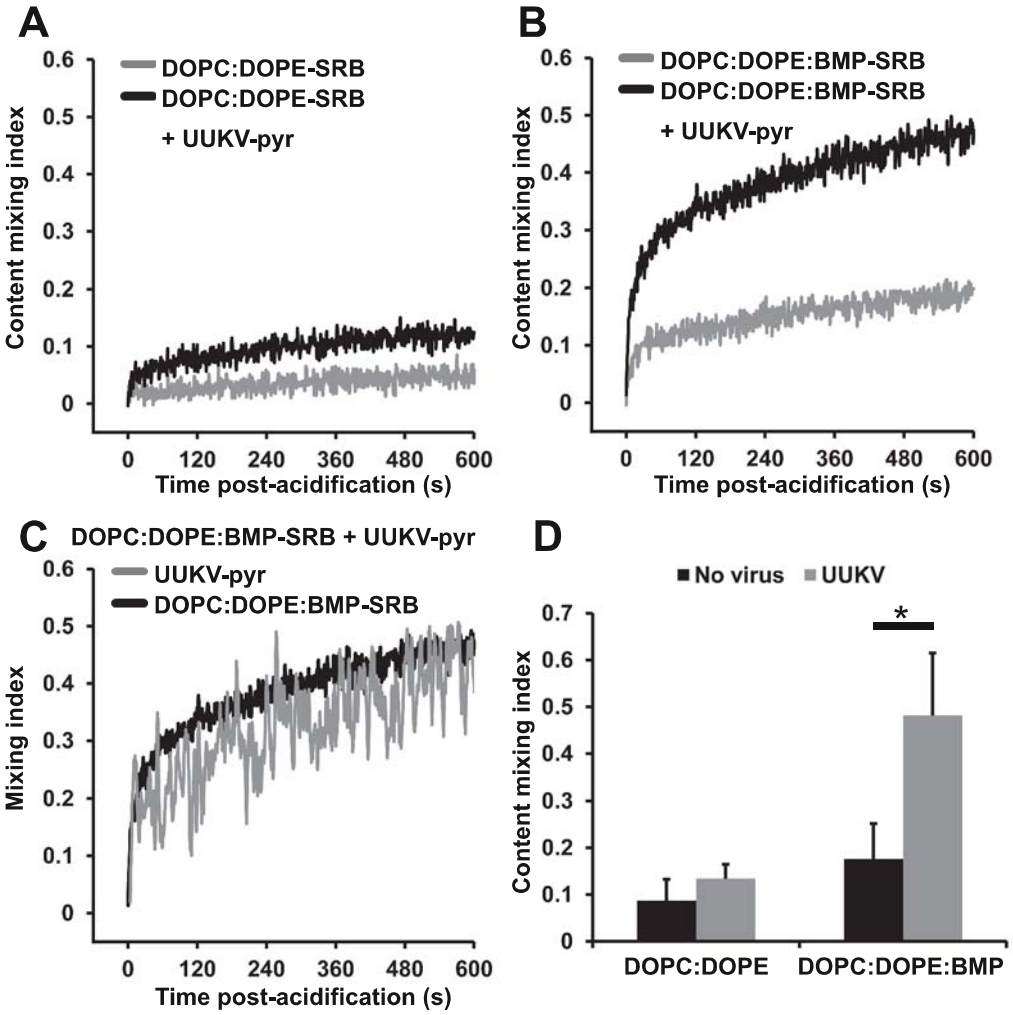


Figure 4.5. Liposome content mixing in presence or absence of UUKV-pyr.

Acidifications were done to pH 5.

A.) Content mixing curves of DOPC:DOPE-SRB liposomes in presence or absence of UUKV-pyr. No pyrene fluorescence is shown.

B.) Content mixing curves of DOPC:DOPE:BMP-SRB liposomes in presence or absence of UUKV-pyr. No pyrene fluorescence is shown.

C.) Lipid mixing and content mixing curve overlay of UUKV-pyr in presence of DOPC:DOPE:BMP-SRB liposomes. The curves were obtained from a single experiment in which lipid mixing and content mixing were measured simultaneously.

D.) Quantifications of content mixing with DOPC:DOPE-SRB or DOPC:DOPE:BMP-SRB liposomes, in presence or absence of UUKV-pyr, 10 minutes post-acidification. Error bars indicate one standard deviation (N=3 for DOPC:DOPE-SRB samples and N=4 for DOPC:DOPE:BMP-SRB samples), *$p \leq 0.05$.

If one neglects the volume of the virus genome and structural proteins, then the inner volume of UUKV should correspond to a sphere of about 90 nm diameter [79]. The inner diameter of DOPC:DOPE:BMP liposomes would correspond to about 130 nm (The liposomes have a hydrodynamic diameter of ~140 nm, from which 2x5=10 nm are subtracted to account for the lipid bilayer thickness). Hence, if one virus fuses to one liposome, then this would correspond to an SRB dilution of about 40% or an SRB fluorescence compatible with 0.6x50mM = 30mM. Therefore, if all viruses fused to all liposomes, the resulting fluorescence intensity should correspond to a fluorescence intensity of 30 mM SRB within encapsulating liposomes. This is the maximal possible (and likely overestimated) fluorescence dequenching in absence of leakage, in which all particles are assumed to be fusogenic. To test if the observed SRB dequenching caused by UUKV in presence of BMP (~50% dequenching) could correspond to a fluorescence of 30 mM SRB in liposomes (in the quenched state), liposomes containing between 30 mM and 50 mM SRB were compared for their fluorescence emission in the quenched state. The principle behind this comparison was the following: During the measurements, the total amount of SRB molecules trapped in liposomes was held constant over the liposome preparations compared, and the only variable between the preparations was the concentration of SRB within the liposomes and thus the quenching levels. The number of SRB molecules in the different preparations was equalized by dissolving liposomes in

0.2% Triton X-100 and determining the SRB end concentration with the help of a standard curve established by measuring free SRB dye in presence of Triton X-100 (Figure S6 F). This allowed the determination of the volume of each liposome preparation to be compared in the quenched state.

When similar amounts of total SRB molecules in the different quenching states were compared, it turned out that the fluorescence of all liposome preparations was more or less similar in the quenched state (Figure S7 A - D). Because the SRB de-quenching observed in the presence of virions reaches ~50%, it can be concluded that possibly the entire dequenching observed corresponds to leakage, and that leakage-free content mixing cannot be observed at all with the current experimental setup. Furthermore, the drastic increase of SRB fluorescence in presence of virions is not due to increased protonation of SRB caused by the low pH outside the liposomes, because SRB fluorescence was pH independent (Figure S7 E). In conclusion, these data show that in presence of the phospholipid BMP in target membranes, and at low pH, UUKV significantly destabilizes the target membranes, to the point that significant leakage from the liposomes is observed.

4.4. Electron cryotomography of phlebovirus–liposome complexes

To directly visualize putative virus to liposome fusion events, the analysis of UUKV fusion was extended to electron cryo-tomography of UUKV in presence of DOPC:DOPE:BMP liposomes at low pH. The aim was to find possible virus–liposome fusion intermediates in order to obtain more evidence that fusion is taking place, as well as a to obtain a deeper insight into the phlebovirus fusion mechanism. Electron cryo-tomography (cryo-ET) allows the acquisition of a single non-symmetric object of interest from different angles in its native state, and thus a three-dimensional image from that single, non-symmetric object. Therefore, cryo-ET is the method of choice to clearly differentiate false positive fusion intermediates (such as virus particles overlapping with liposomes only when viewed from the top but not when viewed from the side) from real fusion intermediates.

When UUKV in presence of liposomes was exposed to low pH, there was a significant amount of aggregation, presumably because of multiple fusion events between virions and liposomes. This was expected, especially because UUKV aggregation in absence of target membranes has been reported previously [79], as well as in chapter 3 of this thesis. A second caveat was that the liposomes preferentially adsorbed to the carbon layer of the EM grid (Figure S6 C and D). Hence, useful isolated virus–liposome complexes were rare and confined to early fusion intermediates. At neutral pH, close interactions between virions and liposomes were visible, although the target membranes were round and

did not seem to be affected by the virions (Figure 4.6 A and B). At pH 5, UUKV formed elongated spike clusters bridging viral and liposome membranes (~18 nm membrane to membrane distance, Figure 4.6.C to H). These elongated spikes were clearly different from the spikes not making contacts with any liposomes at low pH and with spikes at neutral pH (~10 nm length, see also Figure 4.6 A to D), consistent with the UUKV spike length at neutral and low pH in absence of target membranes (Figure 3.6). This is entirely consistent with established models in low pH dependent class II fusion [169, 170], in which the viral glycoproteins extend to target membranes to anchor the fusion loop. This is followed by further conformational changes that pull the membranes into close proximity, thereby deforming lipid bilayers to allow lipid mixing. UUKV also induced a limited level of target membrane deformation (Figure 4.7 A), resembling dimples that were also previously observed in influenza virus fusion [66]. Very rarely, putative membrane fusion events, in which the viral membrane seemed continuous with the liposome membrane, were observed (Figure 4.7 B and C). Interestingly, two-dimensional projection images of UUKV in presence of DOPC:DOPE liposomes at pH 5 also indicated a degree of dimple formation, as well as possible elongated spikes and fused particles (Figure 4.8). Although a tomographic analysis of DOPC:DOPE liposome + UUKV complexes is required to fully exclude the possible caveat of possible false positive interactions, these data already indicate that early fusion intermediates may also be present in

absence of BMP. This would mean that BMP would be required at an intermediate step in the fusion process, such as lipid mixing, which is entirely consistent with the results obtained in pyrene excimer assay. This would raise the possibility that, similarly to dengue virus fusion, BMP may favour the exit from restricted fusion intermediates [59].

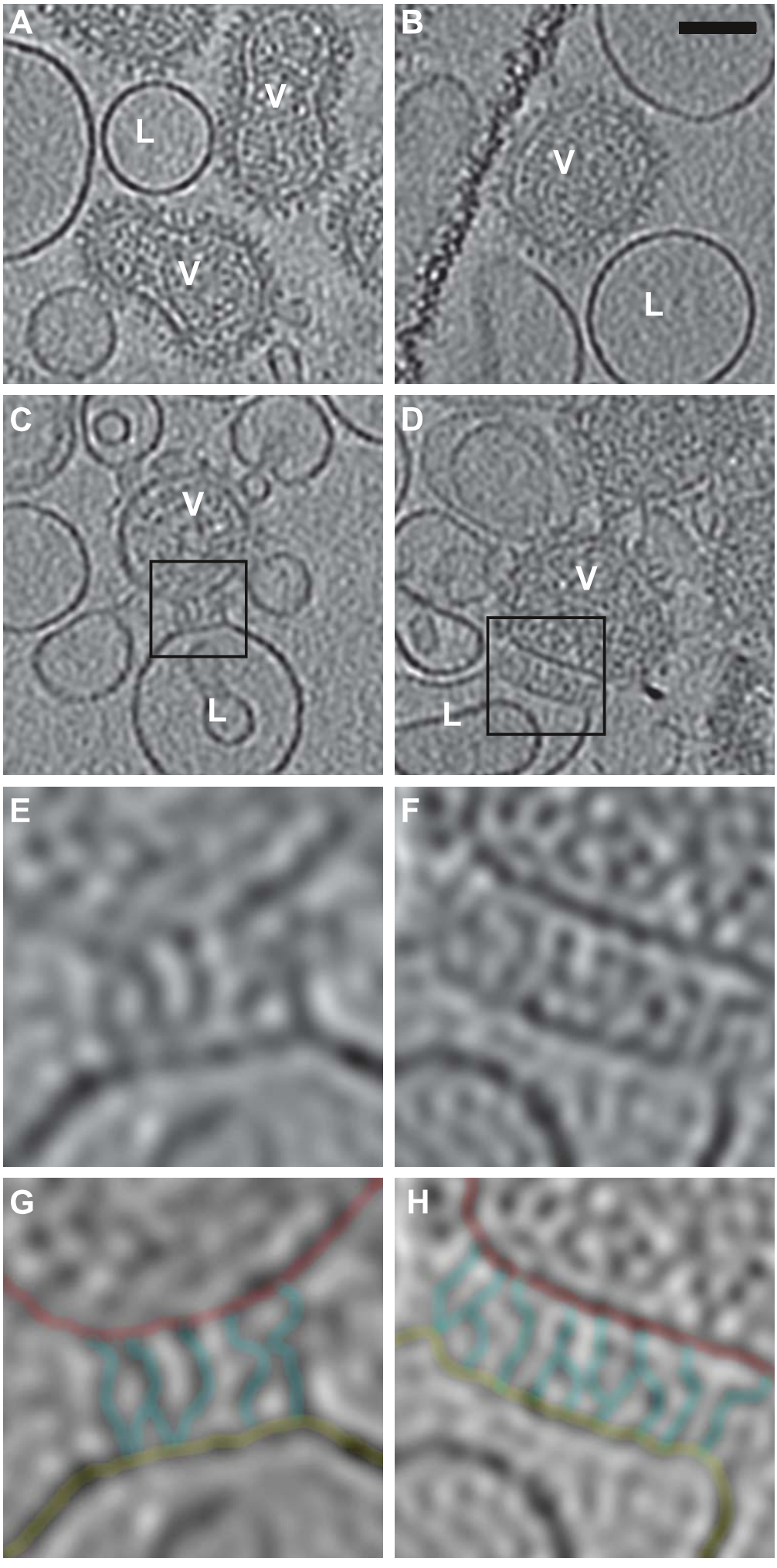

A
V
L
V
B
V
L
C
V
L
D
V
L
E
F
G
H

Figure 4.6. Electron cryo-tomography of Uukuniemi virus in presence of liposomes containing BMP, at neutral and low pH.

UUKV was mixed with DOPC:DOPE:BMP liposomes, exposed to either neutral pH (A and B) or pH 5 (C to H) and plunge frozen in liquid ethane, followed by electron cryotomography at a defocus of –6 µm. Shown are 10 nm thick slices of tomograms. V=Virion, L=liposome. Scale bar = 50 nm.

A.) and B.) UUKV and DOPC:DOPE:BMP liposomes at neutral pH. Note the close interaction between the virions and liposomes, but the absence of any elongated glycoproteins or virus-induced target membrane deformations.

UUKV at pH 5 in presence of C.) DOPC:DOPE:BMP:Chol and D.) DOPC:DOPE:BMP liposomes: Note the presence of elongated glycoprotein arrays, extenting from the virions towards the target membranes, forming a bridge. Close-ups of boxed areas are shown in E.) and F.). Viral membranes (red), glycoproteins (blue) and liposome membranes (yellow) are highlighted in G.) and H.).

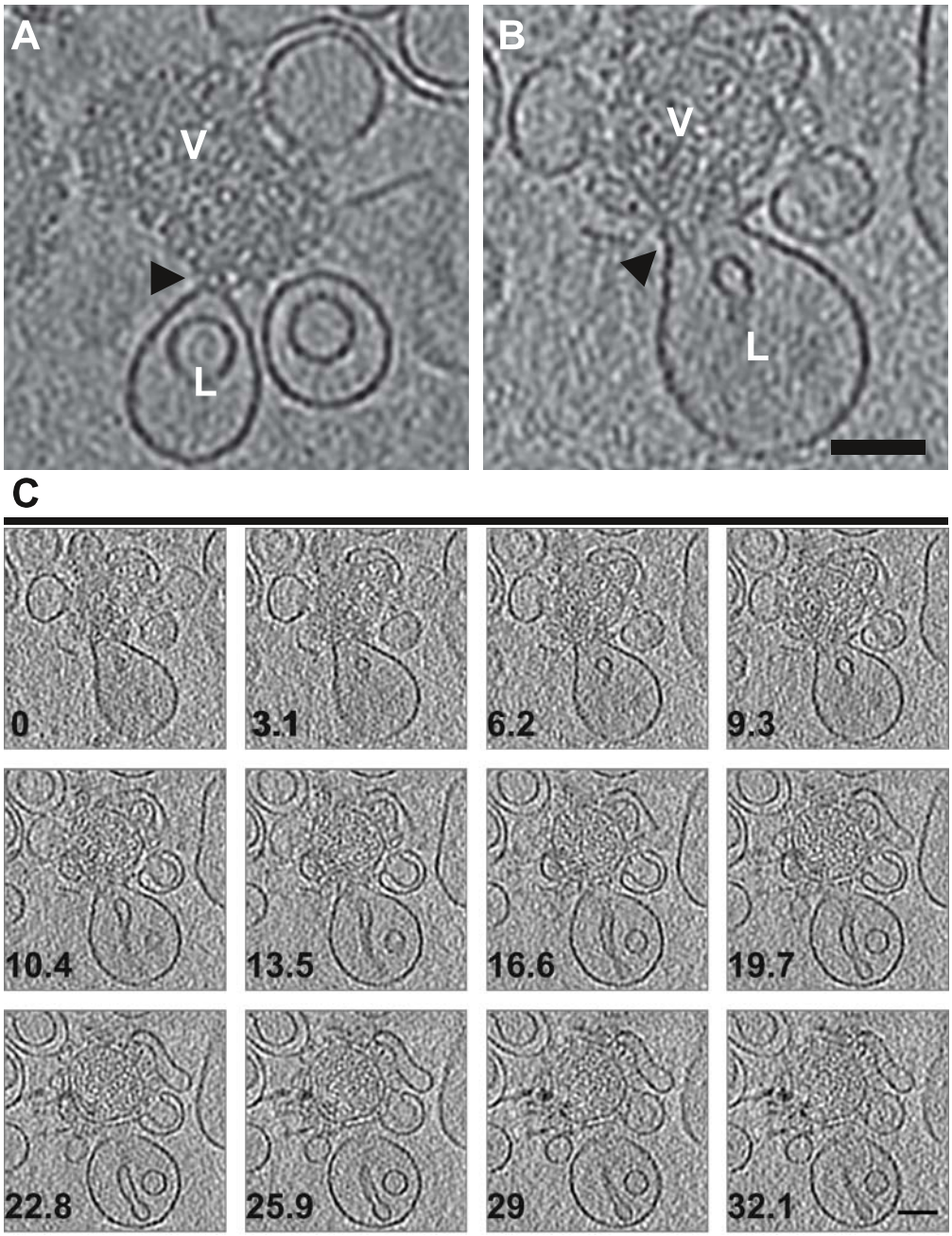


Figure 4.7. Early fusion intermediates of Uukuniemi virus in presence of liposomes containing BMP.

A.) and B.) 10 nm thick tomogram slices (defocus: –6 µm) of UUKV in presence of DOPC:DOPE:BMP liposomes at pH 5. Note the UUKV-induced target membrane deformation in A.), and the presence of a putative fusion/hemifusion intermediate B.), indicated by arrowheads. Scale bar = 50 nm. V = virus, L = liposome.

C.) Serial tomogram slices of the putative fusion complex shown in B.). Numbers indicate the relative z position in nm. Scale bar = 50 nm.

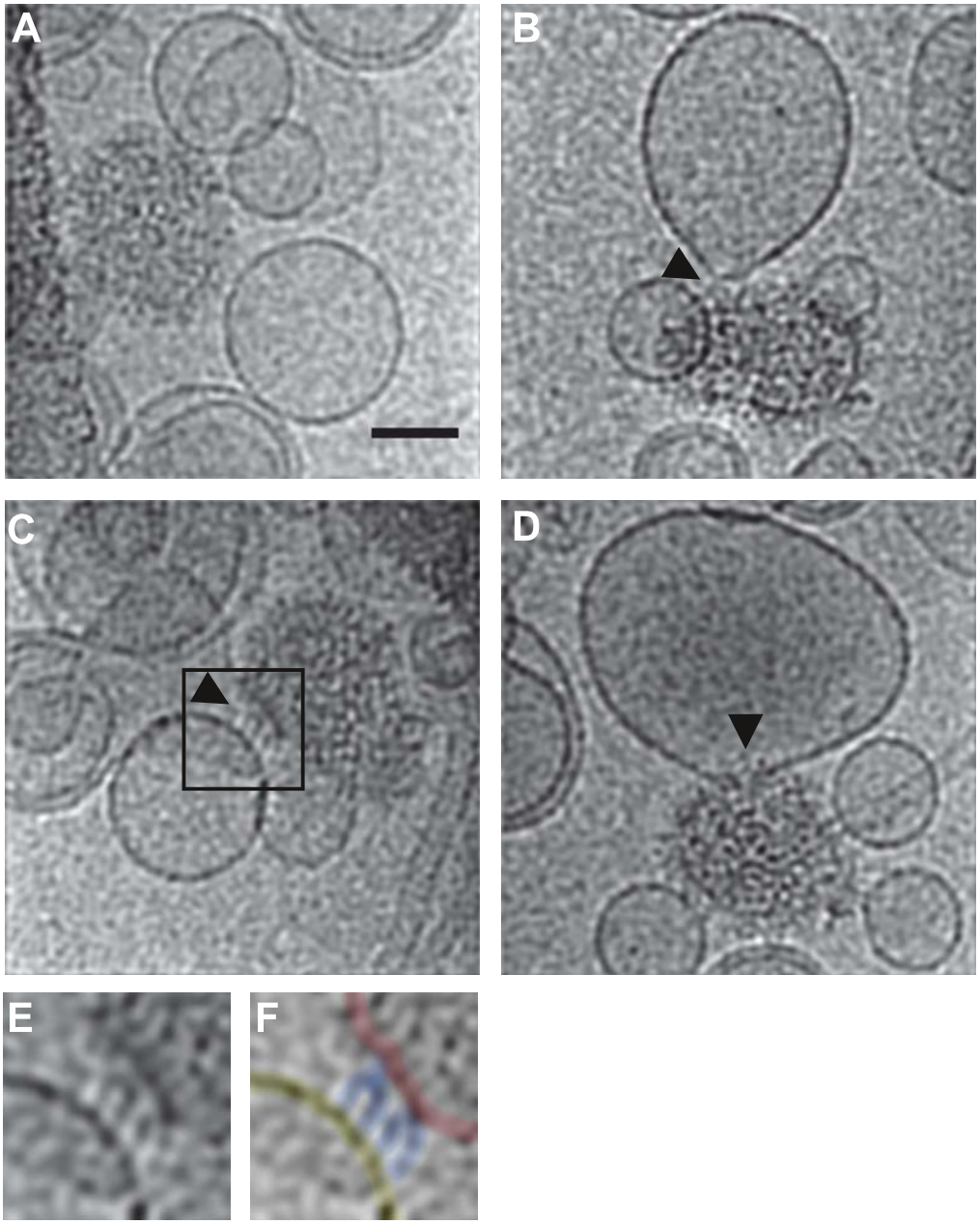


Figure 4.8. Electron cryo-microscopy of Uukuniemi virus in presence of BMP-free liposomes and low pH.

Two-dimensional projection images of UUKV in presence of DOPC:DOPE liposomes at pH 5, taken at a defocus of –6 µm. Close interactions with liposomes but without target membrane deformations A.), virus-induced dimple formation B.), elongated glycoproteins bridging virion and liposomes C.), as well as putative fusion/hemifusion complexes (D.), were found. Close-ups of the elongated glycoproteins in C.) are shown in E.) and F.). Virion membrane (red), spikes (blue) and liposome membrane (yellow) are highlighted. Arrowheads indicate putative fusion intermediates.

4.5. Physiological relevance of BMP in UUKV infection

To test if the *in vitro* fusion enhancement of UUKV caused by BMP is relevant in a cell culture system, I used an anti-BMP antibody to block potential intracellular contact sites that contain BMP, similarly as described previously for testing the entry of Vesicular stomatitis virus (VSV, a member of the *Rhabdoviridae* family), which has been proposed to fuse to BMP-rich intraluminal vesicles (ILV's) [101]. To this end, BHK-21 cells were incubated with an anti-BMP antibody overnight, and then infected at low multiplicity of infection with UUKV. Viral replication was monitored, using a recently developed FACS-based infection assay for UUKV [55]. Viral replication was detected using immunofluorescence against all UUKV structural proteins. Unexpectedly, the anti-BMP antibody did not block the infection, even though it was associated with the cells (Figure 4.9). While these preliminary data might suggest that BMP is not required for UUKV infection of BHK-21 cells, the exact location of the cell-associated anti-BMP antibody was not determined here and hence it remains unclear whether the anti-BMP antibody was indeed targeted to late endosomes and lysosomes to cause BMP depletion in these compartments. A more thorough investigation is needed to confirm the role of BMP in UUKV entry, as further discussed in 6.3.3.

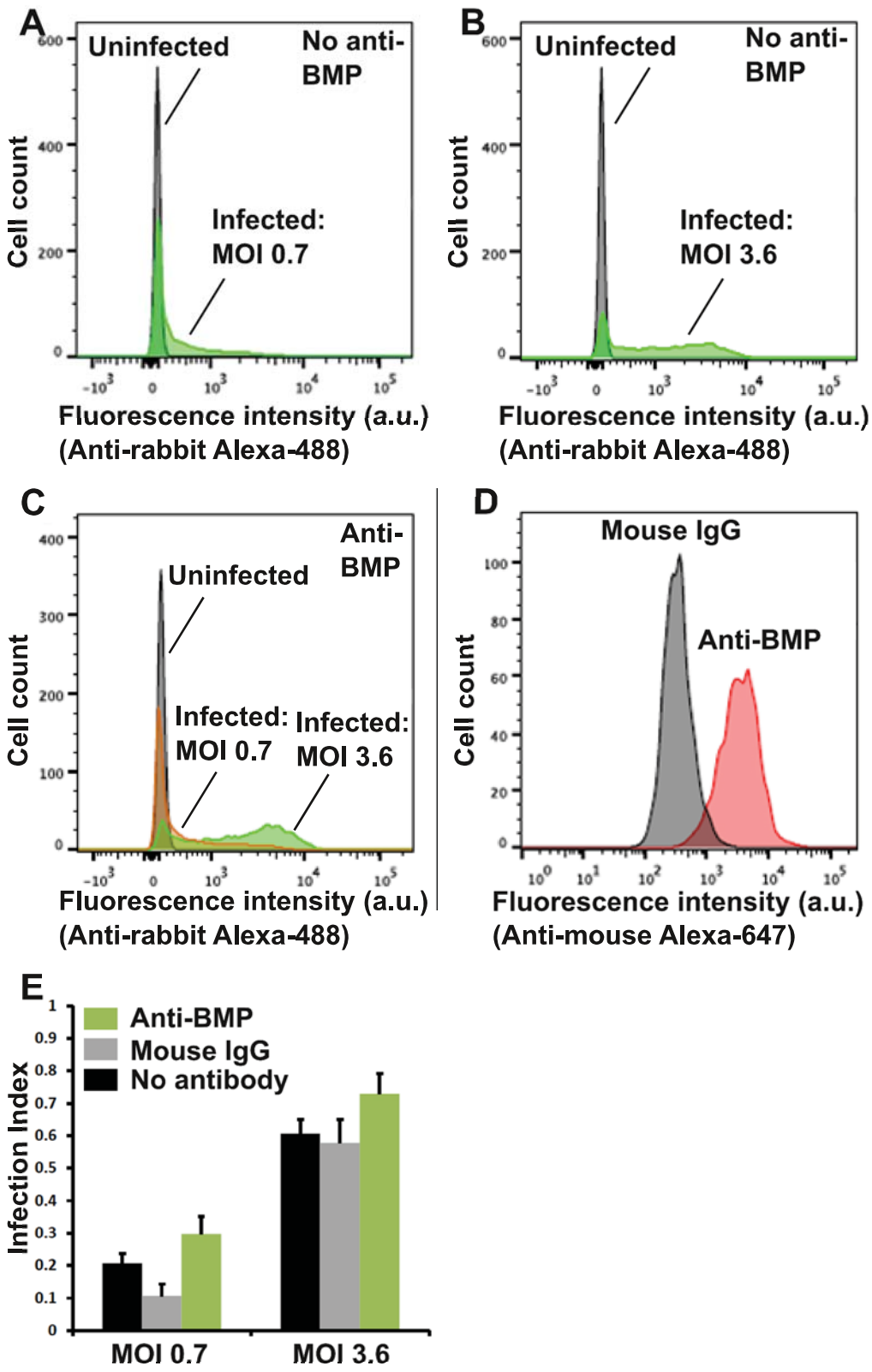

A
Uninfected
No anti-BMP
Infected: MOI 0.7
Cell count
Fluorescence intensity (a.u.)
(Anti-rabbit Alexa-488)
B
Uninfected
No anti-BMP
Infected: MOI 3.6
Cell count
Fluorescence intensity (a.u.)
(Anti-rabbit Alexa-488)
C
Anti-BMP
Uninfected
Infected: MOI 0.7
Infected: MOI 3.6
Cell count
Fluorescence intensity (a.u.)
(Anti-rabbit Alexa-488)
D
Mouse IgG
Anti-BMP
Cell count
Fluorescence intensity (a.u.)
(Anti-mouse Alexa-647)
E
Anti-BMP
Mouse IgG
No antibody
Infection Index
MOI 0.7
MOI 3.6

Figure 4.9. Infection of cells with Uukuniemi virus in presence or absence of an anti-BMP antibody.

Detection of UUKV infection of BHK-21 cells in presence or absence of 0.05 mg/mL anti-BMP antibody, using fluoresence-activated cell sorting. Cells were pre-incubated overnight with an anti-BMP antibody or isotype control (IgG). The cells were then infected with UUKV and viral replication was detected by immunofluorescence against all UUKV structural proteins, using an anti-UUKV serum antibody.

A.) BHK-21 cells, infected with UUKV at MOI 0.7. UUKV structural proteins were detected at ~7 hours post-infection with a polyclonal serum antibody against UUKV and a secondary goat anti-rabbit-Alexa488 antibody. The uninfected control is shown in grey and the infected sample in green.

B.) Same as in A.) with the difference that cells were infected at MOI 3.6.

C.) FACS analysis of BHK-21 cells in presence of 0.05 mg/mL anti-BMP antibody. Note that cells can still get infected. Uninfected cells are in grey. Cells infected at MOI 0.7 are in orange and cells infected at MOI 3.6 are in green.

D.) Mouse anti-BMP treated (red) or isotype control treated (grey), uninfected BHK-21 cells, stained with anti-mouse-Alexa647.

E.) Quantification of UUKV infection in presence of 0.05 mg/mL mouse anti-BMP. Error bars indicate the standard deviation of an intra-experimental duplicate. The infection index represents the fraction of infected cells relative to all counted cells for a given condition (% of infected cells divided by 100).

5. Arbovirus – DC-SIGN interactions

5.1. Rationale

Many arthropod-borne viruses (arboviruses), for example alphaviruses (family *Togaviridae*), flaviviruses (family *Flaviviridae*) or phleboviruses (family *Bunyaviridae*) bind to the calcium-dependent lectin DC-SIGN [44, 46]. DC-SIGN binds high mannose and fucose-based glycans with high affinity [171]. Phleboviruses were the first group of arboviruses shown to hijack DC-SIGN internalization for target cell infection, because expression of DC-SIGN in otherwise non-permissive cells caused infection, whereas expression of endocytosis-deficient DC-SIGN showed significantly reduced infection, despite similar binding at the cell surface. Consistently, immature dendritic cells, which highly express DC-SIGN [39], were also target cells of phleboviruses [44, 172]. Because DC-SIGN expressing immature dendritic cells can be found in the dermis, close to potential sites where arthropod bites occur, they are thought to be among the first cells to be infected and to sustain viral infection, as they migrate towards the lymph nodes. Hence, the current hypothesis is that DC-SIGN is responsible for the initial capture and spread of phleboviruses after an arthropod bite [44]. Therefore, DC-SIGN is a very attractive target for blocking early stages in phlebovirus infection. Other arboviruses, such as flaviviruses or alphaviruses, use DC-SIGN only as attachment factor, in order to boost the infection of permissive cells considerably [40, 42], which

means that DC-SIGN is also an attractive target to control alphavirus and flavivirus infection.

Rational drug design greatly benefits from high-resolution structures of virus–receptor interactions because they provide a chemical basis of the virus–host interaction and thus valuable information required for the synthesis of possible small molecule entry inhibitors. Atomic resolution of such glycoprotein interactions can typically be achieved with X-ray crystallography (*e.g.* [173]). On the other hand, electron cryo-microscopy of virions has been an equally important technique that provides the native scaffold for the fitting of crystal structures and thus puts the interacting components (*e.g.* protein–protein or protein–glycan interactions) into the context of a native virus–receptor interaction. There has so far been only one low resolution electron cryo-microscopy study of an interaction between dengue virus and a recombinantly expressed DC-SIGN carbohydrate recognition domain (CRD) [119]. These data showed that the CRD binds to dengue virus only at discrete positions, which are located around the icosahedral two-fold positions. This DC-SIGN "footprint" at the surface of dengue virus confirmed the identity of the N-glycans involved in the DC-SIGN interaction, which was presumably facilitated by the fact that the E protein is the only N-glycosylated protein at the virion surface and has only two glycosylation sites per E protein that are topologically well separated [108, 119]. In the case of arboviruses that have more than one glycoprotein with multiple (and possibly more closely

located) glycosylation sites, such as bunyaviruses (*e.g.* the Uukuniemi phlebovirus has four N-glycan sequons on each glycoprotein) and alphaviruses (*e.g.* Semliki Forest virus has one sequon on E1 and two sequons on E2), the mapping of N-glycan binding sites at the virion surface becomes more complicated. As an alternative to the fitting of crystal structures, the calculation of cryo-EM difference maps of wild-type and mutant viruses (deficient in certain N-glycans) also has allowed the surface localization of N-glycans on an alphavirus called Sindbis virus [174]. Apart from a requirement of sufficiently high resolution cryo-EM data to subtract glycan densities between three-dimensional maps, the site-directed de-glycosylation that requires sequon mutagenesis is only useful if it comes with a limited impact on the efficiency of virion production (a high enough number of intact virions is needed for electron microscopic analysis). This may not always be granted, depending on the specific mutation in the virus glycoproteins. Importantly, not necessarily all N-glycans at the virus surface are potential DC-SIGN ligands, which may be due to the glycan structure itself (which has to be high mannose and may not necessarily be so, depending on the glycan site), or sterical restrictions at the virion surface not allowing the lectin to interact with its high mannose glycan ligand. Therefore, in summary, to facilitate the mapping of specific glycan–lectin interactions at the virion surface, the predominant glycan species at specific N-glycan sites, all relevant glycoprotein crystal structures, as well as cryo-EM structures of the whole virion, both in

presence or absence of the lectin, should be available. The accumulation of such wide-ranging data and their combination is a product of considerable and coordinated efforts over longer periods of time. Therefore, this chapter is focused on the contribution of cryo-EM data of an arbovirus that has more than one major glycoprotein at the surface. Two important arbovirus species that were taken into consideration for this task were the Uukuniemi phlebovirus and the alphavirus Semliki Forest virus.

5.2. The N-linked glycosylation of UUKV and SFV

Earlier studies suggested that UUKV G_C contains predominantly highly mannosylated glycans, whereas UUKV G_N mainly contains complex N-glycans [175]. However, a more recent study showed that both G_N and G_C had high mannose glycans [44]. To confirm the glycosylation pattern at the UUKV surface, SDS gels were overloaded with UUKV (Figure S8 D), and the glycoprotein bands were cut out and sent to collaborators for ion mobility mass spectrometry (MS) analysis [176] of the UUKV N-glycans. The results were published [177], and confirmed that G_C has predominantly high mannose glycans and that G_N has predominantly more complex glycans, but also that the glycosylation pattern on both glycoproteins represents a distribution of a broad spectrum of glycan species with the most predominant species shifted towards either high mannose or complex glycans. This means that there are also complex glycans on G_C and high mannose glycans on G_N, but in minor amounts, as

compared to the predominant glycan species observed, respectively. Interestingly, low amounts of poly-N-acetyllactosamines (where one N-acetyllactosamine is a covalent heterodimer of galactose and N-acetylglucosamine, linked via a β-1,4 glycosidic bond) were found on glycans of both G_N and G_C. Poly-N-acetyllactosamines are glycan chains that can be found on glycoproteins localized in the Golgi apparatus for prolonged periods of time [178]. This is consistent with an UUKV assembly site at the Golgi apparatus, as previously proposed [179]. However, such poly-N-acetyllactosamines are not expected to play a role in UUKV binding to DC-SIGN. In summary, although G_N is predicted to be more exposed at the virion surface than G_C [83, 180], G_C is more highly mannosylated than G_N, and thus G_C seems to be the more likely candidate glycoprotein to bind DC-SIGN. However, because there is no crystal structure of phlebovirus G_N and no current model showing the surface distribution of all UUKV N-glycans, UUKV may not yet be the first choice for studies of virion-DC-SIGN complexes. Another reason for not choosing UUKV is that the icosahedral symmetry of UUKV seems to be highly susceptible to disruption (as confirmed in chapter 4 in this thesis), and hence icosahedral reconstruction of UUKV–DC-SIGN complexes for potential high resolution information was not attempted here. Finally, it was not possible to work on the more structurally stable Rift Valley fever virus because of biosafety restrictions. Therefore, it was decided to first focus on alphavirus–DC-SIGN interactions.

Lentiviruses pseudotyped with SFV glycoproteins and produced in mammalian cells bind and transduce DC-SIGN expressing target cells more efficiently than non-expressing target cells, and this effect was increased when the SFV pseudotyped lentiviruses were produced in insect cells [43]. Sindbis virus (SBV) also binds to DC-SIGN, but only to significant levels when produced in insect cells [42]. The discrepancy between mammalian cell derived SBV and SFV in binding DC-SIGN could be explained by the non-strict conservation of glycosylation sites between SBV and SFV [50, 174].

Earlier studies suggested that SFV produced in mammalian cells has mainly high mannose glycans on the glycoprotein E2 [181, 182]. On the other hand, different studies suggested that E2 glycans had complex glycosylation [183]. To determine the detailed glycan species found on the surface of SFV produced in mammalian cells, SFV produced in BHK-21 cells (alongside with SFV produced in C6/36 cells) was subjected to SDS-PAGE (Figure S8 A, B and C), the glycoprotein bands were excised and sent to collaborators for glycan analysis using ion mobility mass spectrometry. The data were published [50], and for SFV produced in BHK-21 cells, the majority of the E1 N-glycans had complex glycosylation whereas the majority of E2 glycans were highly mannosylated. As previously published [184], the majority of the E1 glycans of SFV produced in insect cells corresponded to paucimannose structures (N-glycans with a tri-mannosyl core and fucosylated derivatives), whereas E2 was

predominantly highly mannosylated. Altogether, this suggests that the E2 glycoprotein is the most likely DC-SIGN ligand on SFV produced both in insect and mammalian cells. Consistently, only glycoprotein E2, from SFV produced in both insect cells and mammalian cells was susceptible to Endoglycosidase F1 digestion (Figure S8 E).

A sub-nanometer cryo-EM structure is available for SFV [185], but unfortunately, there is only a crystal structure of glycoprotein E1 for SFV [186]. However, there are also crystal structures of both Chikungunya virus (CHIKV, another alphavirus) glycoproteins E1 and E2 in a complex [187]. Because the SFV E2 N-glycan sites are more closely related the CHIKV N-glycans in their primary sequence, than to the SBV E2 glycan sites, the CHIKV E protein crystal structures represent a more reasonable structural surrogate system for the display of SFV glycans in cryo-EM structures [50]. This glycan display model suggested that the potential high mannose glycan ligands for DC-SIGN are localized on the E2 glycoprotein and extend into the narrow areas between the trimeric spikes, distally from the membrane [50].

In this chapter, the objective was to produce both SFV particles and soluble DC-SIGN ectodomains, to form a complex between both components *in vitro* to be analyzed in electron cryo-microscopy, with the expectation that the above mentioned intertrimeric N-glycans are the main sites used in the proposed E2–DC-SIGN interaction. The strategy for structure determination of this interaction was to use electron cryo-

microscopy and icosahedral reconstruction of SFV-DC-SIGN complexes, similarly as described previously for dengue virus–DC-SIGN$_{CRD}$ (CRD = carbohydrate recognition domain) complexes [119].

5.3. Production and purification of soluble DC-SIGN ectodomains for electron cryo-microscopy

DC-SIGN ectodomains of different length were cloned into the pHLsec vector [125], and expressed as C-terminal hexahistidine-tagged proteins in mammalian cells (HEK cells). Three constructs were selected for larger scale expression and purification using nickel-NTA affinity chromatography, followed by gel filtration. These three constructs included the carbohydrate binding domain alone (DC-SIGN$_{CRD}$), DC-SIGN$_{CRD}$ including five neck repeats (DC-SIGN$_{CRD}$ + 5 repeats), or the full extracellular domain (DC-SIGN$_{ECD}$) (See Figure 5.1 A). DC-SIGN ectodomains have previously been expressed in bacteria [127, 188]. Here, the constructs were expressed in HEK 293T cells, to account for the N-glycosylation site found in DC-SIGN$_{ECD,}$ and to avoid the need for protein refolding. The DC-SIGN$_{CRD}$ + 5 repeats construct was expressed in 293S cells (HEK cells that lack N-acetylglucosamine transferase I activity and thus cannot produce complex glycans [126]), but this was not considered a problem here because DC-SIGN$_{CRD}$ + 5 repeats has no predicted N-glycosylation sites.

As expected, the longer DC-SIGN fragments eluted as multiple peaks, presumably corresponding to DC-SIGN tetramers and lower order assemblies, respectively, whereas DC-SIGN$_{CRD}$ eluted as a single peak, presumably as a monomer (Figure 5.1 B, C and D). As expected, the DC-SIGN construct expressing five neck repeats seemed to form a lower relative amount of tetramers than the full extracellular domain (Figure 5.1 C and D). As previously determined in low scale expression cell supernatant (Figure S9 A), the DC-SIGN$_{CRD}$ peak seemed more heterogenous than the DC-SIGN$_{ECD}$ peak.

The qualitative binding capacity of the hexahistidine-tagged DC-SIGN ectodomains was tested by sandwich ELISA, in which UUKV, as a well-established DC-SIGN ligand, formed the bottom of the sandwich and purified DC-SIGN the analyte. DC-SIGN was indirectly detected with an anti-hexahistidine tag antibody and an HRP-coupled secondary antibody (Figure 5.2 A). DC-SIGN$_{CRD}$ only showed close to background binding activity (Figure 5.2 B), although, if functional, it could have been expected to be active in the micromolar range tested [127]. Conversely, both the fragments containing neck repeats showed qualitative binding to UUKV, when applied in the lower micromolar range (Figures 5.2 C and D). The here expressed DC-SIGN$_{CRD}$ seemed unsuitable for virus–DC-SIGN interaction studies due to its negligible affinity in the conditions tested.

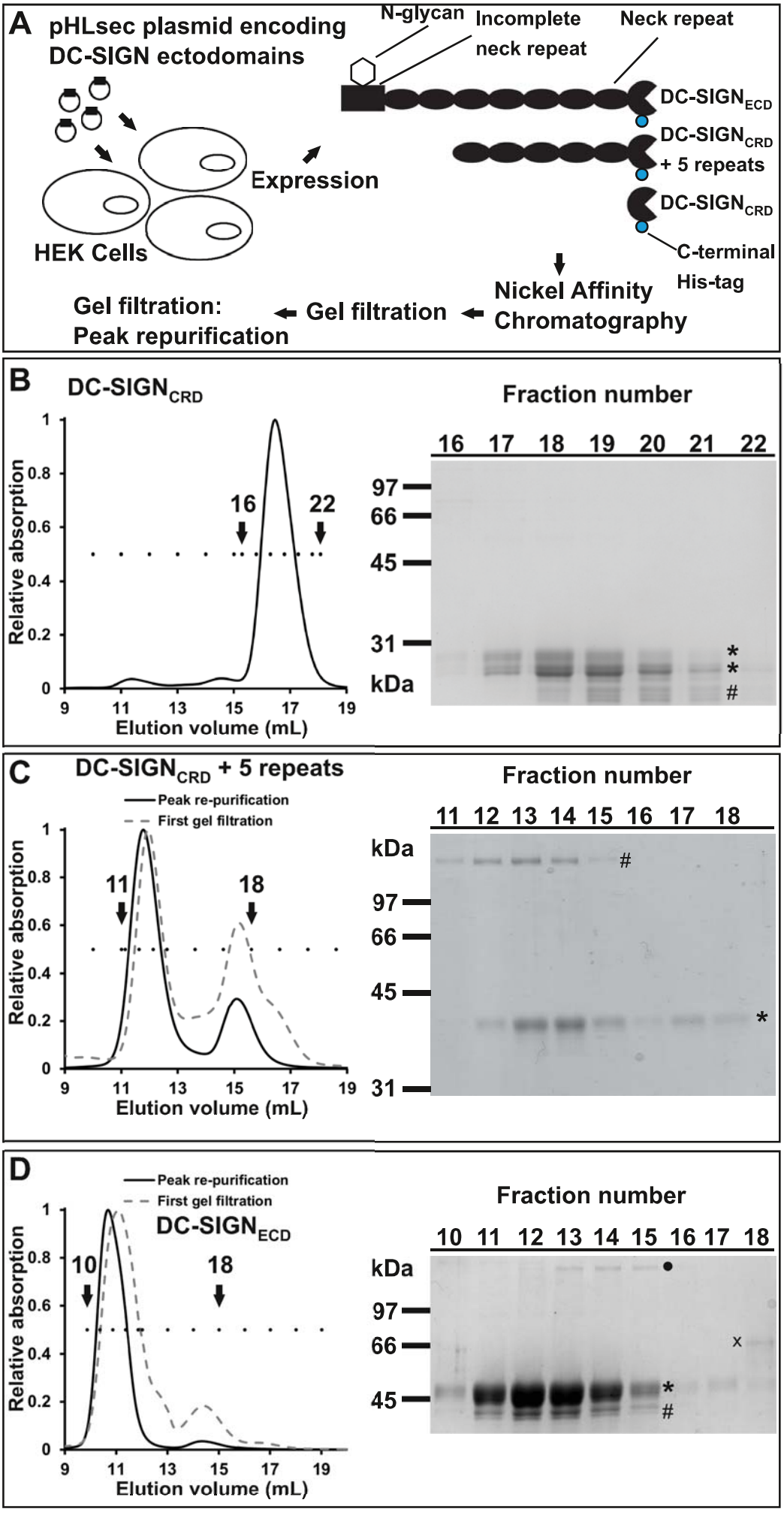

A
pHLsec plasmid encoding
DC-SIGN ectodomains
HEK Cells
Expression
N-glycan
Incomplete
neck repeat
Neck repeat
DC-SIGN$_{ECD}$
DC-SIGN$_{CRD}$
+ 5 repeats
DC-SIGN$_{CRD}$
C-terminal
His-tag
Nickel Affinity
Chromatography
Gel filtration
Gel filtration:
Peak repurification
B
DC-SIGN$_{CRD}$
Relative absorption
Elution volume (mL)
Fraction number
16 17 18 19 20 21 22
97
66
45
31
kDa
C
DC-SIGN$_{CRD}$ + 5 repeats
Peak re-purification
First gel filtration
11
18
Fraction number
11 12 13 14 15 16 17 18
D
Peak re-purification
First gel filtration
DC-SIGN$_{ECD}$
10
18
Fraction number
10 11 12 13 14 15 16 17 18

Figure 5.1. Expression and purification of soluble DC-SIGN constructs.

A.) Sketch of the DC-SIGN expression and purification strategy. HEK 293T cells (or N-acetyglucosamine-transferase I deficient HEK 293S cells for DC-SIGN$_{CRD}$ + 5 neck repeats), were transiently transfected with pHLsec plasmids either encoding the DC-SIGN$_{CRD}$, DC-SIGN$_{ECD}$ or DC-SIGN$_{CRD}$ including five neck repeats (DC-SIGN$_{CRD}$ + 5 repeats), all with a C-terminal hexahistidine tag (His-tag). The expressed proteins were secreted into the supernatant, which was then cleared of cell debris and successively purified over Nickel-NTA and gel filtration columns. For DC-SIGN constructs containing neck domains, the main peaks were reloaded for gel filtration, to determine peak stability.

B.) Gel filtration profile of DC-SIGN$_{CRD}$ (left panel) and SDS-PAGE of peak fractions (right panel). The dots in the left panel indicate collected fractions and the numbers above the dots indicate the range of fractions shown in SDS-PAGE (right panel). Note that there are multiple DC-SIGN$_{CRD}$ bands in the fractions. The asterisks indicate a DC-SIGN CRD double band, possibly corresponding to a full and a shorter form of the CRD. The hash indicates possible DC-SIGN CRD degradation products.

C.) Same as in B.) with the following modifications. The first round of gel filtration profile of a DC-SIGN$_{CRD}$ + 5 repeats construct is shown as a grey dashed line. Fractions of the highest peak were selected and then reloaded on the same gel filtration column. The elution profile of this second run is shown as a continuous black line. Note that there is still a significant secondary lower molecular weight peak (at higher elution volume), showing that the main peak (presumably the tetramer) is not entirely stable. The dots in the left panel indicate collected fractions from the second run and the numbers above the dots indicate the range of fractions of that second run shown in SDS-PAGE (right panel). The asterisk indicates the DC-SIGN construct with five neck repeats and the hash indicates possible DC-SIGN oligomers, possibly corresponding to DC-SIGN tetramers arising due to incomplete protein denaturation prior to SDS-PAGE.

D.) Same as in C.), but with a DC-SIGN$_{ECD}$ construct. On the right panel (SDS-PAGE), the asterisk indicates the DC-SIGN$_{ECD}$ construct. The hash indicates possible shorter DC-SIGN fragments and/or DC-SIGN degradation products. The cross indicates an unidentified weak band (not used for further experiments) and the closed circle indicates possible DC-SIGN oligomers, possibly corresponding to tetramers, arising due to incomplete protein denaturation prior to SDS-PAGE.

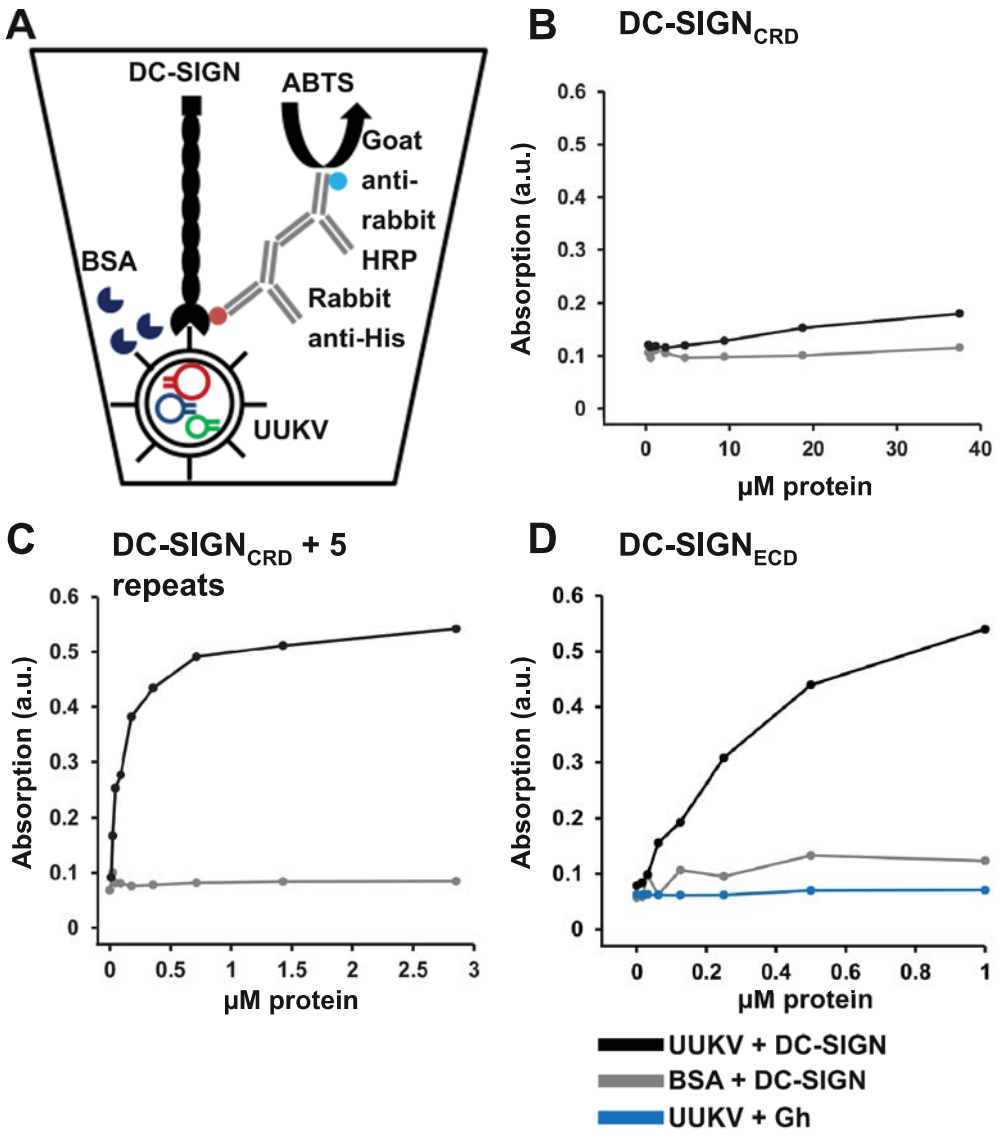


Figure 5.2. Binding capacity of the soluble DC-SIGN constructs.

A.) Sketch of the sandwich ELISA used to test the binding activity of hexahistidine (red dot)-tagged DC-SIGN constructs. UUKV is added to the bottom of the well and blocked with BSA. The DC-SIGN construct is then added and detected with a rabbit anti-hexahistidine antibody. This antibody is then detected with a horseradish-peroxidase (HRP, blue dot) coupled goat anti-rabbit antibody. The presence of HRP (and hence of DC-SIGN bound to UUKV) is monitored by addition of 2,2'-azino-bis(3-ethylbenzthiazoline-6-sulfonic acid (ABTS), which HRP converts to a blue/green product (in presence of hydrogen peroxide) that absorbs light at 405 nm. The intensities of these products in presence of different DC-SIGN constructs are shown in 5.2 B, C and D.

B.) Absorption at 405 nm in presence of the DC-SIGN$_{CRD}$ construct.

C.) Absorption at 405 nm in presence of the DC-SIGN$_{CRD}$ + 5 repeats construct.

D.) Absorption at 405 nm in presence of the DC-SIGN$_{ECD}$. The blue curve represents samples that contained UUKV and to which glycoprotein H of a paramyxovirus (instead of DC-SIGN) was added as a negative control.

On the other hand, the presence of neck repeats allows DC-SIGN tetramerization [128], confers high affinity binding, and finally is closer to physiological glycan–DC-SIGN interactions. Therefore, in a first step, the DC-SIGN construct of choice for electron cryo-microscopy was the DC-$SIGN_{ECD}$.

5.4. Cryo-EM of SFV–DC-SIGN complexes and icosahedral reconstruction

It is known that the DC-SIGN carbohydrate recognition domain is flexibly linked to the neck repeats [128], therefore it could not be expected to obtain a high resolution structure of the full DC-SIGN ectodomain bound to SFV, but rather of the CRD part only, which was the main protein domain of interest. The main advantage with using the DC-$SIGN_{ECD}$ instead of the DC-$SIGN_{CRD}$ is the high avidity of the DC-$SIGN_{ECD}$, caused by the multimerization *via* the neck repeats, which would hopefully allow a high amount of virus–receptor complexes.

Purified SFV was plunge-frozen in presence of the DC-SIGN extracellular domain (ECD) and subjected to single-particle analysis and icosahedral reconstruction in the software RELION, similarly as described for the bacteriophage SSIP-1 (see chapter 3), with the modification that here, the virus–receptor complexes were recorded using a direct electron detector. Direct electron detectors, as opposed to charge-coupled device (CCD) cameras, are capable of recording images at a frame rate high enough to trace sample movement during the acquisition (which can be corrected for

computationally by tracking particle movements between the individual image frames). Because the electrons are counted directly, with no need for scintillators converting the electron signal into a light signal to be re-converted into an electron signal by the CCD chip, images acquired by direct electron detectors are much less noisy than images acquired by CCD cameras. Therefore, direct electron detectors greatly improve the attainable resolution in electron cryo-microscopy.

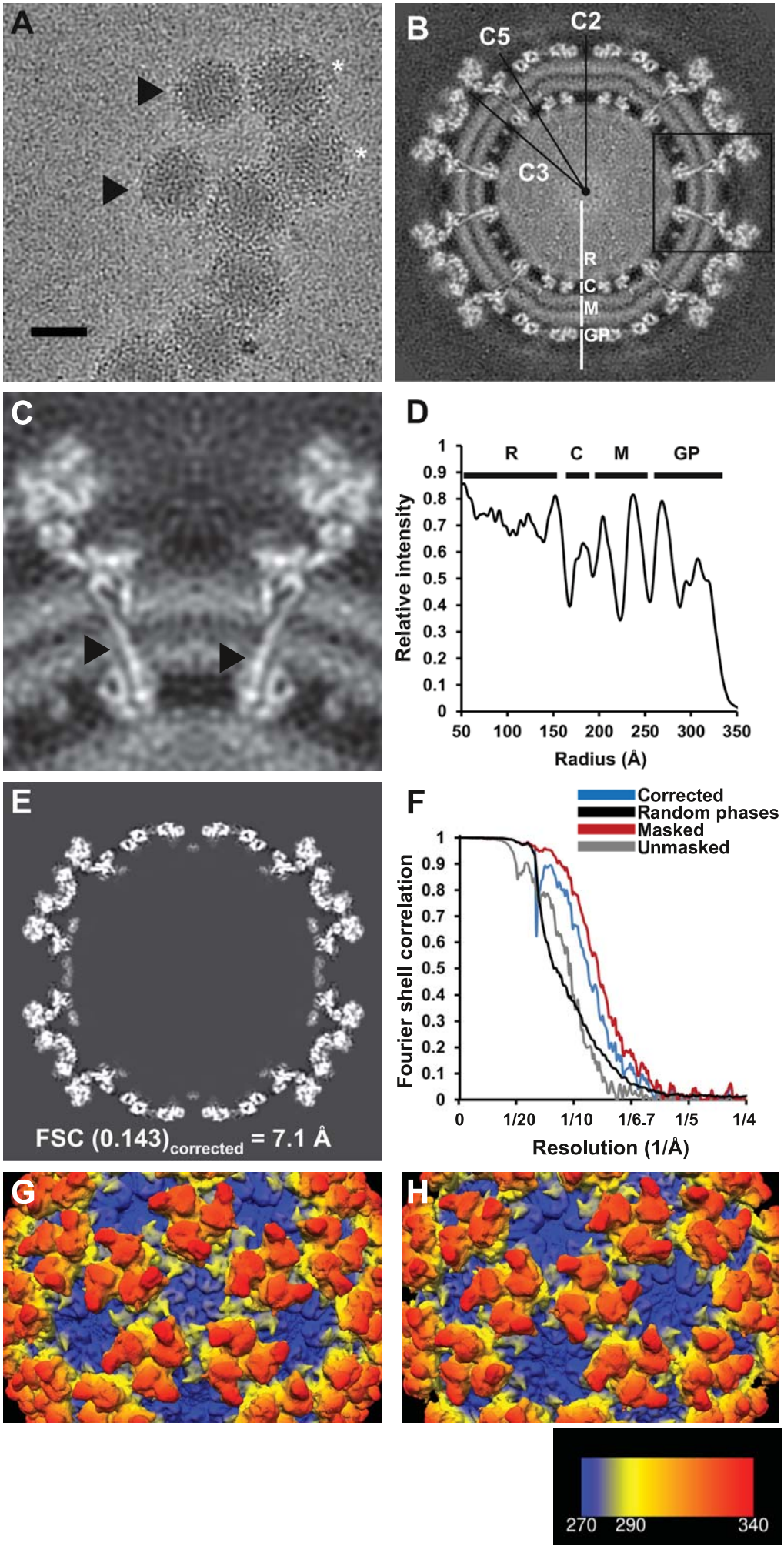
Most SFV particles had a slightly disordered appearance at the surface, which was presumably due to surface-bound DC-SIGN$_{ECD}$. Conversely, more stable-looking virions, but with an apparent slightly smaller size, likely corresponded to SFV particles with no DC-SIGN bound. An interesting observation was that the slightly disordered particles, unlike the more stable-looking particles, had a tendency to closely interact with each other (Figure 5.3 A). In the three-dimensional reconstruction of SFV–DC-SIGN complexes, secondary structure elements, such as transmembrane α-helices were apparent (Figure 5.3 B and C), and the glycoprotein shell of SFV refined to a resolution 7.1 Å (Figure 5.3 E and F). However, there was no striking indication about DC-SIGN binding at the virion surface, just by looking at the isolated structures and radial density profiles (Figure 5.3 B-J).

To have a more precise idea about DC-SIGN binding, the structure obtained here was filtered to 9 Å resolution and compared to the previously published SFV structure at 9 Å resolution [139]. Comparison of

viral particles to virus–DC-SIGN complexes, rendered at one standard deviation above the mean density threshold, showed that there is a small amount of extra density pointing into the inter-trimeric crevices in the SFV–DC-SIGN model, which is absent in the DC-SIGN-free SFV model (Figure 5.4 A and B) and may correspond to a DC-SIGN CRD domain. While this would corroborate the hypothesis that the DC-SIGN binding sites are indeed located within the intertrimeric crevices, the compared cryo-EM structures were reconstructed with different protocols, and therefore a definite conclusion with regards to DC-SIGN binding should not be drawn without comparison to a receptor-free SFV cryo-EM structure obtained by the same reconstruction protocol than for the SFV–DC-SIGN complex obtained here.

Nevertheless, to find out whether the size of the volume that is occupied by the putative DC-SIGN density observed in the SFV–DC-SIGN intertrimeric spike crevices would be realistic in terms of a fully detected DC-SIGN CRD domain, crystal structures of the closely related chikungunya alphavirus (CHIKV) E1/E2 glycoprotein complexes (PDB 2XFC, [187]) were fitted into the trimeric spikes of the SFV–DC-SIGN cryo-EM density map (Figure S9 B). The fitting of the CHIKV glycoprotein crystal structures was done in order to visualize a rough delimitation between viral glycoproteins and the putative DC-SIGN – derived densities. Subsequently, a sphere with defined radius was placed into a putative DC-SIGN–derived density of the SFV–DC-SIGN cryo-EM density map (Figure

S9 B). The volume of this sphere corresponded to ~4200 $Å^3$ (radius of 10 Å), whereas the volume of the DC-SIGN CRD crystal structure in complex with an oligosaccharide (PDB 2IT5, [189]) had a volume of ~17400 $Å^3$, as calculated by the VADAR software [190]. A sphere with a similar volume (~17200 $Å^3$ or radius of 16 Å) could not be placed into the putative DC-SIGN density (Figure S9 B). Although the DC-SIGN CRD cannot be expected to be fully spherical, it altogether appears that the CRD domain of $DC\text{-}SIGN_{ECD}$ in the SFV–DC-SIGN cryo-EM density map is present, but that it is probably not fully resolved. This is corroborated by the fact that the cryo-EM density map of SFV–DC-SIGN had to be rendered at a low density threshold of 1σ for the putative CRD density of DC-SIGN to be well visualized.


A
B
C5
C2
C3
R
C
M
GP
C
D
R
C
M
GP
Relative intensity
1
0.9
0.8
0.7
0.6
0.5
0.4
0.3
0.2
0.1
0
50
100
150
200
250
300
350
Radius (Å)
E
FSC (0.143)corrected = 7.1 Å
F
Corrected
Random phases
Masked
Unmasked
Fourier shell correlation
0
1/20
1/10
1/6.7
1/5
1/4
Resolution (1/Å)
G
H
270
290
340

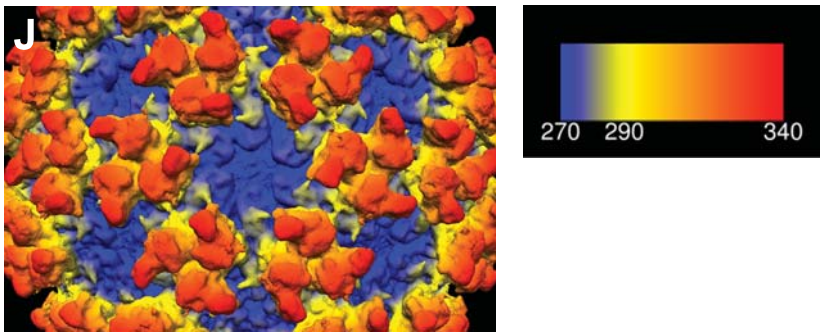


Figure 5.3. Icosahedral reconstruction of SFV - DC-SIGN$_{ECD}$ complexes.

A.) Two-dimensional projection image of SFV - DC-SIGN complexes filtered to 30 Å resolution and downsampled four-fold. Potentially receptor-free SFV particles are indicated by arrowheads. Asterisks indicate DC-SIGN bound forms of SFV. The scalebar is at 50 nm.

B.) 1.35 Å thick central slice of a three-dimensional B-factor sharpened SFV - DC-SIGN cryo-EM density map (2718 particles). C5, C3 and C2 = 5, 3 and 2-fold icosahedral symmetry axes, respectively. GP = viral glycoproteins and DC-SIGN, M = membrane, C = capsid, R = RNA and capsid core.

C.) Close-up view of the boxed area in B.), rotated by 90°. Alpha-helical domains are indicated by arrowheads.

D.) Radial density profile of the B-factor sharpened SFV - DC-SIGN three-dimensional reconstruction, as partly depicted in B.). GP = viral glycoproteins and DC-SIGN, M = membrane, C = capsid, R = RNA and capsid core.

E.) Same as in B.), but masked above a high density threshold and a particle radius higher than 230 Å.

F.) Fourier shell correlation (FSC) curves of the three-dimensional, unmasked SFV - DC-SIGN volume partly depicted in B.) ("unmasked"), the FSC of the masked SFV - DC-SIGN map in E.) ("masked"), and the FSC of the masked SFV - DC-SIGN map corrected for overfitting ("corrected"). The corrected FSC was determined by subtraction of an FSC determined by phase randomization of spatial frequencies higher than 14.8 Å ("Random phases") from the masked FSC.

G.) Close-up view of the non-postprocessed (unmasked and non - B-factor corrected) three-dimensional volume of SFV - DC-SIGN complexes (FSC (0.143) = 8.7 Å), rendered at 2σ above the mean (in UCSF Chimera), viewed along the icosahedral fivefold axis. The colour key indicates the particle radius in Ångstroms.

H.) Same as in G.), but along the threefold axis.

J.) Same as in G.) and H.), but along the twofold axis.

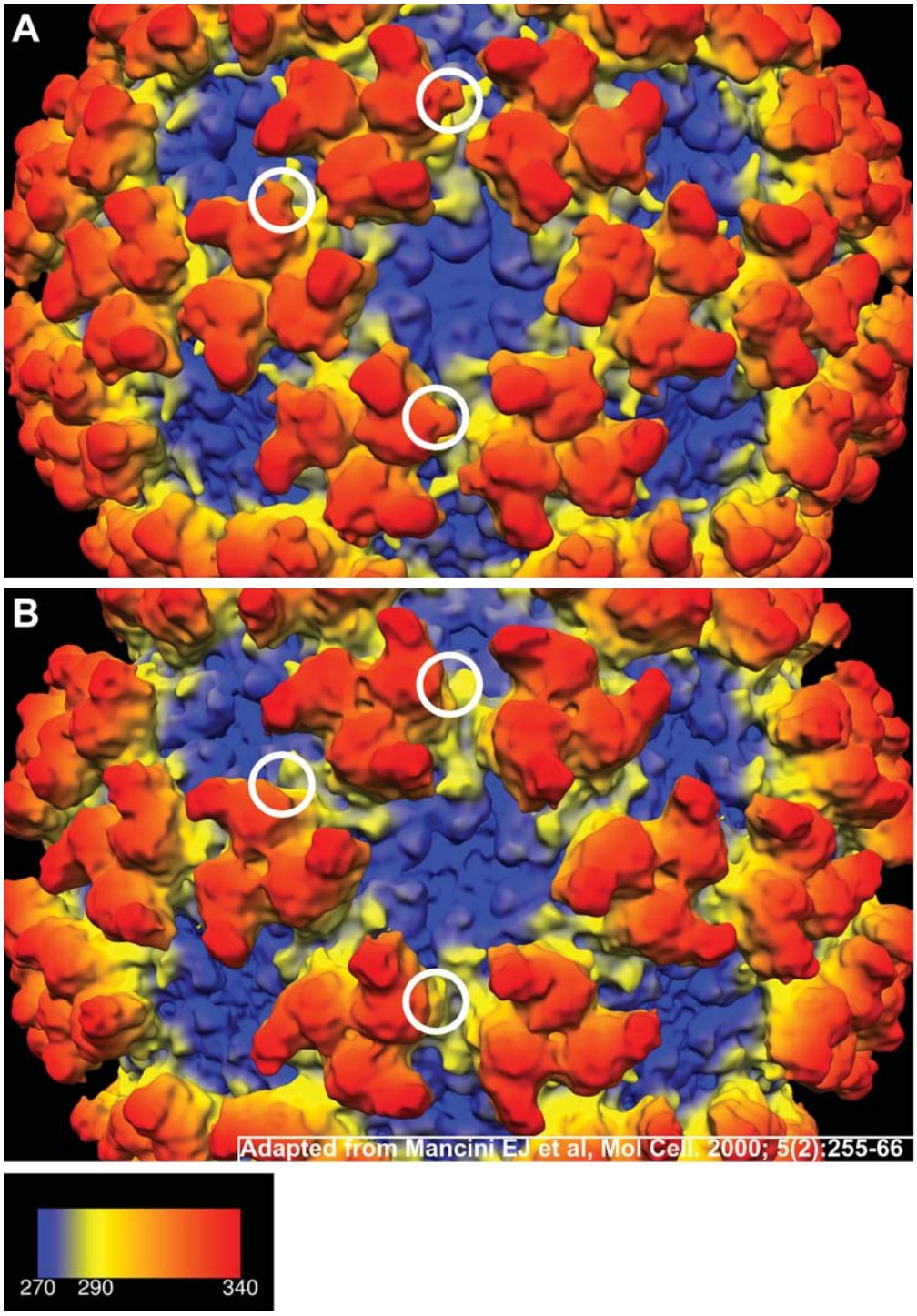


Figure 5.4. Comparison of SFV - DC-SIGN complexes with receptor-free SFV.

A.) Isosurface rendering of the non-postprocessed SFV - DC-SIGN complexes at 1σ above the mean (in UCSF Chimera). The densities potentially belonging to DC-SIGN, within the intertrimeric crevices, are encircled.

B.) Isosurface rendering of a previously published receptor-free SFV structure at 1σ above the mean (in UCSF Chimera). The SFV structure (EMDB-1015) is adapted from Mancini EJ *et al.* 2000, Mol Cell. 5(2):255-66. Note that there is no density in between the intertrimeric crevices, as indicated by circles, positioned in the same areas than in A.).

The colour code indicates radii from the centre of the three-dimensional volumes.

6. Discussion

6.1. Summary

One advantage of *in vitro* models over cell culture models for viral host cell entry is that they allow a more systematic determination of minimal factors required for certain intracellular processes that occur during virus entry. One such process is virus penetration from within intracellular compartments, which, for enveloped viruses, depends on lipid bilayer fusion catalysed by the viral fusion proteins. In that respect, many earlier studies have made use of purified viruses and non-cellular target membranes, resembling biological membranes in their lipid composition, to study viral membrane fusion. Virus groups studied include for example the alphaviruses, flaviviruses, orthomyxoviruses and rhabdoviruses [66, 77, 102, 191]. No such *in vitro* system has been established for any members of the medically relevant *Bunyaviridae* family, notable members of which include Hantaan virus, La Crosse virus, Rift Valley fever virus, severe fever with thrombocytopenia syndrome virus (SFTSV) and Crimean-Congo hemorrhagic fever virus. The main achievement in this thesis includes the development and application of an *in vitro* model for Uukuniemi phlebovirus (UUKV) fusion with liposomes, and constitutes the first *in vitro* model system for phlebovirus fusion. The obtained results highlighted the importance of both negatively charged and conical phospholipids in target membranes, as well as physiological temperatures in low pH mediated phlebovirus fusion. In addition, it was demonstrated

that the presence of target membranes is an essential component for the structural study of early bunyavirus fusion intermediates in native conditions. These results have far-reaching implications within the whole *Bunyaviridae* family, because with the help of the *in vitro* fusion system developed here, it is now possible to study potential fusion inhibitors, as well as fusion mutants, for example using bunyavirus reverse genetics systems [11]. Furthermore, due to the successful establishment of the UUKV-liposome fusion system in electron cryo-microscopy, it is now possible to study the structures of early bunyavirus fusion intermediates in native conditions.

The second outcome of this thesis is the significant advancement in the development of a structural model of alphavirus-receptor interactions. First, with the help of collaborators, it was possible to confirm the N-glycan composition of both Semliki Forest (SFV) virus glycoproteins E1 and E2 [50], (as well as Uukuniemi phlebovirus glycoproteins G_N and G_C [177]) by mass spectrometry, with the main outcome that N-glycans displayed at the virion surface need to be interpreted as predominant glycan species (*e.g.* a majority of high mannose or complex glycans with particular structures) within a whole spectrum of glycan species, rather than one single glycan species. Second, additional densities, possibly corresponding to at least a part of the DC-SIGN receptor, could be seen at the surface of SFV–DC-SIGN electron cryo-microscopy (cryo-EM) structures, as compared to previously published ligand-free SFV cryo-EM structures [185]. While this

was promising, a quantitative analysis of the DC-SIGN densities is still missing, and the possible caveat of DC-SIGN flexibility, causing significant loss of DC-SIGN derived densities at the surface of SFV, will need to be addressed in the future. On the other hand, the resolution obtained here (7.1 Å for the glycoprotein layer, using only 2,718 particles) has been the highest obtained yet with Semliki Forest virus, and promises the possibility of near atomic resolution with increased particle numbers.

6.2. Icosahedral reconstruction of phleboviruses in native conditions

The icosahedral reconstruction of unfixed UUKV particles proved to be unsuccessful with a likely cause of the problem lying in particle distortion causing particle heterogeneity, which in turn makes particle averaging using icosahedral reconstruction impossible. Previous studies already proposed that the icosahedral shape of UUKV may be susceptible to distortion, although ~40% of the particles had a preserved icosahedral symmetry [79]. Taking this into consideration, it was expected that class averaging of single UUKV particles would have separated the non-icosahedral from the icosahedral particles, and hence a significant percentage of icosahedrally shaped class averages could have been selected for angular reconstitution and icosahedral reconstruction. However, this attempt was unsuccessful and hence it was concluded that less than 40% of the particles had a stable icosahedral shape. The same conclusion was drawn by using a different software that uses unsupervised two-dimensional and three-dimensional classification of viral

particles. Last but not least, the icosahedral reconstruction procedure using class averaging was validated by successful icosahedral reconstruction analysis of the bacteriophage SSIP-1. In addition, using a different cryo-EM structure refinement software, the resolution of SSIP-1 could be improved to 11.1 Å resolution (9.5 Å for the capsid alone), as compared to the previously published SSIP-1 model (12.5 Å resolution, [150]). How can the increased UUKV particle stability in [79], as opposed to UUKV particles produced in this thesis be explained? The main difference in the sample preparation was that in [79], the virions were chemically fixed prior to ultracentrifugation, whereas no fixation was performed in this thesis. It is thus likely that the chemical fixation stabilized the icosahedral symmetry of UUKV, which protected the virions from distortion, presumably occurring due to high speed pelleting, to a certain degree. Altogether, this suggested that the employed UUKV concentration protocol by high speed pelleting in native conditions was detrimental, and that an optimized purification method was needed. Therefore, a new UUKV purification protocol that involved a low speed centrifugation step through a filter membrane, followed by virus particle purification via density gradient ultracentrifugation, was developed. Although the suitability of this purification strategy for electron cryo-microscopy was not tested by myself, others successfully obtained a native three-dimensional structure of UUKV at neutral pH by electron cryo-tomography and subtomogram averaging, giving a first impression of the native UUKV structure (addressed in the

next section). Next steps could include a fresh attempt of icosahedral reconstruction of UUKV particles obtained from the new purification protocol. However, the priority will clearly be to apply the same sample preparation approach to the medically more relevant, as well as structurally more stable phlebovirus Rift Valley fever virus (RVFV), because work at higher biosafety level in our containment laboratory has recently been approved. A similar virus purification protocol omitting pelleting steps was previously used with unfixed RVFV particles and led to a 2.7 nm resolution structure [146]. With a pelleting-free virus purification protocol and a high end electron microscopy setup, such as a 300 kV electron cryo-microscope and a direct electron detector, it may be possible to achieve sub-nanometer resolution with unfixed RVFV particles.

6.3. Low pH and phlebovirus fusion

6.3.1. Structural analysis of phlebovirus fusion at low pH

Recent data suggested that phleboviruses are icosahedral at both neutral and low pH [79], and that the neutral pH form has pointed spikes, whereas the low pH form (pH 6), has hollow spikes [79], much like Rift Valley fever virus at neutral pH [78, 145, 146]. In this thesis, raw electron micrographs, as well as two-dimensional analysis of spikes at both pH 7.4 and pH 5 did not support the neutral pH conformation presented in [79]. Furthermore, with the help of the improved UUKV purification protocol, colleagues were able to demonstrate in a three-dimensional UUKV structure, that UUKV particles at neutral pH indeed have hollow spikes (Dr. Juha Huiskonen and

Alessandro Caputo, unpublished results). Because in [79], the analyzed UUKV particles were chemically fixed, it could be speculated that the observed pointed spike conformation at neutral pH may correspond to a more membrane distal spike intermediate that has been captured by the fixative. More pointed surface glycoprotein conformations at neutral pH have recently been demonstrated in dengue virus, but at physiological temperatures [192], as part of a so-called “molecular breathing” mechanism. However, because the pointed spike conformation seemed to have been visible in most of the fixed UUKV particles studied at neutral pH [79], it seemed more likely that it was the fixative that caused this conformational change, and that exposure to pH 6, before fixation, may prevent this conformation from occurring at all, since the spikes at pH 6 were not pointy [79]. A biochemical analysis of phlebovirus protein–protein interactions at pH 5 and 6 versus neutral pH may provide a deeper insight into the conformational changes and/or changes in intermolecular glycoprotein interactions caused by low pH. Suitable approaches may include hydrogen-deuterium exchange mass spectrometry [193] of viral glycoproteins at low pH 5 and 6, as well as neutral pH.

Radial density profiles obtained in this thesis from the two-dimensional analysis of UUKV spikes of isolated particles at pH 5 versus pH 7.4 revealed a small conformational change that described a sub-nanometer (≤ 6 Å) radial outward shift of viral glycoprotein layer density at pH 5. Such small conformational changes in isolated virions at low pH resulting in

increased particle diameter have been previously observed in Semliki Forest virus at pH 5.9–6.2 [194]. As expected, this small shift was not directly visible in two-dimensional UUKV spike class averages at pH 5, as compared to those at pH 7.4. Importantly, a conformational change causing density shifts in the sub-nanometer range is unlikely to be descriptive for a full fusion event that merges two lipid bilayers (assuming 5 nm thickness for each lipid bilayer). Why were the observed changes not more substantial? The lack of significant conformational changes at low pH could be interpreted in two different ways. One possibility was that the observed particles at low pH, if they did not become part of the major aggregates that reproducibly formed in such conditions, were not responsive to low pH and thus not infectious. Another explanation was that the low pH-triggered exposure of the viral fusion loops would have been too short-lasting to be captured as a major conformation in electron cryo-microscopy, because it was thermodynamically unfavourable in absence of a hydrophobic interaction partner, such as a target lipid bilayer. In absence of lipid bilayers and at low pH, a virion would preferably interact with another virion (aggregation), or the activated fusion proteins would fold back onto the virion surface, as to hide the fusion loop from the aqueous environment as much as possible. However, this retraction would not lead to a conformation that is identical to the neutral pH form because the increased protonation state of the viral fusion protein would have changed the chemical environment and thus the non-covalent interactions

between the proteins. The radial profiles of UUKV spikes at pH 5 versus pH 7.4 were consistent with the latter interpretation, in that they were not strictly identical.

Together, these data highlight the fact, that in order to study the structure of fusion protein intermediates in the context of whole virus particles, the fusion event in itself needs to be reconstituted with all its components, which also includes the target membranes. Therefore, in the next step, electron cryo-tomography of UUKV at low pH and in presence of liposomes was performed. Elongated spikes, forming clusters that bridged the viral and target membranes, were observed, along with significant target membrane deformations and putative fusion/hemifusion intermediates. It is not clear, however, which pH threshold these UUKV fusion intermediates have. Interestingly, a recent electron cryo-microscopy study of Semliki Forest virus class 2 fusion, also demonstrated such elongated spike clusters in presence of liposomes [67]. Together with a recent report confirming that the phlebovirus glycoprotein G_c is a class 2 fusion protein [83], this is entirely consistent with a class 2 fusion mechanism for UUKV. In contrary to the study with SFV [67], the UUKV particles were heavily distorted, and the glycoprotein clusters were not as homogenous in size as for SFV, which meant that the only possible approach for a higher resolution three-dimensional analysis with the current experimental setup would be electron cryo-tomography, together with sub-tomogram averaging of locally ordered spikes. This requires the

presence of a sufficient number of fusion events in a particular stage of viral fusion, as synchronized as possible. To this end, the number of early fusion events needs to be improved, because the here described fusion events were rare, and most viral particles and liposomes were trapped in aggregates and/or located on the carbon film of the EM holey carbon grids. Pre-saturation of the holey carbon EM grids with liposomes, followed by application of the virus-liposome sample mixture could help to improve the yield of useful fusion complexes.

Another possibility to optimize the amount of fusion events, would be to screen for UUKV fusion intermediates at lower temperatures (given that UUKV is highly temperature dependent) and/or higher pH values (e.g. 5 < pH < 6), in order to limit low pH mediated aggregation. An alternative possibility would be the generation and use of fusion mutants that are arrested in a particular stage of fusion (which could now be tested using the fusion assay developed here). However, this would necessitate the use of phlebovirus reverse genetics with the appropriate prior knowledge on which glycoprotein residues to mutate, or otherwise, virus production in presence of mutagens, screening for isolates that show liposome binding but lack of lipid and content mixing. Another possible approach, although in absence of target membranes, would be the use of amphiphilic molecules that would stabilize hydrophobic fusion loops at low pH, without affecting the viral membrane. Such candidate molecules may for example be non-detergent sulfobetaines (NDSB's, [195]), which do not form

micelles and thus are not considered to be proper detergents. However, it will be absolutely necessary to determine how NDSB's affect the viral lipid bilayer. If the latter approach would prove to be feasible, icosahedral reconstruction of a stably icosahedral virus, such as Rift Valley fever virus, and thus high resolution information of specific fusion intermediates could be a possibility.

6.3.2. *Phlebovirus* fusion

Before the visualization of phlebovirus fusion complexes at low pH was attempted in electron cryo-tomography (as described in the previous section), it was first necessary to find the minimal requirements for fusion to take place *in vitro*. All that was known beforehand was the fusion permissive pH threshold of UUKV fusion forced at the cell surface (fusion-from-without, [55]). Although this parameter was a useful contribution to the current idea that UUKV is a late penetrating virus [55, 61, 98], the conditions in which this was tested were not physiological. Also, it was not clear whether the fusion threshold determined was entirely dependent on the virus glycoproteins, or also dependent on certain properties found at the plasma membrane (*e.g.* expression of the viral receptor, presence of cell surface glycans, lipids, and proteins). UUKV infection requires endocytosis and traffic to late endosomal compartments, and the chemical environment is quite different at the cell surface from what it is in late endosomes. In [55], the cells were heavily overloaded with UUKV (a multiplicity of infection of ~1,000 was used), which would mean that,

according to the here estimated particle-to-ffu ratio of ~1/500, a few hundred thousand particles per cell would have been present. In such conditions, the ratio of nuclei to number of cells after low pH treatment was still only about 0.5 [55]. This means that fusion-from-without with UUKV is extremely inefficient.

In addition, the host cell entry of UUKV particles is believed to be inefficient, with only ~25% of cell surface bound particles (about 7–9% of input particles bind at the cell surface) entering the host cells [55]. Theoretically, this would mean that only ~2% of the virions that cells are exposed to, get internalized. Therefore, in order to be successful, UUKV fusion in late endosomes could be expected to be more efficient than observed with the fusion-from-without experiment. This in turn means that there must be host cell factors present in the late endosomes, different from low pH, that are capable of increasing the efficiency of UUKV fusion. Because the target membrane in a fusion event is as important as the donor component (the virion), one idea was to test which lipid species were required in the target membrane to allow efficient fusion.

In this thesis, I adapted the so-called pyrene excimer fluorescence assay [123] to phleboviruses, using Uukuniemi virus as model system for phleboviruses, and Semliki Forest virus (SFV, family *Togavirus*) as an established control system with known lipid and low pH requirements. Because the pyrene excimer assay only monitors lipid mixing and not content mixing, UUKV-induced content release from target compartments

was measured by using liposomes that encapsulated a quenched concentration of the hydrophilic dye sulforhodamine B (SRB) [66, 196]. Content mixing leads to transfer of SRB into the virus lumen, which dilutes the dye and thus reads as a fluorescence intensity increase of the dye (de-quenching). The data obtained here confirmed that the phospholipid BMP significantly enhances lipid mixing, and that this is most likely due to the increased fusogenicity of the target membrane, due to the overall shape and negative charge of the phospholipid BMP, rather than a specific requirement for BMP. The evidence for this was that lipid mixing is also facilitated in presence of phosphatidylglycerol (PG) and phosphatidic acid (PA), both of which are negatively charged and conical, but not if only phosphatidylethanolamine (PE) and phosphatidylcholine (PC) were present. In contrast to SFV lipid mixing, no lipid mixing could be observed for UUKV in presence of both sphingomyelin and cholesterol. The lack of observed lipid mixing in presence of PC:PE liposomes, together with the observation that in electron micrographs containing PC:PE liposomes and UUKV at pH 5, early fusion intermediates, such as elongated spikes and target membrane deformations (dimples and potential hemifusion intermediates) were almost equally well visible than in presence of BMP, raised the question about whether UUKV may be held in a restricted fusion intermediate (RH), similarly to dengue virus [59], and that the presence of negatively charged lipids would mediate the release UUKV from this state and progression towards lipid mixing. Chlorpromazine is

able to make RH intermediates progress into the lipid mixing stage in absence of permissive phospholipids, as shown with dengue virus [59], therefore a similar experiment with UUKV could help in validating the RH hypothesis.

In preliminary experiments, both Bunyamwera virus (BUNV, genus *orthobunyavirus*) and UUKV had similar lipid mixing profiles at pH 4.5, indicating that the fusion mechanism might be conserved between bunyavirus genera. On the other hand, earlier studies on orthobunyavirus entry proposed penetration from early endosomes [91], based on the lack of infection inhibition in presence of the expression of dominant-negative Rab7 (blocks the maturation towards late endosomes) and a fusion threshold at pH 6.3 (La Crosse virus, [197]), compatible with early endosomes rather than late endosomes. To my knowledge, there have been no studies addressing the detailed fusion mechanism of Bunyamwera virus, except for [198], in which fusion at the cell surface was performed at pH 5.3. More studies are therefore needed to fully establish a possible link between the fusion mechanism of phleboviruses and certain orthobunyaviruses.

UUKV lipid mixing efficiency at pH 5 depended on the species of the anionic lipids tested, with virtually no lipid mixing observed in presence of phosphatidylserine (PS), followed by increasing lipid mixing with phosphatidylglycerol (PG), BMP and phosphatidic acid (PA) with highest amounts of lipid mixing. Importantly, dengue virus lipid mixing did not

differentiate between PS, PG, or BMP [59]. While a slightly different lipid composition was tested here (phosphatidylethanolamine (PE) was absent in the dengue virus study, where only phosphatidylcholine (PC) and negatively charged lipids were tested), this cannot fully account for the observed differences in UUKV lipid mixing to the different negatively charged phospholipids, because PE was present at the same concentrations in all liposomes tested. It follows that the fusion mechanism between DENV and UUKV may not be entirely similar, and both viruses would need to be tested in parallel to confirm similarities and differences. The main discrepancy, however, is the virtual absence of UUKV lipid mixing in presence of PS at late endosomal pH 5, which at the same time, seems to be important for flavivirus penetration, in that PS is believed to be flipped into luminal membrane leaflets caused by virus triggered calcium release into the cytosol [199]. It is not clear yet what the cause of this discrepancy could be, and such a calcium release mechanism has not been demonstrated for phleboviruses, and to my knowledge, not for any other bunyavirus. However, UUKV, as well as BUNV lipid mixing with PS-containing membranes was observed at lysosomal pH 4.5, and therefore a possible role of PS in UUKV fusion cannot be fully excluded. Although UUKV has been observed to co-localize with the late endosomal and lysosomal marker LAMP-1 [55], penetration from lysosomes seems rather unlikely because of the high protease activity within these compartments, possibly causing UUKV fusion glycoprotein inactivation. Except filoviruses,

due to their requirement for Niemann-Pick-type1 receptors [65] and glycoprotein cleavage by cathepsin cysteine proteases [64], both components of which are found in late endosomes and lysosomes [200], to my knowledge, no other viruses could be real candidates to penetrate cells from within lysosomes. Although recent data on SFTSV (severe fever with thrombocytopenia syndrome virus, genus *Phlebovirus* of the family *Bunyaviridae*) entry showed a potential dependence on serine protease activity (but not on certain cathepsin cysteine proteases, [172]), no such requirements could be confirmed yet for UUKV. On the other hand, blocking the v-SNARE VAMP3 (an eukaryotic fusion protein that has been proposed to be mediate fusion between late endosomes and autophagosomes [99]) prevents UUKV co-localization with the late endosomal/lysosomal marker LAMP-1 and infection [98]. Altogether, this means that there is no clear evidence that either proves or disproves UUKV entry from lysosomes (as opposed to late endosomes), and more experiments are needed to address this possibility, in connection with a possible effect of UUKV on the intracellular calcium concentration and phosphatidylserine distribution.

One possibility for the differential UUKV usage of negatively charged phospholipids, as opposed to dengue virus, might be a different binding affinity towards the different negatively charged phospholipid species involved. Flaviviruses were shown to bind phosphatidylserine [199], and preliminary experiments using UUKV binding to commercially available

lipid strips (onto which different lipid species, including PS, PG and PA, were spotted) showed that only cardiolipin, a mitochondrial phospholipid, but not PS, PG or PA, seemed to significantly bind to UUKV (Figure S10 A). This was promising because the headgroup of cardiolipin is structurally related to the BMP headgroup [201], but it does not explain why lipid mixing with liposomes containing PA is as efficient as lipid mixing with liposomes containing BMP. In preliminary experiments, possible binding to BMP in the context of a functional lipid bilayer (liposomes), using ultracentrifugation over linear sucrose gradients, could not yet be confirmed, because the results were not yet reproducible (Fig. S10 B to E). Due to the fact that a low density UUKV-free liposome band was detected in the sucrose gradient flotation assays (Fig. S10 C to E), it was speculated that the liposomes, in combination with the high sucrose concentrations possibly causing osmotic shock, were too unstable to withstand the high forces acting on them during ultracentrifugation. These liposomes either would have incorporated high density sucrose from the bottom of the tube which prevented them from floating to the top, or the centrifugation may have caused fusion between UUKV particles and liposomes, forcing the viral fusion proteins into a conformation that cannot be recognized anymore by the anti-UUKV antibody. The latter case is unlikely, because UUKV could still be detected in denser fractions different from the bottom fraction. In any case, however, there is a possibility that BMP containing liposomes are too unstable for the flotation experiments,

which may be due to the absence of cholesterol, which in turn is believed to render lipid bilayers more sturdy and has been used in previous virus–liposome flotation assays that have been performed with enveloped viruses [202, 203]. Therefore, the next steps in testing the binding hypothesis would be to repeat the flotation assays, using both negatively charged phospholipids and cholesterol in the target membranes, as well as using gradient media less likely to cause osmotic shock (*e.g.* Nycodenz). If successful, UUKV binding to liposomes containing phosphatidylserine will also be tested. If the binding hypothesis (lower amount of fusion because of lower amount of virus-liposome binding) proves to be wrong, then the possible discrimination in which negatively charged lipids are used in UUKV fusion may lie in downstream fusion events, such as lipid mixing. This, however, might challenge the RH hypothesis in UUKV fusion, because no preference for certain negatively charged lipid headgroups was shown in dengue virus fusion [59].

The lipid mixing threshold at low pH with BMP-containing membranes was determined to occur at pH ~5.6, which is compatible with late endosomal pH and reasonably consistent with the previously established fusion threshold of pH 5.4, as determined by fusion-from-without [55]. In addition, it was established that lipid mixing at room temperature was almost half as efficient as lipid mixing at 37 °C. Interestingly, orthobunyavirus fusion is also highly temperature-dependent [197], thus suggesting another similarity in orthobunyavirus and phlebovirus fusion. SFV lipid mixing is

temperature sensitive as well [204], whereas tick borne encephalitis virus (TBEV, *Flavivirus*) lipid mixing at physiological and room temperature appears more or less identical [77]. It is tempting to speculate that the reason for increased temperature dependence in alphavirus and bunyavirus fusion, as compared to flavivirus fusion, lies in the presence of more prominent accessory proteins to the fusion proteins in mature alphaviruses (glycoprotein E2, [187]) and bunyaviruses (glycoprotein G_N [205]), as compared to flaviviruses (small protein M [108]). These accessory proteins may form more extensive interaction surfaces with the fusion proteins, and thus may cause a higher energy barrier for conformational changes in low pH dependent fusion in the alphavirus E1 and bunyavirus G_C glycoproteins (which could lie in *e.g.* heterodimer dissociation), and the necessary energy would be provided by the elevated physiological temperatures.

Low pH pre-treatment of UUKV particles, in contrary to SFV, did not alter lipid mixing activity towards liposomes, whereas UUKV infectivity was decreased substantially, but incompletely. This means that low pH exposure of UUKV in absence of target membranes does not lead to its complete inactivation, demonstrating an extraordinary resilience towards environmental constraints, such as sudden pH variations, and thus premature inactivation. The results further suggest that the bulk of the low pH-mediated loss of infectivity is rather due to an entry step that is upstream or downstream of lipid mixing, because lipid mixing itself does

not seem to be affected. Affected steps might include fusion pore formation and expansion, or receptor binding at the cell surface. Earlier studies showed that low pH pre-treatment of SFV leads to a loss of liposome binding [206]. As expected, this also leads to loss of fusion capacity [204, 206], which later turned out to be partially reversible under certain conditions (at pH 5.5 [168]), but not in this thesis (1h low pH treatment of SFV). My lipid mixing inhibition experiment with SFV-pyr, conducted at pH 5, and showing almost complete lipid mixing inhibition, demonstrates that the inhibition seems to depend either on the length of the incubation time at low pH, or the specific pH tested, or both. Consistently, earlier studies showed that low pH pre-treatment of SFV also leads to a complete loss of infectivity [207]. Low pH treatment also leads to loss of tick-borne encephalitis virus (TBEV) binding to liposomes [203], as well as Rift Valley fever virus infectivity [208], although in the latter case, the loss of infectivity was incomplete, and in fact even less substantial than tested for UUKV here, possibly because the low pH pre-treatment protocols were slightly different. To my knowledge, there is no study that tested TBEV infectivity after low pH pre-treatment, however, the infectivity of flavivirus hepatitis C virus (HCV) was unaffected by low pH pre-treatment [167]. Altogether, my results indicate that phleboviruses seem to be among the most low pH-resistant (in absence of target membranes) viruses tested so far. Because BMP-containing liposomes did not fuse with BMP-free liposomes, unspecific fusion appears unlikely.

However, it cannot yet be excluded that BMP-containing liposomes may fuse with inactivated virions, and one possible approach may be to repeat the low pH inactivation experiment with SFV in presence of sphingomyelin, cholesterol and BMP, altogether.

UUKV-mediated content release from SRB-labelled target membranes was extensive, which suggested that fusion may be leaky. This was confirmed by control experiments, measuring the fluorescence emission of liposomes with same amounts, but different concentrations (in encapsulating liposomes) of SRB in the quenched state. In fact, the results suggested that all of the observed SRB dequenching corresponded to leakage from the liposomes rather than content mixing, and that the currently used conditions would not allow the detection of content mixing in absence of leakage. Therefore, the content mixing assay requires optimization, such that at least a small amount of content mixing could be demonstrated. Possible approaches may include for example the use of other compounds than SRB, to be used for the readout of content mixing. For example, UUKV nucleoprotein digestion by proteases (*e.g.* trypsin) could be exploited, in which low pH would trigger UUKV fusion with trypsin-encapsulating liposomes, causing nucleoprotein digestion only if fusion pore opening was successful. A similar assay was performed earlier with SFV, in which fusion to trypsin-encapsulating liposomes caused SFV capsid protein digestion [54].

While fusion assays in bulk are useful to study basic principles in virion fusion, such as pH, requirements of certain chemical compounds, or temperature dependence, there are also limitations. The most obvious limitation is the bulk nature itself, which means that all apparent fusion kinetics observed are only an averaged representation of possibly largely unsynchronized fusion events. This prevents the detailed analysis of individual viral fusion events, or the simultaneous tracking of individual fusion events. The importance of this lies for example in tracking the true lipid mixing and content mixing kinetics, such as possible lag times between lipid mixing and content mixing, which is only possible at the single particle level. Such studies have been conducted previously with other low pH dependent viruses, such as vesicular stomatitis virus and influenza virus, by using total internal reflection microscopy [156, 191]. Now that it is known which lipids are needed to observe UUKV (and BUNV) lipid mixing, such a fusion assay can now also be established with a bunyavirus.

6.3.3. Physiological analysis of phlebovirus fusion

From the *in vitro* fusion experiments conducted in this thesis, the late endosomal phospholipid BMP has emerged as a possible candidate that directs UUKV fusion from within late endosomes. The next step was to test this hypothesis in a cell culture based system. Because BMP is mainly located within intraluminal vesicles (ILV's) in late endosomes/lysosomes [22, 23, 209], the most likely scenario is that once UUKV reaches late

endosomes, it fuses with one or multiple ILV's. The hybrid ILV/UUKV complex would then fuse with the limiting endosomal membrane, for example as part of a physiological ILV recycling pathway (ILV back-fusion). ILV recycling is believed to be used for example for mannose-6-phosphate receptor and MHC class 2 receptor recycling [16]. UUKV would thus hijack the BMP-rich ILV's in late endosomes to deliver its genome into the cytosol. A similar mechanism has been proposed for both vesiculoviruses and flaviviruses [101, 199].

The idea was therefore to deplete cellular BMP in late endosomes with the help of an anti-BMP antibody [26, 101], and to test UUKV infection in the antibody treated cells versus untreated cells, using a previously established fluorescence activated cell sorting (FACS) protocol [55], that detects viral replication as a readout for infection. A similar approach, using fluorescence microscopy rather than FACS, was successfully used for testing the requirement of BMP in VSV infection [101]. Unfortunately, UUKV infection inhibition could not be observed in presence of the anti-BMP antibody. The anti-BMP antibody seemed to have been functional because it remained associated with treated cells after the antibody treatment, as shown in chapter 4 by immunodetection against the anti-BMP antibody, whereas the isotype control antibody could not be detected. However, it was not checked if the anti-BMP antibody indeed localized to late endosomes/lysosomes. Although BHK-21 cells were used both in this thesis and in the earlier studies involving VSV infection

inhibition with the anti-BMP antibody at the same concentrations [101], a fluorescence microscopy analysis will be indispensable in confirming the functionality of the anti-BMP antibody in the currently used experimental system. In addition, the experiment will need a positive control for infection inhibition (such as VSV or VSV-G pseudotyped viruses). Unfortunately, the enzyme producing BMP is not known, and therefore, siRNA knockdown experiments with regards to BMP synthesis may not yet be an equally specific alternative to the usage of anti-BMP antibodies.

In order to test the hypothesis whether BMP-rich late endosomal ILV's (early endosomal ILV's do not have BMP [209]) may play a role in phlebovirus entry, a different approach may consist in investigating other factors that are important in endosomal intraluminal vesicle (ILV) formation and ILV back-fusion to the late endosomal limiting membrane. Other factors that regulate the ILV pathway include for example the ESCRT (endosomal sorting complex required for transport) complexes and a protein called Alix [16, 164, 209]. Interestingly, recent studies using siRNA knockdown against ESCRT complexes (which are important in ILV formation) pointed out the importance of the ILV/ESCRT pathway in nairovirus (*Bunyaviridae* family) entry, although the importance of BMP was not examined [97]. UUKV entry was earlier shown to be inhibited by Wortmannin [55], a drug that inhibits PI3-kinase activity, which in turn is important for ILV formation [209]. siRNA knockdown of Alix, another protein thought to regulate ILV formation and back-fusion, has been

shown to drastically reduce the amount of BMP in treated cells, and successfully blocked vesicular stomatitis virus (VSV) infection [164]. Therefore, testing UUKV infection of cells treated with siRNA against Alix may be an interesting future alternative to using anti-BMP antibodies. Interestingly, charged multivesicular body protein 6 (CHMP6), also known as Vps20, which is part of the ESCRT-III complex that is responsible for vesicle scission into endosomal compartments [210], was identified as a hit in a previously conducted UUKV entry screen [98]. Unfortunately, this hit could not yet be validated by an independent screen or inhibition experiment. In summary, and together with the fact that transport of phleboviruses to late endosomes is a requirement for infection [98], there is already potential evidence for the importance of the ILV pathway in phlebovirus entry from late endosomes, however more detailed studies are needed to fully confirm and characterize this, including the role of BMP.

6.4. Arbovirus-receptor interactions at the cell surface

6.4.1. DC-SIGN interactions with Semliki Forest virus

As confirmed by collaborators [50, 177], it is now clearly established that both high mannose and highly processed glycans are present at the surface of both SFV and UUKV produced in mammalian cells. Both SFV E2 and UUKV G_C have a majority of highly mannosylated glycans, whereas SFV E1 and UUKV G_N mostly have complex glycosylation. Consequently, a possible high mannose glycan–DC-SIGN interaction may

not just be important during the first contact of DC-SIGN expressing cells with arthropod-derived virions, but also during later stages, after the primary infection has taken place, which may be critical for the sustainment of the infection directly after an arthropod bite, by hijacking DC-SIGN. Another stage may be the infection in the liver. A high mannose glycan binding relative of DC-SIGN called L-SIGN (or DC-SIGNR) is expressed in the liver [39] and together with the fact that the liver can be severely affected during both phlebovirus [9] and alphavirus [211] infection, L-SIGN may represent an important target in the infection cycle of these viruses. Accordingly, SFV pseudotypes have been shown to bind L-SIGN [43], and is no far-fetched idea that phleboviruses may be able to bind L-SIGN as well [212].

To characterize the DC-SIGN binding at the virion surface at high resolution, it was chosen to perform electron cryo-microscopy and icosahedral reconstruction of virus-DC-SIGN complexes, using the whole DC-SIGN ectodomain. UUKV was not used here because of particle heterogeneity in the preparations, making it unsuitable for icosahedral reconstruction at this point, although sample improvement, as partially attempted in this thesis by skipping UUKV pelleting steps, may change this in the future. In contrast, high resolution icosahedral SFV structures have been published previously [139], and therefore SFV seemed like the ideal (and available) candidate virus to analyze the DC-SIGN/virion interaction in a first step.

Two-dimensional projection images clearly showed that there was a supplementary compound, presumably the DC-SIGN ectodomains, binding at the surface of SFV virions, causing the virions to look less regular and to closely interact, whilst other particles in the same preparation, appearing slightly smaller and more regular, presumably because no DC-SIGN was bound, did rather not engage in such close interactions. Consistently, earlier published SFV projection images also looked more regular than the presumed DC-SIGN bound particles here [139]. Because the large majority of particles seemed to have DC-SIGN bound at the surface, it came as a surprise that in the three-dimensional model, only a rather small density, not too far from the noise level and pointing into the crevices between the trimeric spikes, could be observed. This small density was not observed in the previously published ligand-free SFV structure [139]. Although the observed extra densities in the SFV–DC-SIGN complexes were seen at the positions where they were expected (in the intertrimeric crevices where the high-mannose N-glycans are located [50]), it will be necessary to produce a difference map between DC-SIGN bound SFV and receptor-free SFV reconstructed by the same protocol, in order to identify the real extent of possible DC-SIGN derived densities. In addition, the SFV–DC-SIGN structure refined to a quite high resolution of 7.1 Å from a relatively small number of particles (2718 particles), which is most probably due to the use of a direct electron detector. Therefore, future studies promise SFV structures approaching

near atomic resolution, and it can be expected that this will be achieved by averaging more SFV particles.

Similar studies performed on dengue virus–DC-SIGN complexes showed a clearly distinct surface density appearing in the presence of the DC-SIGN carbohydrate recognition domain (CRD) [119]. Why has this not been achieved here? There could be several reasons as to why the DC-SIGN density on SFV was not well visible. First, one could argue that the DC-SIGN would not bind the SFV particles efficiently. However, based on the disordered extra density found at the SFV surface, together with the fact that the expressed DC-SIGN proteins seemed functional (they bound UUKV in ELISA), inefficient binding seems rather unlikely. In any case, ELISA, as conducted for UUKV, should be performed with SFV, produced both in insect cells and mammalian cells, to confirm that DC-SIGN binding to SFV was indeed efficient. A second, more likely possibility was, that the DC-SIGN bound at the virion surface was too disordered to be averaged using icosahedral reconstruction. The icosahedral averaging may have led to the complete loss of the flexible DC-SIGN$_{ECD}$ neck density in the three-dimensional map. However, what could have caused the almost complete disappearance of the CRD (carbohydrate recognition domain) part of the DC-SIGN$_{ECD}$ at the SFV surface, is unclear. It could have been that the orientations of the CRD bound to the highly mannosylated N-glycans at the virion surface were too heterogenous. The N-glycans would present themselves to DC-SIGN in a lot of different conformations, possibly

causing the DC-SIGN to adopt heterogenous orientations with respect to the virion surface as well. On the other hand, this also may have been the case in the dengue virus study [119]. A possible scenario leading to increased detection of DC-SIGN CRD's in the latter study could have been that the free CRD's, because their orientation was not restricted by a possible boundary to DC-SIGN tetramers, adopted a more uniform, preferential conformation at the virion surface when binding the N-glycans.

Another factor, possibly causing variability in glycan binding site occupancy may be the lower amount of GlcNAc2Man6-9 (GlcNAc = N-acetylglucosamine, Man = Mannose, referring to the N-glycan structure) species on SFV produced in BHK cells, as opposed to SFV produced in insect cells [50]. GlcNac2Man6-9 species are stronger DC-SIGN ligands than N-glycans containing lower amounts of mannose (*e.g.* GlcNac2Man3-5) [171]. Therefore, one attempt in electron cryo-microscopy and icosahedral reconstruction, using insect-derived SFV and DC-SIGN$_{ECD}$ could be tried, followed by the optimization of neck-free DC-SIGN$_{CRD}$ expression.

Because the CRD fragment without any neck repeats appeared unstable, even directly after secretion into the cell culture supernatant, and because it bound UUKV with almost negligible affinity in ELISA, it was concluded that the construct may not be functional. This may need to be confirmed by testing even higher DC-SIGN$_{CRD}$ concentrations (*e.g.* concentrations in the mM range). Alternatively, the CRD may be used as bottom of the

sandwich in the ELISA assay, instead of UUKV. This would cause the CRD's to form glycan arrays at the bottom of the plates, thus causing a "pseudo-multimeric" effect of the CRD, which in turn would allow an avidity effect (increased affinity by multimeric interaction). UUKV could then be detected by anti UUKV antibodies. In fact, a similar approach was done for dengue virus [119]. In a second step, the stability of the CRD needs to be improved, which may be achieved by appending amino acids to the N-terminus of the CRD, which seems to be unstable (because double bands were detected in western blot using anti-hexahistidine antibodies), or by just switching the hexahistidine tag from the C-terminus to the N-terminus. In fact, the CRD expressed in [119] had an undefined N-terminal appendage, which may have helped in the stabilization of the CRD. If an SFV–DC-SIGN structure could be obtained, the next step would be to try the same approach with Rift Valley fever virus, the only bunyavirus for which icosahedral reconstruction in native conditions has worked so far.

6.4.2. Future search for other phlebovirus receptors

Because phleboviruses, including UUKV, can infect a lot of different cell types that do not express DC-SIGN [55], it is evident that DC-SIGN cannot be the only receptor for phleboviruses. The usual approach towards finding potential interactions at the cell surface include screening methods, such as siRNA knockdown screens, chemical inhibitors, or microarrays. However, such screens and ongoing pursuits are long-term projects on their own and were outside the scope of this thesis. The "promiscuous"

nature of phleboviruses in terms of host cell usage predicts that a wide variety, or widely expressed cell surface receptors may be used, which also brought up the question about whether protein–lipid interactions at the cell surface may play a role in phlebovirus entry. Recent data highlighted the importance of phosphatidylserine in virus membranes for virus entry, including for example vaccinia virus, Ebola virus and dengue virus [122, 213, 214]. Important cellular receptors that are capable of binding phosphatidylserine on virions and thus enhancing infection are the T-cell immunoglobulin and mucin (TIM) receptors 1 and 4 [122, 214]. TIM-1 and TIM-4 are expressed on different, but altogether a broad selection of host cell types, which also includes macrophages and epithelial cells [215–217]. Furthermore, phosphatidylserine has been found in UUKV membranes [218], although it is not clear which membrane leaflet contains it. To test a potential phlebovirus–TIM4 interaction, collaborators kindly provided me a purified hexahistidine tagged TIM-4 ectodomain. The TIM-4 protein was tested in ELISA for binding to UUKV particles, analogously to DC-SIGN earlier in this chapter. The data showed that TIM-4 could be a potential ligand for UUKV (Figure S11), however the binding seems rather weak, and the result is preliminary. More experiments are needed to establish the potential role of TIM-4 more firmly, which may also include recombinant expression of the full-length protein in cells, followed by binding and infection studies using different bunyaviruses. Of course, the binding of TIM-4 will also be tested on SFV, bearing in mind a potential for

high resolution in electron cryo-microscopy. However, also here, a possible caveat might be binding site heterogeneity, in the sense that the binding sites at the surface of SFV may not be exposed symmetrically, or used equally well.

6.5. Concluding remarks

In conclusion, this thesis has shown that phlebovirus fusion is selective in the target membrane lipid composition, temperature, as well as low pH threshold and confirmed that target membranes are essential components in the structural study of viral fusion intermediates in the context of whole virions. As the importance of lipids in viral infection is increasingly acknowledged within the field of virus–host interactions, the results in this thesis contributed to highlighting their importance in phlebovirus fusion. Another potential virus–lipid interaction in phlebovirus entry, namely a possible phosphatidylserine receptor (TIM-4)–phlebovirus interaction, has emerged as an attractive novel candidate virus–host interaction to be explored in more detail in the future. Viral lipid–receptor interactions at the cell surface seem to be a widespread virus–host interaction among enveloped viruses [122, 213], and may hold the promise of becoming a broadly distributed target that may be exploited to inhibit viral host cell entry of several medically important viruses at once. Similar broadly distributed virus–host interactions, shared by multiple virus families, include glycan–lectin interactions, such as those mediated between DC-SIGN and highly mannosylated N-glycans on viral glycoproteins.

Preliminary results obtained here through studying alphavirus–DC-SIGN structures in the context of whole virions showed that these interactions can be directly visualized in electron microscopy and assigned to specific surface glycoproteins in enveloped icosahedral viruses with more than one major glycoprotein at the virion surface. I am confident that the electron cryo-microscopy of alphavirus–DC-SIGN interactions will be optimized in the future, and that it will be possible to apply a similar approach to phleboviruses, which will ultimately help in defining the location of the viral glycans used in phlebovirus–DC-SIGN interactions.

This thesis lays an important foundation for future research avenues in phlebovirus and perhaps bunyavirus entry. Although the results obtained here have brought up a lot of new questions, it will be the addressing of these questions in future more in-depth studies, including the structural and cell biology of bunyavirus fusion, as well as the structural biology of phlebovirus-receptor binding, that will hopefully give the answers necessary to combat phlebovirus infection more efficiently.

7. References

1. Elliott RM: **Molecular biology of the Bunyaviridae.** *J Gen Virol* 1990, **71 (Pt 3)**:501–522.

2. Walter CT, Barr JN: **Recent advances in the molecular and cellular biology of bunyaviruses.** *J Gen Virol* 2011, **92**(Pt 11):2467–84.

3. Krautkrämer E, Zeier M, Plyusnin A: **Hantavirus infection: an emerging infectious disease causing acute renal failure.** *Kidney Int* 2013, **83**:23–7.

4. Prins M, Goldbach R: **The emerging problem of tospovirus infection and nonconventional methods of control.** *Trends Microbiol* 1998, **6**:31–5.

5. Sidwell RW, Smee DF: **Viruses of the Bunya- and Togaviridae families: potential as bioterrorism agents and means of control.** *Antiviral Res* 2003, **57**:101–11.

6. Garigliany M-M, Bayrou C, Kleijnen D, Cassart D, Jolly S, Linden A, Desmecht D: **Schmallenberg virus: a new Shamonda/Sathuperi-like virus on the rise in Europe.** *Antiviral Res* 2012, **95**:82–7.

7. Yu X-J, Liang M-F, Zhang S-Y, Liu Y, Li J-D, Sun Y-L, Zhang L, Zhang Q-F, Popov VL, Li C, Qu J, Li Q, Zhang Y-P, Hai R, Wu W, Wang Q, Zhan F-X, Wang X-J, Kan B, Wang S-W, Wan K-L, Jing H-Q, Lu J-X, Yin W-W, Zhou H, Guan X-H, Liu J-F, Bi Z-Q, Liu G-H, Ren J, et al.: **Fever with thrombocytopenia associated with a novel bunyavirus in China.** *N Engl J Med* 2011, **364**:1523–32.

8. Gould EA, Higgs S: **Impact of climate change and other factors on emerging arbovirus diseases.** *Trans R Soc Trop Med Hyg* 2009, **103**:109–21.

9. Ikegami T, Makino S: **The pathogenesis of Rift Valley fever.** *Viruses* 2011, **3**:493–519.

10. Ergönül O: **Crimean-Congo haemorrhagic fever.** *Lancet Infect Dis* 2006, **6**:203–14.

11. Bouloy M, Flick R: **Reverse genetics technology for Rift Valley fever virus: current and future applications for the development of therapeutics and vaccines.** *Antiviral Res* 2009, **84**:101–18.

12. Atkins GJ: **The Pathogenesis of Alphaviruses**. *ISRN Virol* 2013, **2013**:1–22.

13. Doherty GJ, McMahon HT: **Mechanisms of endocytosis.** *Annu Rev Biochem* 2009, **78**:857–902.

14. Mercer J, Schelhaas M, Helenius A: **Virus entry by endocytosis.** *Annu Rev Biochem* 2010, **79**(February):803–33.

15. Saftig P, Klumperman J: **Lysosome biogenesis and lysosomal membrane proteins: trafficking meets function.** *Nat Rev Mol Cell Biol* 2009, **10**:623–35.

16. Huotari J, Helenius A: **Endosome maturation.** *EMBO J* 2011, **30**:3481–500.

17. Marshansky V, Futai M: **The V-type H+-ATPase in vesicular trafficking: targeting, regulation and function.** *Curr Opin Cell Biol* 2008, **20**:415–26.

18. Diering GH, Numata Y, Fan S, Church J, Numata M: **Endosomal acidification by Na+/H+ exchanger NHE5 regulates TrkA cell-surface targeting and NGF-induced PI3K signaling.** *Mol Biol Cell* 2013, **24**:3435–48.

19. Jentsch TJ, Stein V, Weinreich F, Zdebik AA: **Molecular structure and physiological function of chloride channels.** *Physiol Rev* 2002, **82**:503–68.

20. Sasaki T, Sasaki J, Sakai T, Takasuga S, Suzuki A: **The physiology of phosphoinositides.** *Biol Pharm Bull* 2007, **30**:1599–604.

21. Stenmark H: **Rab GTPases as coordinators of vesicle traffic.** *Nat Rev Mol Cell Biol* 2009, **10**:513–25.

22. Möbius W, van Donselaar E, Ohno-Iwashita Y, Shimada Y, Heijnen HFG, Slot JW, Geuze HJ: **Recycling compartments and the internal vesicles of multivesicular bodies harbor most of the cholesterol found in the endocytic pathway.** *Traffic* 2003, **4**:222–31.

23. Kobayashi T, Beuchat M-H, Chevallier J, Makino A, Mayran N, Escola J-M, Lebrand C, Cosson P, Kobayashi T, Gruenberg J: **Separation and characterization of late endosomal membrane domains.** *J Biol Chem* 2002, **277**:32157–64.

24. Kolter T, Sandhoff K: **Lysosomal degradation of membrane lipids.** *FEBS Lett* 2010, **584**:1700–12.

25. Kobayashi T, Beuchat MH, Lindsay M, Frias S, Palmiter RD, Sakuraba H, Parton RG, Gruenberg J: **Late endosomal membranes rich in lysobisphosphatidic acid regulate cholesterol transport.** *Nat Cell Biol* 1999, **1**:113–8.

26. Kobayashi T, Stang E, Fang KS, de Moerloose P, Parton RG, Gruenberg J: **A lipid associated with the antiphospholipid syndrome regulates endosome structure and function.** *Nature* 1998, **392**:193–7.

27. Poorthuis BJ, Hostetler KY: **Studies on the subcellular localization and properties of bis(monoacylglyceryl)phosphate biosynthesis in rat liver.** *J Biol Chem* 1976, **251**:4596–602.

28. Poorthuis BJ, Hostetler KY: **Conversion of diphosphatidylglycerol to bis(monoacylglyceryl)phosphate by lysosomes.** *J Lipid Res* 1978, **19**:309–15.

29. Hullin-Matsuda F, Kawasaki K, Delton-Vandenbroucke I, Xu Y, Nishijima M, Lagarde M, Schlame M, Kobayashi T: **De novo biosynthesis of the late endosome lipid, bis(monoacylglycero)phosphate.** *J Lipid Res* 2007, **48**:1997–2008.

30. Van Meer G, Voelker DR, Feigenson GW: **Membrane lipids: where they are and how they behave.** *Nat Rev Mol Cell Biol* 2008, **9**:112–24.

31. Van Meer G, de Kroon AIPM: **Lipid map of the mammalian cell.** *J Cell Sci* 2011, **124**(Pt 1):5–8.

32. Gruenberg J, Stenmark H: **The biogenesis of multivesicular endosomes.** *Nat Rev Mol Cell Biol* 2004, **5**:317–23.

33. Vonderheit A, Helenius A: **Rab7 associates with early endosomes to mediate sorting and transport of Semliki forest virus to late endosomes.** *PLoS Biol* 2005, **3**:e233.

34. Raiborg C, Stenmark H: **The ESCRT machinery in endosomal sorting of ubiquitylated membrane proteins.** *Nature* 2009, **458**:445–52.

35. Van der Goot FG, Gruenberg J: **Intra-endosomal membrane traffic.** *Trends Cell Biol* 2006, **16**:514–21.

36. Krummenacher C, Carfí A, Eisenberg RJ, Cohen GH: **Entry of herpesviruses into cells: the enigma variations.** *Adv Exp Med Biol* 2013, **790**:178–95.

37. Lindemann D, Steffen I, Pöhlmann S: **Cellular entry of retroviruses.** *Adv Exp Med Biol* 2013, **790**:128–49.

38. Jolly CL, Sattentau QJ: **Attachment factors.** *Adv Exp Med Biol* 2013, **790**:1–23.

39. Soilleux EJ: **DC-SIGN (dendritic cell-specific ICAM-grabbing non-integrin) and DC-SIGN-related (DC-SIGNR): friend or foe?** *Clin Sci (Lond)* 2003, **104**:437–46.

40. Lozach P-Y, Burleigh L, Staropoli I, Navarro-Sanchez E, Harriague J, Virelizier J-L, Rey F a, Desprès P, Arenzana-Seisdedos F, Amara A: **Dendritic cell-specific intercellular adhesion molecule 3-grabbing non-integrin (DC-SIGN)-mediated enhancement of dengue virus infection is independent of DC-SIGN internalization signals.** *J Biol Chem* 2005, **280**:23698–708.

41. Lozach P-Y, Amara A, Bartosch B, Virelizier J-L, Arenzana-Seisdedos F, Cosset F-L, Altmeyer R: **C-type lectins L-SIGN and DC-SIGN capture and transmit infectious hepatitis C virus pseudotype particles.** *J Biol Chem* 2004, **279**:32035–45.

42. Klimstra WB, Nangle EM, Smith MS, Yurochko AD, Ryman KD: **DC-SIGN and L-SIGN Can Act as Attachment Receptors for Alphaviruses and Distinguish between Mosquito Cell- and Mammalian Cell-Derived Viruses DC-SIGN and L-SIGN Can Act as Attachment Receptors for Alphaviruses and Distinguish between Mosquito Cell- and Ma**. 2003.

43. Froelich S, Tai A, Kennedy K, Zubair A, Wang P: **Virus-receptor mediated transduction of dendritic cells by lentiviruses enveloped with glycoproteins derived from Semliki Forest virus.** *PLoS One* 2011, **6**:e21491.

44. Lozach P-Y, Kühbacher A, Meier R, Mancini R, Bitto D, Bouloy M, Helenius A: **DC-SIGN as a receptor for phleboviruses.** *Cell Host Microbe* 2011, **10**:75–88.

45. Hofmann H, Li X, Zhang X, Liu W, Kühl A, Kaup F, Soldan SS, González-Scarano F, Weber F, He Y, Pöhlmann S: **Severe fever with thrombocytopenia virus glycoproteins are targeted by neutralizing antibodies and can use DC-SIGN as a receptor for pH-dependent entry into human and animal cell lines.** *J Virol* 2013, **87**:4384–94.

46. Lozach P, Burleigh L, Staropoli I, Amara A: **Receptors for Viral Glycoproteins**. *Methods Mol Biol* 2007, **379**:51–68.

47. Hammond C, Braakman I, Helenius A: **Role of N-linked oligosaccharide recognition, glucose trimming, and calnexin in glycoprotein folding and quality control.** *Proc Natl Acad Sci U S A* 1994, **91**:913–7.

48. Helenius A, Aebi M: **Roles of N-linked glycans in the endoplasmic reticulum.** *Annu Rev Biochem* 2004, **73**:1019–49.

49. Jones J, Krag SS, Betenbaugh MJ: **Controlling N-linked glycan site occupancy.** *Biochim Biophys Acta* 2005, **1726**:121–37.

50. Crispin M, Harvey DJ, Bitto D, Bonomelli C, Edgeworth M, Scrivens JH, Huiskonen JT, Bowden T a: **Structural plasticity of the Semliki Forest virus glycome upon interspecies transmission.** *J Proteome Res* 2014, **13**:1702–12.

51. Tomiya N, Narang S, Lee YC, Betenbaugh MJ: **Comparing N-glycan processing in mammalian cell lines to native and engineered lepidopteran insect cell lines.** *Glycoconj J* 2004, **21**:343–60.

52. Johannsdottir HK, Mancini R, Kartenbeck J, Amato L, Helenius A: **Host cell factors and functions involved in vesicular stomatitis virus entry.** *J Virol* 2009, **83**:440–53.

53. Cureton DK, Massol RH, Saffarian S, Kirchhausen TL, Whelan SPJ: **Vesicular stomatitis virus enters cells through vesicles incompletely coated with clathrin that depend upon actin for internalization.** *PLoS Pathog* 2009, **5**:e1000394.

54. Helenius a, Kartenbeck J, Simons K, Fries E: **On the entry of Semliki forest virus into BHK-21 cells.** *J Cell Biol* 1980, **84**:404–20.

55. Lozach P-Y, Mancini R, Bitto D, Meier R, Oestereich L, Overby AK, Pettersson RF, Helenius A: **Entry of bunyaviruses into mammalian cells.** *Cell Host Microbe* 2010, **7**:488–99.

56. Sieczkarski SB, Whittaker GR: **Influenza virus can enter and infect cells in the absence of clathrin-mediated endocytosis.** *J Virol* 2002, **76**:10455–64.

57. Racoosin EL, Swanson JA: **Macropinosome maturation and fusion with tubular lysosomes in macrophages.** *J Cell Biol* 1993, **121**:1011–20.

58. Sieczkarski SB, Whittaker GR: **Differential requirements of Rab5 and Rab7 for endocytosis of influenza and other enveloped viruses.** *Traffic* 2003, **4**:333–43.

59. Zaitseva E, Yang S-T, Melikov K, Pourmal S, Chernomordik L V: **Dengue virus ensures its fusion in late endosomes using compartment-specific lipids.** *PLoS Pathog* 2010, **6**:e1001131.

60. Quirin K, Eschli B, Scheu I, Poort L, Kartenbeck J, Helenius A: **Lymphocytic choriomeningitis virus uses a novel endocytic pathway for infectious entry via late endosomes.** *Virology* 2008, **378**:21–33.

61. Lozach P-Y, Huotari J, Helenius A: **Late-penetrating viruses.** *Curr Opin Virol* 2011, **1**:35–43.

62. Kielian MC, Keränen S, Kääriäinen L, Helenius a: **Membrane fusion mutants of Semliki Forest virus.** *J Cell Biol* 1984, **98**:139–45.

63. Kielian MC, Marsh M, Helenius A: **Kinetics of endosome acidification detected by mutant and wild-type Semliki Forest virus.** *EMBO J* 1986, **5**:3103–9.

64. Chandran K, Sullivan NJ, Felbor U, Whelan SP, Cunningham JM: **Endosomal proteolysis of the Ebola virus glycoprotein is necessary for infection.** *Science* 2005, **308**:1643–5.

65. Carette JE, Raaben M, Wong AC, Herbert AS, Obernosterer G, Mulherkar N, Kuehne AI, Kranzusch PJ, Griffin AM, Ruthel G, Dal Cin P, Dye JM, Whelan SP, Chandran K, Brummelkamp TR: **Ebola virus entry requires the cholesterol transporter Niemann-Pick C1.** *Nature* 2011, **477**:340–3.

66. Lee KK: **Architecture of a nascent viral fusion pore.** *EMBO J* 2010, **29**:1299–311.

67. Cao S, Zhang W: **Characterization of an early-stage fusion intermediate of Sindbis virus using cryoelectron microscopy**. 2013:1–6.

68. Chernomordik L V, Frolov V a, Leikina E, Bronk P, Zimmerberg J: **The pathway of membrane fusion catalyzed by influenza hemagglutinin: restriction of lipids, hemifusion, and lipidic fusion pore formation.** *J Cell Biol* 1998, **140**:1369–82.

69. Chernomordik L V, Kozlov MM: **Protein-lipid interplay in fusion and fission of biological membranes.** *Annu Rev Biochem* 2003, **72**:175–207.

70. Chernomordik L V, Kozlov MM: **Mechanics of membrane fusion.** *Nat Struct Mol Biol* 2008, **15**:675–83.

71. Kielian M, Rey F a: **Virus membrane-fusion proteins: more than one way to make a hairpin.** *Nat Rev Microbiol* 2006, **4**:67–76.

72. Backovic M, Jardetzky TS: **Class III viral membrane fusion proteins.** *Adv Exp Med Biol* 2011, **714**:91–101.

73. Modis Y: **Class II fusion proteins.** *Adv Exp Med Biol* 2013, **790**:150–66.

74. Fritz R, Stiasny K, Heinz FX: **Identification of specific histidines as pH sensors in flavivirus membrane fusion.** *J Cell Biol* 2008, **183**:353–61.

75. Smit JM, Bittman R, Wilschut J: **Low-pH-dependent fusion of Sindbis virus with receptor-free cholesterol- and sphingolipid-containing liposomes.** *J Virol* 1999, **73**:8476–84.

76. White J, Helenius a: **pH-dependent fusion between the Semliki Forest virus membrane and liposomes.** *Proc Natl Acad Sci U S A* 1980, **77**:3273–7.

77. Corver J, Ortiz a, Allison SL, Schalich J, Heinz FX, Wilschut J: **Membrane fusion activity of tick-borne encephalitis virus and recombinant subviral particles in a liposomal model system.** *Virology* 2000, **269**:37–46.

78. Huiskonen JT, Overby AK, Weber F, Grünewald K: **Electron cryo-microscopy and single-particle averaging of Rift Valley fever virus: evidence for GN-GC glycoprotein heterodimers.** *J Virol* 2009, **83**:3762–9.

79. Overby a K, Pettersson RF, Grünewald K, Huiskonen JT: **Insights into bunyavirus architecture from electron cryotomography of Uukuniemi virus.** *Proc Natl Acad Sci U S A* 2008, **105**:2375–9.

80. Huiskonen JT, Hepojoki J, Laurinmäki P, Vaheri A, Lankinen H, Butcher SJ, Grünewald K: **Electron cryotomography of Tula hantavirus suggests a unique assembly paradigm for enveloped viruses.** *J Virol* 2010, **84**:4889–97.

81. Overby AK, Pettersson RF, Neve EP a: **The glycoprotein cytoplasmic tail of Uukuniemi virus (Bunyaviridae) interacts with**

ribonucleoproteins and is critical for genome packaging. *J Virol* 2007, **81**:3198–205.

82. Rönkä H, Hildén P, Von Bonsdorff CH, Kuismanen E: **Homodimeric association of the spike glycoproteins G1 and G2 of Uukuniemi virus.** *Virology* 1995, **211**:241–50.

83. Dessau M, Modis Y: **Crystal structure of glycoprotein C from Rift Valley fever virus.** *Proc Natl Acad Sci U S A* 2013, **110**:1696–701.

84. Elliott RM, Weber F: **Bunyaviruses and the type I interferon system.** *Viruses* 2009, **1**:1003–21.

85. Eifan S, Schnettler E, Dietrich I, Kohl A, Blomström A-L: **Non-structural proteins of arthropod-borne bunyaviruses: roles and functions.** *Viruses* 2013, **5**:2447–68.

86. Bowden T a, Bitto D, McLees A, Yeromonahos C, Elliott RM, Huiskonen JT: **Orthobunyavirus ultrastructure and the curious tripodal glycoprotein spike.** *PLoS Pathog* 2013, **9**:e1003374.

87. Kielian M, Chanel-Vos C, Liao M: **Alphavirus Entry and Membrane Fusion.** *Viruses* 2010, **2**:796–825.

88. Uchime O, Fields W, Kielian M: **The role of E3 in pH protection during alphavirus assembly and exit.** *J Virol* 2013, **87**:10255–62.

89. Loewy A, Smyth J, von Bonsdorff CH, Liljeström P, Schlesinger MJ: **The 6-kilodalton membrane protein of Semliki Forest virus is involved in the budding process.** *J Virol* 1995, **69**:469–75.

90. Gavrilovskaya IN, Brown EJ, Ginsberg MH, Mackow ER: **Cellular entry of hantaviruses which cause hemorrhagic fever with renal syndrome is mediated by beta3 integrins.** *J Virol* 1999, **73**:3951–9.

91. Hollidge BS, Nedelsky NB, Salzano M-V, Fraser JW, González-Scarano F, Soldan SS: **Orthobunyavirus entry into neurons and other mammalian cells occurs via clathrin-mediated endocytosis and requires trafficking into early endosomes.** *J Virol* 2012, **86**:7988–8001.

92. Garrison AR, Radoshitzky SR, Kota KP, Pegoraro G, Ruthel G, Kuhn JH, Altamura L a, Kwilas S a, Bavari S, Haucke V, Schmaljohn CS: **Crimean-Congo hemorrhagic fever virus utilizes a clathrin- and early endosome-dependent entry pathway.** *Virology* 2013, **444**:45–54.

93. Jin M, Park J, Lee S, Park B, Shin J, Song K-J, Ahn T-I, Hwang S-Y, Ahn B-Y, Ahn K: **Hantaan virus enters cells by clathrin-dependent receptor-mediated endocytosis.** *Virology* 2002, **294**:60–9.

94. Harmon B, Schudel BR, Maar D, Kozina C, Ikegami T, Tseng C-TK, Negrete O a: **Rift Valley fever virus strain MP-12 enters mammalian host cells via caveola-mediated endocytosis.** *J Virol* 2012, **86**:12954–70.

95. Dunn WA, Hubbard AL, Aronson NN: **Low temperature selectively inhibits fusion between pinocytic vesicles and lysosomes during heterophagy of 125I-asialofetuin by the perfused rat liver.** *J Biol Chem* 1980, **255**:5971–8.

96. Simon M, Johansson C, Lundkvist A, Mirazimi A: **Microtubule-dependent and microtubule-independent steps in Crimean-Congo hemorrhagic fever virus replication cycle.** *Virology* 2009, **385**:313–22.

97. Shtanko O, Nikitina RA, Altuntas CZ, Chepurnov AA, Davey RA: **Crimean-Congo Hemorrhagic Fever Virus Entry into Host Cells Occurs through the Multivesicular Body and Requires ESCRT Regulators.** *PLoS Pathog* 2014, **10**:e1004390.

98. Meier R, Franceschini A, Horvath P, Tetard M, Mancini R, von Mering C, Helenius A, Lozach P-Y: **Genome-Wide Small Interfering RNA Screens Reveal VAMP3 as a Novel Host Factor Required for Uukuniemi Virus Late Penetration.** *J Virol* 2014, **88**:8565–78.

99. Fader CM, Sánchez DG, Mestre MB, Colombo MI: **TI-VAMP/VAMP7 and VAMP3/cellubrevin: two v-SNARE proteins involved in specific steps of the autophagy/multivesicular body pathways.** *Biochim Biophys Acta* 2009, **1793**:1901–16.

100. Carneiro FA, Ferradosa AS, Da Poian AT: **Low pH-induced conformational changes in vesicular stomatitis virus glycoprotein involve dramatic structure reorganization.** *J Biol Chem* 2001, **276**:62–7.

101. Le Blanc I, Luyet P-P, Pons V, Ferguson C, Emans N, Petiot A, Mayran N, Demaurex N, Fauré J, Sadoul R, Parton RG, Gruenberg J: **Endosome-to-cytosol transport of viral nucleocapsids.** *Nat Cell Biol* 2005, **7**:653–64.

102. Waarts B-L, Bittman R, Wilschut J: **Sphingolipid and cholesterol dependence of alphavirus membrane fusion. Lack of correlation with**

lipid raft formation in target liposomes. *J Biol Chem* 2002, **277**:38141–7.

103. Colpitts TM, Moore AC, Kolokoltsov AA, Davey RA: **Venezuelan equine encephalitis virus infection of mosquito cells requires acidification as well as mosquito homologs of the endocytic proteins Rab5 and Rab7.** *Virology* 2007, **369**:78–91.

104. Wang KS, Kuhn RJ, Strauss EG, Ou S, Strauss JH: **High-affinity laminin receptor is a receptor for Sindbis virus in mammalian cells.** *J Virol* 1992, **66**:4992–5001.

105. Klimstra WB, Ryman KD, Johnston RE: **Adaptation of Sindbis virus to BHK cells selects for use of heparan sulfate as an attachment receptor.** *J Virol* 1998, **72**:7357–66.

106. Rose PP, Hanna SL, Spiridigliozzi A, Wannissorn N, Beiting DP, Ross SR, Hardy RW, Bambina SA, Heise MT, Cherry S: **Natural resistance-associated macrophage protein is a cellular receptor for sindbis virus in both insect and mammalian hosts.** *Cell Host Microbe* 2011, **10**:97–104.

107. Kostyuchenko VA, Chew PL, Ng T-S, Lok S-M: **Near-atomic resolution cryo-electron microscopic structure of dengue serotype 4 virus.** *J Virol* 2014, **88**:477–82.

108. Zhang X, Ge P, Yu X, Brannan JM, Bi G, Zhang Q, Schein S, Zhou ZH: **Cryo-EM structure of the mature dengue virus at 3.5-Å resolution.** *Nat Struct Mol Biol* 2013, **20**:105–10.

109. Adrian M, Dubochet J, Lepault J, McDowall AW: **Cryo-electron microscopy of viruses.** *Nature* , **308**:32–6.

110. Baker TS, Henderson R: **Chapter 19 . 6 . Electron cryomicroscopy of biological macromolecules**. In *Int Tables Crystallogr Crystallogr Biol Macromol*; 2012:593–614.

111. Frank J: *Three-Dimensional Electron Microscopy of Macromolecular Assemblies: Visualization of Biological Molecules in Their Native State*. New York, NY: Oxford University Press; 2006.

112. Baker TS, Olson NH, Fuller SD: **Adding the third dimension to virus life cycles: three-dimensional reconstruction of icosahedral viruses from cryo-electron micrographs.** *Microbiol Mol Biol Rev* 1999, **63**:862–922.

113. Erickson HP, Klug A: **Measurement and Compensation of Defocusing and Aberrations by Fourier Processing of Electron Micrographs**. In *Philos Trans R Soc London Ser B, Biol Sci A Discuss New Dev Electron Microsc with Spec Emphas their Appl Biol*. *Volume 261*. The Royal Society; 2007:105–118.

114. Van Heel M, Gowen B, Matadeen R, Orlova E V, Finn R, Pape T, Cohen D, Stark H, Schmidt R, Schatz M, Patwardhan A: **Single-particle electron cryo-microscopy: towards atomic resolution.** *Q Rev Biophys* 2000, **33**:307–69.

115. Fuller SD, Butcher SJ, Cheng RH, Baker TS: **Three-dimensional reconstruction of icosahedral particles--the uncommon line.** *J Struct Biol* 1996, **116**:48–55.

116. Baker TS, Cheng RH: **A model-based approach for determining orientations of biological macromolecules imaged by cryoelectron microscopy.** *J Struct Biol* , **116**:120–30.

117. Sigworth FJ, Doerschuk PC, Carazo J-M, Scheres SHW: **An introduction to maximum-likelihood methods in cryo-EM.** *Methods Enzymol* 2010, **482**:263–94.

118. Scheres SHW: **RELION: implementation of a Bayesian approach to cryo-EM structure determination.** *J Struct Biol* 2012, **180**:519–30.

119. Pokidysheva E, Zhang Y, Battisti AJ, Bator-Kelly CM, Chipman PR, Xiao C, Gregorio GG, Hendrickson W a, Kuhn RJ, Rossmann MG: **Cryo-EM reconstruction of dengue virus in complex with the carbohydrate recognition domain of DC-SIGN.** *Cell* 2006, **124**:485–93.

120. De Alwis R, Smith SA, Olivarez NP, Messer WB, Huynh JP, Wahala WMPB, White LJ, Diamond MS, Baric RS, Crowe JE, de Silva AM: **Identification of human neutralizing antibodies that bind to complex epitopes on dengue virions.** *Proc Natl Acad Sci U S A* 2012, **109**:7439–44.

121. Pejchal R, Doores KJ, Walker LM, Khayat R, Huang P-S, Wang S-K, Stanfield RL, Julien J-P, Ramos A, Crispin M, Depetris R, Katpally U, Marozsan A, Cupo A, Maloveste S, Liu Y, McBride R, Ito Y, Sanders RW, Ogohara C, Paulson JC, Feizi T, Scanlan CN, Wong C-H, Moore JP, Olson WC, Ward AB, Poignard P, Schief WR, Burton DR, et al.: **A potent and broad neutralizing antibody recognizes and penetrates the HIV glycan shield.** *Science* 2011, **334**:1097–103.

122. Moller-Tank S, Kondratowicz AS, Davey R a, Rennert PD, Maury W: **Role of the phosphatidylserine receptor TIM-1 in enveloped-virus entry.** *J Virol* 2013, **87**:8327–41.

123. Pal R, Barenholz Y, Wagner RR: **Pyrene phospholipid as a biological fluorescent probe for studying fusion of virus membrane with liposomes.** *Biochemistry* 1988, **27**:30–6.

124. Kyoung M, Srivastava A, Zhang Y, Diao J, Vrljic M, Grob P, Nogales E, Chu S, Brunger AT: **In vitro system capable of differentiating fast Ca2+-triggered content mixing from lipid exchange for mechanistic studies of neurotransmitter release.** *PNAS* 2011, 108:E304-13.

125. Aricescu a R, Lu W, Jones EY: **A time- and cost-efficient system for high-level protein production in mammalian cells.** *Acta Crystallogr D Biol Crystallogr* 2006, **62**(Pt 10):1243–50.

126. Reeves PJ, Callewaert N, Contreras R, Khorana HG: **Structure and function in rhodopsin: high-level expression of rhodopsin with restricted and homogeneous N-glycosylation by a tetracycline-inducible N-acetylglucosaminyltransferase I-negative HEK293S stable mammalian cell line.** *Proc Natl Acad Sci U S A* 2002, **99**:13419–24.

127. Mitchell D a, Fadden a J, Drickamer K: **A novel mechanism of carbohydrate recognition by the C-type lectins DC-SIGN and DC-SIGNR. Subunit organization and binding to multivalent ligands.** *J Biol Chem* 2001, **276**:28939–45.

128. Feinberg H, Guo Y, Mitchell D a, Drickamer K, Weis WI: **Extended neck regions stabilize tetramers of the receptors DC-SIGN and DC-SIGNR.** *J Biol Chem* 2005, **280**:1327–35.

129. Atanasova NS, Roine E, Oren A, Bamford DH, Oksanen HM: **Global network of specific virus-host interactions in hypersaline environments**. *Environ Microbiol* 2012, **14**:426–40.

130. CYRKLAFF M, ROOS N, GROSS H, DUBOCHET J: **Particle-surface interaction in thin vitrified films for cryo-electron microscopy**. *J Microsc* 1994, **175**:135–142.

131. Grassucci RA, Taylor DJ, Frank J: **Preparation of macromolecular complexes for cryo-electron microscopy.** *Nat Protoc* 2007, **2**:3239–46.

132. Mastronarde DN: **Automated electron microscope tomography using robust prediction of specimen movements.** *J Struct Biol* 2005, **152**:36–51.

133. Mindell JA, Grigorieff N: **Accurate determination of local defocus and specimen tilt in electron microscopy.** *J Struct Biol* 2003, **142**:334–47.

134. Scheres SHW: **A Bayesian view on cryo-EM structure determination.** *J Mol Biol* 2012, **415**:406–18.

135. Sorzano COS, Marabini R, Velázquez-Muriel J, Bilbao-Castro JR, Scheres SHW, Carazo JM, Pascual-Montano a: **XMIPP: a new generation of an open-source image processing package for electron microscopy.** *J Struct Biol* 2004, **148**:194–204.

136. Kivioja T, Ravantti J, Verkhovsky a, Ukkonen E, Bamford D: **Local average intensity-based method for identifying spherical particles in electron micrographs.** *J Struct Biol* 2000, **131**:126–34.

137. Tang G, Peng L, Baldwin PR, Mann DS, Jiang W, Rees I, Ludtke SJ: **EMAN2: an extensible image processing suite for electron microscopy.** *J Struct Biol* 2007, **157**:38–46.

138. Van Heel M, Harauz G, Orlova E V, Schmidt R, Schatz M: **A new generation of the IMAGIC image processing system.** *J Struct Biol* 1996, **116**:17–24.

139. Mancini EJ, Clarke M, Gowen BE, Rutten T, Fuller SD: **Cryo-electron microscopy reveals the functional organization of an enveloped virus, Semliki Forest virus.** *Mol Cell* 2000, **5**:255–66.

140. Rosenthal PB, Henderson R: **Optimal determination of particle orientation, absolute hand, and contrast loss in single-particle electron cryomicroscopy.** *J Mol Biol* 2003, **333**:721–45.

141. Bai X-C, Fernandez IS, McMullan G, Scheres SH: **Ribosome structures to near-atomic resolution from thirty thousand cryo-EM particles.** *Elife* 2013, **2**:e00461.

142. Chen S, McMullan G, Faruqi AR, Murshudov GN, Short JM, Scheres SHW, Henderson R: **High-resolution noise substitution to measure overfitting and validate resolution in 3D structure determination by single particle electron cryomicroscopy.** *Ultramicroscopy* 2013, **135**:24–35.

143. Heymann JB, Belnap DM: **Bsoft: image processing and molecular modeling for electron microscopy.** *J Struct Biol* 2007, **157**:3–18.

144. Kremer JR, Mastronarde DN, McIntosh JR: **Computer visualization of three-dimensional image data using IMOD.** *J Struct Biol* , **116**:71–6.

145. Freiberg AN, Sherman MB, Morais MC, Holbrook MR, Watowich SJ: **Three-dimensional organization of Rift Valley fever virus revealed by cryoelectron tomography.** *J Virol* 2008, **82**:10341–8.

146. Sherman MB, Freiberg AN, Holbrook MR, Watowich SJ: **Single-particle cryo-electron microscopy of Rift Valley fever virus.** *Virology* 2009, **387**:11–5.

147. Hryc CF, Chen D-H, Chiu W: **Near-atomic-resolution cryo-EM for molecular virology.** *Curr Opin Virol* 2011, **1**:110–7.

148. **Multivariate Statistical Analysis in Single Particle (Cryo) Electron Microscopy, in: "An electronic text book: Electron microscopy in Life Science", 3D-EM Network of Excellence, Editors: A. Verkley and E. Orlova (2009)** [http://www.single-particles.org/methodology/MvH_MSA_2009.pdf]

149. Vaisman N, Oren A: **Salisaeta longa gen. nov., sp. nov., a red, halophilic member of the Bacteroidetes.** *Int J Syst Evol Microbiol* 2009, **59**(Pt 10):2571–4.

150. Aalto AP, Bitto D, Ravantti JJ, Bamford DH, Huiskonen JT, Oksanen HM: **Snapshot of virus evolution in hypersaline environments from the characterization of a membrane-containing Salisaeta icosahedral phage 1.** *Proc Natl Acad Sci U S A* 2012, **109**:7079–84.

151. Yoshimura A, Kuroda K: **Infectious Cell Entry Mechanism of Influenza Virus**. *J Virol* 1982, **43**:284–93.

152. Randolph VB, Stollar V: **Low pH-induced cell fusion in flavivirus-infected Aedes albopictus cell cultures.** *J Gen Virol* 1990, **71 (Pt 8)**:1845–50.

153. Wessels L, Elting MW, Scimeca D, Weninger K: **Rapid membrane fusion of individual virus particles with supported lipid bilayers.** *Biophys J* 2007, **93**:526–38.

154. Smit JM, Li G, Schoen P, Corver J, Bittman R, Lin K-C, Wilschut J: **Fusion of alphaviruses with liposomes is a non-leaky process.** *FEBS Lett* 2002, **521**:62–6.

155. Nieva JL, Bron R, Corver J, Wilschut J: **Membrane fusion of Semliki Forest virus requires sphingolipids in the target membrane.** *EMBO J* 1994, **13**:2797–804.

156. Floyd DL, Ragains JR, Skehel JJ, Harrison SC, van Oijen AM: **Single-particle kinetics of influenza virus membrane fusion.** *Proc Natl Acad Sci U S A* 2008, **105**:15382–7.

157. Kooijman EE, Carter KM, van Laar EG, Chupin V, Burger KNJ, de Kruijff B: **What makes the bioactive lipids phosphatidic acid and lysophosphatidic acid so special?** *Biochemistry* 2005, **44**:17007–15.

158. Lakhdar-Ghazal F, Tichadou JL, Tocanne JF: **Effect of pH and monovalent cations on the ionization state of phosphatidylglycerol in monolayers. An experimental (surface potential) and theoretical (Gouy-Chapman) approach.** *Eur J Biochem* 1983, **134**:531–7.

159. MacDonald RC, Simon S a, Baer E: **Ionic influences on the phase transition of dipalmitoylphosphatidylserine.** *Biochemistry* 1976, **15**:885–91.

160. Tsui FC, Ojcius DM, Hubbell WL: **The intrinsic pKa values for phosphatidylserine and phosphatidylethanolamine in phosphatidylcholine host bilayers**. 1986, **49**:459–68.

161. Fuller N, Benatti CR, Rand RP: **Curvature and bending constants for phosphatidylserine-containing membranes.** *Biophys J* 2003, **85**:1667–74.

162. Alley SH, Ces O, Barahona M, Templer RH: **X-ray diffraction measurement of the monolayer spontaneous curvature of dioleoylphosphatidylglycerol.** *Chem Phys Lipids* 2008, **154**:64–7.

163. Kooijman EE, Chupin V, Fuller NL, Kozlov MM, de Kruijff B, Burger KNJ, Rand PR: **Spontaneous curvature of phosphatidic acid and lysophosphatidic acid.** *Biochemistry* 2005, **44**:2097–102.

164. Matsuo H, Chevallier J, Mayran N, Le Blanc I, Ferguson C, Fauré J, Blanc NS, Matile S, Dubochet J, Sadoul R, Parton RG, Vilbois F, Gruenberg J: **Role of LBPA and Alix in multivesicular liposome formation and endosome organization.** *Science* 2004, **303**:531–4.

165. Renkonen O, Kääriäinen L, Pettersson R, Oker-Blom N: **The phospholipid composition of Uukuniemi virus, a non-cubical tick-borne arbovirus.** *Virology* 1972, **50**:899–901.

166. Zambrano F, Fleischer S, Fleischer B: **Lipid composition of the Golgi apparatus of rat kidney and liver in comparison with other subcellular organelles.** *Biochim Biophys Acta* 1975, **380**:357–69.

167. Tscherne DM, Jones CT, Evans MJ, Lindenbach BD, McKeating JA, Rice CM: **Time- and temperature-dependent activation of hepatitis C virus for low-pH-triggered entry.** *J Virol* 2006, **80**:1734–41.

168. Waarts B, Smit JM, Aneke OJC, Mcinerney GM, Bittman R, Wilschut J: **Reversible Acid-Induced Inactivation of the Membrane Fusion Protein of Semliki Forest Virus**. *journal9med.net* 2005, **79**:7942–7948.

169. Modis Y: **Relating structure to evolution in class II viral membrane fusion proteins.** *Curr Opin Virol* 2014, **5**(Figure 1):34–41.

170. Kielian M: **Class II virus membrane fusion proteins.** *Virology* 2006, **344**:38–47.

171. Van Liempt E, Bank CMC, Mehta P, Garciá-Vallejo JJ, Kawar ZS, Geyer R, Alvarez R a, Cummings RD, Kooyk Y Van, van Die I: **Specificity of DC-SIGN for mannose- and fucose-containing glycans.** *FEBS Lett* 2006, **580**:6123–31.

172. Hofmann H, Li X, Zhang X, Liu W, Kühl A, Kaup F, Soldan SS, González-Scarano F, Weber F, He Y, Pöhlmann S: **Severe fever with thrombocytopenia virus glycoproteins are targeted by neutralizing antibodies and can use DC-SIGN as a receptor for pH-dependent entry into human and animal cell lines.** *J Virol* 2013, **87**:4384–94.

173. Bowden T a, Aricescu a R, Gilbert RJC, Grimes JM, Jones EY, Stuart DI: **Structural basis of Nipah and Hendra virus attachment to their cell-surface receptor ephrin-B2.** *Nat Struct Mol Biol* 2008, **15**:567–72.

174. Pletnev S V, Zhang W, Mukhopadhyay S, Fisher BR, Hernandez R, Brown DT, Baker TS, Rossmann MG, Kuhn RJ: **Locations of carbohydrate sites on alphavirus glycoproteins show that E1 forms an icosahedral scaffold.** *Cell* 2001, **105**:127–36.

175. Pesonen M, Kuismanen E, Pettersson RF: **Monosaccharide sequence of protein-bound glycans of Uukuniemi virus.** *J Virol* 1982, **41**:390–400.

176. Harvey DJ, Sobott F, Crispin M, Wrobel A, Bonomelli C, Vasiljevic S, Scanlan CN, Scarff C a, Thalassinos K, Scrivens JH: **Ion mobility mass spectrometry for extracting spectra of N-glycans directly from incubation mixtures following glycan release: application to glycans**

from engineered glycoforms of intact, folded HIV gp120. *J Am Soc Mass Spectrom* 2011, **22**:568–81.

177. Crispin M, Harvey DJ, Bitto D, Halldorsson S, Bonomelli C, Edgeworth M, Scrivens JH, Huiskonen JT, Bowden T a: **Uukuniemi phlebovirus assembly and secretion leave a functional imprint on the virion glycome.** *J Virol* 2014, **88**:10244–51.

178. Nabi IR, Dennis JW: **The extent of polylactosamine glycosylation of MDCK LAMP-2 is determined by its Golgi residence time.** *Glycobiology* 1998, **8**:947–53.

179. Jäntti J, Hildén P, Rönkä H, Mäkiranta V, Keränen S, Kuismanen E: **Immunocytochemical analysis of Uukuniemi virus budding compartments: role of the intermediate compartment and the Golgi stack in virus maturation.** *J Virol* 1997, **71**:1162–72.

180. Rusu M, Bonneau R, Holbrook MR, Watowich SJ, Birmanns S, Wriggers W, Freiberg AN: **An assembly model of rift valley Fever virus.** *Front Microbiol* 2012, **3**(July):254.

181. Mattila K, Luukkonen A, Renkonen O: **Protein-bound oligosaccharides of Semliki Forest virus**. *Biochim Biophys Acta - Biomembr* 1976, **419**:435–444.

182. Garoff H, Simons K, Renkonen O: **Isolation and characterization of the membrane proteins of Semliki Forest virus**. *Virology* 1974, **61**:493–504.

183. Pesonen M: **Sequence analysis of lactosamine type glycans of individual membrane proteins of Semliki Forest virus.** *J Gen Virol* 1979, **45**:479–87.

184. Naim HY, Koblet H: **Asparagine-linked oligosaccharides of Semliki Forest virus grown in mosquito cells.** *Arch Virol* 1992, **122**:45–60.

185. Mancini EJ, Clarke M, Gowen BE, Rutten T, Fuller SD: **Cryo-electron microscopy reveals the functional organization of an enveloped virus, Semliki Forest virus.** *Mol Cell* 2000, **5**:255–66.

186. Roussel A, Lescar J, Vaney M-C, Wengler G, Wengler G, Rey F a: **Structure and interactions at the viral surface of the envelope protein E1 of Semliki Forest virus.** *Structure* 2006, **14**:75–86.

187. Voss JE, Vaney M-C, Duquerroy S, Vonrhein C, Girard-Blanc C, Crublet E, Thompson A, Bricogne G, Rey F a: **Glycoprotein organization of Chikungunya virus particles revealed by X-ray crystallography.** *Nature* 2010, **468**:709–12.

188. Tabarani G, Thépaut M, Stroebel D, Ebel C, Vivès C, Vachette P, Durand D, Fieschi F: **DC-SIGN neck domain is a pH-sensor controlling oligomerization: SAXS and hydrodynamic studies of extracellular domain.** *J Biol Chem* 2009, **284**:21229–40.

189. Feinberg H, Castelli R, Drickamer K, Seeberger PH, Weis WI: **Multiple modes of binding enhance the affinity of DC-SIGN for high mannose N-linked glycans found on viral glycoproteins.** *J Biol Chem* 2007, **282**:4202–9.

190. Willard L, Ranjan A, Zhang H, Monzavi H, Boyko RF, Sykes BD, Wishart DS: **VADAR: a web server for quantitative evaluation of protein structure quality.** *Nucleic Acids Res* 2003, **31**:3316–9.

191. Matos PM, Marin M, Ahn B, Lam W, Santos NC, Melikyan GB: **Anionic lipids are required for vesicular stomatitis virus G protein-mediated single particle fusion with supported lipid bilayers.** *J Biol Chem* 2013, **288**:12416–25.

192. Fibriansah G, Ng T-S, Kostyuchenko VA, Lee J, Lee S, Wang J, Lok S-M: **Structural changes in dengue virus when exposed to a temperature of 37°C.** *J Virol* 2013, **87**:7585–92.

193. Bereszczak JZ, Watts NR, Wingfield PT, Steven AC, Heck AJR: **Assessment of differences in the conformational flexibility of hepatitis B virus core-antigen and e-antigen by hydrogen deuterium exchange-mass spectrometry.** *Protein Sci* 2014, **23**:884–96.

194. Haag L, Garoff H, Xing L, Hammar L, Kan S-T, Cheng RH: **Acid-induced movements in the glycoprotein shell of an alphavirus turn the spikes into membrane fusion mode.** *EMBO J* 2002, **21**:4402–10.

195. Expert-Bezançon N, Rabilloud T, Vuillard L, Goldberg ME: **Physical-chemical features of non-detergent sulfobetaines active as protein-folding helpers.** *Biophys Chem* 2003, **100**:469–79.

196. Kyoung M, Srivastava A, Zhang Y, Diao J, Vrljic M, Grob P, Nogales E, Chu S, Brunger AT: **In vitro system capable of differentiating fast Ca2+-triggered content mixing from lipid exchange for mechanistic studies of neurotransmitter release.** *Proc Natl Acad Sci U S A* 2011, **108**:E304–13.

197. Gonzalez-Scarano F, Pobjecky N, Nathanson N: **La Crosse bunyavirus can mediate pH-dependent fusion from without.** *Virology* 1984, **132**:222–5.

198. Shi X, Kohl A, Li P, Elliott RM: **Role of the cytoplasmic tail domains of Bunyamwera orthobunyavirus glycoproteins Gn and Gc in virus assembly and morphogenesis.** *J Virol* 2007, **81**:10151–60.

199. Nour AM, Li Y, Wolenski J, Modis Y: **Viral membrane fusion and nucleocapsid delivery into the cytoplasm are distinct events in some flaviviruses.** *PLoS Pathog* 2013, **9**:e1003585.

200. Appelqvist H, Wäster P, Kågedal K, Öllinger K: **The lysosome: from waste bag to potential therapeutic target.** *J Mol Cell Biol* 2013, **5**:214–26.

201. Hatch GM: **Regulation of cardiolipin biosynthesis in the heart.** *Mol Cell Biochem* 1996, **159**:139–48.

202. Kielian MC, Helenius a: **Role of cholesterol in fusion of Semliki Forest virus with membranes.** *J Virol* 1984, **52**:281–3.

203. Stiasny K, Allison SL, Schalich J, Heinz FX: **Membrane interactions of the tick-borne encephalitis virus fusion protein E at low pH.** *J Virol* 2002, **76**:3784–90.

204. Bron R, Wahlberg JM, Garoff H, Wilschut J: **Membrane fusion of Semliki Forest virus in a model system: correlation between fusion kinetics and structural changes in the envelope glycoprotein.** *EMBO J* 1993, **12**:693–701.

205. Bowden TA, Bitto D, McLees A, Yeromonahos C, Elliott RM, Huiskonen JT: **Orthobunyavirus ultrastructure and the curious tripodal glycoprotein spike.** *PLoS Pathog* 2013, **9**:e1003374.

206. Wahlberg JM, Bron R, Wilschut J, Garoff H: **Membrane fusion of Semliki Forest virus involves homotrimers of the fusion protein.** *J Virol* 1992, **66**:7309–18.

207. McInerney GM, Smit JM, Liljeström P, Wilschut J: **Semliki Forest virus produced in the absence of the 6K protein has an altered spike structure as revealed by decreased membrane fusion capacity.** *Virology* 2004, **325**:200–6.

208. De Boer SM, Kortekaas J, Spel L, Rottier PJM, Moormann RJM, Bosch BJ: **Acid-activated structural reorganization of the Rift Valley fever virus Gc fusion protein.** *J Virol* 2012, **86**:13642–52.

209. Nour AM, Modis Y: **Endosomal vesicles as vehicles for viral genomes.** *Trends Cell Biol* 2014, **24**:449–54.

210. Im YJ, Wollert T, Boura E, Hurley JH: **Structure and function of the ESCRT-II-III interface in multivesicular body biogenesis.** *Dev Cell* 2009, **17**:234–43.

211. Economopoulou A, Dominguez M, Helynck B, Sissoko D, Wichmann O, Quenel P, Germonneau P, Quatresous I: **Atypical Chikungunya virus infections: clinical manifestations, mortality and risk factors for severe disease during the 2005-2006 outbreak on Réunion.** *Epidemiol Infect* 2009, **137**:534–41.

212. Hofmann H, Pöhlmann S: **DC-SIGN: access portal for sweet viral killers.** *Cell Host Microbe* 2011, **10**:5–7.

213. Mercer J, Helenius A: **Vaccinia virus uses macropinocytosis and apoptotic mimicry to enter host cells.** *Science* 2008, **320**:531–5.

214. Meertens L, Carnec X, Lecoin MP, Ramdasi R, Guivel-Benhassine F, Lew E, Lemke G, Schwartz O, Amara A: **The TIM and TAM families of phosphatidylserine receptors mediate dengue virus entry.** *Cell Host Microbe* 2012, **12**:544–57.

215. Miyanishi M, Tada K, Koike M, Uchiyama Y, Kitamura T, Nagata S: **Identification of Tim4 as a phosphatidylserine receptor.** *Nature* 2007, **450**:435–9.

216. Kondratowicz AS, Lennemann NJ, Sinn PL, Davey RA, Hunt CL, Moller-Tank S, Meyerholz DK, Rennert P, Mullins RF, Brindley M, Sandersfeld LM, Quinn K, Weller M, McCray PB, Chiorini J, Maury W: **T-cell immunoglobulin and mucin domain 1 (TIM-1) is a receptor for Zaire Ebolavirus and Lake Victoria Marburgvirus.** *Proc Natl Acad Sci U S A* 2011, **108**:8426–31.

217. Rennert PD: **Novel roles for TIM-1 in immunity and infection.** *Immunol Lett* 2011, **141**:28–35.

218. Renkonen O, Kääriäinen L, Pettersson R, Oker-Blom N: **The phospholipid composition of uukuniemi virus, a non-cubical tick-borne arbovirus**. *Virology* 1972, **50**:899–901.

8. Abbreviations

BUNV	Bunyamwera virus
BSA	Bovine serum albumin
CHIKV	Chikungunya virus
CRD	Carbohydrate recognition domain
DC-SIGN	Dendritic cell-specific ICAM-3 grabbing non-integrin
DLS	Dynamic light scattering
ECD	Extracellular domain
Excimer	Excited dimer
FBS	Fetal bovine serum
FCS	Fetal calf serum
FFU	Focus-forming unit
HRP	horseradish peroxidase
kDa	kilodalton
LB	Luria-Bertani
PCR	Polymerase chain reaction
PFU	Plaque-forming unit

PMT	Photomultiplier
Pyr	Pyrene
SBV	Sindbis virus
RVFV	Rift Valley fever virus
SFV	Semliki Forest virus
SOC	Super Optimal broth with Catabolite repression
SPG	Succinate, phosphate, glycine
SRB	Sulforhodamine B
SSIP-1	Salisaeta icosahedral phage 1
TBEV	Tick-borne encephalitis virus
UUKV	Uukuniemi virus

9. Appendix

9.1. Codon optimized DC-SIGN cDNA sequence (Geneart, 5' to 3')

ATGAGCGACAGCAAAGAGCCCCGGCTGCAGCAGCTGGGCCTGCTGG
AAGAGGAACAGCTGCGGGGCCTGGGCTTCCGGCAGACCAGAGGCTA
CAAGAGCCTGGCCGGCTGTCTGGGCCACGGCCCTCTGGTGCTGCAG
CTGCTGAGCTTTACCCTGCTGGCCGGACTGCTGGTCCAGGTGTCCAA
GGTGCCCAGCAGCATCAGCCAGGAACAGAGCCGGCAGGACGCCATC
TACCAGAACCTGACCCAGCTGAAGGCCGCCGTGGGCGAGCTGAGCG
AGAAGTCCAAGCTGCAGGAAATCTATCAGGAACTCACCCAGCTCAAA
GCAGCTGTGGGAGAACTGCCCGAGAAAAGCAAACTCCAGGAAATCTA
CCAGGAACTGACAAGACTGAAAGCTGCCGTCGGAGAGCTGCCTGAG
AAATCTAAGCTGCAGGAAATCTACCAGGAACTGACCTGGCTGAAGGC
TGCAGTGGGGGAACTGCCTGAAAAGTCAAAAATGCAGGAAATCTACC
AGGAACTCACAAGGCTCAAGGCCGCTGTCGGGGAGCTGCCAGAAAA
GAGTAAACAGCAGGAAATCTATCAGGAACTGACTCGCCTGAAGGCCG
CTGTCGGCGAACTCCCTGAGAAAAGCAAGCAGCAGGAAATCTACCAG
GAACTCACTCGCCTCAAAGCTGCAGTCGGAGAACTCCCCGAAAAATC
CAAACAGCAGGAAATCTACCAGGAACTGACCCAGCTCAAGGCTGCC
GTCGAGAGACTGTGCCACCCCTGCCCCTGGGAGTGGACCTTCTTCC
AGGGCAACTGCTACTTCATGAGCAACAGCCAGCGGAACTGGCACGA
CAGCATCACCGCCTGCAAAGAAGTGGGCGCCCAGCTGGTGGTCATC
AAGAGCGCCGAGGAACAGAACTTCCTGCAGCTCCAGAGCAGCAGAA
GCAACAGATTCACCTGGATGGGCCTGAGCGACCTGAACCAGGAAGG
CACCTGGCAGTGGGTGGACGGCAGCCCCCTGCTGCCCAGCTTCAAG
CAGTATTGGAACCGGGGCGAGCCCAACAACGTGGGCGAAGAGGATT
GCGCCGAGTTCAGCGGCAACGGCTGGAACGACGACAAGTGCAACCT
GGCCAAGTTCTGGATCTGCAAGAAGTCCGCCGCCAGCTGCTCCCGG
GATGAGGAACAGTTTCTGAGCCCTGCCCCAGCCACCCCCAATCCTCC
ACCAGCT

9.2. Protein sequence encoded by the Geneart DC-SIGN nucleotide sequence

MSDSKEPRLQQLGLLEEEQLRGLGFRQTRGYKSLAGCLGHGPLVLQLL
SFTLLAGLLVQVSKVPSSISQEQSRQDAIYQNLTQLKAAVGELSEKSKLQ
EIYQELTQLKAAVGELPEKSKLQEIYQELTRLKAAVGELPEKSKLQEIYQE
LTWLKAAVGELPEKSKMQEIYQELTRLKAAVGELPEKSKQQEIYQELTRL
KAAVGELPEKSKQQEIYQELTRLKAAVGELPEKSKQQEIYQELTQLKAAV
ERLCHPCPWEWTFFQGNCYFMSNSQRNWHDSITACKEVGAQLVVIKSA
EEQNFLQLQSSRSNRFTWMGLSDLNQEGTWQWVDGSPLLPSFKQYW
NRGEPNNVGEEDCAEFSGNGWNDDKCNLAKFWICKKSAASCSRDEEQ
FLSPAPATPNPPPA

This sequence is identical to CD209 antigen isoform 1 [Homo sapiens], NCBI Reference Sequence: NP_066978.1.

9.3. Publications and manuscripts in preparation based on work performed in this thesis

Bitto D, Caputo A, Halldorsson S, Huiskonen JT. **Uukuniemi phlebovirus uses the late endosomal phospholipid bis(monoacylglycero)phosphate (BMP) to facilitate low pH mediated fusion**, *Manuscript in preparation*.

Crispin M, Harvey DJ, **Bitto D**, Halldorsson S, Bonomelli C, Edgeworth M, Scrivens JH, Huiskonen JT, Bowden T a: **Uukuniemi phlebovirus assembly and secretion leave a functional imprint on the virion glycome.** *J Virol* 2014, **88**:10244–51.

Crispin M, Harvey DJ, **Bitto D**, Bonomelli C, Edgeworth M, Scrivens JH, Huiskonen JT, Bowden T a: **Structural plasticity of the Semliki Forest virus glycome upon interspecies transmission.** *J Proteome Res* 2014, **13**:1702–12.

Aalto AP, **Bitto D**, Ravantti JJ, Bamford DH, Huiskonen JT, Oksanen HM: **Snapshot of virus evolution in hypersaline environments from the characterization of a membrane-containing Salisaeta icosahedral phage 1.** *Proc Natl Acad Sci U S A* 2012, **109**:7079–84.

9.4. Supplementary figures

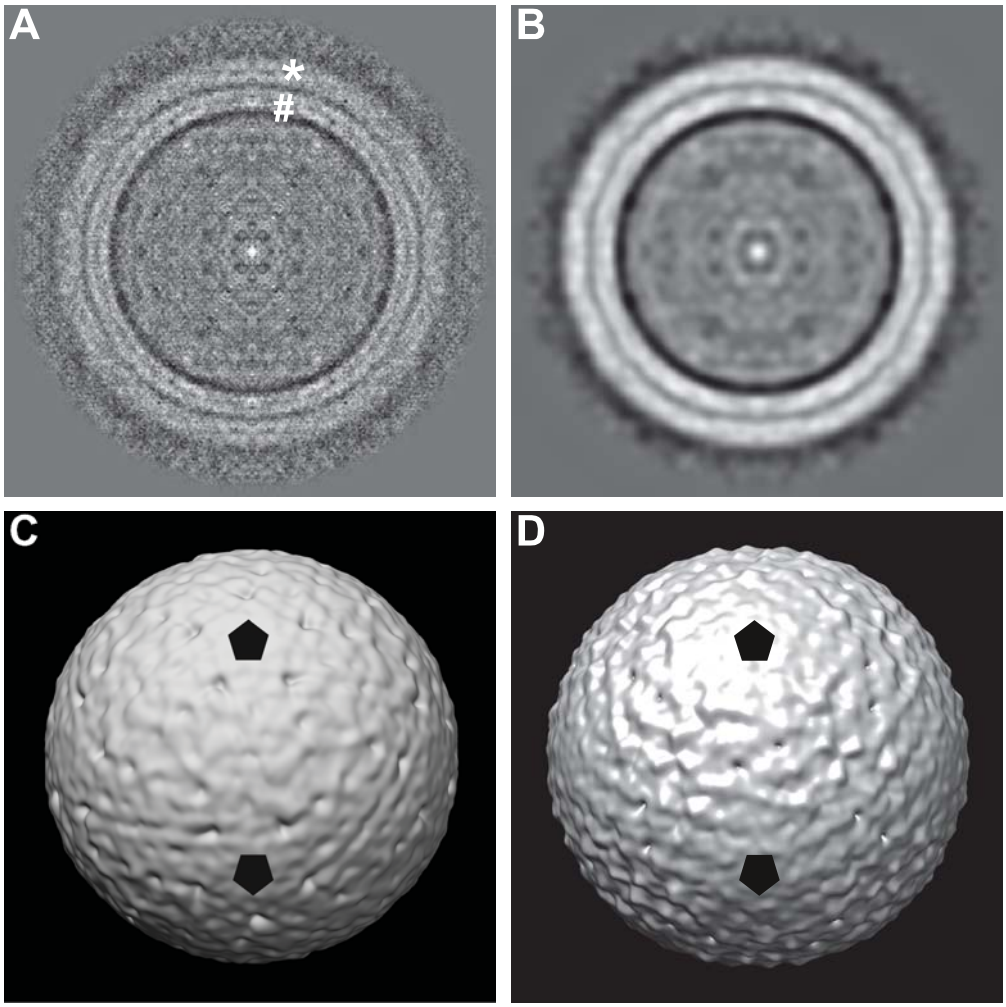


Figure S1. Icosahedral reconstruction of Uukuniemi virus.

A.) Central slice of initial UUKV model reconstructed by angular reconstitution of class averages in IMAGIC. The hash (#) indicates the membrane and the asterisk indicates the surface glycoprotein layer.

B.) Same as in A.), but filtered to 5 nm resolution.

C.) Three-dimensional representation of the initial UUKV model depicted in A and B, rendered to 2σ above the mean and filtered to 5 nm resolution. Pentagons indicate the icosahedral fivefold symmetry axis. Note that no distinct spikes are visible.

D.) UUKV model from three dimensional classification in RELION (Class 1 of 2), using the UUKV reference model as obtained by angular reconstitution from IMAGIC. Pentagons indicate the icosahedral fivefold symmetry axis. Note that no spikes are visible.

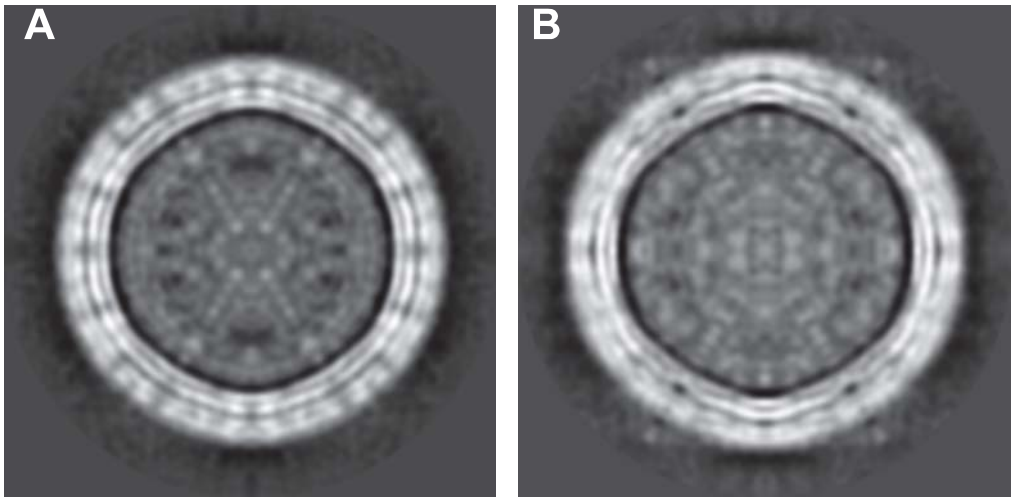


Figure S2. Three-dimensional classification of Uukuniemi virus particles, using the related Rift Valley fever virus as a reference.

A.) Central slice of three-dimensional UUKV class 1, obtained in RELION, using a previously published Rift Valley fever virus electron cryo-microscopy structure (EMDB 1550, Huiskonen *et al.* 2009, J Virol. 83(8): 3762-9) as a reference.

B.) Same as in A.), but Class 2.

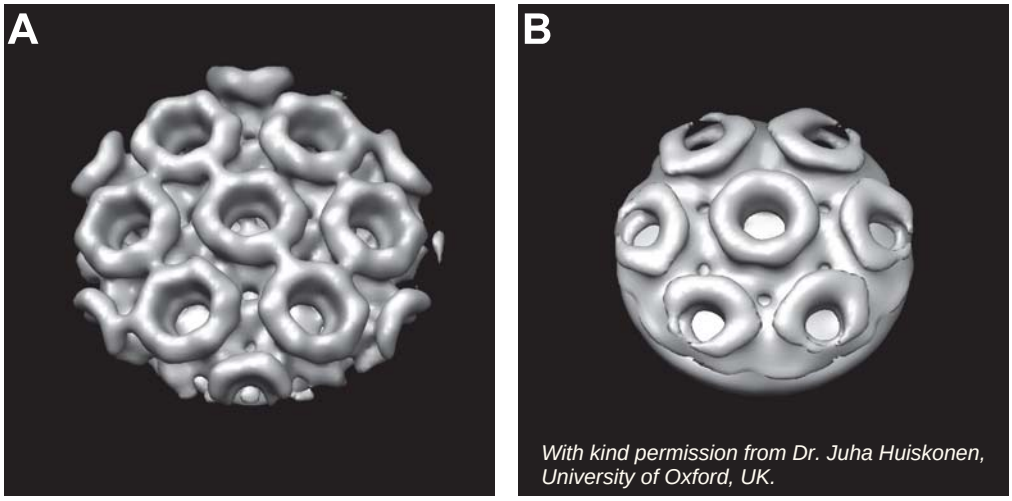


Figure S3. Electron cryo-tomography and sub-tomogram averaging of Uukuniemi virus spikes.

A.) Isosurface rendering of fixed Rift Valley fever virus hexamers, produced by icosahedral reconstruction, low-pass filtered to 30 Å resolution, and adapted from Huiskonen *et al.* 2009, J Virol, 83:3762–9.

B.) Isosurface rendering of native UUKV hexamers at 30 Å resolution, produced by electron cryo-tomography and subtogram averaging, using the software Jsubtomo (http://www.opic.ox.ac.uk/wiki/index.php/Jsubtomo).

Both images have been kindly provided by Dr. Juha Huiskonen, and the UUKV structure shown here is the work of both Alessandro Caputo and Dr. Juha Huiskonen.

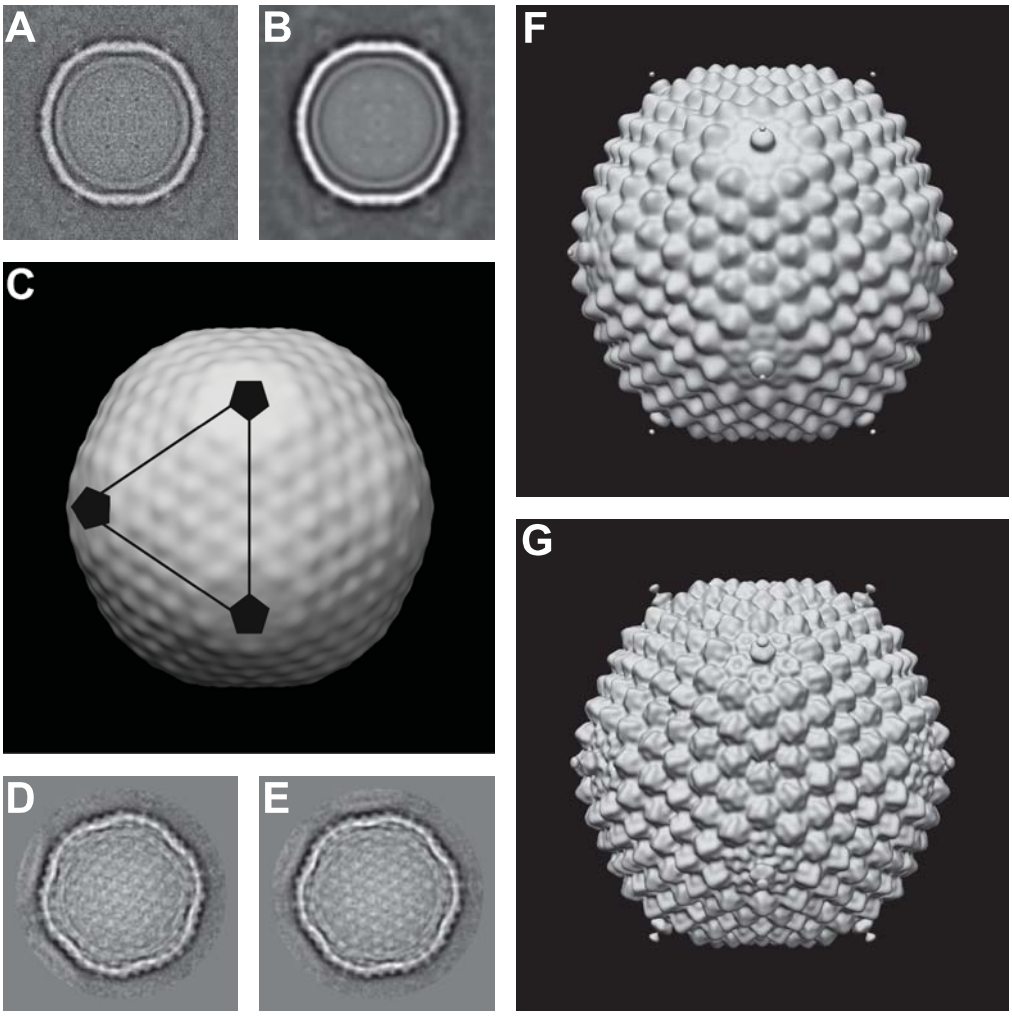


Figure S4. Icosahedral reconstruction of the bacteriophage SSIP-1: Initial model building in IMAGIC and particle classification in RELION.

A.) Central slice of Initial model of SSIP-1, reconstructed from 44 class averages in IMAGIC.

B.) Same as in A.), but filtered to 5 nm resolution.

C.) Same as in B.), but represented as full three-dimensional model. Fivefold symmetry axes are represented by pentagons.

D.) and E.) Two representative "good" two-dimensional class averages, as obtained in RELION.

F.) "Bad" three-dimensional class average (RELION), not selected for particle refinement.

G.) "Good" three-dimensional class average (RELION), representative of three class averages used for further processing steps.

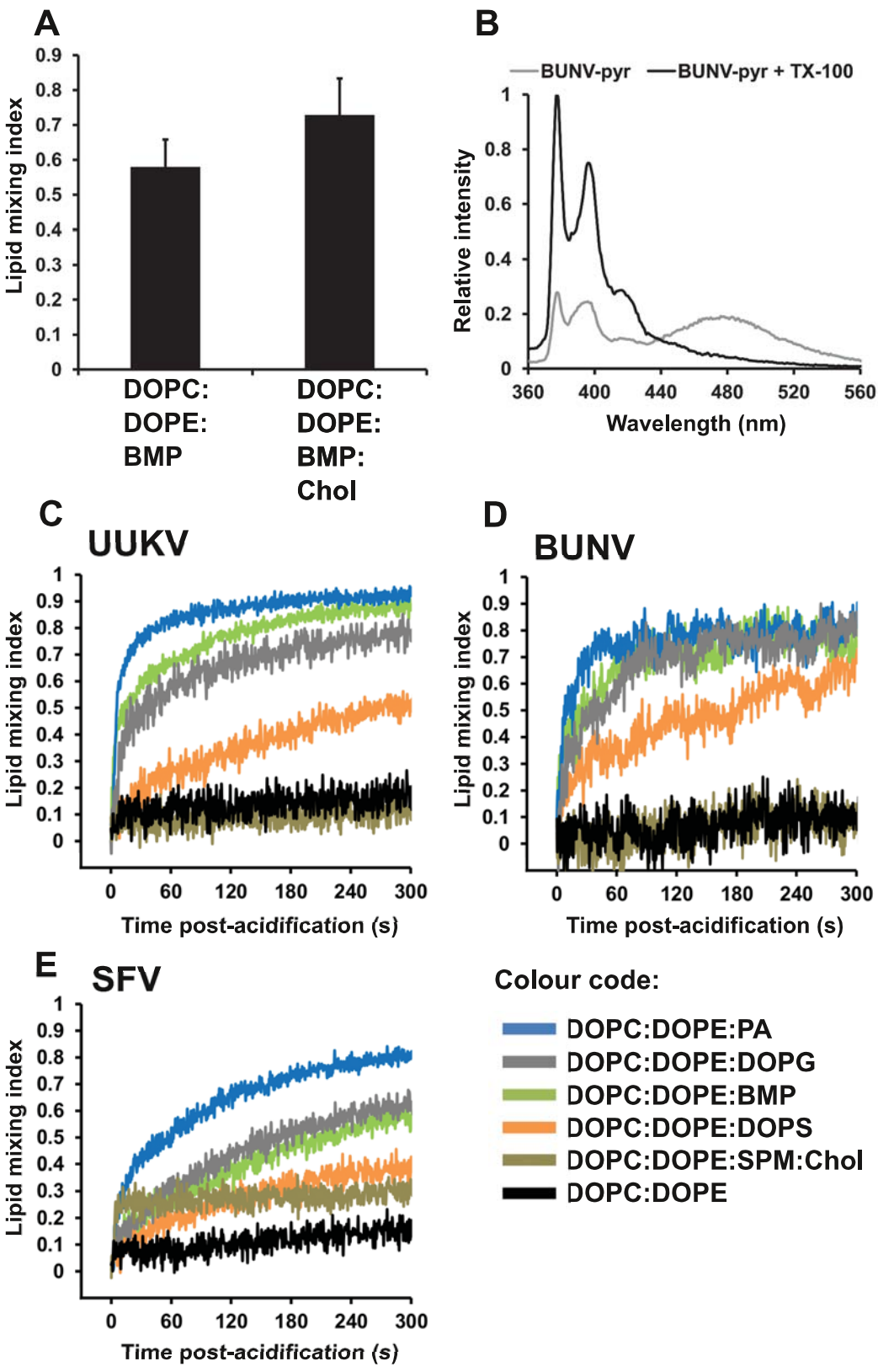

A
Lipid mixing index
0.9
0.8
0.7
0.6
0.5
0.4
0.3
0.2
0.1
0
DOPC: DOPE: BMP
DOPC: DOPE: BMP: Chol
B
BUNV-pyr
BUNV-pyr + TX-100
Relative intensity
1
0.8
0.6
0.4
0.2
0
360
400
440
480
520
560
Wavelength (nm)
C
UUKV
Lipid mixing index
0
60
120
180
240
300
Time post-acidification (s)
D
BUNV
Lipid mixing index
Time post-acidification (s)
E
SFV
Lipid mixing index
Time post-acidification (s)
Colour code:
DOPC:DOPE:PA
DOPC:DOPE:DOPG
DOPC:DOPE:BMP
DOPC:DOPE:DOPS
DOPC:DOPE:SPM:Chol
DOPC:DOPE

Figure S5: Supplemental data on viral lipid mixing.

A.) Lipid mixing of UUKV-pyr in presence of an excess of DOPC:DOPE:BMP liposomes or DOPC:DOPE:BMP:Chol liposomes, 5 minutes post-acidification. Note that there is no difference. Error bars indicate one standard deviation (N=3).

B.) BUNV-pyr (pyrene-labeled Bunyamwera virus) emission spectra in presence or absence of Triton X-100 (excitation at 345 nm). Note that the monomer peaks look slightly sharper than the ones in Figure 4.1 B and C, which is due to different excitation and emission slitwidths used.

C.) Lipid mixing curves at pH 4.5 in presence of UUKV-pyr.

D.) Same as C.), but with pyrene-labeled Bunyamwera virus (BUNV-pyr).

E.) Same as C.) and D.), but with SFV-pyr.

For all lipid ratios and abbreviations, please refer to table 1, chapter 2.

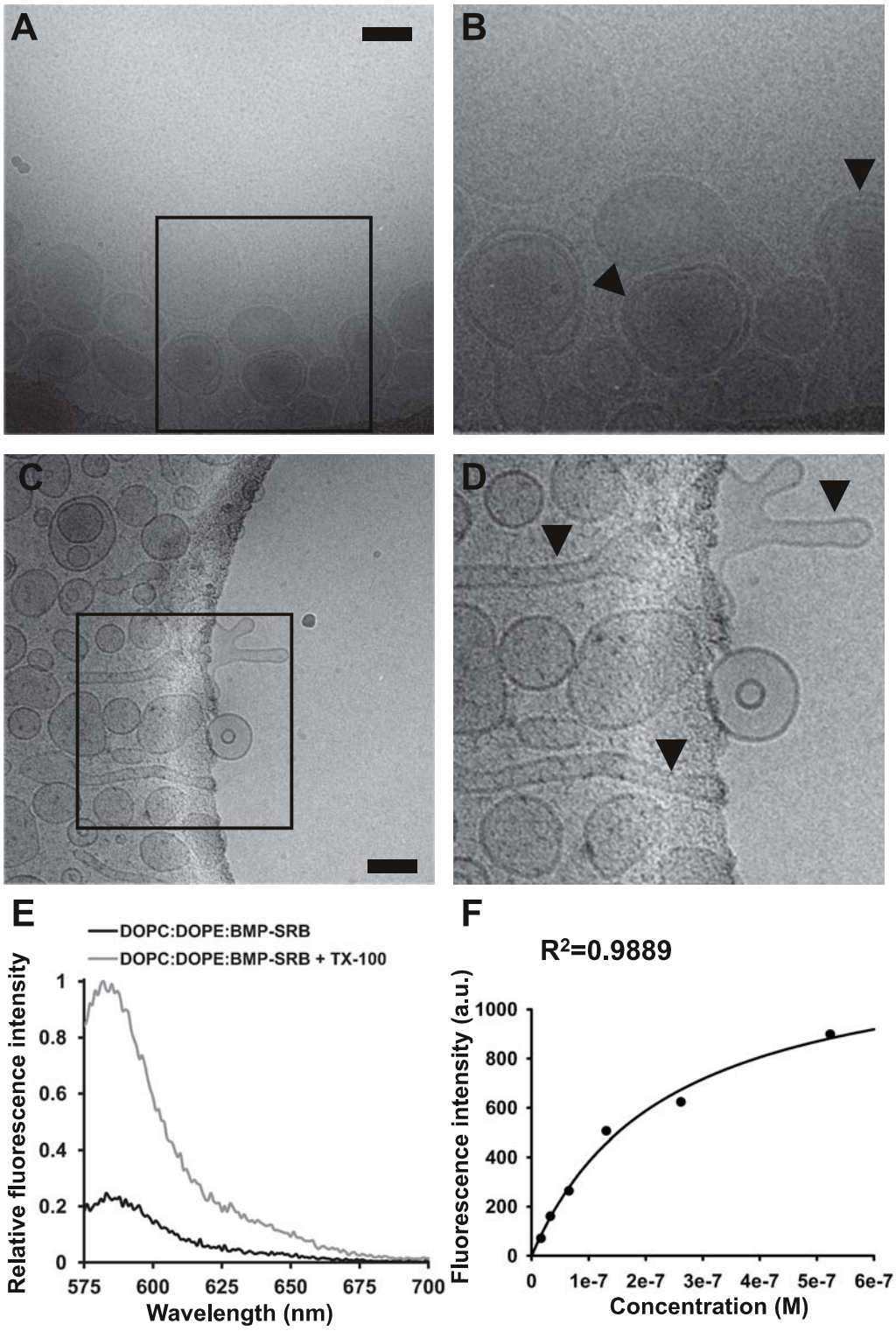

A
B
C
D
E
DOPC:DOPE:BMP-SRB
DOPC:DOPE:BMP-SRB + TX-100
Relative fluorescence intensity
Wavelength (nm)
F
R²=0.9889
Fluorescence intensity (a.u.)
Concentration (M)
G
**
Lipid mixing index
-Chol
+Chol
H
Content mixing index
-Chol
+Chol

Figure S6. Supplemental data on the Uukuniemi virus content release assay.

A.) DOPC:DOPE:BMP liposomes at neutral pH without freeze-thaw cycles in vitreous ice. Scale bar = 100 nm.

B.) Close-up of the boxed area in A.). Arrowheads indicate multilamellar liposomes.

C.) DOPC:DOPE:BMP liposomes at neutral pH with 10 freeze-thaw cycles in vitreous ice. Scale bar = 100 nm.

D.) Close-up of the boxed area in C.). Arrowheads indicate elongated, highly curved membrane structures of liposomes, which presumably are BMP-rich. Also note that most liposomes are unilamellar.

E.) Emission spectra of DOPC:DOPE:BMP liposomes labeled with 50mM SRB in presence or absence of Triton X-100 (TX-100) at neutral pH.

F.) Calibration curve of free SRB in the same fluorescence range as measured with SRB-labeled liposomes in fusion assays, including a hyperbolic curve fit and correlation coefficient.

G.) Lipid mixing of UUKV-pyr in presence of DOPC:DOPE:BMP-SRB liposomes ("-Chol") or DOPC:DOPE:BMP:Chol-SRB liposomes ("+Chol"), 10 minutes post-acidification. Liposomes are present in similar amounts than virions. Note that there is significantly less lipid in absence of cholesterol (**$p < 0.05$). Error bars indicate one standard deviation (N=3).

H.) Same as in G.) but showing the content mixing (SRB dequenching). Note that there is no significant difference in content mixing. Error bars indicate one standard deviation (N=4 for "-Chol" and N=3 for "+Chol").

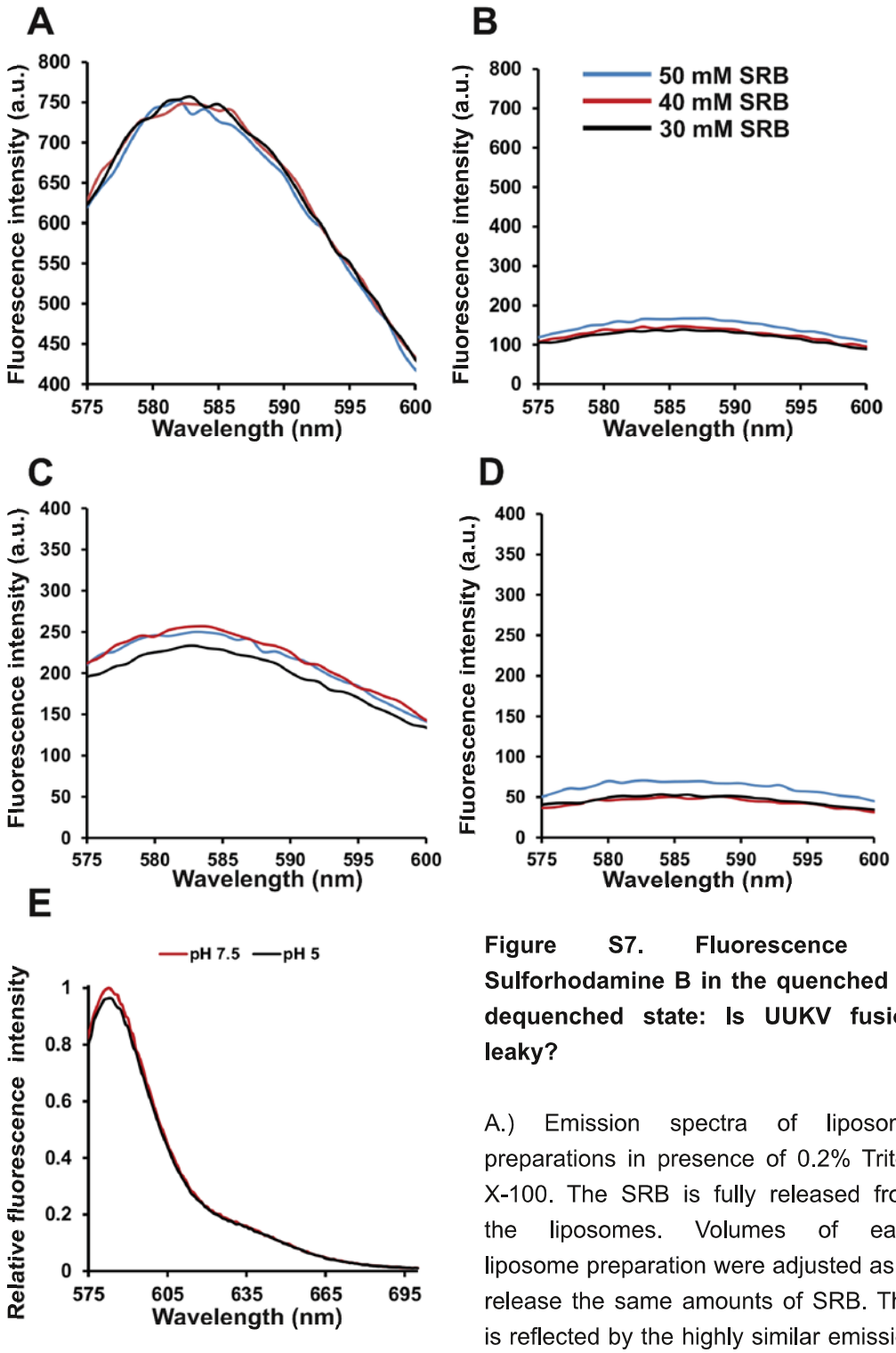


Figure S7. Fluorescence of Sulforhodamine B in the quenched or dequenched state: Is UUKV fusion leaky?

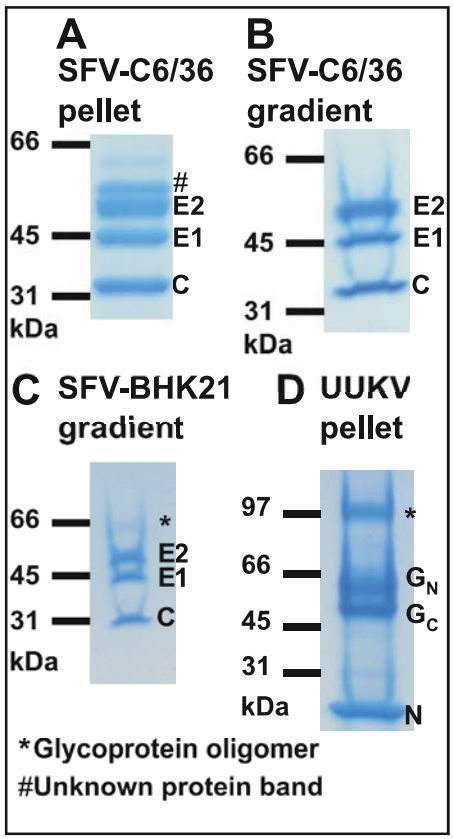
A.) Emission spectra of liposome preparations in presence of 0.2% Triton X-100. The SRB is fully released from the liposomes. Volumes of each liposome preparation were adjusted as to release the same amounts of SRB. This is reflected by the highly similar emission intensities.

B.) Same as in A.), but in absence of 0.2% Triton X-100. The same amount of liposome preparation for each respective preparation is added as in A.). Note that in this case, the fluorescence emission intensities are still very similar.

C.) Same as in A.), but in a lower fluorescence intensity range (less liposomes were measured but they were kept in the same ratio than in A.)).

D.) Same as in B.), but quenched fluorescence of liposomes in C.)

E.) Emission spectra of 50mM SRB liposomes at neutral and low pH.



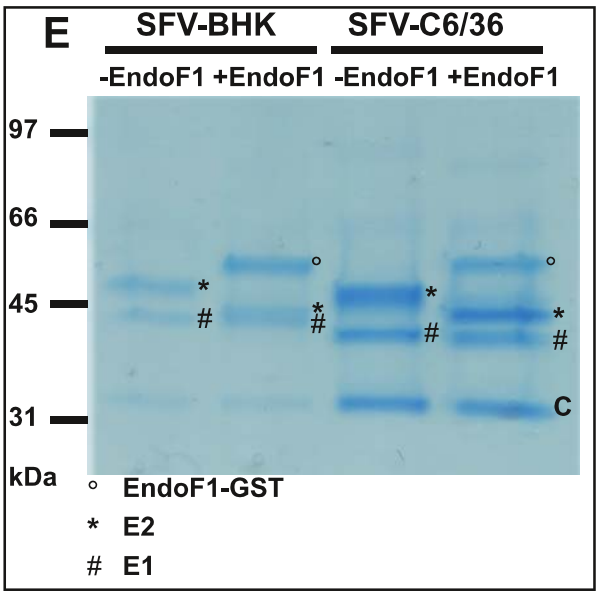


Figure S8: SDS-PAGE of virus preparations.

A.) SDS-gel overloaded with concentrated pellet of SFV produced in C6/36 cells.

B.) Same as in A.), but purified over a sucrose gradient. Note that the unassigned band above the E2 protein has disappeared.

C.) Same as in B.), but SFV produced in BHK-21 cells.

D.) Same as in A.) but with UUKV produced in BHK-21 cells.

E.) Gradient-purified SFV produced in either C6/36 cells or BHK-21 cells was subjected to EndoF1 digestion. Note that E2, but not E1 is EndoF1-sensitive in both virus preparations. C = capsid protein.

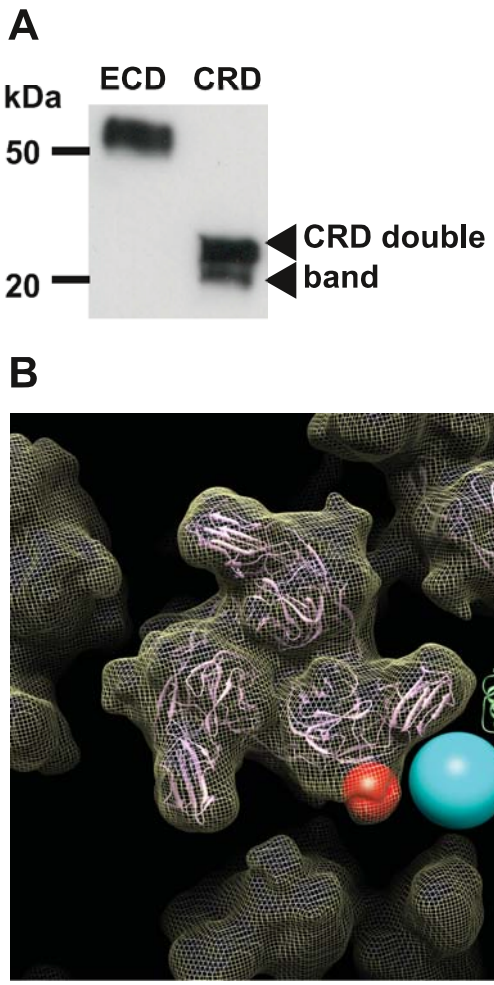


Figure S9: DC-SIGN expression and electron cryo-microscopy of SFV-DC-SIGN complexes

A.) Western blot of a DC-SIGN$_{CRD}$ and DC-SIGN$_{ECD}$ cell supernatant. 10 µL of supernatant were loaded in each lane, and the hexa-histidine tag was detected with a mouse anti-pentahistidine (first antibody) and a goat anti-mouse-HRP (second antibody)

B.) The SFV-DC-SIGN cryo-EM density map obtained in this thesis is depicted as a yellow mesh rendered at 1σ above the mean, with a close-up view on a trimeric spike. Chikungunya alphavirus (CHIKV) E1/E2 glycoprotein complexes (PDB 2XFC, in pink) are fitted into the trimeric SFV spikes (using UCSF Chimera), leaving a glycoprotein-free area in the intertrimeric spike crevices, corresponding to a putative DC-SIGN derived area (presumably the CRD domain, arrowhead). A red sphere with a volume of ~4200 Å^3 (radius of 10 Å) is placed into the latter density to give a scale to the putative DC-SIGN derived density. As a comparison, a DC-SIGN CRD crystal structure in complex with an oligosaccharide (PDB 2IT5) is shown in green, next to a blue sphere that has a similar volume (~17200 Å^3 or radius of 16 Å) than predicted for the CRD crystal structure (~17400 Å^3, as calculated for 2IT5 by the VADAR software (Leigh Willard, Anuj Ranjan,Haiyan Zhang,Hassan Monzavi, Robert F. Boyko, Brian D. Sykes, and David S. Wishart "VADAR: a web server for quantitative evaluation of protein structure quality" Nucleic Acids Res. 2003 July 1; 31 (13): 3316-3319)). Note that the blue sphere cannot be placed into the putative DC-SIGN derived density.

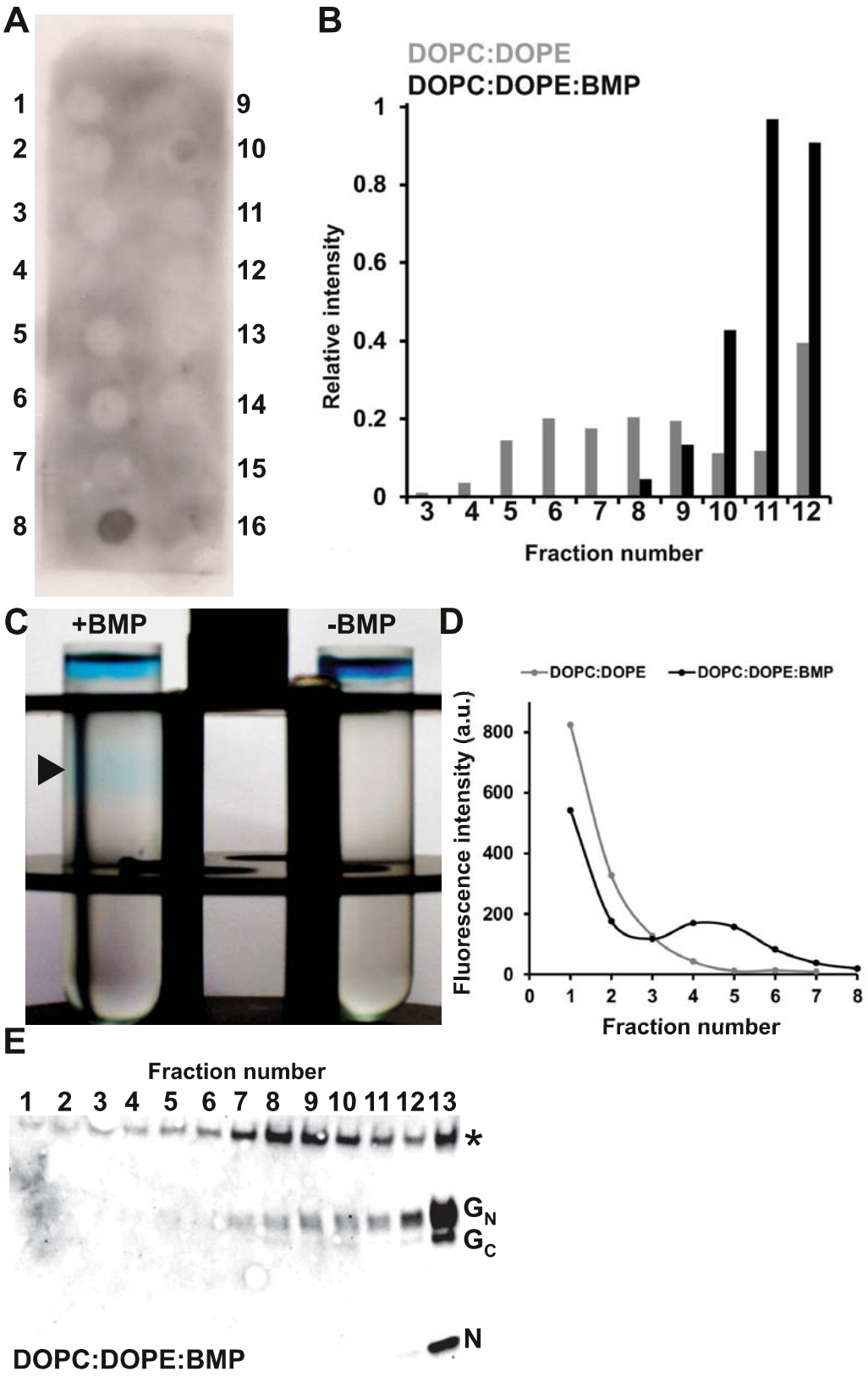

A
1
2
3
4
5
6
7
8
9
10
11
12
13
14
15
16
B
DOPC:DOPE
DOPC:DOPE:BMP
Relative intensity
0
0.2
0.4
0.6
0.8
1
3 4 5 6 7 8 9 10 11 12
Fraction number
C
+BMP
-BMP
D
DOPC:DOPE
DOPC:DOPE:BMP
Fluorescence intensity (a.u.)
0
200
400
600
800
0 1 2 3 4 5 6 7 8
Fraction number
E
Fraction number
1 2 3 4 5 6 7 8 9 10 11 12 13
*
G_N
G_C
N
DOPC:DOPE:BMP

Figure S10: Binding of Uukuniemi virus to liposomes.

A.) Lipid dot blot in presence of sucrose gradient purified UUKV particles. The phospholipids spotted on the dot blot were the following: 1=Triglyceride, 2=Diacylglycerol, 3=Phosphatidic acid, 4=Phosphaditylserine, 5=Phosphatidyleethanolamine, 6=Phosphatidylcholine, 7=Phosphatidylglycerol, 8=Cardiolipin, 9=Phosphatidylinositol, 10=Phosphatidylinositol-4-phosphate, 11=Phosphatidylinositol-4,5-bisphosphate, 12=Phosphatidylinositol-3,4,5-trisphosphate, 13=Cholesterol, 14=Sphingomyalin, 15=Sulfatide, 16=Blank (no lipid)

B.) Linear sucrose gradient profile of virus-liposome mixtures centrifuged over a linear gradient from the top down. Fractions of either DOPC:DOPE liposomes or DOPC:DOPE:BMP, both in presence of UUKV, were collected from the top of the gradient downwards (top = fraction 1, bottom = fraction 12) and subjected to SDS-PAGE and western blot analysis. The glycoprotein band intensity on western blots was measured for each fraction, normalized against a UUKV loading control with known concentration, and represented as a function of the respective fraction number. Note that here, UUKV sediments at lower densities in presence of DOPC:DOPE liposomes than in presence of DOPC:DOPE:BMP liposomes.

C.) Linear sucrose gradients of virus-liposome mixtures (in presence or absence of BMP containing liposomes), centrifuged over a linear gradient from the bottom up (flotation). Note the liposome-indicating blue band close to the middle of the sucrose gradient that is only visible in presence of BMP.

D.) Quantification of the DiD fluorescence emission associated with liposomes, obtained from a replicate experiment representative of C.).

E.) Western blot analysis of UUKV structural proteins in presence of BMP, from the same experiment as in D.). Note that the UUKV bands don't overlap with the liposome bands in C.) and D.). The asterisk indicates a glycoprotein oligomer.

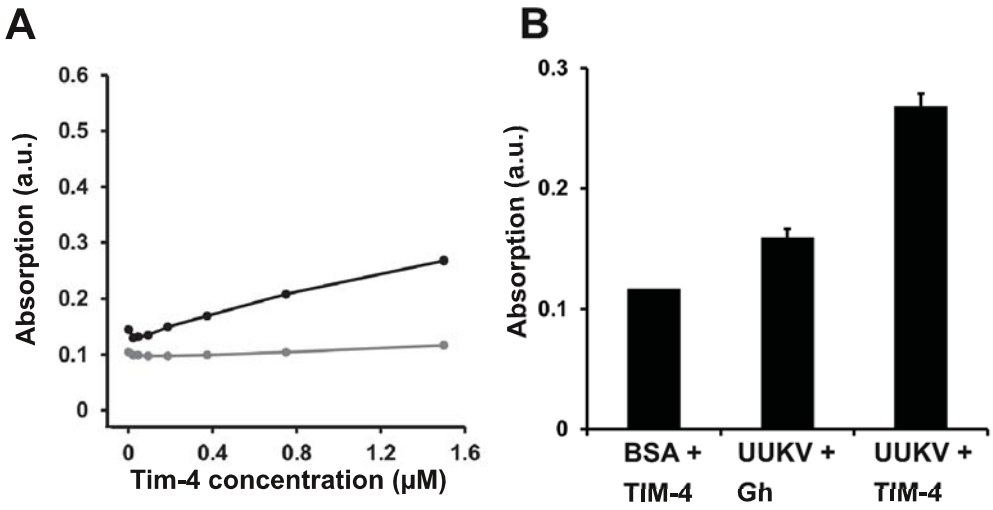


Figure S11: Binding of TIM-4 to Uukuniemi phlebovirus.

A.) Absorption at 405 nm in ELISA of UUKV in presence of the TIM-4. The curves are representative of two independent experiments. The grey curve indicates Tim-4 binding to BSA and the black curve indicates Tim-4 binding to UUKV.

B.) Quantification of TIM-4 binding at 1.5 µM. Error bars indicated are derived from one experimental duplicate. The difference between 1.5 µM Tim-4 and 1.5 µM G_h (negative control for TIM-4 binding to UUKV) binding to UUKV is statistically not significant ($p = 0.063$, $n=2$).